



**Synthesis, Characterisation and Radiolabelling of  
Nanoparticles for Applications in  
Medical Imaging**

being a Thesis submitted for the Degree of  
Doctor of Philosophy in the  
University of Hull

by

Tahani Meatag Alresheedi, MChem (KSU)

January 2020

## Abstract

Nanoparticles for medical applications are on the verge of having a major impact in modern medicine. They can be radiolabelled with a range of radionuclides and the accumulation in the target tissues can be observed by positron emission tomography (PET) or single photon emission computed tomography (SPECT) imaging, which can be combined with other imaging modalities such as magnetic resonance imaging (MRI). The colloidal and structural stability of radiolabelled nanoparticles is crucial to achieve targeting and an appropriate biodistribution *in vivo*. This work focuses on the development of radiolabelling methodologies for nanoparticles to enhance their stability for SPECT and PET imaging.

The chemical and magnetic properties of superparamagnetic iron oxide nanoparticles (SPIONs) are attractive for biomedical applications. Combining the use of SPIONs as MRI contrast agents with PET or SPECT isotopes can overcome some limitations. Chelator free approaches have been used to synthesise SPIONs that show good colloidal stability with hydrodynamic sizes of *ca.* 73 and 58 nm. The SPIONs were radiolabelled with technetium-99m to give a SPECT/MRI contrast agent. This method reduces the number of radiochemical synthesis steps required and would allow rapid adoption into clinical pathways.

A novel CXCR4-SPION targeted PET tracer was synthesised and radiolabelled with gallium-68 at up to 99% RCY. This was achieved by attaching a CXCR4 antagonist to surface of the SPION and relying on the chelator-free interaction of gallium-68 with the silica coating for radiolabelling.

Nanocarriers have new exciting applications that are emerging with potential for their use as drug delivery systems or in diagnostic techniques, both require understanding of their *in vivo* behaviour. Liposomes and polymeric micelles were radiolabelled with gallium-68 to allow tracking *in vivo*. Optimisation of the radiolabelling yields was carried out and preliminary *in vivo* experiments used to monitor the biodistribution of these particles.

## Acknowledgments

Firstly, I would like to express my deep gratitude and thanks to my supervisor Prof Steve Archibald for his continuous guidance, support and encouragement throughout my work. Thank you for your patience and understanding my situation to achieve this degree. I would also like to thank Dr Benjamin Burke for his expertise and all of his advice and guidance.

Special thanks to my sponsor the Saudi government and Qassim University for providing me the scholarship and for their unlimited support. I would also like to thank all members of the Archibald group past and present (Dr Juozas Domarkas, Isaline, Naomi, George, Alicija, Hayley, Becky, Farah, Michelle, Mitch and Dave) for their caring and support. A big thanks to Zainab Al-Ali, Fatimah, Eman, Shahenaz, Haya, Monerah, Fada and Bassim for their advice and friendship along the way. I would like to say thanks to all technical staff in the University of Hull, especially Dr Bob Knight and Mike Thompson for the ICP results. Thanks to Carol Kennedy for C, H, N analysis and Ann Lowry for TEM images.

Finally, a tremendous thank you is owed to my family. My mother, sisters, brothers and cousins who were by my side every time encouraging and praying for me. Last but not the least, I am grateful to my husband Hejab and my children Sultan, Renad, Musaad and Leen for their patience and supporting me spiritually throughout the PhD journey and my life in general, I promise you that life will be different in the next years.

## **Risk assessments**

All experiments were carried out in accordance with the University of Hull's Health and safety guidelines. A COSHH (Control of Substances Hazardous to Health) forms and risk assessments were carried out for each new experiment and signed by the undertaking student, supervisor (S. J. Archibald) and the departmental safety officer Dr T. McCreedy or Dr Mackenzie. The COSHH forms carried the reference format TR.

## Abbreviations

Å	Angstrom
Asp	Aspartate
AMD3100	1,1-[1,4-Phenylenebis(methylene)]bis[1,4,8,11-tetraaza cyclotetradecane]
Bo	Magnetic field strength
BOLD	Blood Oxygenation Level Dependent
BP	Bis phosphonate
BSA	Bovine serum albumin
BFC	Bifunctional chelator
β-	Electron
β+	Positron
CAs	Contrast agents
CMC	Critical micelles concentration
CT	Computed tomography
CB	Cross-bridged
Cyclam	1,4,8,11-Tetraazacyclotetradecane
Cyclen	1,4,7,10-Tetraazacyclododecane
Dox	Doxorubicin
DLS	Dynamic light scattering
DOTA	1,4,7,10-Tetraazacyclododecane-1,4,7,10-tetraacetic acid
DTPA	Diethylenetriaminepentaacetic acid

DSPE	1, 2-distearoyl-sn-glycero-3-phosphoethanolamine
EDTA	Ethylenediaminetetraacetic acid
EPR	Enhanced permeability and retention
FDA	Food and Drug Administration
FTIR	Fourier transform infrared
FACS	Fluorescence activated cell sorting
FDG	2-Deoxy-2-fluoro-D-glucose
GEM	Gemcitabine
GPTES	(3-Glycidyloxypropyl)triethoxysilane
HPLC	High Performance Liquid Chromatography
ICP-OES	Inductively coupled plasma- optical emission spectroscopy
ID/g	Incubated Dose per Gram
keV	Kilo electron volt
kDa	Kilodaltons
M	Molar
$\mu$ M	Micromolar
mM	Milimolar
mg	Milligram
mmol	Milimole
mL	Millilitre
MRI	Magnetic resonance imaging
MR	Magnetic resonance
Mo	Magnetisation vector

MS	Mass spectrometry
MBq	Mega Becquerel
MHz	Mega hertz
MWCO	Molecular weight cut off
mAb	Monoclonal antibody
NPs	Nanoparticles
NSF	Nephrogenic system fibroses
nm	Nanometres
NOTA	1,4,7-Triazacyclononane-1,4,7-triacetic acid
NMR	Nuclear magnetic resonance
NIRF	Near infrared fluorescence
OI	Optical imaging
PAA	Polyacrylic acid
PDI	Polydispersity index
PEG	Polyethylene glycol
PET	Positron emission tomography
PBS	Phosphate buffer solution
PM	Polymeric micelles
RT	Room temperature
RF	Radiofrequency
RCY	Radiochemical yield
RES	Reticuloendothelial system
RGD	Arginine-glycine-aspartate

SPECT	Single photon emission computed tomography
SPIONs	Superparamagnetic iron oxide nanoparticles
SIOPP	Superparamagnetic iron oxide platinum particles
SLN	Sentinel Lymph Node
SHH	Sonic hedgehog
SB	Side-bridged
TETA	1,4,8,11-Tetraazacyclotetradecane-1,4,8,11-tetraacetic acid
T	Tesla
$T_1$	Longitudinal relaxation
$T_2$	Transverse relaxation
TLC	Thin layer chromatography
TM	Transmembrane
TEM	Transmission electron microscopy
U87	Human primary glioblastoma
UV-Vis	Ultraviolet-visible
US	Ultrasound
XRD	X-ray diffraction
$\alpha$	Alpha
$\omega_0$	Precession frequency
$\lambda$	Wavelength
$\gamma$	Gyromagnetic ratio

# Table of contents

ABSTRACT .....	I
ACKNOWLEDGMENTS .....	II
RISK ASSESSMENTS .....	III
ABBREVIATIONS .....	IV
TABLE OF CONTENTS.....	VIII
LIST OF FIGURES .....	XIV
LIST OF TABLES .....	XIX
LIST OF SCHEMES .....	XX
LIST OF EQUATIONS .....	XXI
1. CHAPTER ONE: INTRODUCTION .....	2
1.1. Medical imaging .....	2
1.1.1 Nuclear medicine .....	4
1.1.2 Production of radionuclide .....	4
1.1.3 Production of a radionuclide from a generator .....	5
1.1.4 Production of a radionuclide from a cyclotron .....	5
1.1.5 Positron emission tomography (PET) imaging .....	6
1.1.6 Physical principles of PET imaging .....	7
1.1.7 Gallium-68 as PET radioisotope .....	8
1.1.8 Production of gallium-68 from a generator .....	8
1.1.9 Gallium chelators .....	9
1.1.10 Single photon emission computed tomography (SPECT) imaging.....	10
1.1.11 Magnetic Resonance Imaging (MRI) .....	14
1.1.12 Multi-Modality (PET/SPECT-MRI) imaging agents .....	20
1.2 Nanotechnology .....	24
1.2.1 Nanomaterials in medicine .....	24
1.2.2 Radiolabelling of nanoparticles.....	25
1.3 Superparamagnetic iron oxide nanoparticles (SPIONs) as contrast agents and in other medical applications.....	27
1.3.1 Chemical properties of Fe <sub>3</sub> O <sub>4</sub> nanoparticles.....	28
1.3.2 Synthesis of SPIONs.....	30
1.3.3 Surface Modification of SPIONs .....	31

1.4	Nanocarriers.....	32
1.4.1	Liposomes .....	33
1.4.2	Micelles .....	34
1.5	Research aims .....	36
2	CHAPTER TWO: CHELATOR-FREE TECHNETIUM-99M RADIOLABELLING OF SPIONS TO FORM DUAL MODALITY SPECT/MRI AGENTS .....	38
2.1	Aims.....	38
2.2	Superparamagnetic iron oxide nanoparticles (SPIONs) in medical applications .....	39
2.3	<sup>99m</sup> Tc radiolabelling of SPIONs for dual modality SPECT/MRI contrast agents	41
2.3.1	Radiolabelling of iron oxide nanoparticles for multi-modality imaging agents	42
2.4	Synthesis of SPIONs.....	44
2.4.1	Synthesis of SPIONs core by the co-precipitation method.....	44
2.4.2	Synthesis of siloxane derivatives coated- SPIONs.....	46
2.4.3	Synthesis of polyacrylic acid coated iron oxide nanoparticles via polyol	49
2.4.4	Synthesis of PAA-coated SPIONs.....	50
2.5	Characterisation of SPIONs .....	51
2.5.1	Structure characterisation (X-ray crystallography (XRD), particle size morphology and size distribution).....	51
2.5.2	Surface analysis by FT-IR .....	55
2.5.3	Zeta potential and elemental analysis .....	57
2.5.4	Relaxivity studies of the synthesised SPIONs.....	60
2.6	Radiochemistry reactions and stability studies for synthesised SPIONs with technetium-99m .....	63
2.6.1	<sup>99m</sup> Tc radiolabelling procedure for coated SPIONs .....	63
2.6.2	Stability study of <sup>99m</sup> Tc radiolabelling SPIONs.....	73
2.6.3	Stability of hydrodynamic size .....	79
2.7	Conclusion .....	80
3	CHAPTER 3: DEVELOPMENT OF <sup>68</sup> GA-LABELLED CXCR4-TARGETED SPIONS .....	83
3.1	Aims.....	83
3.1.1	Chemokine and chemokine receptors .....	85
3.1.2	CXCR4 chemokine receptor .....	85
3.1.3	CXCR4 antagonists.....	85

3.2	Introduction to nanomaterials targeting cancer cells .....	87
3.2.1	Multivalency and potential applications for nanoparticles .....	90
3.3	Design and functionalisation of CXCR4 targeted SPIONs .....	93
3.3.1	Synthesis of CB cyclam (1, 4, 8, 11-tetraazabicyclo[6.6.2]-hexadecane) 93	
3.3.2	Attachment of a siloxane derivative the cross-bridged cyclam.....	96
3.3.3	Functionalisation of SPIONs with Si-CB cyclam.....	98
3.3.4	Metal complex formation of SPION-SiO <sub>2</sub> -CB cyclam .....	100
3.4	Flow cytometry .....	104
3.5	Chelator-free <sup>68</sup> Ga radiolabelling of SPIONs-CXCR4 for PET imaging .....	106
3.5.1	<sup>68</sup> Ga radiolabelling procedure for SPIONs-CXCR4 antagonist.....	106
3.5.2	Stability study of <sup>68</sup> Ga radiolabelling SPIONs-Si-CXCR4 antagonist.....	112
3.5.3	Variation of hydrodynamic size .....	114
3.6	Conclusion .....	115
4	CHAPTER FOUR: <sup>68</sup> GA RADIOLABELLED NANOCARRIERS (LIPOSOMES AND POLYMERIC MICELLES) FOR <i>IN VIVO</i> PET IMAGING.....	117
4.1	Aims.....	117
4.2	Liposomes and polymeric micelles in medical applications .....	118
4.2.1	Liposomes .....	118
4.2.2	Micelles .....	119
4.3	Radiolabelling of liposomes and polymeric micelles .....	120
4.4	Radiolabelled liposomes 14 and micelles 15 for <i>in vivo</i> biodistribution studies 125	
4.4.1	Characterisation of liposomes and PM 14 and 15 .....	125
4.5	Radiochemistry reactions and radiolabelling stability studies for liposomes and polymeric micelles 14 and 15 with gallium-68 .....	126
4.5.1	<sup>68</sup> Ga radiolabelling procedure for liposomes and polymeric micelles 14 and 15 126	
4.5.2	<sup>68</sup> Ga radiolabelling liposomes and polymeric micelles in saline.....	128
4.5.3	<sup>68</sup> Ga radiolabelling of liposomes 14 and polymeric micelles 15 in sodium acetate.....	130
4.5.4	<sup>68</sup> Ga radiolabelling liposomes and polymeric micelles in sodium acetate at 250 MBq.....	131
4.5.5	Radiolabelled stability test for liposomes 14 and polymeric micelles 15. 133	

4.5.6	Size distribution stability of <sup>68</sup> Ga-liposomes 14 and <sup>68</sup> Ga-polymeric micelles 15.....	135
4.6	<i>In vivo</i> studies of <sup>68</sup> Ga radiolabelled liposomes and micelles.....	136
4.7	Conclusions .....	141
	CONCLUSION AND FUTURE DIRECTIONS .....	142
5	CHAPTER FIVE: CONCLUSION AND FUTURE DIRECTIONS .....	143
5.1	Conclusion .....	143
5.1	Future directions .....	146
5.1.1	Radiolabeling of chelator-free SPIONs.....	146
5.1.2	CXCR4-targeted SPIONs .....	147
5.1.3	Radiolabeling of liposomes and polymeric micelles .....	149
6	CHAPTER SIX: EXPERIMENTAL.....	151
6.1	General methodologies.....	151
6.2	Materials .....	151
6.3	Instrumentation .....	152
6.3.1	NMR spectroscopy .....	152
6.3.2	MRI phantom images .....	152
6.3.3	Mass Spectrometry (MS).....	152
6.3.4	CHN elemental analysis.....	153
6.3.5	ICP-OES analysis .....	153
6.3.6	DLS and zeta potential .....	153
6.3.7	TEM and EDX analysis .....	153
6.3.8	PXRD analysis .....	153
6.3.9	FT-IR spectroscopy .....	153
6.3.10	UV-Vis spectroscopy.....	154
6.3.11	Hot cell (PET centre).....	154
6.3.12	Elution for <sup>99</sup> Mo/ <sup>99m</sup> Tc generator .....	154
6.3.13	Preparation of <sup>68</sup> Ga .....	154
6.3.14	Radio- TLC scanner .....	155
6.3.15	Gamma counter .....	155
6.3.16	PET/CT scanning.....	155
6.4	Synthesis of coated SPIONs.....	157
6.4.1	Synthesis of “bare” iron oxide (magnetite nanoparticles) 1.....	157
6.4.2	Synthesis of siloxane coated SPIONs 2.....	158

6.4.3	Synthesis of PAA coated SPIONs 3 .....	160
6.5	<sup>99m</sup> Tc radiolabelled SPIONs .....	161
6.5.1	Reducing <sup>99m</sup> Tc(VII) to <sup>99m</sup> Tc(V) .....	161
6.5.2	<sup>99m</sup> Tc(VII) radiolabelled SPIONs.....	162
6.5.3	<sup>99m</sup> Tc(I) radiolabelled of SPIONs 2 and 3 .....	163
6.5.4	<sup>99m</sup> Tc radiolabelling SPIONs 2 and 3 at different concentrations .....	164
6.5.5	<sup>99m</sup> Tc radiolabelling of SPIONs 2 and 3 in different buffers.....	165
6.5.6	<sup>99m</sup> Tc radiolabelling of SPIONs 2 and 3 in NaOAc at different pH.....	165
6.5.7	<sup>99m</sup> Tc radiolabelling of SPIONs 2 and 3 in NaOAc at different pH.....	166
6.5.8	<sup>99m</sup> Tc radiolabelling of SPIONs 2 and 3 in saline at 37°C.....	166
6.5.9	<sup>99m</sup> Tc radiolabelling of SPIONs 2 and 3 in saline at 90°C.....	167
6.5.10	<sup>99m</sup> Tc radiolabelling of SPIONs 2 and 3 in NaOAc and PBS at 37°C..	167
6.5.11	<sup>99m</sup> Tc radiolabelling of SPIONs 2 and 3 in NaOAc and PBS at 90°C..	168
6.5.12	Stability of <sup>99m</sup> Tc radiolabelling of SPIONs 2 and 3 in EDTA.....	168
6.5.13	Stability of <sup>99m</sup> Tc radiolabelling of SPIONs 2 and 3 over a range of pH values	169
6.5.14	Stability of <sup>99m</sup> Tc radiolabelling SPIONs at different proteins.....	170
6.6	Synthesis of CXCR4 antagonist-conjugated SPIONs.....	171
6.6.1	Synthesis of cis-3a, 5a, 8a, 10a-tetraazaperhydropyrene (Bridged cyclam) 4 <sup>200</sup> .....	171
6.6.2	Synthesis of 3a, 8a-dibenzyl-decahydro-3a, 5a, 8a, 10a-tetraazapyrenium dibromide 5 <sup>201</sup> .....	172
6.6.3	Synthesis of 4,11-dibenzyl-1,4,8,11-tetraazabicyclo [6.6.2] hexadecane 6 <sup>201</sup>	173
6.6.4	Synthesis of 1,4,8,11-tetraazabicyclo[6.6.2]hexadecane (Cross-bridged cyclam) 7 .....	174
6.6.5	Synthesis of siloxane derivative ligand on cross-bridged cyclam (Si-CB cyclam) 8 .....	175
6.6.6	Synthesis of SPIONs core compound 9 .....	175
6.6.7	Functionalisation of SPIONs with Si-CB cyclam (SPIONs-Si-CB cyclam)	176
6.6.8	Metal complexation of SPIONs-Si-CB cyclam 11.....	177
6.6.9	Zinc acetate attached SPIONs-Si-CB cyclam (Zn-SPIONs-Si-CB cyclam)	178
6.6.10	Nickel acetate attached SPIONs-Si-CB cyclam (Ni-SPIONs-Si-CB cyclam) 13 .....	179

6.7	<sup>68</sup> Ga radiolabelling SPIONs-Si-CB cyclam .....	180
6.7.1	<sup>68</sup> Ga radiolabelled Cu-SPIONs-Si-CB cyclam at RT, 50°C and 90°C .....	180
6.7.2	<sup>68</sup> Ga radiolabelled different SPIONs-Si-CB cyclam at 50°C .....	181
6.7.3	Stability of <sup>68</sup> Ga radiolabelled SPIONs-Si-CB cyclam 10 in <i>Apo</i> -transferrin 181	
6.7.4	Stability of <sup>68</sup> Ga radiolabelled Cu-SPIONs-Si-CB cyclam 11 in <i>Apo</i> - transferrin .....	182
6.7.5	Stability of <sup>68</sup> Ga radiolabelled Zn-SPIONs-Si-CB cyclam 12 in <i>Apo</i> - transferrin .....	182
6.7.6	Stability of <sup>68</sup> Ga radiolabelled Ni-SPIONs-Si-CB cyclam 13 in <i>Apo</i> - transferrin .....	183
6.8	Radiolabelling liposomes 14 and micelles 15 with <sup>68</sup> Ga .....	184
6.8.1	Radiolabelling method for liposomes 14 and micelles 15 with <sup>68</sup> Ga...	184
6.8.2	<sup>68</sup> Ga radiolabelling liposomes 14 and polymeric micelles 15 in saline at room temperature .....	184
6.8.3	<sup>68</sup> Ga radiolabelling liposomes 14 and polymeric micelles 15 in saline at 60°C	185
6.8.4	<sup>68</sup> Ga radiolabelling liposomes 14 and polymeric micelles 15 in sodium acetate .....	186
6.8.5	<sup>68</sup> Ga radiolabelling liposomes 14 and polymeric micelles 15 in sodium acetate at 250 MBq.....	187
6.8.6	Radiolabelling stability of liposomes 14 and polymeric micelles 15 ...	188

## List of figures

Figure 1: Characteristics of different medical imaging techniques. ....	3
Figure 2: The process of production of a radionuclide from a generator or cyclotron followed by radiochemical reaction in a hot cell and the analysis or purification steps before the PET/CT scan. ....	5
Figure 3: Example of a clinical PET-CT scanner (Toshiba Celestion) (Reproduced from Toshiba America Medical System). ....	6
Figure 4: Diagram shows the principles of positron emission and gamma detection involved in a PET scan. ....	7
Figure 5: Nuclear decay diagram of germanium-68 to gallium-68 to zinc-68. ....	8
Figure 6: Chemical structures for macrocyclic chelators DOTA, TETA and NOTA. ....	9
Figure 7: Chemical structures for acyclic compounds DEDPA and DTPA. ....	10
Figure 8: Principles of single photon emission computed tomography (SPECT) scanner design. ....	11
Figure 9: A) $^{99m}\text{Tc}$ generators and B) decay scheme of $^{99}\text{Mo}$ from $^{99}\text{Mo}/^{99m}\text{Tc}$ generator. ....	13
Figure 10: A) Clinical MRI scan and B) preclinical MRI scan. ....	14
Figure 11: A nucleus shows a parallel magnetic moment to the external magnetic field resulting in a precession motion. ....	15
Figure 12: Alignment of proton spins in the presence and absence of the magnetic field. ....	16
Figure 13: Diagram shows the rotation of protons by $90^\circ$ by application of an external magnetic field. ....	17
Figure 14: $T_1$ and $T_2$ MR Images for a patient with focal nodular myositis. <sup>[25]</sup> ....	17
Figure 15: Longitudinal relaxometry curve. ....	18
Figure 16: Structures of three clinical MRI gadolinium contrast agents. ....	19
Figure 17: Transverse relaxometry curve for $T_2$ relaxation. ....	19
Figure 18: Potential of multimodal contrast agents based on MRI iron oxide contrast agent. ....	21

Figure 19: In vivo images for dual modalities, using PET/MRI contrast agents. <sup>[35]</sup> ...	21
Figure 20: Functionalised iron oxide NPs with several moieties. ....	23
Figure 21: Schematic representation of the accumulation of nanoparticles in tumour tissue by either the EPR effect or active targeting. ....	25
Figure 22: Common methods for radiolabelling nanoparticles including chelator- free method, final-step chelator and two step chelator methods. ....	26
Figure 23: Multi-domains for ferromagnetic particles and the single domain for superparamagnetic nanoparticles aligned with the external magnetic field. ....	28
Figure 24: Magnetite structure is a cubic inverse spinel with locations of Fe <sup>3+</sup> and Fe <sup>2+</sup> ions at the tetrahedral and octahedral sites. ....	28
Figure 25: Coated SPIONs with core and hydrodynamic size shown. ....	29
<i>Figure 26: Structure and types of liposomes, MLV= multilamellar vesicles, LUV= large unilamellar vesicles, and SUV= small unilamellar vesicles. ....</i>	<i>33</i>
<i>Figure 27: Schematic representation for the structure of polymeric micelle. ....</i>	<i>34</i>
Figure 28: Gallium-68 radiolabelling A) CXCR4 antagonist conjugated SPIONs, B) radiolabelling of chelator functionalised liposomes. ....	36
Figure 29: SPIONs coated with siloxane derivatives and polyacrylic acid. ....	38
Figure 30: PEGylated siloxane used to modify the SPIONs surface forming a silica shell with PEG chains and functional groups for further reaction. ....	40
Figure 31: Technetium-99m radiolabelled nanoparticles <sup>99m</sup> Tc-SPIONs. ....	41
Figure 32: Synthesis of siloxane coated iron oxide nanorods for radiolabelling with <sup>68</sup> Ga. ....	43
Figure 33: The DLS analysis shows the hydrodynamic size for siloxane@SPIONs <b>2</b> . ....	48
Figure 34: Structures of PAA and DEG used with the polyol method in this work. ....	50
<i>Figure 35: The DLS analysis shows the hydrodynamic size for PAA@SPIONs <b>3</b>. ....</i>	<i>51</i>
<i>Figure 36: PXRD patterns for SPIONs synthesised by the co-precipitation method, siloxane@SPIONs <b>2</b> and PAA@SPIONs <b>3</b>. Peaks are indexed according to the reference pattern for magnetite. ....</i>	<i>53</i>
<i>Figure 37: TEM images for coated nanoparticles A) siloxane@SPIONs <b>2</b>, and B) PAA@SPIONs <b>3</b>. ....</i>	<i>54</i>
<i>Figure 38: Histograms for SPIONs, A) coated with siloxane <b>2</b>, and B) coated with PAA <b>3</b> (minimum 80 nanoparticles were counted). ....</i>	<i>55</i>

<i>Figure 39: FT-IR spectrum for siloxane@SPIONs 2</i> .....	56
<i>Figure 40: FT-IR spectrum for PAA@SPIONs 3</i> .....	57
<i>Figure 41: T<sub>1</sub> and T<sub>2</sub> MRI relaxivity plots of siloxane@SPIONs 2 and PAA@SPIONs 3 at range of Fe concentrations (0.1-1 mM) at 1.4 T</i> .....	60
<i>Figure 42: Phantom images of A) T<sub>1</sub> and B) T<sub>2</sub> for PAA@SPIONs 3 measured under 3 T clinical scanner at range of Fe concentrations</i> .....	62
<i>Figure 43: Technetium(V) coordination chemistry, (left) the square pyramidal configuration for TcO<sup>3+</sup>, (right) the octahedral configuration for TcO<sub>2</sub><sup>+</sup></i> .....	64
<i>Figure 44: Schematic representation of <sup>99m</sup>Tc radiolabelling SPIONs procedure</i> .....	65
<i>Figure 45: RCY for <sup>99m</sup>Tc-siloxane@SPIONs in saline at different concentrations incubated for 30 minutes at RT (n=2)</i> .....	66
<i>Figure 46: RCY% for <sup>99m</sup>Tc-PAA@SPIONs in saline at different concentrations incubated for 30 minutes at RT (n=2)</i> .....	67
<i>Figure 47: RCY% for both <sup>99m</sup>Tc-SPIONs in PBS and NaOAc buffers both at pH 7 incubated for 30 minutes at RT (n=2)</i> .....	68
<i>Figure 48: RCY% for both <sup>99m</sup>Tc-SPIONs at different pH 4, 5 and 7 incubated for 30 min at RT (n=2)</i> .....	69
<i>Figure 49: RCY% for both <sup>99m</sup>Tc-SPIONs in saline incubated for 30 minutes at 37°C and 90°C (n=2)</i> .....	70
<i>Figure 50: RCY% for both <sup>99m</sup>Tc-SPIONs in PBS pH 7 incubated for 30 minutes at 37°C and 90°C (n=2)</i> .....	71
<i>Figure 51: RCY% for both <sup>99m</sup>Tc-SPIONs in NaOAc pH 4 incubated for 30 minutes at 37°C and 90°C (n=2)</i> .....	72
<i>Figure 52: Stability reactions for both <sup>99m</sup>Tc-SPIONs in (100 µl, 0.1 M) EDTA incubated for 30 and 60 minutes at RT (n=2)</i> .....	74
<i>Figure 53: Radiochemical stability for <sup>99m</sup>Tc-SPIONs in ammonium acetate at range of pH (3, 5 and 11) incubated for 30 minutes at RT (n=2)</i> .....	75
<i>Figure 54: schematic representation for stability procedure of <sup>99m</sup>Tc-SPIONs in serum using the gel electrophoresis technique and measured the gel with gamma counter</i> .....	76
<i>Figure 55: The DLS analysis for A) siloxane@SPIONs 2 and B) PAA@SPIONs 3, the red line before radiolabelling, the green line after radiolabelling with <sup>99m</sup>Tc</i> .....	79

Figure 56: Structure of mono-macrocyclic compound AMD3465 prepared by Bridger et al. <sup>[123]</sup> .....	86
Figure 57: Structure of bis-macrocycle AMD 3100. ....	86
Figure 58: Schematic representation describes the multivalence approach. ....	91
Figure 59: Schematic illustration of $\alpha v \beta 3$ receptor binding of A) NP-cRGD100-2k, B) NP-cRGD100-3.5K, C) NP-cRGD100-5k. Reproduced from Abstins et al. <sup>[144]</sup> .....	91
Figure 60: Electrospray mass spectra for synthesised macrocycles A) formation of bridged cyclam, B) formation of bis-benzy bridged cyclam, C) formation of bis-benzyl cross-bridged cyclam and D) formation of cross-bridged cyclam.....	95
Figure 61: A) <sup>1</sup> H NMR and B) MS for Si-CB cyclam <b>8</b> . ....	97
Figure 62: A) XRD pattern and B) TEM images for SPIONs-Si-CB cyclam <b>10</b> .....	99
Figure 63: FT-IR spectrum of SPION-Si-CB cyclam <b>10</b> . ....	100
Figure 64: Metal complex formation of SPION-SiO <sub>2</sub> -CB cyclam with copper(II), zinc(II) and nickel(II). ....	101
Figure 65: Analysis for three metal complexation SPIONs, A) PXRD for Fe <sub>3</sub> O <sub>4</sub> and complexes <b>11</b> , <b>12</b> and <b>13</b> . The TEM images for B) copper C) zinc and D) nickel complexed SPIONs. ....	102
Figure 66: Flow cytometry A) histograms and B) dot plots for samples <b>10</b> and <b>11</b> .105	
Figure 67: Schematic representation of <sup>68</sup> Ga radiolabelling of SPIONs-Si-CXCR4 antagonist.....	108
Figure 68: <sup>68</sup> Ga radiolabelling of Cu-SPIONs-Si-CXCR4 in ammonium acetate buffer pH 5 at RT, 50 °C and 90 °C for 15 min (n=3). ....	109
Figure 69: <sup>68</sup> Ga radiolabelling of zinc(II), nickel(II) and free metal SPIONs-Si-CXCR4 antagonist in ammonium acetate pH 5 at 50°C for 15 min (n=3).....	111
Figure 70: Schematic representation of the stability test for SPIONs-Si-CXCR4 antagonist with apo-transferrin.....	112
Figure 71: Stability test of <sup>68</sup> Ga-SPIONs-Si-CXCR4 antagonists <b>10</b> , <b>11</b> , <b>12</b> and <b>13</b> with apo-transferrin during 60 minutes (n=3). ....	113
Figure 72: Schematic representation of radiolabelling liposomes and polymeric micelles with Ga-68.....	117
Figure 73: schematic diagram for radiolabelling methods of liposomes. <sup>[166]</sup> .....	120

Figure 74: SPECT images for <sup>99m</sup> Tc-DTPA-PM administration in tumour-bearing mice after 1 (A), 4 (B), 8 (C) and 24 hours (D), arrows indicate tumour site.....	123
Figure 75: The hydrodynamic sizes for (A) DTPA-L <b>14</b> and (B) DTPA-PM <b>15</b> . .....	126
Figure 76: Schematic representation of the <sup>68</sup> Ga radiolabelling procedure used for liposomes and micelles <b>14</b> and <b>15</b> . .....	128
Figure 77: Radio-TLC scan for <sup>68</sup> Ga-radiolabelled liposomes <b>14</b> in saline for 15 minutes at RT. ....	129
Figure 78: Radio-TLC in saline of the <sup>68</sup> Ga-radiolabelled nanocarriers incubated for 15 minutes at 60°C for A) Liposome <b>14</b> and B) PM <b>15</b> . ....	130
Figure 79: Radio-TLC of <sup>68</sup> Ga radiolabelled (50 MBq) <b>14</b> and <b>15</b> in sodium acetate buffer (pH 5) at RT and 60°C for 15 minutes. ....	131
Figure 80: Radio-TLC of <sup>68</sup> Ga-radiolabelled <b>14</b> and <b>15</b> with 250 MBq of activity in sodium acetate buffer, pH 5 at 60°C for 15 minutes (n=2). ....	132
Figure 81: Plot of radio-TLC stability measurements for <sup>68</sup> Ga- <b>14</b> and <sup>68</sup> Ga- <b>15</b> incubated in serum after 5, 15, 30 and 45 minutes.....	134
Figure 82: DLS analysis of the hydrodynamic sizes of <sup>68</sup> Ga-radiolabelled <b>14</b> and <b>15</b> . .....	135
Figure 83: Dynamic PET/CT scan for gallium radiolabelling liposomes <sup>68</sup> Ga-14 from 0 to 66 minutes. ....	138
Figure 84: PET/CT scan for gallium radiolabelling polymeric micelles <sup>68</sup> Ga-15 A) dynamic scan from 0 66 min, B) static scan after four hours (30 min acquisition). 140	

## List of tables

Table 1: Properties of commonly used PET radioisotopes. ....	7
Table 2: Commonly used SPECT radioisotopes, decay characteristics and production methods. <sup>[15b, 16]</sup> .....	11
Table 3: Constants of selected nuclei used in MRI. ....	16
Table 4: Comparison between different synthetic methods for SPIONs.....	31
Table 5: List of FDA-approved SPIONS products. <sup>[79]</sup> .....	39
<i>Table 6: Crystallite sizes for siloxane@SPIONs and PAA@SPIONs.....</i>	<i>53</i>
Table 7: Elemental analysis and zeta potential for siloxane@SPIONs and PAA@SPIONs.....	58
<i>Table 8: The hydrodynamic sizes and relaxivity rates for PAA@SPIONs and RGD-PAA@SPIONs from reference 40. ....</i>	<i>61</i>
Table 9: Radiolabelling of SPIONs in <sup>99m</sup> Tc (VII) and (I). ....	65
Table 10: Stability of <sup>99m</sup> Tc-siloxane@SPIONs in different proteins.....	78
Table 11: Stability of <sup>99m</sup> Tc-PAA@SPIONs in different proteins. ....	78
Table 12: The DLS measurements and core sizes for <b>11</b> , <b>12</b> and <b>13</b> .....	102
Table 13: The hydrodynamic sizes (diameter) for SPIONs-SiO <sub>2</sub> -CXCR4 before and after <sup>68</sup> Ga radiolabelling.....	114

## List of schemes

Scheme 1: Schematic representation of the synthetic steps required for SPIONs core production by co-precipitation method. ....	45
Scheme 2: Chemical reaction for synthesis of the SPIONs core. ....	45
Scheme 3: Schematic representation of silica coating of the SPIONs with a siloxane derivative.....	46
Scheme 4: Schematic representation of the A) hydrolysis and B) condensation steps for coating SPIONs with a siloxane derivative. ....	47
Scheme 5: Schematic representation of the synthetic steps used to form PAA@SPIONs via the polyol method. ....	50
Scheme 6: Schematic representation of SPIONs-SiO <sub>2</sub> -CB cyclam (CXCR4 antagonist) radiolabelling and biological interaction. ....	84
Scheme 7: Formation of CB cyclam from cyclam.....	94
Scheme 8: Macrocyclic siloxane reaction to form siloxy-CB cyclam 8. ....	97
Scheme 9: Schematic representation the reaction of siloxy-CB cyclam with SPIONs. ....	98
Scheme 10: Formation of <sup>68</sup> Ga complexation with SPIONs-Si-CXCR4 antagonist <b>10</b> , <b>12</b> and <b>13</b> .....	110
Scheme 11: Representative scheme of the synthesis of DSPE-PEG <sub>2000</sub> -DTPA. <sup>[157]</sup> ..	122
Scheme 12: Schematic representative showing the conjugation of CB bis-tetraazamacrocyclic unit with GPTES in order to functionalise the SPIONs surface. ....	148

## List of equations

Equation 1 .....	15
Equation 2 .....	52

# **Chapter 1**

## **Introduction**

# **1. Chapter one: Introduction**

## **1.1. Medical imaging**

Medical imaging is a fundamental part of modern medicine, it includes several techniques for visualisation of the human body in order to diagnose, monitor or treat medical conditions, see Figure 1. The concept for all imaging techniques is the interaction between electromagnetic or chemical energy with an object. Those interactions cause some physical process such as absorption, emission or scatter which leads to a change in the energy that can be detected and used to generate an image.<sup>1-3</sup>

A number of imaging modalities are employed for clinical purposes such as optical imaging (OI), Ultrasound (US), Computed Tomography (CT), Positron Emission Tomography (PET), Single Photon Emission Computed Tomography (SPECT) and Magnetic Resonance imaging (MRI), see Figure 1 .

Each type of imaging technique has advantages and disadvantages. Therefore, it gives different information depending on the tissue depth, spatial resolution and sensitivity. To enhance these properties, development of additional imaging contrast agents is required. Moreover, multimodal imaging can reduce limitations by combining modalities such as PET/MRI, SPECT/MRI or PET/CT to form powerful combination techniques that can provide reliable and accurate information.<sup>4</sup>

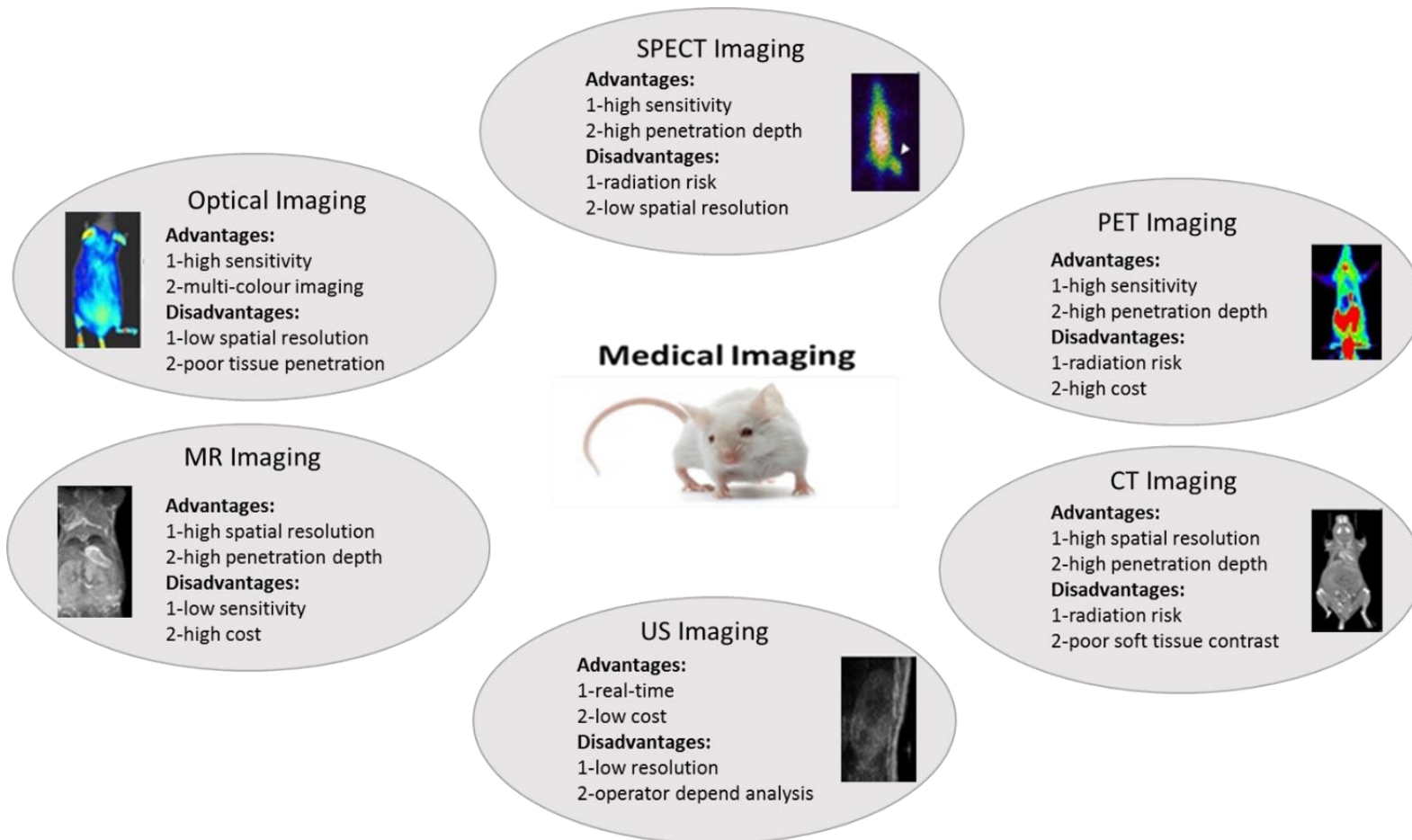


Figure 1: Characteristics of different medical imaging techniques.

### **1.1.1 Nuclear medicine**

The term nuclear medicine or radionuclide imaging was recognised in 1946 following the use of radioactive iodine-131 to treat thyroid cancer. Nuclear medicine has now become wide-spread in both clinical and preclinical applications. {Boros, 2019 #442} Radionuclide imaging laboratories exist in almost every hospital, performing numerous procedures that reach thousands of imaging studies per month to help diagnose and treat patients.<sup>5,6</sup>

Nuclear medicine has increased the understanding of disease stages by detecting the distribution of the radiotracers and tracking biochemical pathways, the information gained by these processes *in vivo* is called molecular imaging.<sup>7</sup> The most common nuclear modalities are positron emission tomography (PET) and single photon emission computed tomography (SPECT) which involve radioactive tracers. The mechanism of radiotracer detection depends on the decay mechanism which defines the type of detector, with both modalities working on the same principle, detection gamma rays to build 3D images.<sup>6</sup>

### **1.1.2 Production of radionuclide**

Radioisotopes are present in all groups of the periodic table, some can occur naturally but more have been produced experimentally. {Talip, 2020 #451} Radionuclides can be generated by cyclotron or generators for on-site routine clinical pharmaceutical productions that can be used *in vivo* to show bio-distribution or to characterise disease, see Figure 2. The important properties for radioisotopes in medical applications (diagnostic or therapy) are:<sup>8</sup>

1. Availability/production
2. Radioactive half-life
3. Activity and emitting species
4. Reaction or coordination chemistry (metal only)

### 1.1.3 Production of a radionuclide from a generator

The generator is a piece of equipment that is used to separate a daughter radionuclide produced by the decay of the parent radionuclide. The generator contains a stationary phase on which the parent radionuclide is immobilised within a shielded column and the daughter radionuclide is eluted from the column by an ion exchange process.<sup>9</sup>

### 1.1.4 Production of a radionuclide from a cyclotron

The first cyclotron/accelerator was developed in Berkeley, California. The concept of a cyclotron is to produce radioisotopes by the bombardment of stable nuclei with high energy particles such as protons or alpha particles ( $^4\text{He}^{2+}$ ). This process is carried out in a vacuum chamber between two electromagnetic poles that allow the acceleration. A magnetic field is formed and causes the travel of ions in a circular path with a gain in kinetic energy. A nuclear reaction occurs when the accelerating ions collide with the targeted nuclei. This then results in other particles leaving the target nucleus after the energy is transferred or absorbed to give the desired radionuclide.<sup>10</sup>

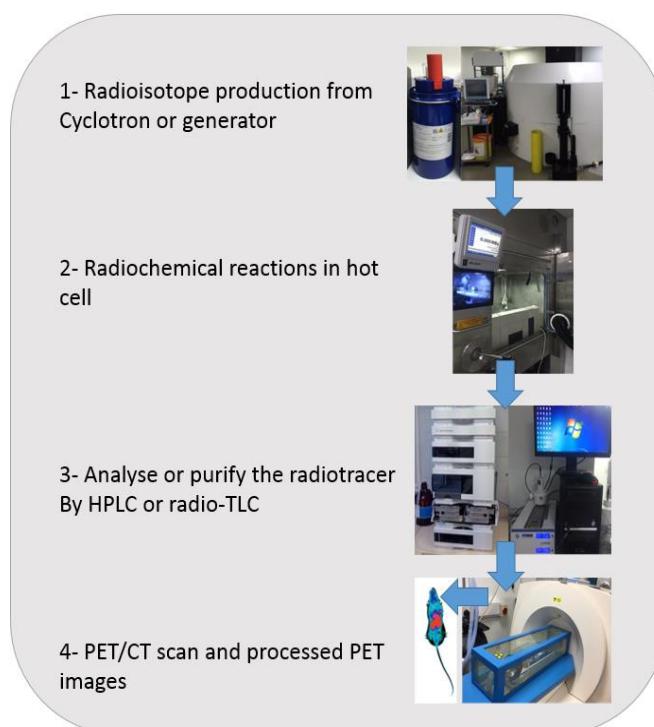


Figure 2: The process of production of a radionuclide from a generator or cyclotron followed by radiochemical reaction in a hot cell and the analysis or purification steps before the PET/CT scan.

### 1.1.5 Positron emission tomography (PET) imaging

Over the past decade the use of PET and PET-CT has increased in clinical imaging facilities. This imaging technique is widely used for localisation of cancerous tumours. PET is considered to be a sensitive and quantitative imaging technique. It can detect early stages of disease by tracking biological changes on a molecular level. PET radionuclides are used at nanomolar/picomolar levels; this low concentration is enough for detection without any conflict with other biological processes. Figure 3 shows a typical PET-CT scanner, the combination of these two imaging modalities is currently the most common.<sup>11, 12</sup>



*Figure 3: Example of a clinical PET-CT scanner (Toshiba Celestion) (Reproduced from Toshiba America Medical System).*

The utility of a PET radionuclide depends on its decay half-life. They can be classified in two categories, non-metals and metals. They are produced by transformation of a stable nuclide to an unstable configuration by using a cyclotron or generator. Each group of the radionuclides is used for different diagnostic procedures. The non-metal or organic radioisotopes are particularly biologically relevant as labelled versions of metabolic substrates can be synthesised. For example, [ $^{11}\text{C}$ ] glucose, [ $^{13}\text{N}$ ]NH<sub>3</sub> and [ $^{15}\text{O}$ ]H<sub>2</sub>O without any change occurs in the biological properties of the labelled molecule, see Table 1.<sup>6, 13, 14</sup>

Table 1: Properties of commonly used PET radioisotopes.

Radionuclide	Half-life	Method of production	Decay characteristic
$^{11}\text{C}$	20.3 mins	Cyclotron	$\beta^+$
$^{13}\text{N}$	9.97 mins	Cyclotron	$\beta^+$
$^{15}\text{O}$	2.04 mins	Cyclotron	$\beta^+$
$^{18}\text{F}$	110 mins	Cyclotron	$\beta^+$
$^{68}\text{Ga}$	1.1 hours	Generator	$\beta^+$
$^{64}\text{Cu}$	12.7 hours	Cyclotron	$\beta^+$ 19% EC 41% $\beta^-$ 40%
$^{89}\text{Zr}$	78.5 hours	Cyclotron	$\beta^+$ 23% EC 77%

### 1.1.6 Physical principles of PET imaging

The principle behind the generation of the PET image is dependent on radionuclide that decays via positron emission, which travels a short distance through surrounding tissue before an annihilation reaction. The PET scanning process starts when a patient is injected with a radioactive tracer, it localises in the tissue and then produces a positron that interacts with a surrounding electron. A complete annihilation occurs that releases two photons, travelling in opposite direction (511 keV each at approximately 180°) which are detected in coincidence by a gamma camera ring when they strike opposing detectors simultaneously, see Figure 4. <sup>6, 11</sup>

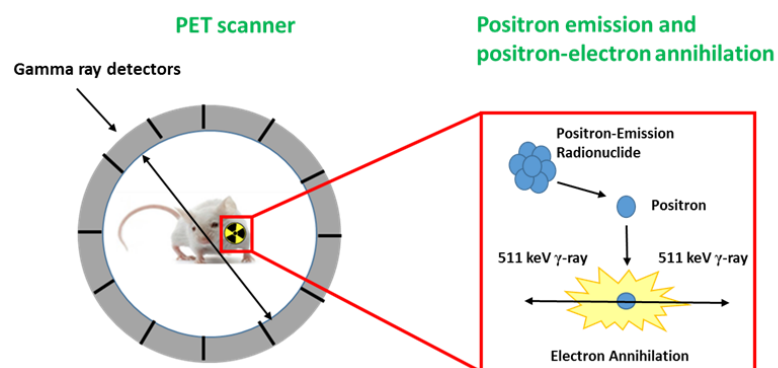


Figure 4: Diagram shows the principles of positron emission and gamma detection involved in a PET scan.

### 1.1.7 Gallium-68 as PET radioisotope

In recent years, the positron emitting radiometal gallium-68 has gained much attention in the development of imaging agents. {Boros, 2019 #442} Gallium is a group 13 post-transition metal. In aqueous solution and physiological pH, gallium has the oxidation state III. The attraction of gallium-68 is the suitable half-life of 68 minutes with 89% positron emission, this half-life considered sufficient to carry out synthetic procedures but not so long to cause radiosynthetic handling challenges. Furthermore, the availability of production from a generator and the variety of bifunctional chelators available to bind the metal attaching it to targeting vectors, are also key strengths. Importantly, gallium-68 also has a reasonable positron energy (1.92 MeV) for PET imaging.<sup>15, 16</sup>

### 1.1.8 Production of gallium-68 from a generator

The facile production of gallium-68 from a germanium/gallium generator is the major advantage for this PET isotope. The parent isotope germanium-68 has a half-life of 270 days and decays to give the daughter isotope gallium-68 with a half-life of 68 minutes, as shown in Figure 5. The generator contains a stationary phase such as alumina that absorbs germanium, the advantage of this generator that gallium-68 can be eluted twice a day by using 0.1M hydrochloric acid. Most radiochemical reactions are carried out in the presence of weak interacting ligands at a controlled pH to avoid formation of any undesired low solubility hydroxides.<sup>10, 17</sup>

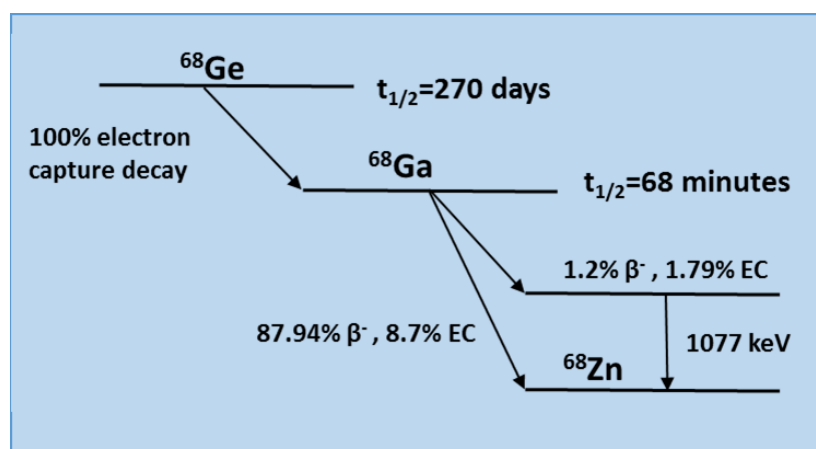


Figure 5: Nuclear decay diagram of germanium-68 to gallium-68 to zinc-68.

### 1.1.9 Gallium chelators

The stability of gallium-68 radiolabelling is normally achieved through complex formation with a multidentate chelator. {Jackson, 2020 #443} A chelator is a multidentate ligand which provides stability for the formed complex due to the chelate effect. Therefore, macrocyclic and acyclic ligands are common chelating agents for gallium-68 due to their ease of synthesis and efficient metal binding kinetics. A range of both macrocyclic and acyclic chelators have been reported in application of  $^{68}\text{Ga(III)}$ .<sup>18, 19</sup>

#### 1.1.9.1 Bifunctional chelators (BFCs)

To stabilise the radiotracer and attach it to a targeting vector, a chelator must possess bifunctionality. A bifunctional chelator (BFC) provide a metal binding site and includes a moiety suitable for bioconjugation. The main properties for stable radiopharmaceutical BFC is that the complex must be thermodynamically stable and kinetically inert to avoid any potential hydrolysis or ligand exchange during the *in vivo* targeting process. Also, the BFC should have high selectivity for the radiometal and rapid complex formation kinetics. Metal radiolabelling would ideally occur under mild physiological conditions in order to protect the biomolecule from degradation.<sup>20</sup>

#### 1.1.9.2 Macrocyclic chelators for gallium-68

Macrocyclic chelators based on cyclam and cyclen are widely used to form complexes with metal ions that have high kinetic and thermodynamic stability. For example, TETA, NOTA and DOTA ligands form six-coordinate complexes with gallium(III) and increase the stability due to the presence of both carboxylate groups and nitrogen donors, see Figure 6.<sup>21</sup>

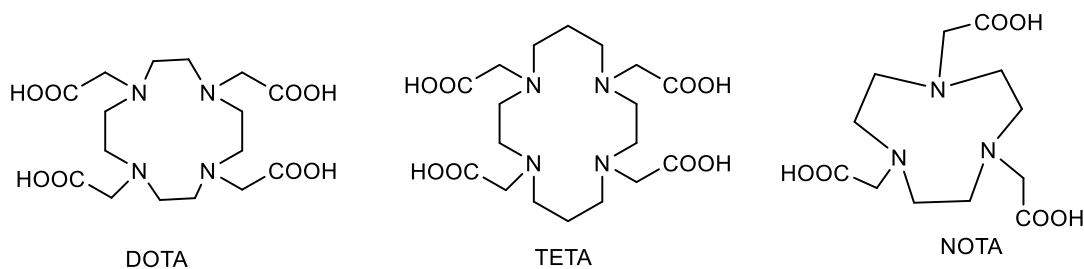


Figure 6: Chemical structures for macrocyclic chelators DOTA, TETA and NOTA.

### 1.1.9.3 Acyclic BFCs for gallium-68

Acyclic BFCs, for example, DTPA and DEDPA, offer fast metal ion binding kinetics. However, the complexes formed are considered less kinetically inert and thermodynamically stable than their macrocyclic counterparts. Gallium(III) may form sufficiently stable complexes with acyclic chelators for *in vivo* use, see Figure 7.

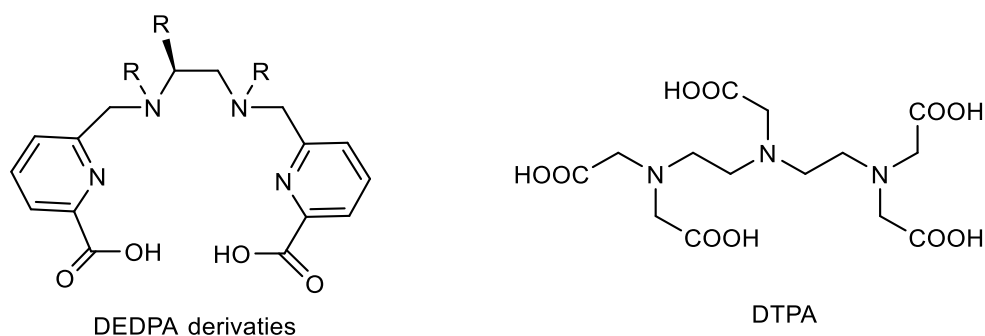


Figure 7: Chemical structures for acyclic compounds DEDPA and DTPA.

In this research, gallium-68 was selected for studying and radiolabelling different types of nanoparticles such as iron oxide nanoparticles, liposomes and polymeric micelles due to the favourable properties and availability of a gallium-68 generator in the preclinical PET Research Centre at the University of Hull.

### 1.1.10 Single photon emission computed tomography (SPECT) imaging

SPECT imaging is the most common nuclear imaging technique, which depends on the radioactive decay of radioisotope to emit a gamma ray, see Figure 8. {Boschi, 2019 #447} The single photon travels through tissues and can be detected by a gamma camera to form an image of the localised radioactivity. In SPECT, the positional information of the photon is limited (i.e. its origin or the direction of travel). To solve this problem, a collimator is added between the source and the detector to limit the direction of the travelling photon that will reach the detector.<sup>6</sup>

In clinical system, the patient is surrounded by planar scintillation detectors with collimators that only allow detection of gamma rays falling normally onto the detectors blocks. These collimators work as a filter rejecting most of the photons that are not travelling along the defined directions. The obtained images are modified to form three-dimensional image.<sup>22, 23</sup>

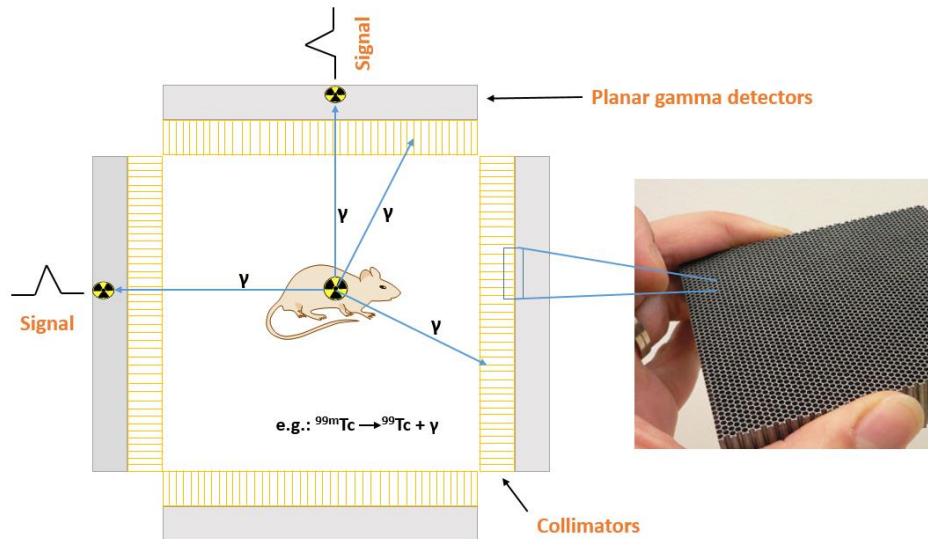


Figure 8: Principles of single photon emission computed tomography (SPECT) scanner design.

SPECT scanners combined with CT are widely found in hospitals around the world. This combination can overcome the low spatial resolution of SPECT and provide both structural and functional information. The majority of radioisotopes used in SPECT decay by gamma emission via the electron capture mechanism (EC) or isomer transfer (IT), see Table 2.

Table 2: Commonly used SPECT radioisotopes, decay characteristics and production methods.<sup>23, 24</sup>

Radionuclide	Half-life	Energy (keV)	Mode of decay	Method of production
${}^{99m}\text{Tc}$	6.02 h	149	IT	${}^{99}\text{Mo}/{}^{99m}\text{Tc}$ generator
${}^{123}\text{I}$	13.22 h	159	EC	Cyclotron
${}^{111}\text{In}$	2.80 d	171, 245	EC	Cyclotron
${}^{67}\text{Ga}$	3.26 d	93, 185, 300, 394	EC	Cyclotron

### 1.1.10.1 Technetium

The properties of this element were predicted by Dmitri Mendeleev whilst organising the periodic table before the element was first isolated in 1937 by Segre' and Perrier. Technetium has atomic number 43 and has twenty-two isotopes, ten of them are man-made, and the most common of these radioisotopes is technetium-99m. This isotope is commonly used in diagnostic nuclear medicine for many reasons:<sup>25-27</sup>

1. The suitable half-life of 6.02 hours, this is optimal for diagnosis because it is long enough to allow the radiopharmaceutical preparation, quality control, administration to the patient, image acquisition and sufficiently short to give low doses of radiation to the patient.
2. The energy emission (140 keV) is considered sufficiently low to prevent any high radiation dose to the patient and at the same time it is sufficiently high to penetrate the tissues.
3. The availability of  $^{99m}\text{Tc}$  from a cheap commercial generator,  $^{99}\text{Mo}/^{99m}\text{Tc}$  generators can be found in most hospitals around the world.
4. Technetium-99m has varied coordination chemistry, therefore, the synthesis of wide variety of complexes with different physiochemical and biological properties is possible.

### 1.1.10.2 Technetium-99m production

Technetium-99m is produced in a closed system form  $^{99}\text{Mo}/^{99m}\text{Tc}$  generator (e.g. Ultra TechnoKow™ FM Generator), see Figure 9A. The  $^{99}\text{Mo}$  is adsorbed onto the alumina column shielded by lead, tungsten or depleted uranium. The sterile solution contains sodium pertechnetate ( $[\text{}^{99m}\text{Tc}]\text{NaTcO}_4$ ) in 0.9% sodium chloride, this solution should be clear, colourless and free of visible foreign materials. This product is a radiopharmaceutical in itself and, using a range of oxidation processes, it can be used to radiolabel other precursors.<sup>28</sup>

Figure 9B, shows the decay process in the  $^{99}\text{Mo}/^{99m}\text{Tc}$  generator. The  $^{99}\text{Mo}$  (half-life= 66 h) decays to  $^{99m}\text{Tc}$  by  $\beta^-$  decay (88.75%), the produced isotope  $^{99m}\text{Tc}$  is a nuclear isomer of  $^{99}\text{Tc}$  in a metastable state, which decays to stable form  $^{99}\text{Tc}$  by emitting a

gamma ray (11.25%). The  $^{99}\text{Tc}$  then converts to  $^{99}\text{Ru}$  by  $\beta^-$  decay with a much longer half-life.<sup>25</sup>

$^{99\text{m}}\text{Tc}$ -pharmaceutical production depends on the coordination chemistry properties of  $^{99\text{m}}\text{Tc}$ , such as the stable oxidation states and preferred coordination numbers. Technetium has several different oxidation states (-I to +VII) and several coordination geometries.  $^{99\text{m}}\text{Tc(VII)}$  is eluted from a generator and is the most stable form in aqueous solution, however, this form does not bind directly to any ligand. Thus,  $^{99\text{m}}\text{Tc(VII)}$  need to be reduced to a lower oxidation state, such as (V) or (I) to form complexes that can be used as SPECT radiopharmaceuticals.<sup>25</sup>

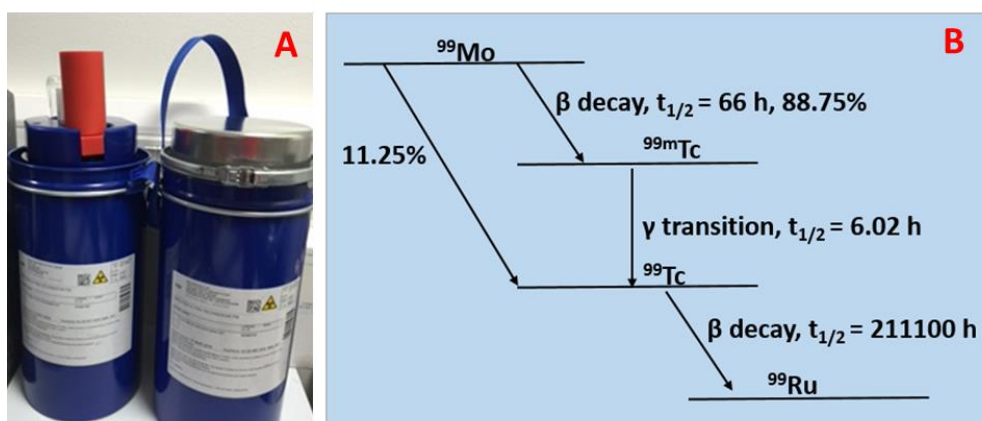


Figure 9: A)  $^{99\text{m}}\text{Tc}$  generators and B) decay scheme of  $^{99}\text{Mo}$  from  $^{99}\text{Mo}/^{99\text{m}}\text{Tc}$  generator.

### 1.1.11 Magnetic Resonance Imaging (MRI)

Magnetic resonance imaging (MRI) is an essential medical imaging technique for clinical diagnosis. {Wahsner, 2019 #448} It is a non-invasive technique with high resolution and in-depth anatomical images which gives a three dimensional view of the internal organs and tissues, see Figure 10.<sup>29</sup>

In MRI there is no requirement for radioactive materials. Therefore, the patient will not be exposed to ionizing radiation which is found in the nuclear imaging methods as already discussed (SPECT and PET).<sup>30, 31</sup>



Figure 10: A) Clinical MRI scan and B) preclinical MRI scan.

#### 1.1.11.1 Physical Principles of MRI

The interaction between an external magnetic field and a nucleus with a nuclear spin angular momentum ( $I$ ) is the basis of magnetic resonance. This property depends on the atomic weight and atomic number of the nucleus, if it has an odd atomic weight it can interact with the magnetic field ( $I = \frac{1}{2}, \frac{3}{2}, \frac{5}{2}$ ).<sup>32, 33</sup>

On the other hand, a nucleus which has an even atomic weight has no spin ( $I=0$ ), in this case it is insensitive to the magnetic field, and is not suitable for MRI. The  $^1\text{H}$  isotope, is widely analysed in magnetic resonance because it has a spin angular momentum equal to  $\frac{1}{2}$ , and shows one of largest responses to an applied magnetic field. Another reason, is that the human body is mainly made from water and fat,

both of which contain hydrogen in their structures, making magnetic resonance an ideal technique for human studies.<sup>33,34</sup>

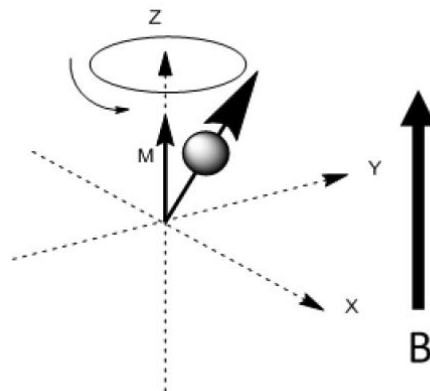


Figure 11: A nucleus shows a parallel magnetic moment to the external magnetic field resulting in a precession motion.

A positively charged nucleus which has spin produces a local magnetic field, called the magnetic moment, that is oriented parallel to the axis of orientation. The MRI signal depends on the changes of this magnetic moment. In the absence of magnetic field, the magnetic moment of the protons will be able to rotate randomly, and the net magnetisation will be zero. However, in the presence of an external field (**B**), the proton aligns with the magnetic field, and the proton will start to precess about the magnetic field at constant rate, see Figure 11 and 12.<sup>33</sup> According to Larmor equation the precession frequency is proportional to the magnetic field strength (**B**) as follow:

$$\omega = \gamma B$$

Equation 1

Where  $\omega$  is the Larmor frequency (MHz),  $\gamma$  is the gyromagnetic ratio (MHz/Tesla) and **B** is the magnetic field strength (Tesla). The protons align in two ways, either parallel or anti-parallel to the magnetic field.<sup>34</sup>

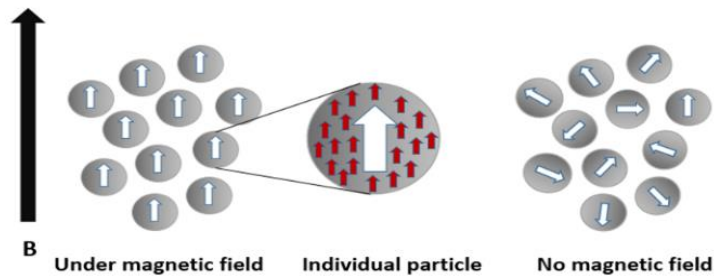


Figure 12: Alignment of proton spins in the presence and absence of the magnetic field.

Table 3: Constants of selected nuclei used in MRI.

Element	Nuclear spin I	Gyromagnetic Ratio (MHz/T)	NMR Frequency at 2.35 T	Natural abundance (%)
<sup>1</sup> H	1/2	42.577	100	99.985
<sup>3</sup> He	1/2	32.436	76.181	0.000138
<sup>13</sup> C	1/2	10.708	25.14	1.1
<sup>15</sup> N	1/2	4.317	10.137	0.366
<sup>17</sup> O	5/2	5.778	13.56	0.038
<sup>19</sup> F	1/2	40.077	94.09	100
<sup>23</sup> Na	3/2	11.268	26.46	100

The majority of the aligned parallel protons have low energy (spin-up), and the rest have high energy (spin-down). This energy difference depends on the strength of the magnetic field and the density of the protons in each energy level. The net magnetisation can be enhanced by increasing the number of aligned protons (spin-up) in order to increase the difference in energy levels that can be reached by applying a high magnetic strength.<sup>35</sup>

As mentioned above, the protons will precess, and when a radiofrequency pulse is applied, it generates a transient magnetic field which is perpendicular to the main magnetic field  $B_0$  and causes a net magnetisation vector, by rotating the magnetic moment of the nuclear spins (usually by  $90^\circ$  from the longitudinal to transverse

plane). It also gives energy to some protons to become anti-parallel to the magnetic field. After the pulse has been applied, the magnetisation eventually returns to its equilibrium (non-disturbed) position along with z-axis. This return (relaxation) emits energy at the frequency  $\omega_0$ , the changes in magnetic field ( $\mathbf{B}$ ) by the precessed protons can be detected by a receiver coil placed perpendicular to the transverse plane.<sup>32, 33</sup>

Relaxation times depend on this process, when the proton returns to its equilibrium and release energy, there are two types of relaxation important in MRI,  $T_1$  and  $T_2$ . Therefore, the MRI signal depends on the longitudinal magnetisation ( $M_z$ ) and the transverse magnetisation ( $M_{xy}$ ) before and after the RF pulse, see Figure 13.<sup>32</sup>

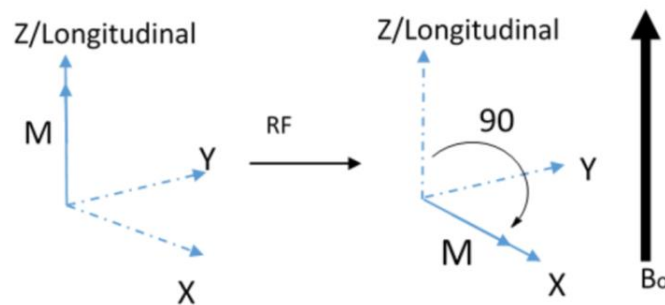


Figure 13: Diagram shows the rotation of protons by 90° by application of an external magnetic field.

### 1.1.11.2 MRI Contrast Agents

One of the major advantages of MRI is the excellent spatial resolution with optimal contrast within soft tissues, this is a result of the differences in  $T_1$  or  $T_2$  relaxation times of different tissues. MRI contrast agents can be used to make a specific area darker or brighter than the surrounding, see Figure 14 , by shortening the relaxation times,  $T_1$  or  $T_2$ .<sup>36</sup>

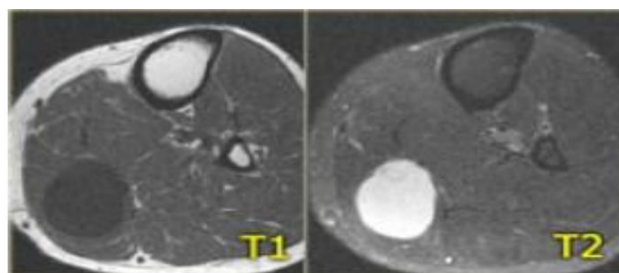


Figure 14:  $T_1$  and  $T_2$  MR Images for a patient with focal nodular myositis.<sup>37</sup>

### 1.1.11.3 $T_1$ Relaxation

The relaxation time  $T_1$  is the time required for nuclei to emit the energy gained to the surrounding molecules and realign to the longitudinal plane. This mechanism is known as spin-lattice relaxation time or longitudinal relaxation time and is characterised by a time constant  $T_1$ . This is an exponential process and 63% of the original longitudinal magnetisation is reached, see Figure 15.<sup>32</sup>

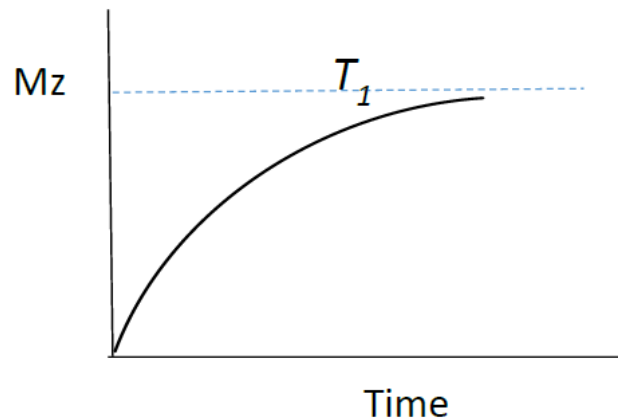
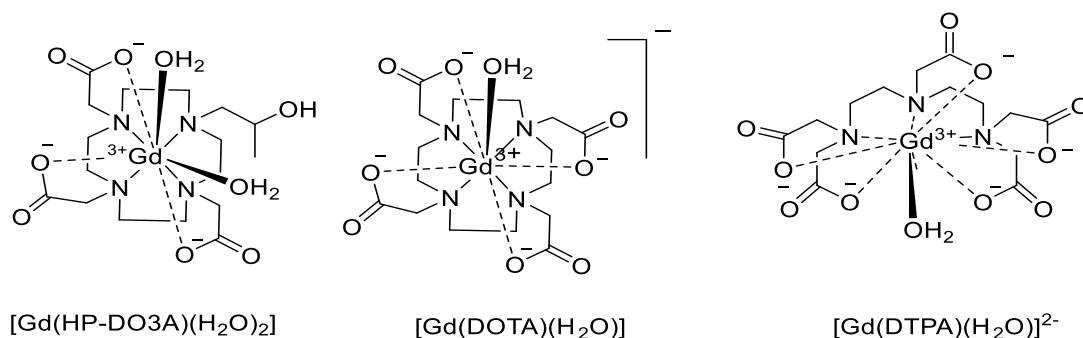


Figure 15: Longitudinal relaxometry curve.

$T_1$  contrast agents (positive CAs) give a bright image for fat, and water appears dark. These contrast agents are based on paramagnetic ions, for example, gadolinium ( $Gd^{3+}$ ) and manganese ( $Mn^{2+}$ ). Mn-based CAs give weaker contrast, and so are less commonly used in MRI, although the low toxicity of manganese is increasing current interest.<sup>38</sup>

Gadolinium(III) based is one of the common  $T_1$  contrast agent for many reasons: a highly paramagnetic nature and seven unpaired electrons which gives a longer relaxation time.<sup>39, 40</sup> However, gadolinium is considered as highly toxic to the body, the recommended doses are (15.7-47.1 mg Gd/kg B.W) and it can also cause nephrogenic system fibroses (NSF).<sup>41</sup> Therefore organic chelates are used to form stable gadolinium complexes and decrease its toxicity. For example, three commonly used clinical MRI contrast agents are Gd-DTPA (magnevist), Gd-DOTA (DOTArem) and Gd-HP-DO3A (ProHance), see Figure 16, these complexes with gadolinium leave one or two free coordination sites for water molecules to bind.<sup>21, 42</sup>



*Figure 16: Structures of three clinical MRI gadolinium contrast agents.*

A new approach for  $T_1$  contrast agents is based on nanoparticles of paramagnetic ions such as gadolinium oxide nanoparticles ( $Gd_2O_3$ ) and manganese oxide ( $MnO$ ); this new field depends on the nano-size of the particles and the extended residence time of water molecules at the surface.<sup>43</sup>

### 1.1.11.4 $T_2$ relaxation

$T_2$  relaxation time is the decay time of the transverse magnetisation to reach 37% of its original magnetisation after dephasing and the nucleus realigning with the magnetic field. It is known as (spin-spin relaxation) because the excited proton transfers the energy to a neighbouring proton shows the decay of magnetisation with time.

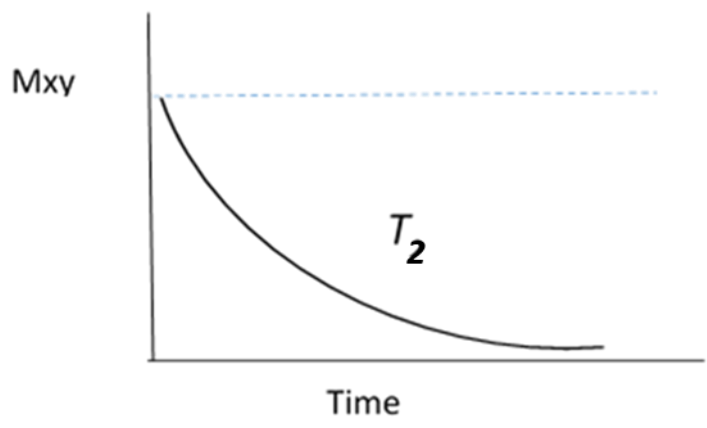


*Figure 17: Transverse relaxometry curve for  $T_2$  relaxation.*

$T_2$  contrast agents (negative CAs) darken the image with increasing concentration (without the agent present water has a short  $T_2$  hence appears brighter in comparison to the longer  $T_2$  of fat molecules which appear dark). Examples of  $T_2$  CAs that shorten the transverse relaxation are, cobalt iron alloy (FeCo), manganese diiron oxide ( $\text{MnFe}_2\text{O}_4$ ) and iron oxide nanoparticle derivatives.<sup>36</sup> The majority of these  $T_2$  CAs are iron oxide nanoparticles, such as magnetite ( $\text{Fe}_3\text{O}_4$ ) and maghemite ( $\gamma\text{-Fe}_2\text{O}_3$ ) or a mixture of the two phases. The magnetic particles possess unique properties that make them suitable for biomedical applications, including size and colloidal stability.<sup>44</sup> Other research is ongoing and recently a new approach for using superparamagnetic iron oxide platinum particles (SIOPPs) in medical imaging was developed, showing improved  $T_2$  relaxivities compared with iron oxide nanoparticles.<sup>36, 45</sup>

#### **1.1.12 Multi-Modality (PET/SPECT-MRI) imaging agents**

Imaging modalities vary in sensitivity, resolution and quantitative information. For example, the modalities with the highest sensitivity have relatively poor resolution, while those with high resolution tend to have relatively poor sensitivity. {Ge, 2020 #450} This problem can be overcome by multimodal imaging because each imaging modality gives its own unique benefits. To reduce the intrinsic limitations of specific technique, dual or multimodal imaging can be utilised. Iron oxide MRI contrast agents can be combined with a different agent for multimodal imaging agents, moreover, they can also be combined with different targeting vectors for specific tissue or tumour imaging, see Figure 18. Therefore, multiple imaging modalities will enable the clinician to better understand the mechanism of disease progression at the tissue specific level.

PET and SPECT are usually combined with CT, to enhance information regarding spatial anatomy. Replacing CT with MRI can decrease patient radiation dose and increase soft tissue contrast. Furthermore, MRI contrast agents are more widely applicable and versatile than CT contrast agents.

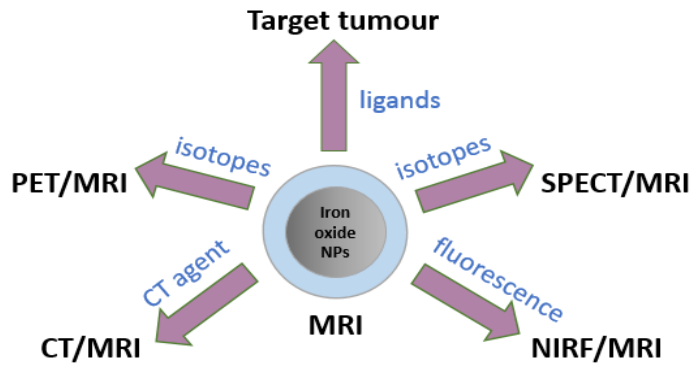


Figure 18: Potential of multimodal contrast agents based on MRI iron oxide contrast agent.

### 1.1.12.1 PET/MRI

As discussed, PET is a highly sensitive imaging modality whereas MRI gives a high spatial resolution. A combination of PET and MRI provides good spatial resolution of anatomy and spatial image fusion. PET/MRI also gives multi-functional information on physiological processes in the body, such as blood oxygenation level dependent (BOLD). In addition, the soft tissue contrast is increased with reduction of the radiation dose.<sup>46-48</sup> Recently,  $T_2$  MRI contrast agent based on super paramagnetic iron oxide nanoparticles (SPIONs) have been combined with positron emission radioisotopes, see Figure 19. The combination of MRI with positron emission tomography gives excellent information about bio-distribution of nanoparticles *in vivo*.<sup>49, 50</sup>

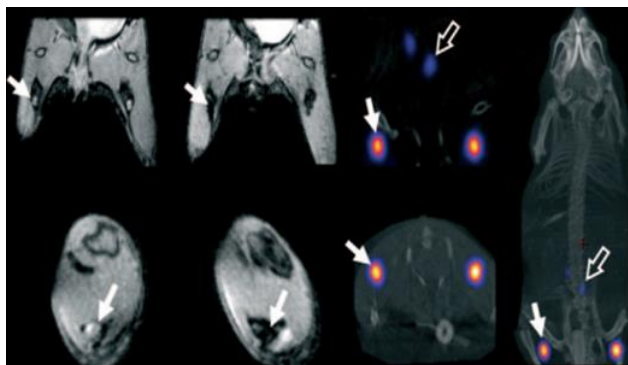


Figure 19: In vivo images for dual modalities, using PET/MRI contrast agents.<sup>51</sup>

Bao *et al.* have reported PET/MRI dual modality CAs using SPIONs functionalised with DOTA-NHS ester to enable  $^{64}\text{Cu}$  chelation. The radiolabelled SPIONs were stable in serum for 24 h and producing useful MR and PET signals.<sup>52</sup> In different study, Patel *et al.* reported encapsulation of SPIONs in a porous silica shell functionalised with a chelator for  $^{64}\text{Cu}$ . The radiolabelled iron oxide nanoparticles were highly effective in PET/MRI imaging.<sup>53</sup>

#### **1.1.12.2 SPECT/MRI**

Similarly the combination between SPECT and MRI can obtain high quality anatomical images for combination with the nuclear imaging technique.<sup>54</sup> Recently, SPECT/MRI was investigated for sentinel lymph node (SLN) imaging by developing  $^{99\text{m}}\text{Tc}$ -labelled PEG coated iron oxide nanoparticles as a SPECT/MRI contrast agent. The images identify the SLN and offer pre-surgical information on the location and characteristics of the lymph nodes and spread of the cancer through the lymphatic system. The radiolabelling efficiency of the SPIONs with  $^{99\text{m}}\text{Tc}$  reached 99%. The results encourage use of these method for diagnosis of other types of cancer.<sup>55</sup>

Ruiz-se-Angulo *et al.* prepared a system for SPET/MRI contrast agent based on functionalisation of iron oxide with specific vaccine. The construct nanoparticles were radiolabelled with gallium-67, a SPECT radionuclide. The NPs enhanced antigen-specific immunity by image tracked delivery of antigen and CpG to lymph nodes, see Figure 20.

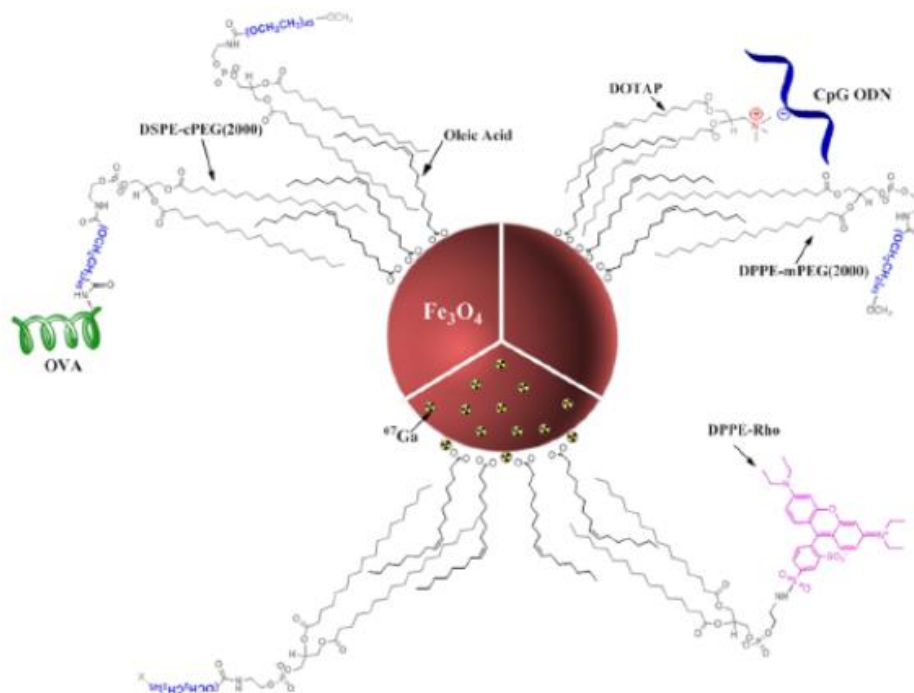


Figure 20: Functionalised iron oxide NPs with several moieties.

## 1.2 Nanotechnology

Nanotechnology and nanomaterials have undergone rapid development during the last decades. {Sun, 2017 #445} Nanoscience defines a nanosized particle as roughly 1-100 nm in dimensions, although this range may extend up to 1000 nm. Nanomaterials can have novel optical, electronic and structural properties that differ from the individual bulk materials. Nanomedicine is a part of nanotechnology that applies nanomaterials in medical science. These nanoparticles (NPs) are expected to offer novel physical and biological behaviour and a range of different interactions with biomolecules. An advantage of NPs is that they have a large surface area compared to their bulk materials, which allows for surface modification and functionalisation to improve their pharmacokinetic properties and prolong their circulation life-time in order to enhance their bio-distribution *in vivo*.<sup>56-58</sup>

### 1.2.1 Nanomaterials in medicine

Several nanoparticle materials are currently used for medical applications such as quantum dots, dendrimers, nanotubes, liposomes, micelles, gold nanoparticles and magnetic NPs. Different types of nanoparticles can have different biomedical purposes for example, medical imaging, drug delivery and targeted therapy.<sup>59</sup>

The accumulation of nanoparticles in malignant tissues is either by passive or active targeting, see Figure 21. The passive targeting is based on specific pathophysiological characteristic of tumours where the vasculature of tumour is different from healthy tissues, presenting large gaps that allow nanoparticles to accumulate in tumours due to the enhanced permeability and retention effect (EPR).<sup>60, 61</sup> while active targeting requires a suitable modification and functionalisation of nanoparticle surface to promote interactions with molecular elements of the tumour. Several targeting moieties have been used to target receptors expressed on the tumour surface including antibodies, peptides and small molecules.

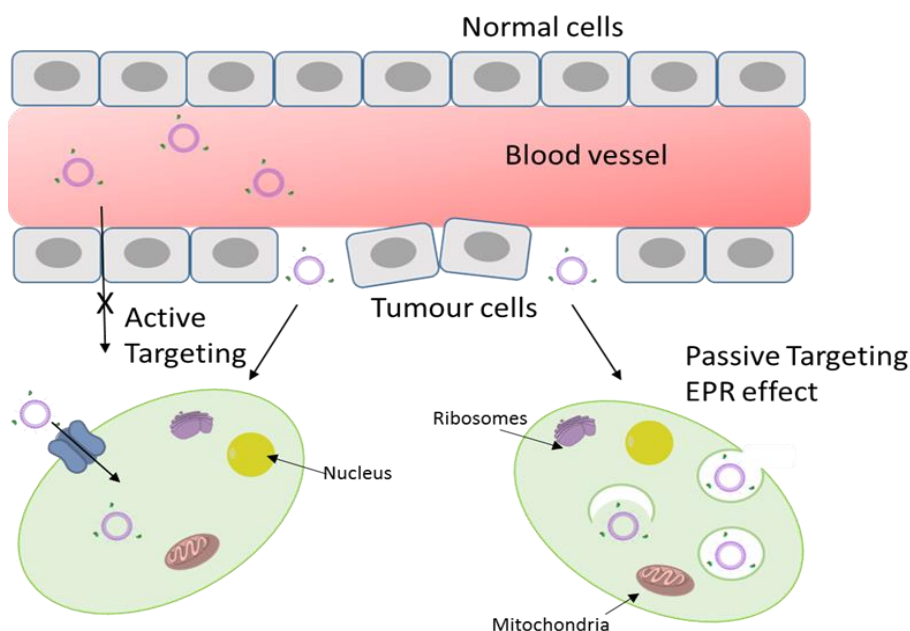


Figure 21: Schematic representation of the accumulation of nanoparticles in tumour tissue by either the EPR effect or active targeting.

## 1.2.2 Radiolabelling of nanoparticles

NPs are ideal constructs for as nuclear imaging agents due to the facile surface functionalisation compared to small molecules. Radiolabelling of nanoparticles with PET or SPECT isotopes allows their tumour targeting and drug delivery properties to be determined using rapid and non-invasive methods. For the radiolabelling of NPs, there are important considerations that must be followed; formation of a stable system to allow for *in vivo* biodistribution that reflects the nanoparticles fate in biological environment. Moreover, using a simple radiolabelling method is preferable, and it should not affect the inherent properties of NPs such as magnetisation and targeting.<sup>62, 63</sup> The radiolabelling process of nanoparticles can be classified into three categories, see Figure 22.

### 1.2.2.1 Chelator-free radiolabelling method

This method also known as direct radiolabelling, due to the direct interaction between the radioisotope and the surface of nanoparticles in absence of any type of chelator. It is a simple and fast method for radiolabelling NPs without significant alteration of surface properties. The aim of this method is to form a stable system at

low concentrations of nanoparticles by optimising the radiolabelling conditions. For example, the NPs concentration, pH, type of buffer, temperature and reaction time.

#### 1.2.2.1.1 Chelator-based radiolabelling method

In many cases, chelators are used to stabilise the radiolabelled nanoparticle system. Development of this method depends on the correct selection of chelator to match with the radiometal used for radiolabelling the NPs.<sup>64</sup>

#### 1.2.2.1.2 Final-step radiolabelling method

In this development of chelator-based radiolabelling, the nanoparticles are functionalised with chelators prior the addition of radiometal. The chelators are attached to the NPs surface during the synthesis or coating steps and should protect the nanoparticles properties. The bifunctional chelators must match with the coordination chemistry of the metal radionuclide to give rapid binding kinetics and formation of a stable complex.<sup>62, 64</sup>

#### 1.2.2.2 Two-step radiolabelling method

This method requires initial radiolabelling of bifunctional chelator with radiometal followed by conjugation of this complex to the nanoparticle surface. In this method, a stable radiometal complex is formed before attachment to the nanoparticle.<sup>62</sup>

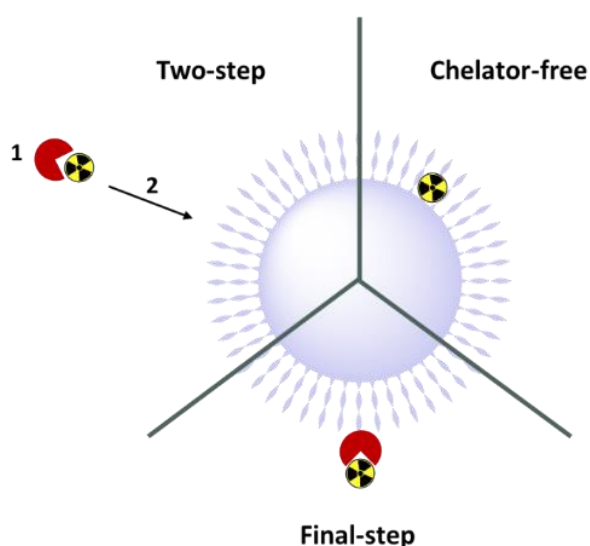


Figure 22: Common methods for radiolabelling nanoparticles including chelator-free method, final-step chelator and two step chelator methods.

### **1.3 Superparamagnetic iron oxide nanoparticles (SPIONs) as contrast agents and in other medical applications**

Iron oxide nanoparticles in the magnetite phase ( $\text{Fe}_3\text{O}_4$ ) named as (SPIONs) are the most commonly used iron oxide nanoparticles. {Ni, 2017 #449} These particles exhibit superparamagnetic behaviour, this phenomenon is the basic requirement for using SPIONs as contrast agents in MRI. In fact, SPIONs can be utilised as  $T_1$  or  $T_2$  contrast agents, but their relaxation effect is generally larger in  $T_2$ . Other important properties include low toxicity, the recommended dose is (0.5-0.9 mg Fe/kg B.W) which make them biocompatible. NPs have a unique small size that gives the superparamagnetic behaviour, which means that thermal energy may be enough to change the magnetisation of individual particles.<sup>36, 44, 57</sup>

Due to decrease of the particles' size below a critical value, it becomes a single domain, see Figure 23, and the coercivity reaches zero with no hysteresis loop in the absence of magnetic field. In other words, when a magnetic field is applied, a net alignment of magnetic moments will be observed, similar to that observed in paramagnetic materials, although it is much larger (about  $10^4$  times in superparamagnetic materials).<sup>65, 66</sup>

On the other hand, in the absence of a magnetic field, the net magnetisation is zero and this lack of magnetisation imparts colloidal stability to the nanoparticles preventing aggregations.<sup>36, 67</sup> For example, Feridex, Resovite and Ferumoxytol are commercial MRI contrast agents based on SPIONs coated with dextran that have been clinically approved by the US food and drug administration agency (FDA) and the European medicine agency (EMA), these CAs can be used to differentiate between normal and abnormal liver tissue.<sup>68-70</sup>

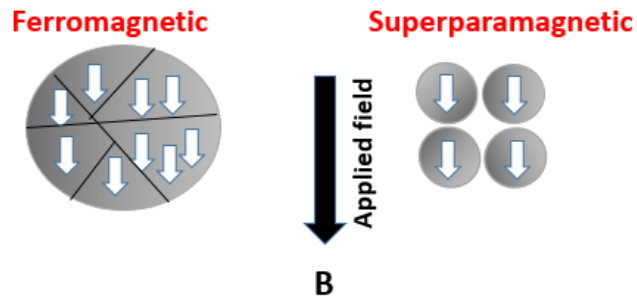


Figure 23: Multi-domains for ferromagnetic particles and the single domain for superparamagnetic nanoparticles aligned with the external magnetic field.

### 1.3.1 Chemical properties of $\text{Fe}_3\text{O}_4$ nanoparticles

Magnetite is an opaque, black ceramic crystal, the family structure of magnetite is cubic inverse spinel, in this structure the  $\text{Fe}^{3+}$  ions are located in all of the tetrahedral sites (T-sites) and half of the octahedral sites (O-sites), whereas  $\text{Fe}^{2+}$  ions are distributed in the remaining (O-sites), see Figure 24 . Compounds in this category show unique electrical and magnetic properties as a result of the transfer of electrons between  $\text{Fe}^{3+}$  and  $\text{Fe}^{2+}$  in the octahedral sites.<sup>71, 72</sup>

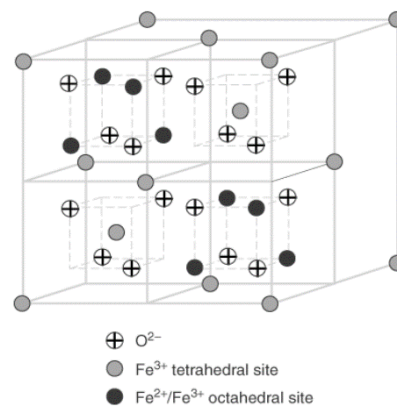


Figure 24: Magnetite structure is a cubic inverse spinel with locations of  $\text{Fe}^{3+}$  and  $\text{Fe}^{2+}$  ions at the tetrahedral and octahedral sites.

In the past decades, technological developments have developed the use SPIONs for medical purposes such as cancer therapy and diagnosis. The design of the nanoparticles makes them effective for *in vivo* studies and biomedical applications particularly in terms of the following properties:

1. Particle size and hydrodynamic size: In SPIONs, the core size refers to the metal containing core ( $\text{Fe}_3\text{O}_4$ ), and the hydrodynamic size refers to the dimension of the nanoparticles after coating with polymers or inorganic shell and solvent interactions, see Figure 25. In biomedical studies, the hydrodynamic size of SPIONs is important for passing biological barriers (cells and vesicles) an penetration into tissues.<sup>44, 57</sup>

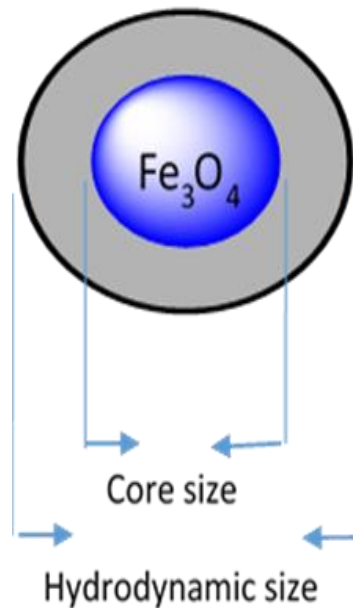


Figure 25: Coated SPIONs with core and hydrodynamic size shown.

SPIONs with a hydrodynamic size below 20 nm are rapidly excreted and cleared by the renal system, and if more than 150 nm they are often captured by the reticuloendothelial system (RES) that is found in the liver and spleen, in this case they would only be suitable for imaging and diagnosis of hepatic and spleen tumours. Nanoparticles with a hydrodynamic diameter between 20-150 nm can accumulate in the bones, kidneys or stomach and also be used to detect abnormal tissues.<sup>38</sup> It is also important to have a narrow size distribution.

2. Magnetic susceptibility: SPIONs have a high magnetic susceptibility to provide effective contrast.<sup>57, 73</sup>

3. High surface area: High surface area offers the potential to modify and functionalise the magnetic core with biological groups or molecules to ensure their biocompatibility.<sup>36, 74</sup>
4. Colloidal stability in physiological media: SPIONs are considered stable if they do not visibly precipitate over a certain time period. This issue can be prevented by coating the nanoparticles with a biocompatible shell.<sup>44</sup>

### 1.3.2 Synthesis of SPIONs

During the last decade, several methodologies were applied to the synthesis of SPIONs to control the size and mono-dispersity to form biomedical compatible NPs, see Table 4. The magnetic properties of the SPIONs depend on the composition and the morphology, therefore, the correct selection of synthetic route is needed to control the shape, size, size distribution and crystallinity. Common methods suitable for synthesis of SPIONs for medical applications are co-precipitation,<sup>75-77</sup> thermal decomposition,<sup>78-80</sup> microemulsion<sup>81, 82</sup> and hydrothermal processes.<sup>83,57, 84</sup>

The co-precipitation technique is a simple and efficient synthesis procedure for SPIONs, most of commercially available magnetite NPs are prepared via this method. The co-precipitation process was first reported by Massart in 1981, SPIONs are obtained via a mixture of ferrous and ferric salts (usually chlorides) in a ratio of 1:2 in alkaline media and inert atmosphere. The products from this method are highly polydisperse and unstable.<sup>57, 85</sup> Researchers are continually improving this method by modifying the acidity, ionic strength and coating the nanoparticles (using capping ligands).<sup>76, 86, 87</sup>

Table 4: Comparison between different synthetic methods for SPIONs.

Synthetic method	Co-precipitation	Thermal decomposition	micro emulsion	Hydrothermal
Reaction temp.	20-90	100-320	20-50	220
Time	minutes	Hours-days	hours	Hours-days
Solvent	Water	Organic compound	Organic compound	Water-ethanol
Surface capping agent	Addition during or after reaction	Addition during reaction	Addition during reaction	Addition during reaction
Size dispersion	narrow	Very narrow	Relatively narrow	Very narrow

### 1.3.3 Surface Modification of SPIONs

Surface modification is a crucial aspect in synthesis of SPIONs for any medical application. The modification can include coating the nanoparticle surface with inorganic (gold colloids or silica), organic molecules (citrate) or suitable polymers.<sup>57, 84, 88-90</sup> The reasons for coating SPIONs are:

- 1- Prevention of undesired reactions between SPIONs and the biological molecules in the body that may cause toxicity.<sup>71</sup>
- 2- Protection of NPs from agglomeration and enhancing their stability to increase the circulation lifetime inside the body.<sup>91</sup>
- 3- Conversion of the hydrophobic character of the SPIONs to hydrophilic, particularly dextran, polyethylene glycol (PEG) and polyethylene alcohol, to encourage the stability of the suspension in physiological media (e.g. water or phosphate buffer solution (PBS)).<sup>44</sup>
- 4- Functionalisation of the SPIONs for conjugation with biological molecules (proteins, enzymes, DNA and genes) and drugs.<sup>36</sup>

As already mentioned, these modified and functionalised SPIONS are commonly used as MRI contrast agents and for other biomedical applications including hyperthermia, magnetic cell separation, drug delivery and nanotheranostic techniques.<sup>92, 93 94-96</sup>

## **1.4 Nanocarriers**

Nanocarriers are widely used in drug delivery systems which are attracting more attention.<sup>{Sun, 2017 #445}</sup> Recently, nanocarriers (including liposomes and micelles) are becoming important as new treatments for various diseases such as cancer, inflammation and infections.<sup>97</sup>

Recent developments in the use of nanocarriers has expanded due to the ease of design and synthesis of these nanoparticles. Furthermore, the flexibility of modification and functionalisation of their surfaces to prevent binding with serum proteins and increase their circulation blood time is possible.<sup>98</sup> The therapeutic nanoparticles for cancer treatment require accumulation in tumours which can be based on the enhanced permeability and retention effect (EPR). The ability of the nanocarrier to encapsulate a wide variety of diagnostic and therapeutic agents is essential for theranostic applications.<sup>99</sup>

The inherent advantages of liposomes and micelles can be illustrated in main four points:

- 1- High agent loading efficiency.
- 2- High stability in biological environments.
- 3- Controllable release kinetics.
- 4- Biocompatibility.

Furthermore, the nanocarriers are considered non-toxic and degradable in the body because of their lipid structure. This structure allows entrapment of different types of drug and reduces toxicity due to minimised uptake in other tissues such as the heart and kidneys.

### 1.4.1 Liposomes

Liposomes are spherical vesicles constructed from lipid bilayers, see Figure 26. {Man, 2019 #446} The structure of liposomes allows them to entrap hydrophobic agents within the lipid bilayers and encapsulate hydrophilic agents inside the aqueous centre which will protect the agents from degradation. They can be used for the delivery of insoluble drugs.<sup>100, 101</sup> Uncoated liposomes were discovered in 1960s, and had limited success in applications due to the unprotected lipid surface.<sup>102</sup> To minimise this disadvantage, surface modification and functionalisation were developed in research carried out since the 1980s. The surface of liposomes was coated with different polymers such as PEG.<sup>97, 103</sup>

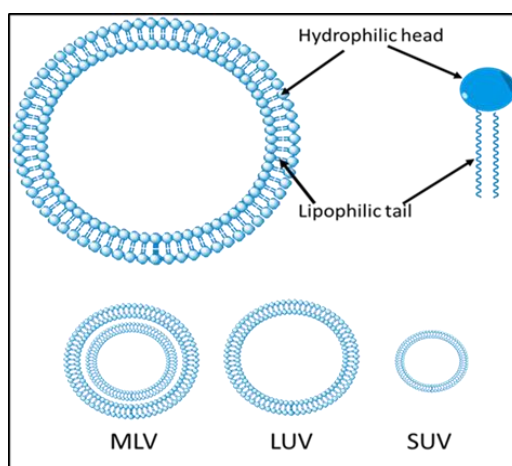


Figure 26: Structure and types of liposomes, MLV= multilamellar vesicles, LUV= large unilamellar vesicles, and SUV= small unilamellar vesicles.

PEGylated liposomes have been used as advanced drug delivery systems and led to clinically approved therapeutic drug formulations including clinical anti-cancer treatments such as Caelys, Myocet and Doxil.<sup>97, 104</sup>

Although the PEGylated liposomes have improved stability and enhanced circulation time, they still suffer from selectivity for disease targets and lack of controlled delivery timing/dosage. To overcome these problems, further engineered modifications of liposomes were carried out.<sup>105</sup> For example, liposomes were functionalised with ligands for disease biomarkers in order to allow targeted delivery.<sup>106</sup> Also, the surface of liposomes could incorporate  $Gd^{3+}$  or magnetic NPs

for MRI and/or  $^{64}\text{Cu}$  or  $^{18}\text{F}$  for PET imaging.<sup>107, 108</sup> To date, hundreds of imaging agents and drugs have been combined with liposomes for a wide range of theranostic techniques allowing detection and evaluation of the efficiency of loaded liposomes.

### 1.4.2 Micelles

Polymeric micelles (PM) are small vesicles having both polar or charged group and non-polar regions, see Figure 27.<sup>109</sup> PM are formed by self-assembly of amphiphilic copolymer chains in aqueous media. These type of nanoparticles can be formed in two types: direct micelles and inverse micelles, dependent on the media, at the critical micelle concentration (CMC).<sup>110</sup>

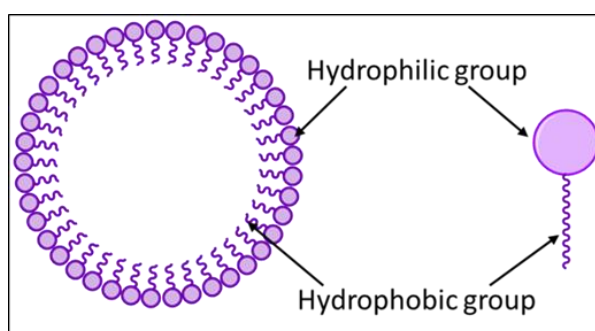


Figure 27: Schematic representation for the structure of polymeric micelle

The PM have a narrow size distribution, with diameters ranging from 10-100 nm and the core can be loaded with a drug for delivery.

Parameters affecting the aggregation of micelles and their size:<sup>99, 111</sup>

1. The length of the non-polar tail.
2. The nature and size of the polar or ionic head.
3. Acidity of the solution.
4. Temperature.

Similar to liposomes, the combination of micelles with different imaging agents and drugs has expanded recently for theranostic applications and also to determine the loading efficiency of micelles. PM encapsulating DOX (anti-cancer drug) were conjugated with *cRGD* and the macrocyclic chelator NOTA for radiolabelling with  $^{64}\text{Cu}$  (PET) and also using  $^{131}\text{I}$  for radioisotope therapy.<sup>112, 113</sup> Different molecules can be

encapsulating in the core of micelles to form a hybrid PM, with magnetic NPs, QDs or gold NPs trapped in the core of micelles so that they can be used for MRI or optical imaging.<sup>99, 114</sup> Drug delivery applications have also been extensively investigated at both the micro-and nano-scale.<sup>115</sup>

## 1.5 Research aims

The main aims of this work are synthesis, characterisation and radiolabelling of different types of nanoparticles for medical imaging applications. SPECT isotope technetium-99m and PET isotope gallium-68 can be utilised for the development of radiolabelling magnetic nanoparticles, liposomes and polymeric micelles.

A range of coating and synthetic methods were conducted to modify the iron oxide nanoparticles in order to investigate their ability as potential platforms for SPECT/MRI contrast. Novel technetium-99m labelled SPIONs as dual modality agents are of interest in SPECT/MR imaging, with optimised radiolabelling reaction and stability studies to determine the most promising functionalised SPIONs for future development *in vivo*.

The second aim is to develop a radiolabelling methodology that combines the of direct radiolabelled SPIONs with gallium-68 for PET imaging and surface coating of a CXCR4 antagonist to allow targeting and *in vitro* validation, see Figure 28. This work builds on previously reported study by the Archibald group that involve in the use of configurationally restricted cross-bridged cyclam to enhance binding toward the CXCR4 chemokine receptor.

Nanocarriers (liposomes and polymeric micelles) have been recently investigated as potential nanotheranostic technologies. The aim is to develop a radiolabelling method for the nanocarriers with gallium-68. *In vivo* validation in a mouse model is required to assess their biodistribution using PET imaging, see Figure 28.

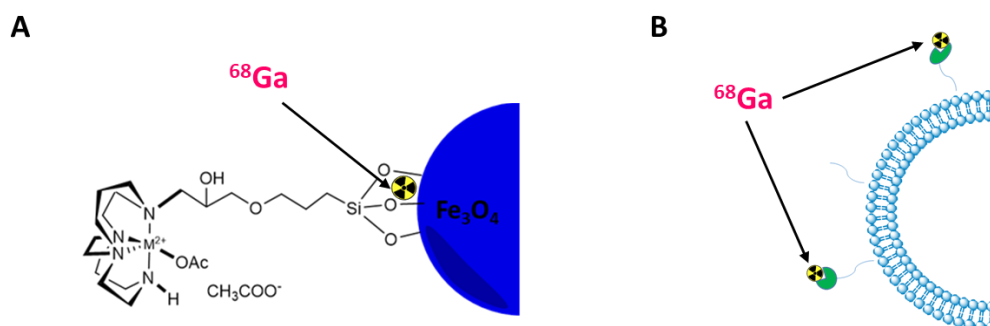


Figure 28: Gallium-68 radiolabelling A) CXCR4 antagonist conjugated SPIONs, B) radiolabelling of chelator functionalised liposomes.

# **Chapter 2**

**Chelator-free technetium-99m  
radiolabelling of SPIONs to form  
dual modality SPECT/MRI agents**

## 2 Chapter two: Chelator-free technetium-99m radiolabelling of SPIONs to form dual modality SPECT/MRI agents

### 2.1 Aims

The aim of the work reported in this chapter is to develop simple and effective methods for radiolabelling SPIONs with the SPECT radioisotope technetium-99m to form a platform for dual modality SPECT/MRI imaging agents based on chelator-free superparamagnetic iron oxide nanoparticles (SPIONs).

This work investigates the effect of coating and synthetic procedures on radiolabelling of SPIONs with a SPECT radioisotope. The first step in this study is the synthesis of chelator-free SPIONs employing different experimental procedures such as the co-precipitation method which is an *ex-situ* method to produce SPIONs coated with siloxane derivatives to form a silica shell. A second procedure utilised for synthesising SPIONs in this work, and coating with polyacrylic acid *in-situ*, is the polyol method. The coated SPIONs shown in Figure 29, have been fully characterised by a range of analytical techniques to investigate the sizes, coating efficiency, surface charge and relaxivity studies to determine the properties of the SPIONs as MRI contrast agents, see section 2.5.4.

The SPECT radiolabelling efficiency of coated SPIONs with technetium-99m has been studied by varying different parameters. The radiochemical stability measurements to analyse the attachment between SPIONs and radionuclide are discussed. For this goal, competitive binding reactions were investigated using EDTA and proteins, see section 2.6.

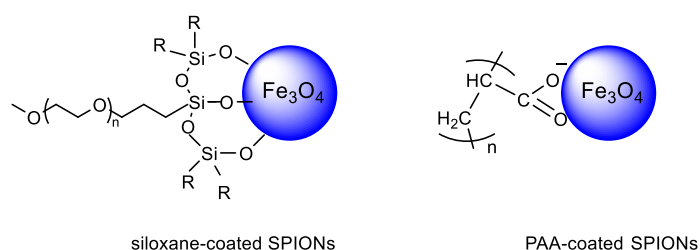


Figure 29: SPIONs coated with siloxane derivatives and polyacrylic acid.

## 2.2 Superparamagnetic iron oxide nanoparticles (SPIONs) in medical applications

The application of SPIONs for biomedical imaging requires specific and effective preparation methods. Methods were developed to give high quality nanoparticles of a uniform size and shape with a low degree of agglomeration and a suitable surface chemistry to ensure that the magnetic properties of the magnetite cores are retained. In order to increase hydrophilicity for colloidal stability (prevention of aggregation) and to functionalise the nanoparticle surface for bio-conjugation, coating of the nanoparticles can be carried out *ex-situ* or *in-situ* during the synthesis. In general, an appropriate coating will increase the circulation time of nanoparticles in the body to improve accumulation at the target organ or tissue (avoiding rapid excretion or accumulation in non-target tissue), see Table 5.<sup>116</sup>

Table 5: List of FDA-approved SPIONs products.<sup>117</sup>

Table 5: List of FDA-approved SPIONs products. <sup>117</sup>	Material/Functionality	Applications
Feridex I.V. <sup>®</sup> , Endorem <sup>®</sup>	Dextran	Imaging of liver lesions
Resovist <sup>®</sup> , Clivast	Carboxydextran	Imaging of liver lesions
Gastromark, Lumirem <sup>®</sup>	Silicone	Enhance of bowel imaging
Ferumoxtran-10, Sinerem <sup>®</sup>	Dextran	Lymph node metastases

SPIONs can be synthesised by a range of methods including co-precipitation, thermal decomposition, and polyol methods.

Preparation of magnetite nanoparticles as PET/SPECT-MRI dual modality contrast agents can involve many steps and different procedures. In general the first step, synthesis of the superparamagnetic iron oxide nanoparticle (NP) core, is followed by coating the NPs with the desired capping agents such as polymers, an inorganic shell, organic surfactants or bioactive molecules. Siloxane agents are considered to an excellent class of surface modifiers for SPIONs due to the ease of inclusion of

functional groups into a silica shell that can bind or react with other polymers, metal ions or other biomolecules.<sup>44</sup> In addition, a silica-shell increases the stability of SPIONs and protects their magnetisation.<sup>57</sup> The freshly synthesised magnetite NPs are usually stirred in a basic solution mixed with an ethanol/water particle suspension to form hydroxyl groups on the surface of the iron oxide nanoparticles. The hydroxyl groups react with the alkoxy group of alkoxy silane to form Si-O-Fe bonds leaving the outer functional groups available for further reaction. For example, Kohler et al.<sup>118</sup> coated iron oxide NPs with PEGylated silane using this method. The PEG chains prevented the nanoparticles from aggregating, with further conjugation reactions possible at the amine group on the end of the chains, see Figure 30 .

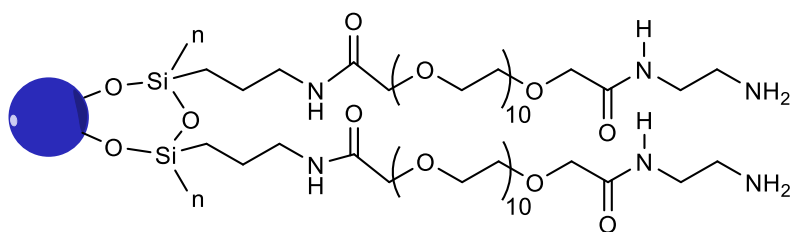


Figure 30: PEGylated siloxane used to modify the SPIONs surface forming a silica shell with PEG chains and functional groups for further reaction.

## 2.3 $^{99m}\text{Tc}$ radiolabelling of SPIONs for dual modality SPECT/MRI contrast agents

In this work, magnetic SPIONs with different coatings were radiolabelled with the SPECT radioisotope,  $^{99m}\text{Tc}$ , which is the most common radionuclide used for nuclear medicine applications worldwide. Hence, technetium-99m is attractive for radiolabelling nanoparticles due to its excellent physical and chemical properties, widespread availability from a cost effective source ( $^{99}\text{Mo}/^{99m}\text{Tc}$ ) and suitable decay characteristic with a 6.02 hours half-time.<sup>119</sup>

The main objective of this work is to develop technetium-99m radiolabelled SPIONs for dual modality SPECT/MRI contrast agent based on chelator-free functionalised iron oxide nanoparticles synthesised by different routes and varying coating methods, see Figure 31. The nanoparticles were radiolabelled with technetium-99m in oxidation state (V), generated using characterised literature methods<sup>120</sup> under several conditions by using stannous chloride as a reducing agent and without any presence of ligand on the surface of SPIONs to stabilise the radionuclide.

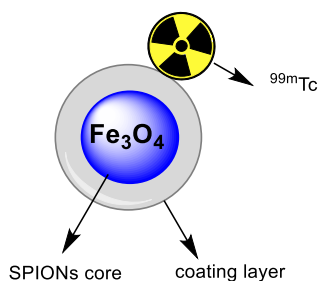


Figure 31: Technetium-99m radiolabelled nanoparticles  $^{99m}\text{Tc}$ -SPIONs.

### 2.3.1 Radiolabelling of iron oxide nanoparticles for multi-modality imaging agents

The new approach of using SPIONs as SPECT/MRI dual modality contrast agents is a promising field in molecular imaging for highly sensitive and high resolution imaging. Usually, SPIONs were designed with ligands in order to get stable radiolabelling and high specific activity product.<sup>121</sup> Recently, a chelator-free iron oxide nanoparticles for multimodal SPECT/MRI imaging agents has been an emerging field due to the ease of synthesis and functionalisation of the NPs simultaneously with different functional groups and the radionuclide, thereby providing useful imaging capability and high target avidity.<sup>19</sup>

Sandiford *et al.*, used Endorem/Feridex (a liver MRI contrast agent based on iron oxide nanoparticles) and conjugated with <sup>99m</sup>Tc-dipicolylamine (DPA)-alendronate, a bisphosphonate (BP) SPECT agent, to provide a SPECT/MRI contrast agent. Their results show that increasing the temperature enhanced the radiolabelling yield while the <sup>99m</sup>Tc-DPA-alendronate-Endorem system showed high stability in serum for more than 48 hours.<sup>122</sup> Torres de Rosales *et al.* demonstrated a simple ligand exchange system for synthesis of ultra-small iron oxide nanoparticles coated with PEG and conjugated with a terminal BP group. The PEGylated SPIONs were radiolabelled with technetium-99m and showed low uptake in the reticuloendothelial system (RES) and a high positive contrast signal, indicating suitability as a  $T_1$ -weighted MRI/SPECT contrast agent.

The same group developed an alternative method using non-macrocyclic chelator functionalised iron oxide nanoparticles that were radiolabelled with <sup>64</sup>Cu to serve as a PET/MRI contrast agent. The SPIONs were functionalised with a bisphosphonate group and conjugated with a dithiocarbamate group for <sup>64</sup>Cu binding. This construct showed *in vitro* stability for at least 48 hours.<sup>50</sup>

Burke *et al.* synthesised iron oxide nanorods with different ratios of PEG and macrocyclic siloxane compounds as PET/MR imaging agents. The SPIONRs were radiolabelled with PET radionuclide  $^{68}\text{Ga}$  in ammonium acetate at pH5, and all nanoparticles constructs showed a high radiochemical yield, even in the absence of macrocyclic ligands suggesting that chelator free labelling of the silica shell was occurring, see Figure 32.<sup>19</sup>

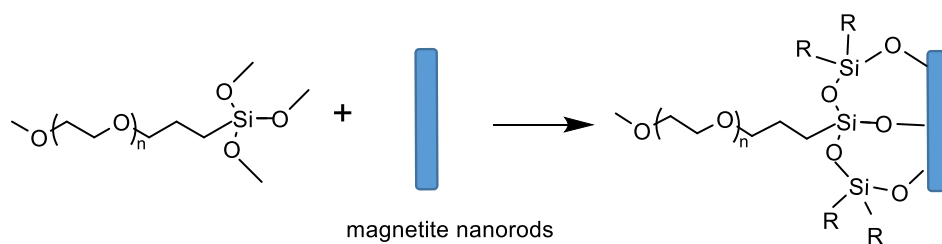


Figure 32: Synthesis of siloxane coated iron oxide nanorods for radiolabelling with  $^{68}\text{Ga}$ .

## 2.4 Synthesis of SPIONs

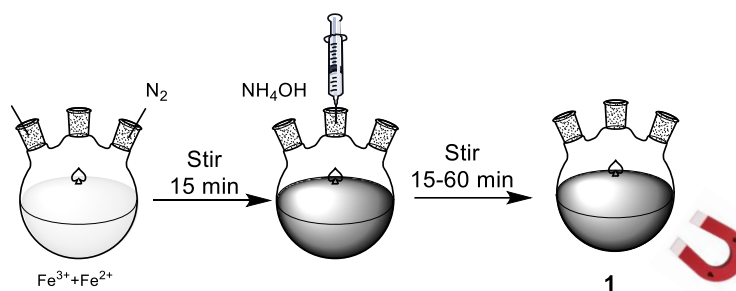
The aim of the work reported in this chapter is to investigate the effect of silica coating and variations in the synthetic procedure on the radiolabelling of SPIONs with the SPECT radioisotope technetium-99m. In order to achieve this goal, two methods were used to synthesise iron oxide nanoparticles, the first was an *ex-situ* procedure by using co-precipitation method to prepare the cores of the SPIONs, followed by coating the particles with a siloxane-PEG derivative. The second method is an *in-situ* procedure for synthesis coating iron oxide nanoparticles with polyacrylic acid following the polyol method.

Selection criteria for the co-precipitation and polyol methods for synthesis of iron oxide nanoparticles for SPECT/MRI imaging agent lie in the ease and simplicity of the techniques with high yields of controlled size SPIONs achieved in water.

### 2.4.1 Synthesis of SPIONs core by the co-precipitation method

Co-precipitation is considered a standard method for obtaining magnetite nanoparticles. Many researchers have investigated the impact of varying different synthetic parameters on the morphology, structure and magnetic properties of the particles. In order to form siloxane coated-superparamagnetic nanoparticles for the SPECT/MRI agent, the magnetic core was constructed first. The synthesis of SPIONs via co-precipitate route is suitable for siloxane coating and provides direct dispersion in water and controlled size.<sup>84</sup>

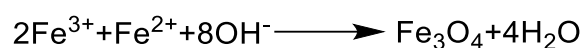
The synthesis of the SPIONs core followed the procedure reported by Barreto *et al.* with some modifications.<sup>123</sup> Magnetite Fe<sub>3</sub>O<sub>4</sub> core **1** was prepared by addition of base to an aqueous mixture of Fe<sup>3+</sup> and Fe<sup>2+</sup> salts at a 2:1 molar ratio. In a typical synthesis, 0.16 g FeCl<sub>3</sub> and 0.1 g FeCl<sub>2</sub> were dissolved in 10 ml distilled water under nitrogen gas over 15 minutes. Within 10 minutes, 28% ammonia solution was added into the reaction vessel and a black precipitate formed immediately. This reaction was carried out at 80°C and the mixture was stirred for a further 60 minutes, see Scheme 1.



*Scheme 1: Schematic representation of the synthetic steps required for SPIONs core production by co-precipitation method.*

The formation of superparamagnetic iron oxide nanoparticles,  $\text{Fe}_3\text{O}_4$ , is expected between pH 9 and 14 in an oxygen-free environment.<sup>124</sup> According to the thermodynamics of this reaction,  $\text{Fe}_3\text{O}_4$  is not very stable, and an inert atmosphere was used in order to prevent the oxidation of magnetite to  $\gamma\text{-Fe}_2\text{O}_3$ , which would affect the physical and chemical properties of the nanoparticles.<sup>37</sup> Use of an inert atmosphere also decreases the hydrodynamic size when compared with synthesis of iron oxide NPs in an oxygen containing environment.<sup>57, 124, 125</sup>

The chemical reaction to form magnetite core is as follows:

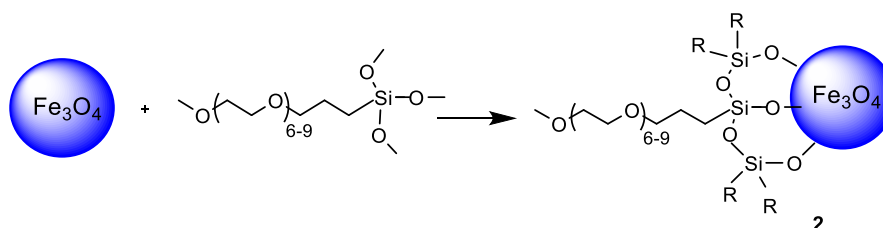


*Scheme 2: Chemical reaction for synthesis of the SPIONs core.*

In the co-precipitation method, there are two steps to control nanoparticle formation. The first is the nucleation step, in which small nuclei are formed first, followed by the crystal growth step. These steps must be separated, which means that the nucleation step should not occur during the crystal growth step.<sup>125</sup> In magnetite nanoparticle synthesis, variation in the temperature, pH, ionic strength, stirring rate and synthetic time have effects on the crystallinity and monodispersity of the nanoparticles produced.<sup>126</sup> For example, Babes *et al.* studied the influence of temperature on the iron oxide nanoparticle size, their study showing that particle size decreases when temperature is increased.<sup>127</sup>

## 2.4.2 Synthesis of siloxane derivatives coated- SPIONs

In order to study the effect of co-precipitation method and coating of SPIONs on radiolabelling with technetium-99m, the coating step with a siloxane derivative is required. Forming a silica shell can provide several beneficial properties to the magnetic cores. These include: ease of functionality, increased stability and biocompatibility. Silica coating provides an opportunity for the enhancement of colloidal properties and functions by using core-shell rational designs to overcome the limitations of nanoparticles such as low stability, high chemical reactivity and undesired aggregation processes. Silica coating of superparamagnetic nanoparticles (SPIONs) requires certain conditions: low temperature, high pH, specific concentration of siloxane and small amounts of water.<sup>123</sup> The SPIONs prepared from the co-precipitation method, **1**, were used for coating with 2-methoxy (polyethyleneoxy)propyltrimethoxysilane to form siloxane@SPIONs **2**, see Scheme 3.

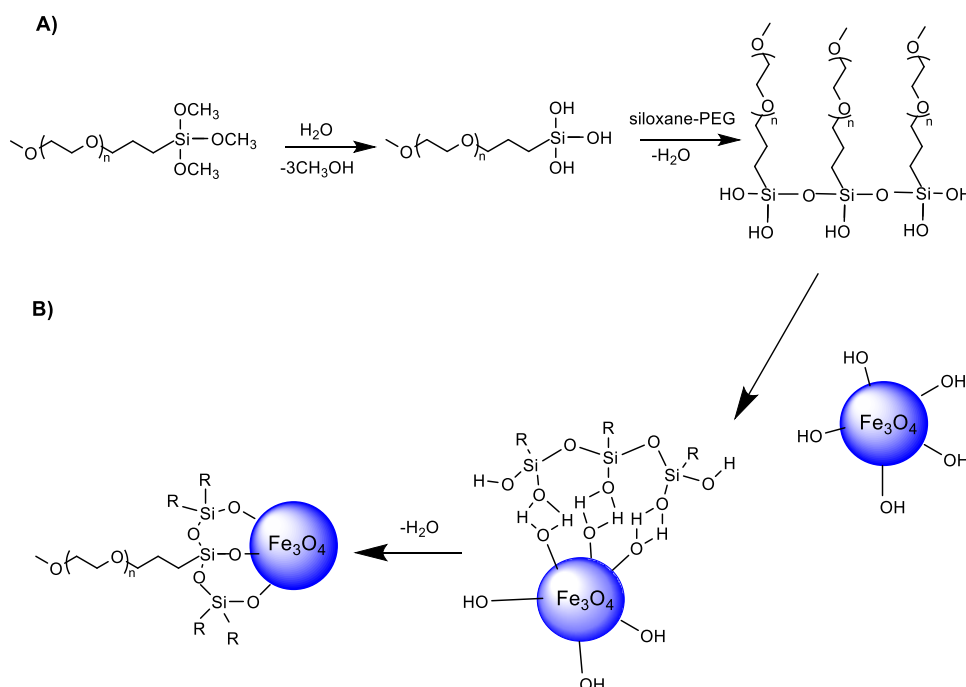


*Scheme 3: Schematic representation of silica coating of the SPIONs with a siloxane derivative.*

Instead of using only magnetic separation or centrifugation independently to purify the nanoparticles as in the literature<sup>19</sup>, the product was separated by strong rare earth magnet with successive washing using a series of solvents and centrifugation steps to remove impurities.

The combination of these methods promoted the isolation of small diameter SPIONs that were purified by passing through a 220 nm filter. First, the sample was exposed to a magnet to remove the large particles and the supernatant was centrifuged at 13000 rpm for 45 minutes to ensure full separation. The supernatant was then removed and the precipitate was washed twice with ethanol using a high centrifugation speed. Then, ultra-pure water was added and again the sample was centrifuged at the same speed. This step was repeated twice for further purification. Finally, the siloxane-coated SPIONs were filtered and kept suspended in solution.

As mentioned, the siloxane-PEG coating is suitable for modifying the surface of iron oxide nanoparticles and increases their stability. The physicochemical mechanism for this process includes two steps. First, the hydrolysis of ethoxy groups presenting siloxane-PEG under the influence of a basic solution after the addition of ammonia to form Si-OH. Secondly, a condensation reaction in order to connect the hydroxyl groups on SPIONs and those on siloxane-PEG and releasing water molecules. Scheme 4 illustrates these mechanisms.<sup>128</sup>



Scheme 4: Schematic representation of the A) hydrolysis and B) condensation steps for coating SPIONs with a siloxane derivative.

The size of nanoparticles is crucial for biological applications because nanoparticles with a hydrodynamic size above 200 nm are mainly taken up by the liver and spleen. However, particle sizes less than 150 nm are considered suitable for biological *in vivo* application such as using NPs for imaging agents.<sup>38</sup> Therefore, measuring the hydrodynamic size of nanoparticles is the first step after synthesis and coating the NPs. The hydrodynamic sizes for nanoparticles were obtained by Dynamic Light Scattering (DLS) of the particles dispersed in liquid. The variability of particle size within the batches is quantified by the polydispersity index (PDI), polydispersity below 0.5 is considered to be relatively monodisperse and usually stable in aqueous solutions.<sup>129, 130</sup>

The hydrodynamic size for siloxane@SPIONs obtained by DLS was 73 nm and the PDI is 0.189, see Figure 33. This result close to previous where the Archibald group prepared iron oxide nanorods using similar methods, the hydrodynamic size for these rods was 99 nm measured by NTA, with a diameter for the rod cores of *ca.* 70 nm from TEM images.<sup>19</sup> Hamley and Fu discussed the effect of coating on the SPION's hydrodynamic size, concluding that coating SPIONs with polymers or silica enables them to form barriers between SPIONs cores, so preventing them from aggregating by using steric force repulsion.<sup>124, 131</sup>

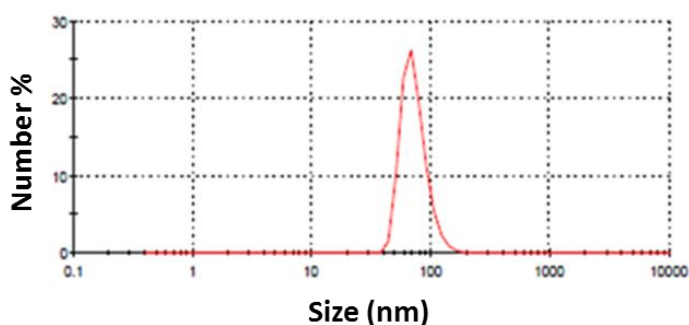


Figure 33: The DLS analysis shows the hydrodynamic size for siloxane@SPIONs 2 .

### 2.4.3 Synthesis of polyacrylic acid coated iron oxide nanoparticles via polyol

In order to investigate the effect of different synthetic procedures and coating on radiolabelling of iron oxide nanoparticles with technetium-99m, the polyol method and polyacrylic acid were selected to prepare *in-situ*, ultra-small nanoparticles coated with polymer. The polyol method is shown to produce water-dispersible and narrow hydrodynamic size NPs. The first description of this method was by Fievet *et al.* in 1989. They introduced the polyol synthesis process which has been developed quickly to form high quality nanoparticles.

The process relies on using high boiling point polyols (poly hydroxyl alcohol), which increases with increasing number of hydroxyl groups and its molecular weight. The viscosity and polarity of the polyols depend on their molecular weight.<sup>132, 133</sup> The chelating effect of polyols is useful to control the nucleation, growth step and agglomeration of NPs by adherence of polyol on the surface of nanoparticles and it also serves as a colloidal stabiliser to form a highly stable suspension. Recent reports include the polyol method being used in the presence of polyol solvents such as ethylene glycol (EG), diethylene glycol (DEG), tetraethylene glycol (TEG) and triethylene glycol (TREG), which acts as solvent, as surfactant as well as a reducing agent.<sup>134</sup> These solvents are known to reduce the metal salts to form metal nuclei, which contribute to the formation of metal particles.<sup>135, 136</sup>

In this method and during synthesis, different capping agents can be added to increase hydrophilicity of SPIONs. In this study, polyacrylic acid was chosen due to its high biocompatibility and the improved stability of the nanoparticles in aqueous suspensions in the presence of high boiling point alcohol diethylene glycol (DEG); the result is high crystallinity and ultra-small size NPs<sup>137, 138</sup>, see Figure 34.

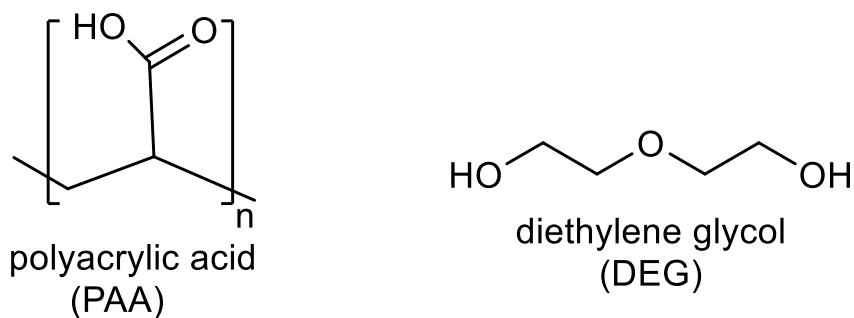
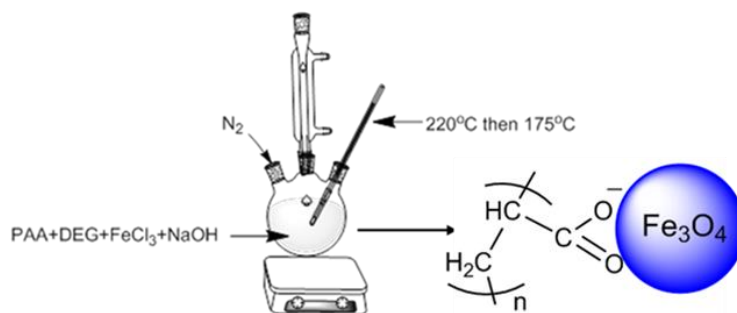


Figure 34: Structures of PAA and DEG used with the polyol method in this work.

#### 2.4.4 Synthesis of PAA-coated SPIONs

Polyacrylic acid (PAA) is a hydrophilic polymer used as a capping agent for various nanoparticles in biomedical applications such as drug delivery and MRI contrast agents. Coated SPIONs with PAA are considered non-toxic, with no signs of inflammation caused by the interaction of coated SPIONs with mononuclear phagocytes that are responsible for most of the inflammation in different diseases.<sup>138, 139</sup>

The synthetic protocol to produce PAA@SPIONs **3** followed the He *et al.* method.<sup>140</sup> In brief, 1 g of PAA with molecular weight 2.1 kDa was used as a capping agent of iron oxide NPs in the presence of iron chloride and diethylene glycol (DEG). The mixture was heated to 220°C for 45 minutes, after which sodium hydroxide dissolved in DEG was added and heated for another 2 hours and then the temperature was reduced to 175°C for 24 hours, see Scheme 5. The resultant NPs were suspended in water and exhibited a high colloidal stability for more than 2 years



Scheme 5: Schematic representation of the synthetic steps used to form PAA@SPIONs via the polyol method.

As previously described, the first physical property to be tested was the hydrodynamic size using dynamic light scattering. The aqueous solution of PAA@SPIONs **3** were filtered with a 220 nm filter prior to measurement. As can be seen in Figure 35, the average hydrodynamic size is 58 nm with a low polydispersity index around 0.2, which indicates that the coated SPIONs are monodisperse and likely to be stable in solution.

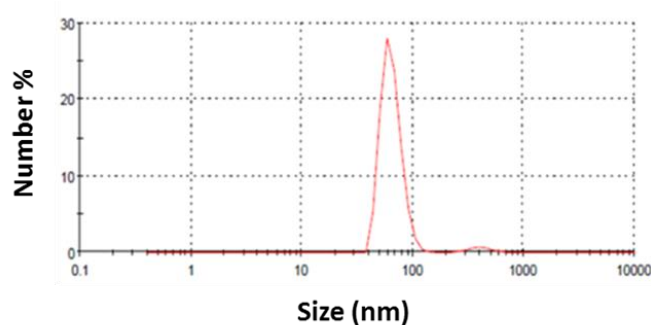


Figure 35: The DLS analysis shows the hydrodynamic size for PAA@SPIONs **3**.

## 2.5 Characterisation of SPIONs

The synthesised nanoparticles, siloxane@SPIONs and PAA@SPIONs were investigated using a series of characterisation techniques in order to analyse the SPIONs core, their coating and stability. At a later stage, the application of the synthesised SPIONs was investigated in relaxivity and radiochemistry studies.

### 2.5.1 Structure characterisation (X-ray crystallography (XRD), particle size morphology and size distribution)

XRD diffraction (XRD) is known as a non-destructive and quantitative technique used to identify materials. This method provides information about phase composition, crystal orientation, and crystal defect and crystallite size. This technique can be used to confirm the formation of a magnetite phase that shows a very high magnetisation.<sup>141</sup>

The crystalline structure of the obtained iron oxide nanoparticles was investigated by powder XRD for the freeze-dried samples to confirm phases and identify any impurities. The XRD pattern for siloxane@SPIONs and PAA@SPIONs in Figure 36 showed a formation of a single phase iron oxide with a cubic structure, which agrees with crystallography database reference nr: 00-003-0863. It is clear that both samples are coherent with a magnetite pattern with no identified impurities.

The X-ray diffraction and the transmission electron microscopy TEM can be used to determine the iron oxide crystal size. Scherrer theory describes the relation between size of particles and the intensity of XRD peaks, and in this the size of the crystallites are inversely proportional to the width of the highest intensity low-angle Bragg reflection.<sup>142</sup> The highest peak at  $2\theta$  equal to  $35.5^\circ$  refers to (311) plane of magnetite, which was used to calculate the crystal size using the Debay-Scherrer equation, see Equation 2.

$$D = k \cdot \lambda / B \cdot \cos \theta$$

*Equation 2*

D is the mean size of the nanoparticles, k is constant for iron oxide is 0.839,  $\lambda$  is the X-ray wavelength, B is the line broadening at the half maximum intensity (FWHM) and  $\theta$  is the Bragg angle. Therefore, when the co-precipitation method was followed to synthesise siloxane@SPIONs, the core size of magnetite measured at  $35^\circ$  in the X-ray diffractogram was larger than in the PAA@SPIONs sample in which the polyol method was used to synthesise the ultra-small size nanoparticles, see Figure 36.

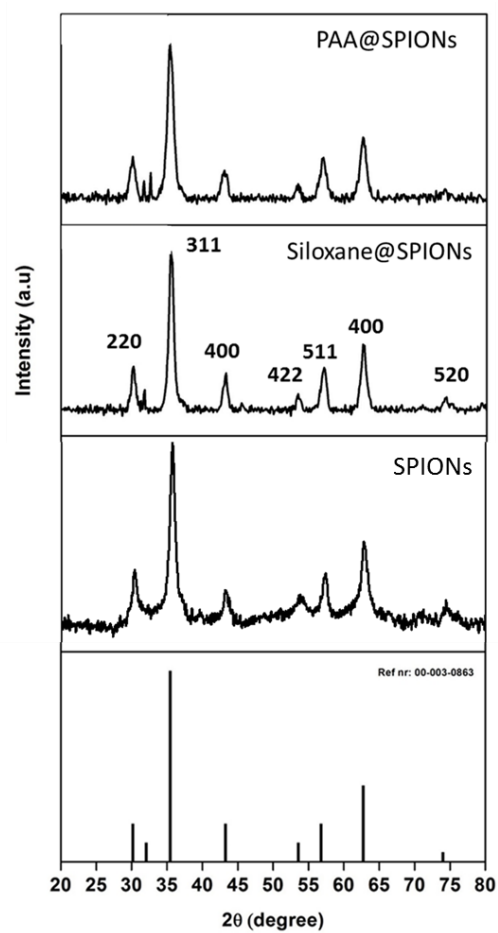


Figure 36: XRD patterns for SPIONs synthesised by the co-precipitation method, siloxane@SPIONs 2 and PAA@SPIONs 3. Peaks are indexed according to the reference pattern for magnetite.

Table 6: Crystallite sizes for siloxane@SPIONs and PAA@SPIONs.

Sample	Peak position (2θ)	FWHM (radians)	Crystallite size (nm)
siloxane@SPIONs	35.43	0.016	9.5
PAA@SPIONs	35.43	0.052	4.8

The crystalline phase and the core size of nanoparticles were affected by the synthetic procedures. The core size for PAA@SPIONs is 4.8 nm which is in agreement with the results reported by Kuwahara *et al.* They synthesised iron oxide nanoparticles coated with PAA by polyol method to gain cores with diameter around 4 nm. They found that the addition of polymer in the presence of DEG inhibits the nucleation step and slowed crystal growth due to the ionic interaction between PAA and the magnetite nuclei.<sup>143</sup> The core sizes for siloxane@SPIONs is around 9.5 nm,

which agreed with other literature reports that used the co-precipitation method for synthesis of SPIONs. In a study by Hauser et al. SPIONs were formed by co-precipitation method and coated with dextran, the core size measured by XRD gives particles with 10 nm.<sup>76</sup>

TEM is an advanced electron microscope technique utilising an energetic beam of electrons to obtain a high level of magnification of a sample compared to conventional optical microscopes. TEM images for the prepared samples can be seen in Figure 37, with different iron oxide nanoparticle cores and sizes, dependent on synthetic methods and coating. For siloxane@SPIONs, Figure 37A shows selected TEM images of SPIONs cores. Most particles appear as spherical shapes with a mean diameter of 9.2 nm which is in agreement with XRD measurements. However, a small number of SPIONs have a more cubic shape. The irregularity of shapes and sizes is related to the co-precipitation method which suffers from an inability to control the size and shapes of nanoparticles due to the preparation conditions. For example, Mascolo *et al.* used the co-precipitation method to prepared SPIONs with different base solutions to gain SPIONs cores between 7 to 11 nm.<sup>144</sup> The image in Figure 37A also shows an agglomeration of SPIONs, which may be due to the magneto dipole interaction of magnetite nanoparticles.

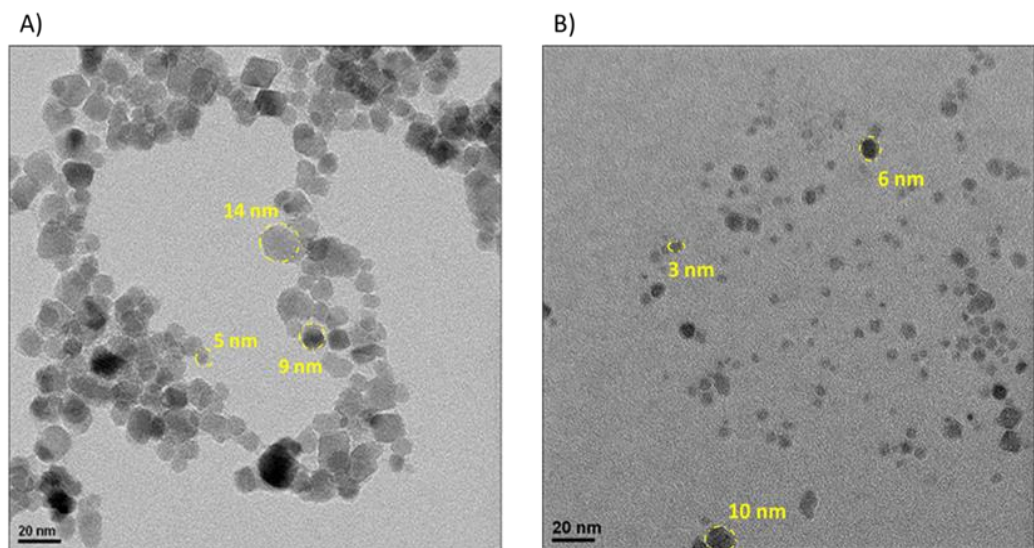


Figure 37: TEM images for coated nanoparticles A) siloxane@SPIONs 2, and B) PAA@SPIONs 3.

In Figure 37B, the TEM image for the PAA@SPIONs exhibits ultra-small core sizes, with a very narrow diameter of 4.4 nm. This result is in good agreement with the XRD measurement and with the literature.<sup>143</sup> The polyol method is widely known to offer a high degree of control over the size and shape of nanoparticles compared to the co-precipitation method. The histograms of sizes, calculated by TEM for both SPIONs in Figure 38A and B, show the size distribution of iron oxide cores. It is clear that the average of the siloxane@SPIONs core is double that of the PAA@SPIONs.

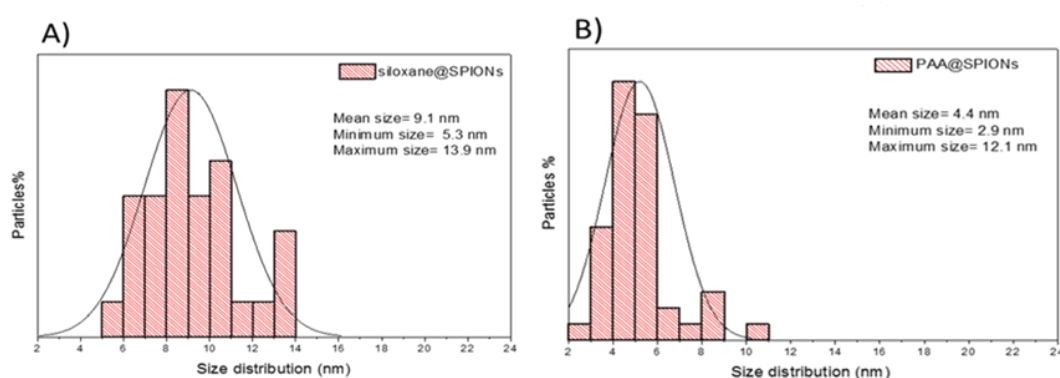


Figure 38: Histograms for SPIONs, A) coated with siloxane **2**, and B) coated with PAA **3** (minimum 80 nanoparticles were counted).

## 2.5.2 Surface analysis by FT-IR

Fourier transform infra-red spectroscopy (FT-IR) can be used to obtain absorption peaks which correspond to the frequencies of vibrations between the bonds of the atoms in the material. Therefore, FT-IR can identify the functional groups, the materials and the relative amount present.<sup>145</sup> FT-IR has been used in this study to confirm the presence of coating materials, PAA and siloxane derivatives, on the SPIONs surfaces. The IR spectrum for siloxane@SPIONs is shown in Figure 39, with a strong peak observed at  $578\text{ cm}^{-1}$  in the low frequency region ( $1000\text{-}500\text{ cm}^{-1}$ ) which corresponds to Fe-O stretching. This pattern is consistent with a magnetite phase (band between  $570\text{-}580\text{ cm}^{-1}$ ) or the maghemite ( $\gamma\text{-Fe}_2\text{O}_3$ ) spectrum (broadband between  $520\text{-}610\text{ cm}^{-1}$ ). The band at  $587\text{ cm}^{-1}$  of Fe-O shows that siloxane@SPIONs consists mainly of a magnetite phase.

The other peaks between 630 to 800  $\text{cm}^{-1}$  indicate the presence of silica coating on the surface of SPIONs, which can be attributed to Si-O-Fe and C-Si-O respectively. The siloxane derivative consists chains of PEG; therefore, peaks at 1310 and 2890  $\text{cm}^{-1}$  can be assigned to C-O-C and C-H stretching frequencies.

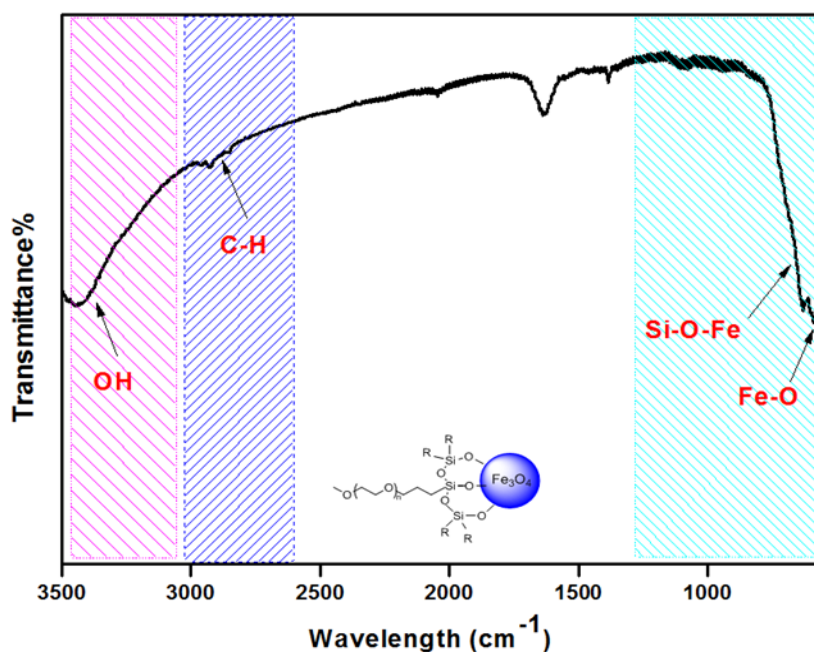


Figure 39: FT-IR spectrum for siloxane@SPIONs 2.

For PAA@SPIONs, the FT-IR spectrum is displayed in Figure 40. The characteristic Fe-O stretching vibration band is present in a low frequency area. Moreover, bands at 1126 and 1053  $\text{cm}^{-1}$  are characteristic of C-O stretching. The vibration bands for the carboxylate group are also assigned at 1575 and 1409  $\text{cm}^{-1}$  and refer to asymmetric and symmetric ( $\text{COO}^-$ ) attached to the surface of iron oxide nanoparticles. The other broad band at 3315  $\text{cm}^{-1}$  is due to hydrogen bonded O-H stretching vibration from hydroxyl groups on the SPIONs surface and probably the presence of water. There are intense peaks at 2875 and 2934  $\text{cm}^{-1}$  attributed to stretching vibration bands of C-H. The FT-IR analysis confirms the attachment of PAA on the SPION surface. Many researchers have investigated the interaction between a coating polymer and the magnetite surface.<sup>146</sup> For example, Zhang et al. reported that carboxylic acid polymers adhere to magnetite nanoparticles via coordination linkages between the carboxylate groups and iron.<sup>147</sup>

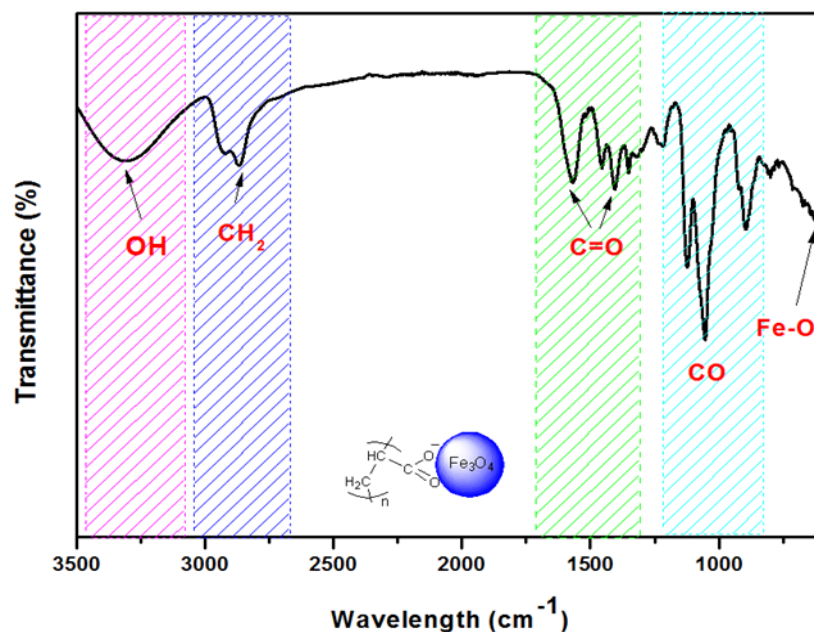


Figure 40: FT-IR spectrum for PAA@SPIONs 3.

### 2.5.3 Zeta potential and elemental analysis

In the preparation of nanoparticles, measuring their stability is a critical step to predict the nanoparticle behaviour in a biological system. Hence, studying the nanoparticle surface charges is an important requirement before investigating the NPs *in vivo*. Zeta potential is used to measure the surface charges of NPs, and high positive or high negative charges indicate high electrostatic repulsion. Therefore, the stability of NPs will be improved and aggregation reduced. Consequently, the zeta potential is one of the fundamental parameters to indicate the stability of nanoparticles as it measures the magnitude of the charge repulsion/ attraction between particles.

The charge of nanoparticles vary according to the type of coating. The aim of this part of the research is to study the stability of synthesised SPIONs using different coating and synthetic techniques.

Table 7 shows the zeta potential measurements of prepared samples in PBS solution at pH 7. The siloxane@SPIONs has a negative value of zeta potential about -10.98 mV which is due to the nature of siloxane derivatives and also related to the steric effect of the PEG chain. PAA@SPIONs have the largest surface charge due to the presence

of carboxylate groups indicating a high colloidal stability of NPs. The NPs showed a high colloidal stability, with no sign of aggregation for up to two years for PAA@SPIONs, compared to a few months for siloxane@SPIONs.

*Table 7: Elemental analysis and zeta potential for siloxane@SPIONs and PAA@SPIONs.*

<b>Sample</b>	<b>C%</b>	<b>H%</b>	<b>Fe%</b>	<b>Si%</b>	<b>Zeta potential (mV)</b>
<b>Siloxane@SPIONs</b>	<b>5.6</b>	<b>0.7</b>	<b>55.25</b>	<b>1.2</b>	<b>-10.98 ( ±5.03)</b>
<b>PAA@SPIONs</b>	<b>34.5</b>	<b>6.6</b>	<b>12.00</b>	<b>0</b>	<b>-24.00 (±2.80)</b>

The long-term stability of the synthesised nanoparticles, indicates that the coating procedures that had been used were appropriate. Table 3 illustrates the presence of inorganic and organic layers on the surface of SPIONs which was confirmed by elemental analysis. Inductively coupled plasma-optical emission (ICP-OES) is an ideal method for trace metal analysis and gives quantitative data. The sample is usually digested in nitric acid prior to analysis by ICP-OES. In the case of silica coated SPIONs, the sample needs the harsh acid environment in order to digest the silica shell.

The siloxane@SPIONs was investigated by ICP. The first step of the analysis was dissolving NPs in a mixture of two strong acids, hydrofluoric acid and nitric acid in a ratio 1:3. The ICP was combined with elemental analysis to indicate the coating of iron oxide nanoparticles with the silica shell. This analysis is used to quantifying the percentage of NPs contents, and gives an idea about the silica coverage of the SPIONs surfaces after several washing steps.

The silica percentage was 1.2% which indicates the presence of a very thin Si shell on the NPs surface and consequently the iron composition was 55.25%. A comparison can be made with a study by Burke et al.<sup>19</sup> which used a similar procedure to coat SPIONs. The Archibald group found 52.64% of iron which is very similar to the data in this work. However, the carbon results were different. In their study the carbon was 1.73% while in this study it was 5.63% as the result of differences in the silica shell and may also have been influenced by the particle shape (rods vs. spheres). In the case of PAA@SPIONs, the high amount of PAA used (1 g) has a huge impact on the reduction of iron percentage. From the elemental analysis, it is clear that a greater thickness of organic layer is present on the surface of SPIONs which led to the relative increase in suspension stability of the SPIONs. The results indicate that PAA or silica shells on the nanoparticle surfaces represent a significant percentage of the overall mass. As a result, the percentage of iron varies with the synthetic techniques used and the scale of the reactions carried out.

## 2.5.4 Relaxivity studies of the synthesised SPIONs

The relaxivity of contrast agents depends on the ability of the agent to enhance MRI contrast by increasing the relaxation of the surrounding hydrogen proton nuclear spin. SPIONs can serve as a dual  $T_1$ - $T_2$  contrast agents based on the core size. However, increase in  $T_2$  relaxation of SPIONs is expected to correlate to iron concentration, whereas,  $T_1$  relaxation is effected slowly and inconsistently against the applied magnetic field. The magnetic behaviour of the synthesised SPIONs was investigated at 1.4 T (60 MHz). The concentration of iron for the measurement of longitudinal and transversal relaxation times was controlled based on the ICP-OES results. The magnitude of the relaxivity rates and their ratios are important parameters in evaluating SPIONs as MR contrast agents.

In Figure 41, it is clear that both SPIONs are relatively weak  $T_1$  contrast agents. As  $T_2$  contrast agents, both SPIONs showed fast relaxivity rates. The siloxane@SPIONs has a higher relaxation rate  $41.4 \text{ mM}^{-1}\text{s}^{-1}$  which is almost double the relaxation rate for the PAA@SPIONs. This results agreed with observations made by Ahmad *et al.* indicating that the relaxivity of SPIONs increased linearly with increasing core size, it can explained that larger SPIONs core possess higher magnetisation values therefore exhibit fast relaxation rates.<sup>148</sup>

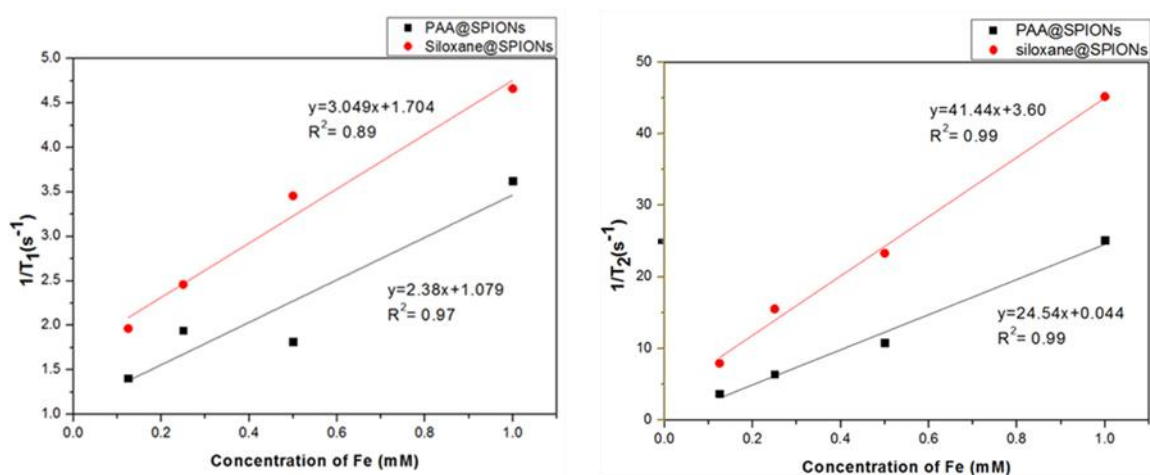


Figure 41:  $T_1$  and  $T_2$  MRI relaxivity plots of siloxane@SPIONs 2 and PAA@SPIONs 3 at range of Fe concentrations (0.1-1 mM) at 1.4 T.

Moreover, a comparison can be made between PAA@SPIONs in this study and SPIONs prepared by Zhang *et al.* to confirm the relationship between core size and relaxation rates. In their study, PAA coated SPIONs were made by the polyol method with a surface modified to include the arginine-glycine-aspartic acid (RGD) peptide (to evaluate binding to the integrin  $\alpha_v\beta_3$  on hepatic stellate cells). The  $r_1$  and  $r_2$  were measured at 1.4 T, it is clear that the core size of their SPIONs are threefold larger than the core size in this study, and therefore increased relaxation rates, see Table 8.<sup>149</sup>

Table 8: The hydrodynamic sizes and relaxivity rates for PAA@SPIONs and RGD-PAA@SPIONs from reference 40.

Sample	Hydrodynamic size nm	Core size nm	$r_1$ (mMS) <sup>-1</sup>	$r_2$ (mMS) <sup>-1</sup>
RGD-PAA@SPIONs	37.50	14.5	8.7	137.8
PAA@SPIONs	58.00	4.40	2.38	24.54

The ratio of relaxivity ( $R_2/R_1$ ) reflects the influence of coating material on the SPIONs magnetic properties. The  $R_2/R_1$  ratio was calculated for the prepared SPIONs based on relaxation studies. Siloxane@SPIONs has 13.5 L/mmol-S, whereas the SPIONs coated with PAA have a ratio around 10 L/mmol-S. These results can be explained by the water diffusing through the coating layer thickness and its permeability to reach the surface of nanoparticles.

The interpretation of these results have been confirmed by many researchers. For example, La Conte *et al.* investigated the thickness effect of SPIONs coated with PEG on relaxation rates and concluded that ratio of relaxivity rates can be affected by the coating thickness.<sup>150</sup> A similar result was found by Vuong *et al.* when SPIONs were coated with PAA (Mw=5 KDa). This indicates that not only the size and the colloidal stability have an impact on the magnetic properties, but also that the coating material and thickness can affect the relaxation rates.<sup>134, 151</sup>

When the PAA@SPIONs were measured at 3T using a clinical scanner, the SPIONs showed strong negative contrast enhancement with an increase in iron concentrations, see Figure 42.

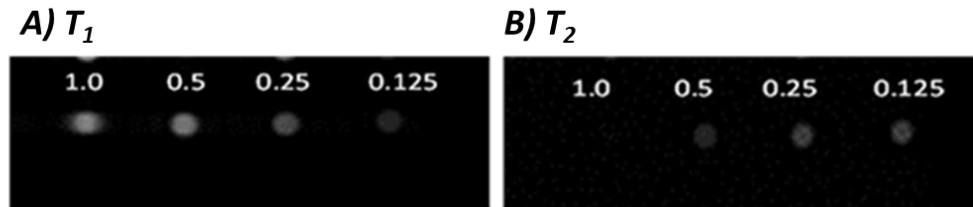


Figure 42: Phantom images of A)  $T_1$  and B)  $T_2$  for PAA@SPIONs 3 measured under 3 T clinical scanner at range of Fe concentrations.

## 2.6 Radiochemistry reactions and stability studies for synthesised SPIONs with technetium-99m

In this part of the research work, the iron oxide nanoparticles (SPIONs), with two different coatings, were radiolabelled with SPECT isotope technetium-99m. The radiolabelling reactions for siloxane@SPIONs **2** and PAA@SPIONs **3** with technetium-99m were carried out at wide range of pH, temperatures and buffers in order to improve the radiochemical yield (RCY%), which reflects the attachment of radionuclide on the surface of SPIONs. Furthermore, radiolabelling stability studies will be investigated in order to mimic the radiolabelled SPIONs in physiological environments. For example, the radiolabelled SPIONs will be investigated in ethylenediaminetetraacetic acid (EDTA) and different proteins.

The radiolabelling reactions are controlled by several parameters such as temperature, pH value, SPIONs concentrations, reaction time, and type of solvent or reducing agents in addition to the possible presence of ligands on the surface of nanoparticles.

### 2.6.1 <sup>99m</sup>Tc radiolabelling procedure for coated SPIONs

Technetium-99m is a radionuclide with suitable half-life which gives sufficient time for metal ion coordination, purification and SPECT imaging application after elution from the generator. <sup>99m</sup>Tc is eluted from the <sup>99</sup>Mo/<sup>99m</sup>Tc generator as pertechnetate ion (TcO<sub>4</sub><sup>-</sup>) with highest oxidation state (VII). The earliest technetium compound was used for imaging organs such as the liver, brain and thyroids based on <sup>99m</sup>Tc-sodium pertechnetate with oxidation state +7 (d<sup>0</sup> configuration).<sup>152</sup>

Therefore, different compounds were developed for other organs, which required changing the technetium oxidation state by utilising reducing agents. Number of reducing agents, such as ascorbic acid, ferrous ion, sodium borohydride and sodium dithionate, were investigated to reduce the oxidation state of technetium-99m. These often led to incomplete reduction which effect the radiolabelling yield. Recently, stannous chloride in an acidic media has been considered the most effective method for reduction technetium(VII) to (V) which is preferred for radiolabelling nanoparticles.<sup>10, 120, 153, 154</sup>

Pertechnetate ion is an inactive oxidation state that does not bind directly to any ligand. Thus, for synthesis of  $^{99m}\text{Tc}$ -pharmaceuticals, reduction to lower oxidation state is required for production of  $^{99m}\text{Tc}$ -labelled compounds in the presence of suitable ligand which stabilise the new oxidation state to form metal complexes. Technetium in these complexes can have several coordination numbers and configurations. The technetium is considered the central atom and acts as a Lewis acid, whereas atoms or functional groups in ligands act as Lewis base. One example of a ligand that is suitable for technetium-99m is diethylene triaminepentaacetic acid (DTPA), known as chelating agent, which stabilises technetium in an oxidation state (V). Recent studies confirmed that SPIONs with no presence of ligands on the surface can give a high radiochemical and stability efficiency when radiolabelled with technetium-99m. This means that the technetium ion is stabilised by the atoms or the functional groups on the surface of SPIONs or the coating layer.<sup>19, 50</sup>

The reduction step for technetium(VII) to active oxidation state(V) is an essential for radiolabelling SPIONs. Stannous chloride ( $\text{SnCl}_2$ ) in acidic media is commonly used as a reductant of technetium(VII), this leading to form complexes that technetium ion forms  $\text{TcO}^{3+}$  and  $\text{TcO}_2^+$  cores. The  $\text{TcO}^{3+}$  can exist in two configurations, octahedral (six-coordinated) or square pyramidal (five-coordinated), whereas  $\text{TcO}_2^+$  core has an octahedral configuration, see Figure 43. Therefore, the majority of  $^{99m}\text{Tc}$ -pharmaceuticals contains technetium in an oxidation state (V).<sup>120</sup>

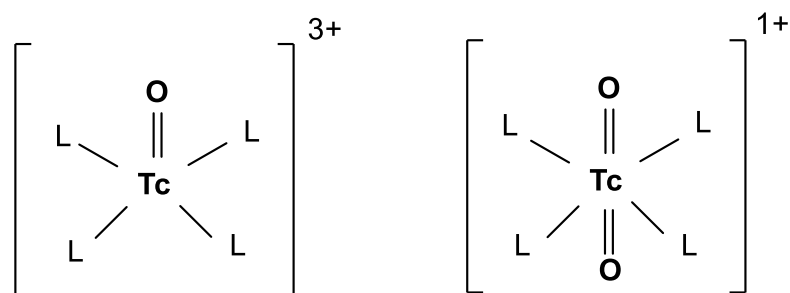


Figure 43: Technetium(V) coordination chemistry, (left) the square pyramidal configuration for  $\text{TcO}^{3+}$ , (right) the octahedral configuration for  $\text{TcO}_2^+$ .

To confirm the presence of a new oxidation state (V), a thin layer chromatography (TLC) silica gel plate was used after spotting *ca.* 3 microliters of reaction mixture and eluted by saline and the reduction process was analysed by radio-TLC. This method shows that the technetium(VII) is moving with the solvent front whereas technetium(V) stays on the baseline of the TLC. It is obvious that the reduction step is very fast as only five minutes were required for complete reduction, this is in agreement with other literature. The radiolabelling of SPIONs with technetium-<sup>99m</sup>Tc(V) was started with the inactive form of technetium(VII) in order to investigate the impact of an oxidation state on the radiolabelling efficiency and the radiochemical yield of SPIONs. Another oxidation state of technetium was tested technetium(I), which had been reduced by sodium boranocarbonate. For radiolabelling SPIONs, the technetium was added to SPIONs suspension siloxane@SPIONs and PAA@SPIONs in saline 0.9% at room temperature for 30 minutes.

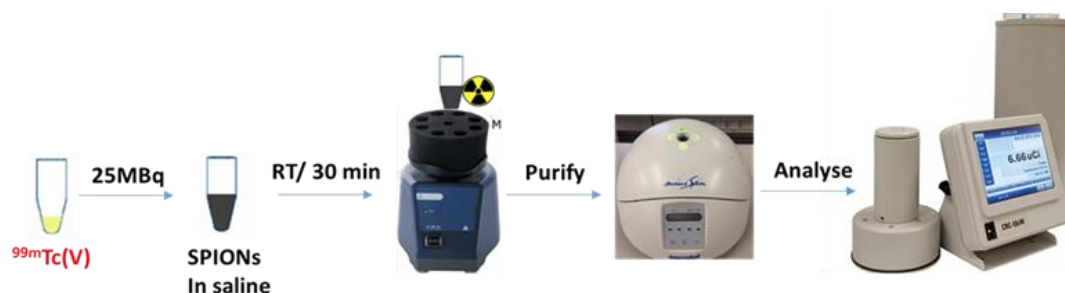


Figure 44: Schematic representation of <sup>99m</sup>Tc radiolabelling SPIONs procedure.

Later, the radiolabelled SPIONs were isolated using spin filter (MWCO 100 KDa) and washed twice with saline. The RCY% was measured based on the radioactivity trapped in spin filter and the washing solution. Figure 44 shows the radiolabelling procedure for SPIONs with different oxidation states.

Table 9: Radiolabelling of SPIONs in <sup>99m</sup>Tc (VII) and (I).

Sample	RCY% in Oxidation state (VII)	RCY% in Oxidation state (I)
siloxane@SPIONs	33.0	22.0
PAA@SPIONs	28.0	8.0

As expected, attempts to radiolabel SPIONs with oxidation states of technetium other than the oxidation state (V) showed poor radiolabelling efficiency. As can be seen in Table 9, both oxidation states are unsuitable for radiolabelling iron oxide nanoparticles.

### 2.6.1.1 $^{99m}\text{Tc}$ radiolabelling SPIONs at different concentrations

As discussed previously, the concentration of sample is considered one of the most important parameters that affect the radiolabelling efficiency. Therefore, the impact of SPIONs concentration on RCY was investigated at room temperature in saline solution.

The labelling procedures for siloxane@SPIONs and PAA@SPIONs with technetium(V) were carried out by a stannous chloride reduction method to reduce technetium(VII) to technetium(V), which is considered the oxidation state suitable to radiolabel various nanoparticles. The procedure started with suspending these particles in saline 0.9% and reduced technetium-99m solution at room temperature. Typically, 25  $\mu\text{l}$ , 30 MBq of technetium(V) was added to 100  $\mu\text{l}$  of SPIONs in saline with different concentrations (0.5, 1 and 1.5 mg/ml) and incubated under constant shaking for 30 minutes at RT to give the labelled product. The reaction mixture was purified by centrifugation and washed with saline solution twice. The samples were analysed using the dose calibrator to determine the radiochemical yield.

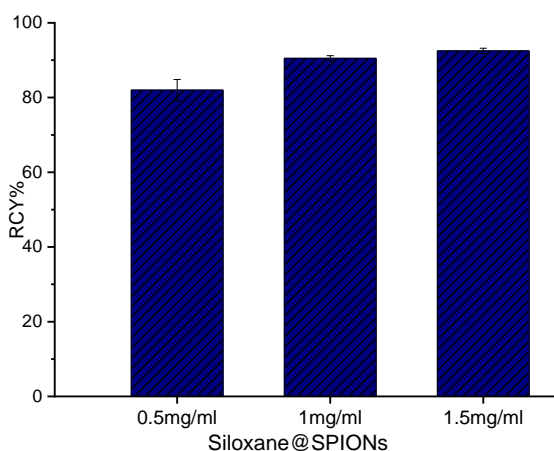


Figure 45: RCY for  $^{99m}\text{Tc}$ -siloxane@SPIONs in saline at different concentrations incubated for 30 minutes at RT ( $n=2$ ).

As expected, there was a significant increase in radiolabelling efficiency with an increase in SPIONs concentrations, see Figure 45 and Figure 46, for both samples **2** and **3** it was found that the concentration of SPIONs impacted on RCY. This is probably because there was more opportunity for the technetium to have a coordination interaction with donor atoms such as the oxygen atoms present on coating layers. In the absence of chelators, this coordination attachment was considered weaker compared to ligand attachment. In the case of siloxane@SPIONs, it is clear that RCY reached more than 80% at low concentration of SPIONs compared to PAA@SPIONs. The main reason for this is the silica layer on the surface of nanoparticles, the mesoporous shell of silica may offer cavities for technetium coordination on the surface of nanoparticles.

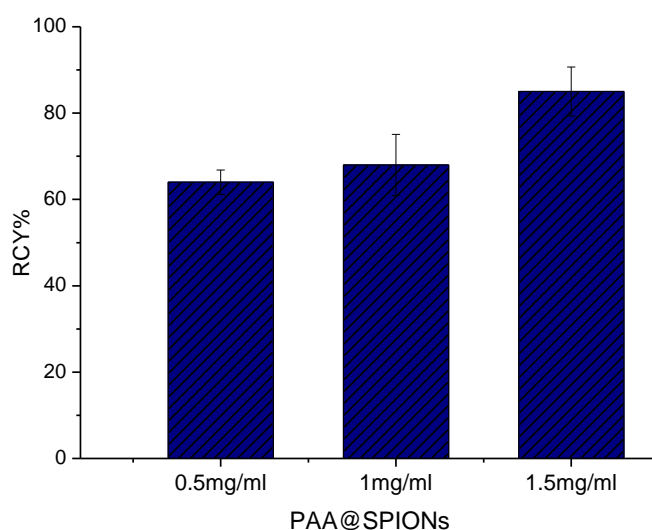


Figure 46: RCY% for  $^{99m}\text{Tc}$ -PAA@SPIONs in saline at different concentrations incubated for 30 minutes at RT ( $n=2$ ).

### 2.6.1.2 $^{99m}\text{Tc}$ radiolabelling in different buffers

The second parameter that has an impact on radiolabelling efficiency is the pH of the solution. Therefore, this factor was investigated on technetium radiolabelling siloxane@SPIONs **2** and PAA@SPIONs **3** suspended in two buffers phosphate buffer saline (PBS) and sodium acetate (NaOAc), at pH 7. The mixtures were incubated with technetium(V) for 30 minutes at room temperature and the radiochemical efficiencies were measured by dose calibrators.

Figure 47 shows the effect of the pH on RCY. There is a clear evidence that using buffers such as PBS and NaOAc reduced the RCY compared to using saline at room temperature. For example, there is a significant decrease in RCY for siloxane@SPIONs, where about 20-30% of technetium(V) has been released compared to suspending these SPIONs in saline. The RCY for PAA@SPIONs decreased slightly when the SPIONs were dispersed in PBS, while around 15% of technetium(V) was released in the presence of NaOAc. Both buffers are chelating ligands for metal centres. Hence, the buffer can compete for binding to the technetium(V) ion to form stable complexes with acetate or phosphate.

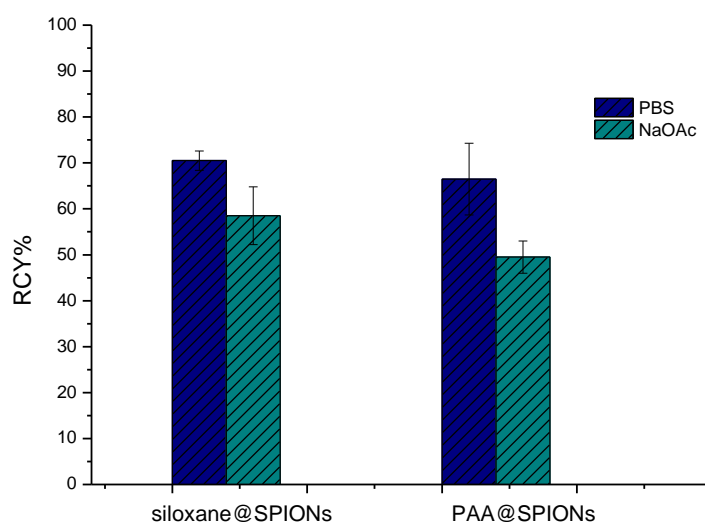


Figure 47: RCY% for both  $^{99m}\text{Tc}$ -SPIONs in PBS and NaOAc buffers both at pH 7 incubated for 30 minutes at RT ( $n=2$ ).

### 2.6.1.3 $^{99m}\text{Tc}$ radiolabelling SPIONs in NaOAc at different pH

To complete the investigation of pH impact on radiochemical efficiency, another test was carried out under a range of pH. The siloxane@SPIONs and PAA@SPIONs were incubated in NaOAc at different pH 4, 5 and 7 then radiolabelled with technetium(V) at room temperature for 30 minutes. Figure 48 illustrates the relation between pH and RCY and shows there is an obvious reverse relation between this parameter and radiolabelling yield. For both SPIONs the radiolabelling yield has increased with increasing the acidity of suspension. This is probably due to an increase of protons in solution which reduces the chelating effect between technetium(V) and acetate ions. Therefore, the binding between oxygen atoms on polymer or mesoporous shell of silica has increased again to form complexes with technetium(V) on the surface of SPIONs.

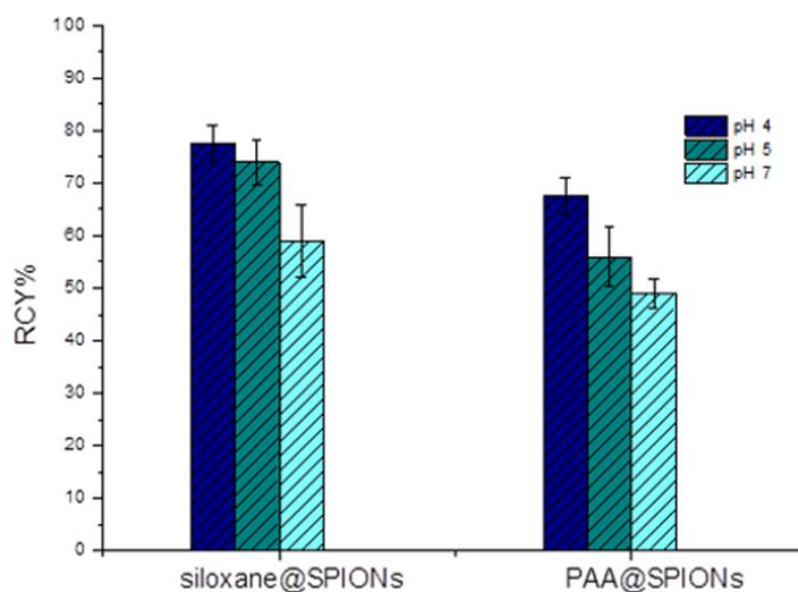


Figure 48: RCY% for both  $^{99m}\text{Tc}$ -SPIONs at different pH 4, 5 and 7 incubated for 30 min at RT (n=2).

#### 2.6.1.4 $^{99m}\text{Tc}$ radiolabelling SPIONs at different temperatures

The third factor that has a huge impact on radiolabelling efficiency is temperature. Many researchers have studied this factor on radiolabelling SPIONs. A study by Sandiford and Torres showed that temperature has a large effect on the obtained radiochemical yield. The SPIONs were functionalised with DPA-ale (a bifunctional bisphosphate) and radiolabelled with technetium(V). It was found that the RCY varied from 2% to 47% by using a temperature gradient from 25-90°C over 10 minutes.<sup>122</sup>

In this work, a similar result has been noticed by incubation the siloxane@SPIONs **2** and PAA@SPIONs **3** in saline and technetium(V) with continuous shaking for 30 minutes at two temperatures (37° and 90°C). Figure 49 shows the siloxane@SPIONs has a RCY > 90% at two temperatures which is almost similar to radiolabelling these SPIONs in saline at RT. This means that this compound is already saturated with technetium(V) due to the silica shell around the magnetic core. However, the PAA@SPIONs increased significantly when the temperature increased. In this case, the RCY jumped from 66% at RT to over 95% at high temperatures. This is perhaps due to the diffusion of technetium(V) through the chain of polymers when temperature rises and induce radioisotopes to chelate with oxygen at carboxylic acid group.

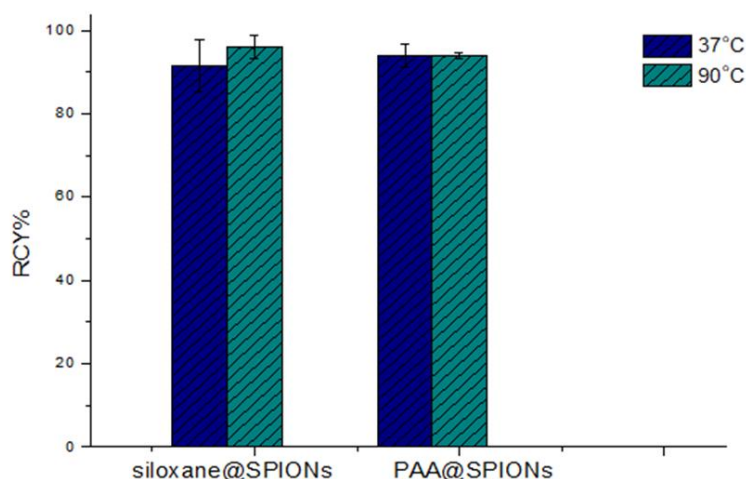


Figure 49: RCY% for both  $^{99m}\text{Tc}$ -SPIONs in saline incubated for 30 minutes at 37°C and 90°C (n=2).

### 2.6.1.5 $^{99m}\text{Tc}$ radiolabelling SPIONs in PBS at different temperatures

To complete the effect of temperature and buffers on radiolabelling efficiency, further investigations were carried out. In these, the synthesised SPIONs **2** and **3** were suspended in PBS at pH 7. The NPs were incubated with technetium(V) for 30 minutes at two temperatures (37° and 90°C) after which the SPIONs were isolated by spin filter, washed twice with buffers and the RCY was measured by dose calibrators.

Figure 50 shows that increasing temperatures raised the radiochemical yield for both samples. The siloxane@SPIONs increased by 20% in RCY with high statistical significance for both temperatures. On the other hand, PAA@SPIONs in PBS seems affected only at 90°C, when the RCY had risen from 60% to 80%. A reason for these results is that rising temperature has increased technetium diffusion through the coating layer which decreased the chelating effect of phosphate ions.

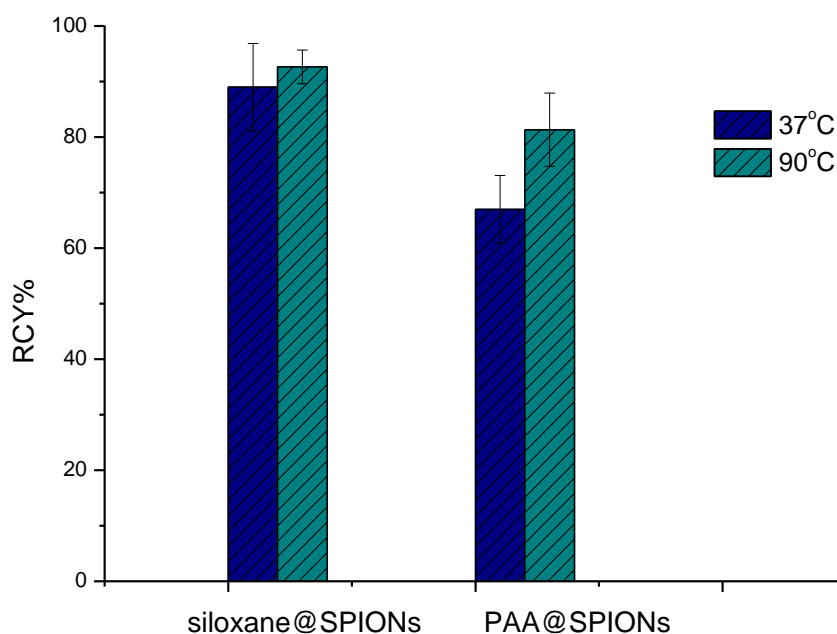


Figure 50: RCY% for both  $^{99m}\text{Tc}$ -SPIONs in PBS pH 7 incubated for 30 minutes at 37°C and 90°C (n=2).

### 2.6.1.6 $^{99m}\text{Tc}$ radiolabelling SPIONs in NaOAc at different temperatures

At the same time, the synthesised SPIONs have the same trend when suspended in NaOAc, pH 4 and heated to high temperatures. Both samples were radiolabelled with technetium(V) to gain a RCY >90%, see Figure 51.

The siloxane@SPIONs increased 10-15% in RCY, which means the weak chelator between acetate ion and technetium(V) decreased during the temperature increase and let the radionuclide diffuse through the PEG chain to coordinate with oxygen atoms or to chelate in the silica shell and be adsorbed on the magnetite surface. A similar trend was noticed for radiolabelling PAA@SPIONs in NaOAc at high temperatures. The radiochemical efficiency changed from 63% to over 94% with a high statically significance ( $p=0.001$ ).

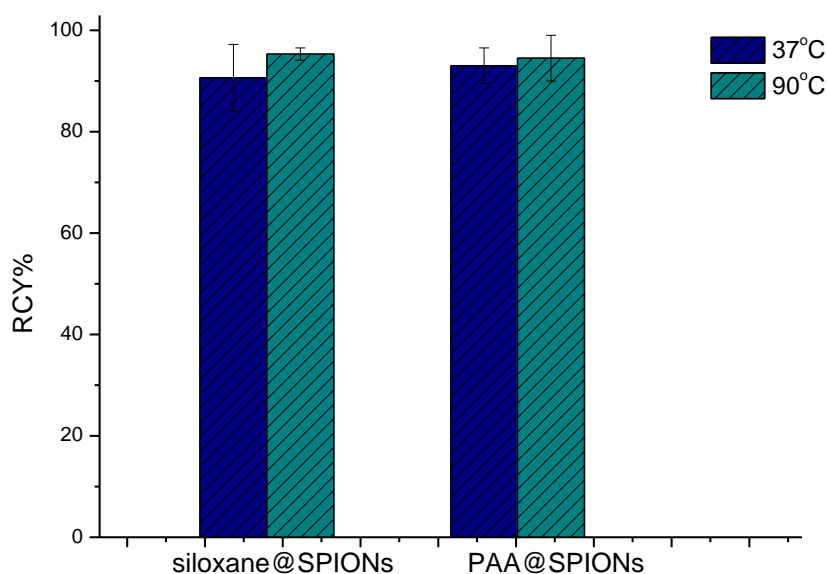


Figure 51: RCY% for both  $^{99m}\text{Tc}$ -SPIONs in NaOAc pH 4 incubated for 30 minutes at 37°C and 90°C ( $n=2$ ).

## 2.6.2 Stability study of $^{99m}\text{Tc}$ radiolabelling SPIONs

After conditions were determined to successfully radiolabel SPIONs with SPECT isotope technetium(V) to above 90% yield, competition tests were carried out to determine the attachment between technetium and chelators-free functionalised SPIONs. Competition tests can be defined as the stability of radiolabelling process and it describes the strength of attachment between radioisotope and functionalised nanoparticles.

### 2.6.2.1 Stability in EDTA

To investigate the weak or strong bound between SPIONs and technetium(V), a competition test was carried out with ethylenediminetetraacetic acid (EDTA) which is known to form complexes with small charged ions and commonly used for chelating iron(III). The procedure for the stability test in EDTA started with incubation synthesised siloxane@SPIONs and PAA@SPIONs with technetium(V) at 90°C for 30 minutes. Then the mixtures were cooled to room temperature and 100  $\mu\text{l}$  of 0.1 M of EDTA solution was added to the radiolabelled SPIONs and completely shaken for 30 and 60 minutes respectively.

Later, the mixtures were analysed by spin filtration to determine the percentage of EDTA/ $^{99m}\text{Tc}$  and  $^{99m}\text{Tc}$ -SPIONs radiolabelling yield. Upon increasing competition reaction time from 30 to 60 minutes, there was clear evidence of high stability for both samples, see Figure 52. A small percentage of technetium(V) was lost from the SPIONs surface and complex with EDTA. This high stability result indicates that the radioisotope is attached strongly on the nanoparticles surface or among the polymer structure chains of siloxane-PEG or polyacrylic acid.

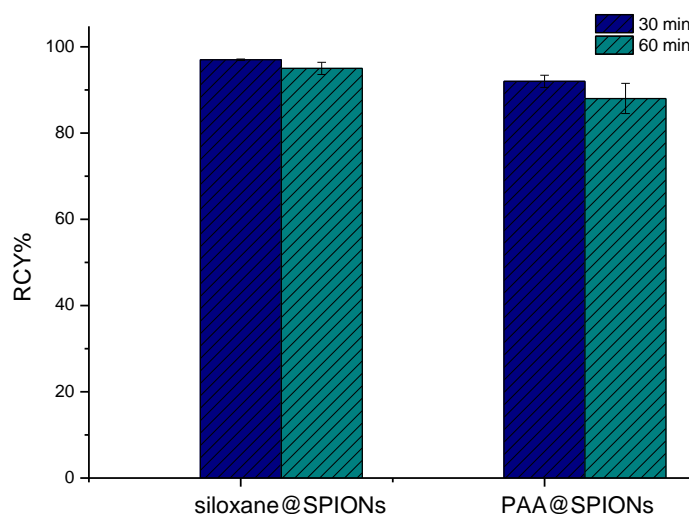


Figure 52: Stability reactions for both  $^{99m}\text{Tc}$ -SPIONs in (100  $\mu\text{l}$ , 0.1 M) EDTA incubated for 30 and 60 minutes at RT ( $n=2$ ).

### 2.6.2.2 Stability over a range of pH

The attachment of radioisotopes with nanoparticles surface has two types of interactions. The first is in the presence of ligands or chelators, which were considered strong and desired attachment, while the second was described as a weak attachment between the nuclide and the nanoparticles surface due to the absence of ligands that can stabilise the coordination of radioisotope in the produced complexes. However, recent studies have shown that chelator-free SPIONs can provide a high attachment with different radioisotopes such as  $^{68}\text{Ga}$  and  $^{99m}\text{Tc}$  according to their coating on the magnetite core.<sup>19, 50</sup>

Therefore, the stability of synthesised siloxane@SPIONs and PAA@SPIONs were investigated in a wide range of pH after radiolabelling with technetium(V) in order to study the attachment of a SPECT radioisotope with iron oxide nanoparticles surface. The synthesised SPIONs were first successfully radiolabelled with technetium(V) at 90°C for 30 minutes to gain over 90% radiochemical yield. After cooling, 50  $\mu\text{l}$  of ammonium acetate at pH 3, 5 and 11 were added with continuous shaking at room temperature for 30 minutes. The RCY were measured after using spin filtration and washed twice with a buffer.

According to results shown in Figure 53, both samples seem to lose some of their activity of technetium-99m when incubated over a wide range of pH. For example, siloxane@SPIONs tend to be more stable in basic conditions rather than in an acidic medium. A similar trend can be seen for PAA@SPIONs, with no significant difference in the three pH conditions ( $p=0.13$ ).

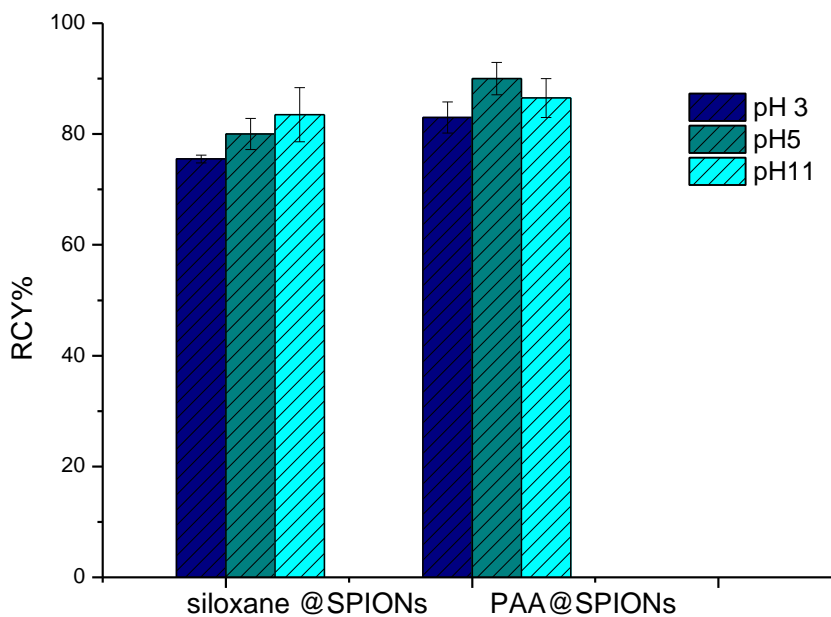


Figure 53: Radiochemical stability for  $^{99m}\text{Tc}$ -SPIONs in ammonium acetate at range of pH (3, 5 and 11) incubated for 30 minutes at RT ( $n=2$ ).

### 2.6.2.3 Stability in serum

Stability of radioisotopes is a critical criterion for any biological investigation. The tracer (the radiolabelled molecules) should be metabolically stable for *in vivo* studies in order to avoid any nonspecific uptake that can affect the final SPECT image. Therefore, the stability studies of  $^{99m}\text{Tc}$ -SPIONs were investigated in different proteins such as *apo*-transferrin and bovine serum albumin to mimic the physiological conditions and detect the attachment between technetium(V) and SPIONs. The electrophoresis method was used to separate and analyse the proteins based on their molecular size and charge by applying an electric field to move the charged molecules through agarose gel.

The analytic technique started by incubating radiolabelled  $^{99m}\text{Tc}$ –SPIONs **2** and **3** in bovine serum albumin and *apo*-transferrin (20  $\mu\text{l}$ , 2 MBq) which was loaded into prepared agarose gel and then placed in an electric field (60 V, 1.5 hours) as shown in figure 54. The agarose gel had been stained using InstantBlue stain for 15 minutes for the visualisation of protein bands. Then the gel was sliced and measured in the gamma counter. This procedure is considered as a competition study to assess the stability of the radiolabelled nanoparticles up to 48 hours.

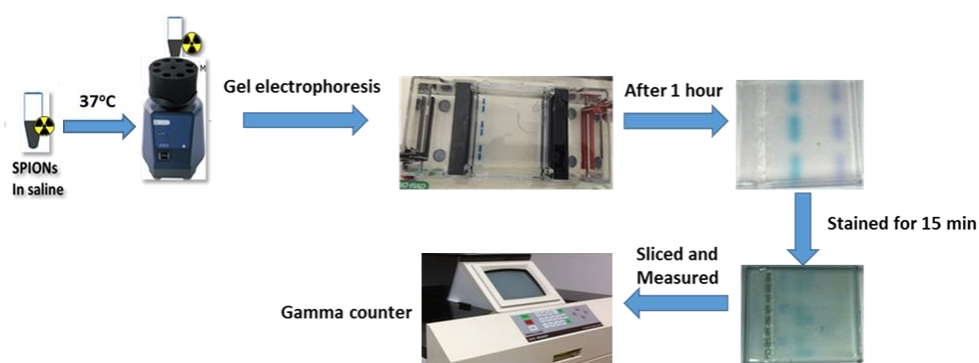


Figure 54: schematic representation for stability procedure of  $^{99m}\text{Tc}$ -SPIONs in serum using the gel electrophoresis technique and measured the gel with gamma counter.

Examining SPIONs under physiological conditions indicates if the samples are stable enough to be progressed for *in vivo* applications. The actions of technetium(V) radiolabelled SPIONs **2** and **3** in these conditions were listed in Table 10 and Table 11.

After 24 hours of incubation, siloxane@SPIONs showed high stability in both proteins, achieving 94% and 95% in bovine serum albumin and apo-transferrin respectively. After 48 hours these radiolabelled particles also seemed stable in transferrin.

This is in agreement with a study done by our group when SPIONs were radiolabelled with PET isotope gallium-68.<sup>19</sup> On the other hand, the stability in bovine serum decreased to 70% which means that the technetium(V) has may be complexed with disulfide or amino acids present in proteins. The stability of radiolabelled PAA@SPIONs showed a dramatic decrease in both proteins, probably due to the carboxylic groups on the surface of iron oxide nanoparticles which are considered less stable than bisphosphonate-iron oxide bond or other anchors.<sup>155</sup> The instability of SPIONs in serum was also observed in Tsipaet study for aminosilane-coated iron oxide nanoparticles with further functionalisation for the surface with RGD for targeting issues. Both (non-targeted and the targeted) NPs were showed a decreased in serum stability from 20-35% only were remaining intact to SPIONs. The group attributed this observation to ligand exchange mechanisms on the iron oxide surface and/or decomposition of iron oxide possibly aided by iron-binding proteins such as transferrin or ferritin.<sup>156</sup>

Table 10: Stability of <sup>99m</sup>Tc-siloxane@SPIONs in different proteins.

	In Bovine Serum Albumin		In Transferrin	
	SPIONs%	Protein band %	SPIONs%	Protein Band%
After 2h	95	4.6	96	3.9
After 24h	94	6	95	4.4
After 48h	70	30	95	4.6

Table 11: Stability of <sup>99m</sup>Tc-PAA@SPIONs in different proteins.

	In Bovine Serum Albumin		In Transferrin	
	SPIONs%	Protein band %	SPIONs%	Protein Band%
After 3h	92	7.3	70.5	29.4
After 18h	89	10.8	60	39.4
After 24h	45.6	54.4	7.46	92.5

### 2.6.3 Stability of hydrodynamic size

Size and size distribution is important for *in vivo* application to act as SPECT/MRI imaging agents. If the size of SPIONs increases after radiolabelling with technetium(V) they can be easily detected by the immune system and excreted by the liver and spleen, resulting in short blood circulation time and resulting an inadequate uptake. After the technetium(V) radiolabelled samples had decayed, the DLS measurements were repeated to study the effect of radiolabelling on the hydrodynamic size. From Figure 55 it is observed that there is a slight increasing of the hydrodynamic size after the samples were exposed to technetium(V). For example, the size of PAA@SPIONs changed from 58 nm to 68 nm while a minor increase was noticed for the siloxane@SPIONs, in which the size has changed from 100 nm to 103 nm. The changes on hydrodynamic size of SPIONs may occur due to radiolabelling at high temperatures, or using different salts in buffers.

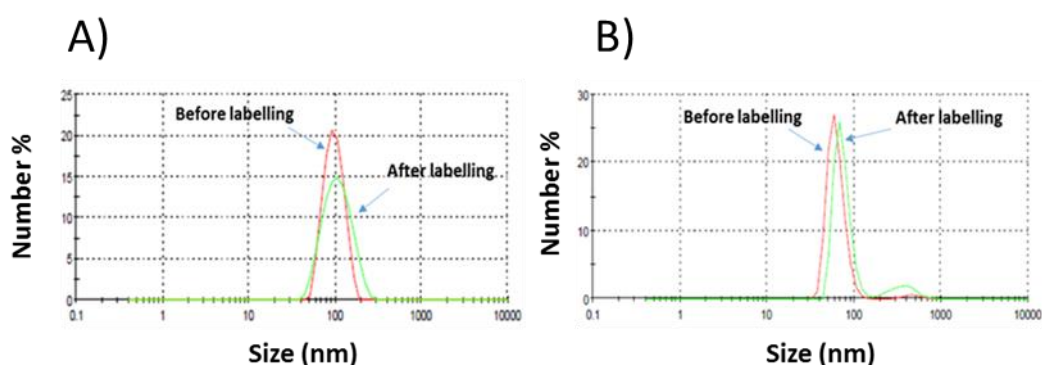


Figure 55: The DLS analysis for A) siloxane@SPIONs **2** and B) PAA@SPIONs **3**, the red line before radiolabelling, the green line after radiolabelling with  $^{99m}\text{Tc}$ .

## 2.7 Conclusion

In this part of the work, SPECT/MR contrast agents based on iron oxide nanoparticles were prepared employing various chelator-free coatings and two different methods. *Ex-situ* method (co-precipitation) was used to encapsulate SPIONs with a siloxane-PEG coating to form a stable suspension with a diameter of 100 nm measured by dynamic light scattering. Centrifugation was used to purify the SPIONs after coating with siloxane-PEG by varying the time and washing steps with solvents. An *in-situ* (polyol) method was used to encapsulate the SPIONs with polyacrylic acids coating during synthesis to form a monodisperse nanoparticles with diameter of 58 nm. The synthesised SPIONs showed a high stable colloidal suspensions in ultrapure water and PBS at neutral pH. The siloxane@SPIONs were stable for more than 2 months while the PAA@SPIONs were stable for more than 2 years due to preparation method.

The characterization of synthesised SPIONs proved the presence of magnetite phase for both samples by using X-ray diffraction analysis. The core sizes and size distribution were measured to gain around 9 and 4 nm for siloxane@SPIONs and PAA@SPIONs respectively, which is in agreement with TEM results. It is clear that the polyol method provide more compact coating and controlled the growth of SPIONs core. The presence of organic layers on the SPIONs surface was confirmed by FT-IR, EDX, ICP-OES, zeta potential and elemental analysis.

The relaxivity study ( $r_1$  and  $r_2$ ) for synthesised SPIONs was conducted using 1.4 T MR Machine to determine their potential as MRI contrast agents. In this study, both samples gave a high transverse relaxation rates which corresponded to the small crystallite sizes of SPIONs. In the case of siloxane coating, the  $r_2$  value was  $41.4 \text{ mM}^{-1} \text{ s}^{-1}$  which was doubled the PAA@SPIONs due to the nature of coating.

Several reactions were carried out for radiolabelling synthesised SPION samples with technetium(V) as a potential SPECT agent. The samples showed high loading capacity when increasing the concentrations of nanoparticles. A number of parameters were manipulated to determine the optimum radiolabelling conditions, include rising temperatures, changing buffers and varying the pH. In general, it was found that temperature has a huge impact on the radiolabelling yields in saline and other buffers (PBS and sodium acetate); the radiochemical yield increased gradually with increasing temperatures. The pH also affected the RCY; it was found that decreasing the pH of sodium acetate increased the radiolabelling yield for both samples. All of  $^{99m}\text{Tc}$ -SPIONs samples demonstrated excellent stability in several competition reactions. For example, using EDTA and a wide range of pH in different serum proteins. The siloxane@SPIONs showed high stability in transferrin and bovine serum albumin for 48 hours, while the PAA@SPIONs lost a high amount of technetium-99m during the 24 hour measurement period.

The data reported in this chapter as preliminary results indicate that SPION samples with suitable coating and optimised radiolabelling conditions can serve as dual modality SPECT/MRI imaging agents. These results can be compared to recent studies that use SPIONs for dual or trimodal imaging agents. For example, Motiei and co-worker synthesised hybrid nano-structure for trimodal SPECT/CT/MRI imaging agent. The system consists of  $\text{Fe}_3\text{O}_4@\text{Au}$ , iron oxide is used for MRI signal while Au for CT, and the surface was functionalised with DOTA for to stabilise the technetium-99m for SPECT imaging. The hybrid nanoparticles with total diameter of 27 nm and 8 nm for SPIONs core were radiolabelled successfully with  $^{99m}\text{Tc}$ , showed high radiolabelling yield and stability of 98%, moreover, these nano-construct showed an effective MRI contrast.<sup>157</sup> Another study utilise the SPIONs as dual modality imaging agent was done by Portilho et al, the group prepared mesoporous silica NPs with magnetic core for dual modality imaging agents. Dacarbazine (cutaneous melanoma treatment) was entrapped in the silica shell. The mesoporous nanoparticles were radiolabelled with  $^{99m}\text{Tc}$  with high yield of 98% and high stability in the human albumin solution.<sup>158</sup>

# **Chapter 3**

## **Development of $^{68}\text{Ga}$ -labelled CXCR4 targeted SPIONs**

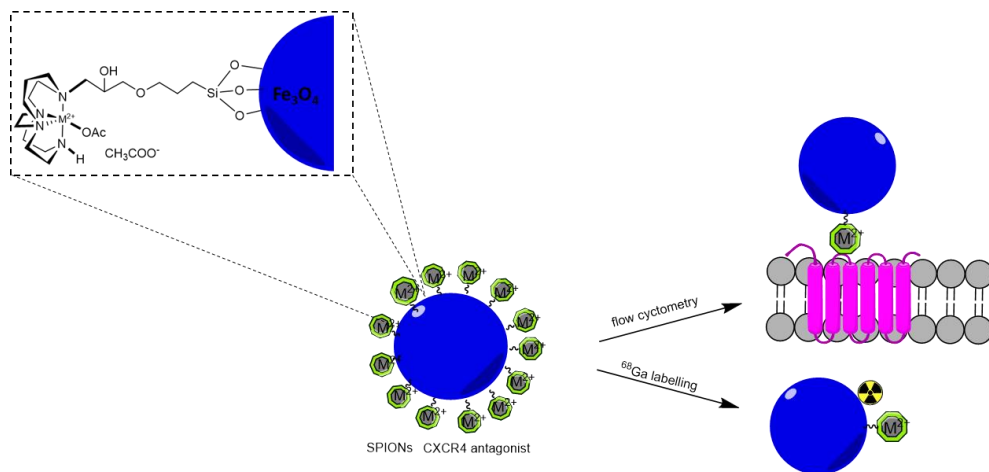
## 3 Chapter 3: Development of <sup>68</sup>Ga-labelled CXCR4-targeted SPIONs

### 3.1 Aims

The unique properties of nanomaterials are opening up a broad field of targeted cancer diagnosis and therapy, particularly when combined with the use of radioisotopes. Nanoparticles can be surface functionalised for a variety of targeted therapeutic, diagnostic and other multifunctional applications. The aim of this work reported chapter is to develop a radiolabelled targeted agent suitable for use in biological systems that is based on iron oxide nanoparticles that are surface functionalised with a CXCR4 antagonist. A key aspect is the plan to exploit the potential for multivalent interactions from an array of lower affinity CXCR4 antagonists on the surface of the nanoparticle that will give overall higher affinity.

The synthesis, radiolabelling and *in vitro* biological validation of the functionalised nanoparticles using the positron emitting radionuclide gallium-68 has been investigated in this work, see Scheme 6. The initial step in this process is the synthesis of an azamacrocyclic molecule based on cross-bridged cyclam (to act as the CXCR4 antagonist), this is modified with a siloxane derivative to allow attachment to the surface of the superparamagnetic iron oxide nanoparticles (SPIONs) to form SPIONs-SiO<sub>2</sub>-CB cyclam constructs. The CB cyclam can then be used to form a complex with transition metal ions (copper(II), nickel(II) and zinc(II)).

The efficiency of the radiolabelling reaction was tested under different conditions and the stability of gallium-68 labelled nanoparticles was also studied under a range of conditions. The interaction of the nanoparticles with the CXCR4 chemokine receptor was investigated *in vitro* (CXCR4 over expressing cancer cell line) using flow cytometry.



*Scheme 6: Schematic representation of SPIONs-SiO<sub>2</sub>-CB cyclam (CXCR4 antagonist) radiolabelling and biological interaction.*

### **3.1.1 Chemokine and chemokine receptors**

The chemokine network plays a number of important roles in the body and chemokines are found in a range of cells in the immune system, central nervous system and endothelial cells. They are responsible for cell migration processes, particularly for leukocytes transferring to the locations of inflammation.<sup>159</sup> Chemokines are small proteins with a mass of 8-14 kDa which, in some cases, can bind to more than one type of chemokine receptors whilst some types of chemokine receptors can bind to more than one type of chemokine. There are at least 50 chemokines and around 20 chemokine receptors that have been identified so far.<sup>160</sup>

### **3.1.2 CXCR4 chemokine receptor**

CXCL12 is a CXC chemokine that can bind to the CXCR4 and CXCR7 receptors. The receptors are presents on a number of tissues and are also expressed in various organs such as heart, brain, bone marrow and liver. The main role of CXCL12 is to control both the movement of hematopoietic stem cells and the structure of lymphoid tissue.<sup>159</sup>

The CXCR4 receptor has been widely studied due its role in the growth and spread of cancer and for entry of HIV into cells as part of the infective cycle.<sup>161, 162</sup> CXCR4 has been found to be overexpressed in many types of cancer including ovarian, leukaemia, breast cancer and prostate cancer. The CXCR4 overexpression is correlated with increased tumour aggressiveness and formation of metastases.<sup>163</sup>

### **3.1.3 CXCR4 antagonists**

For targeting the CXCR4 receptor, small molecule tetraazamacrocyclic compounds were identified. The macrocycles have shown effective binding to the CXCR4 receptor both *in vitro* and *in vivo*. One of these macrocyclic compounds is AMD3100, also known as Plerixafor, clinically tested for CXCR4 binding and haematopoietic stem cell mobilisation. Macrocycles based on cyclam and cyclen have been used in the design of these antagonists as they contain amino groups that are protonated at physiological pH and provide the positive charge to form electrostatic interactions with the carboxylate groups of aspartate residues on the surface of the CXCR4

protein. H-bonding interactions are also present and coordination interactions are possible if a metal centre is present in the macrocyclic cavity. Cyclam and cyclen have a suitable cavity size and donor atoms for metal ion complexation, and it is found that macrocycle metal complexes generally have a higher affinity for the CXCR4 receptor than the free macrocycles.<sup>164, 165</sup> During formation of the metal complexation, the flexible structure of cyclam gives different possible configurations, and the four nitrogen atoms become chiral. Ethylene bridges can be used to control the configurations that are observed, and this is an important way to enhance the affinity.

The interaction between the mono-macrocycles and the CXCR4 receptor is dependent on the aspartate residues. Gerlach *et al.* found that binding of the cyclam ring to CXCR4 receptor was through Asp<sup>171</sup>.<sup>166</sup> This result is in agreement with Bridger *et al.* work, they synthesised mono-macrocyclic AMD3465 and observed that only one aspartate residue is essential for binding,<sup>167</sup> see Figure 56.

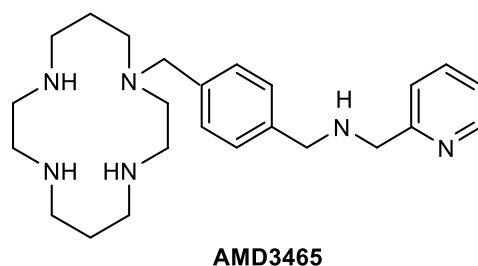


Figure 56: Structure of mono-macrocyclic compound AMD3465 prepared by Bridger *et al.*<sup>168</sup>

The bis-macrocycles have greater affinity for CXCR4 receptor compared to mono-macrocycles due to additional interactions with CXCR4 receptor (e.g. AMD3100,<sup>167</sup> see figure 57).

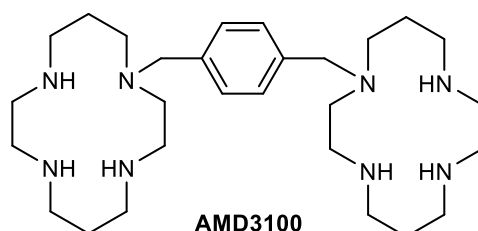


Figure 57: Structure of bis-macrocyclic AMD 3100.

Increasing the number of macrocyclic rings increases the interactions with aspartate residues and results in a higher affinity for CXCR4. Several studies support this theory and it was found that bis-macrocycles interacted with multiple aspartate residues, and that Asp<sup>171</sup> and Asp<sup>262</sup> are the most important for bis-macrocycle binding.<sup>169</sup>

Some studies showed the affinity of AMD3100 towards CXCR4 has increased after metal complexation with Cu<sup>2+</sup>, Zn<sup>2+</sup> and Ni<sup>2+</sup> as follow 7, 36, 50 fold respectively.<sup>170</sup> Side-bridged bis-macrocycles have been also investigated as CXCR4 antagonist. Archibald *et al.* studied the SB bis-cyclams after complexation with Zn<sup>2+</sup> and Ni<sup>2+</sup> ions and found them to have enhanced the binding affinity toward CXCR4, due to the configurational restriction.<sup>171, 172</sup>

### **3.2 Introduction to nanomaterials targeting cancer cells**

Various nanoparticles including inorganic or organic materials such as quantum dots, gold NPs, magnetic NPs, liposomes, dendrimers and carbon nanotubes have been investigated in both preclinical and clinical studies for the detection, diagnosis and treatments of many disease states. Cancer cells can be targeted by using nanoparticles where the surface has been modified with molecules/ proteins, for example, antibodies and peptides, which can bind to specific biomarkers of cancer. This type of targeted imaging could provide information about the cancer and, potentially, the development of the disease (prognosis), hence, helping to select the most appropriate treatment.<sup>173, 174</sup>

Nanomaterials have improved opportunities for detection of cancer after systemic administration, with selective tumour uptake observed by either active or passive targeting. Active targeting strategies enhance the selective uptake of nanoparticles into the tumour through binding to specific biomarkers. In this case, the surface of the nanoparticles is conjugated with molecules to target specific markers that are overexpressed on the cancer cells.<sup>175, 176</sup> The passive targeting strategy depends on accumulation of nanoparticles in tumour tissue based on the enhanced permeability and retention (EPR) effect, that was first described by Maeda and Matsumura. This effect is based on the size of the NPs and the features of tumour tissue, including the leaky vasculature and impaired lymphatic drainage.<sup>177</sup>

Superparamagnetic iron oxide nanoparticles (SPIONs) can be modified and their surfaces functionalised with ligands that bind to specific protein targets. They have been used in biomedical applications since the mid-1970s, for example in immunomagnetic cell separation and in MRI. The field has expanded and additional studies with targeting at a molecular level have been developed, for example, using SPIONs to target receptors that are overexpressed on cancer cells or other biological antigens.<sup>178, 179</sup> Several researchers have studied the applications of conjugated SPIONs in tumour imaging with a range of biological targets, such as the transferrin receptor<sup>180</sup>, the folic acid receptor<sup>181</sup> or  $\alpha_v\beta_3$ -integrin (to probe angiogenesis).<sup>182</sup>

Lee *et al.* coated SPIONs with polyaspartic acid and attached the cyclic RGD peptide to bind to integrin receptor  $\alpha_v\beta_3$  with inclusion of the DOTA chelator on the surface of nanoparticles to allow radiolabelling with <sup>64</sup>Cu to produce a dual PET/MRI contrast agent.<sup>183</sup> In a study carried out by Landmark *et al.* they conjugated folic acid with SPIONs and successfully demonstrated that the resulting construct binds to the folic receptor. The conjugated SPIONs showed enhanced tumour contrast in an imaging study compared to non-conjugated SPIONs.<sup>184</sup>

He *et al.* studied the effect of bioconjugated SPIONs on the growth of a pancreatic tumour using MRI. Anti-CXCR4 chemokine receptor monoclonal antibodies and bovine serum albumin were attached to surface of the SPIONs and the conjugated NPs were then incubated with four pancreatic cancer cell lines. The T<sub>2</sub> values were measured with an 1.5 T MRI scanner. The CXCR4-SPIONs have enhanced the T<sub>2</sub> values and effectively report on the cellular CXCR4 expression levels.<sup>185</sup> Long, Aboagye and co-workers have also studied targeting of CXCR4 after modifying the surface of the iron oxide NPs with the bioorthogonal azide and alkyne pair for the copper catalysed click reaction. The surface was functionalised using this method with a PEG chain and a targeting cyclopentapeptide that has high affinity for the CXCR4 chemokine receptor. The capability of the functionalised SPIONs to target the receptor was investigated by *in vitro* MRI using the U87 cell line, showing a T<sub>2</sub> signal enhancement.<sup>186</sup>

In a recent study, the coating of SPIONs with curcumin, which known as nontoxic, anti-inflammatory and anti-cancer agent, were investigated. Khan *et al.* developed

SPIONs with curcumin on the surface for delivery of gemcitabine (GEM) therapy in tumour by targeting CXCR4/CXCL12 signalling via the sonic hedgehog (SHH) pathway. The formulated constructs were examined in different cancer cell lines. Increased GEM uptake was observed by inhibiting the activation of receptor/ligand SHH signalling.<sup>187</sup>

Vila-Boas *et al.* published for a study using SPIONs for CXCR4-targeted magnetic hyperthermia treatment (MHT) in safe and efficient way. In this study, non-targeted SPIONs *ca.*20 nm were used at different concentrations with anti-CXCR4-targeted magnetic nanoparticles (MP-CXCR4) to boost the effectiveness of the treatment with MHT. The non-targeted and targeted SPIONs were incubated with three different cell lines, LN229 has moderate expression levels of CXCR4 receptor, Jurkat has a high number of receptors per cell and finally HK-2 cell has a low expression level of the CXCR4 receptor. Using the two types of MNPs in tandem increases the effectiveness of the magnetic hyperthermia treatment compared to only using the targeted-MNPs.<sup>188</sup>

Recently, hybrid nanoparticles have been of interest in the development of theranostic techniques. Guifeng *et al.* synthesised dumbbell shape Au-Fe<sub>2</sub>O<sub>3</sub> NPs using Au NPs with a diameter of 3.3 nm and Fe<sub>2</sub>O<sub>3</sub> NPs with a diameter of 8.7 nm. The surface of hybrid NPs were functionalised with a cyclic peptide for targeting the CXCR4 receptor on cancer cells. The anti-CXCR4-Au-Fe<sub>2</sub>O<sub>3</sub> NPs were used for tumour targeting and for MR imaging. The hybrid NPs were incubated with two cancer cell lines, MCF-7 and MDA-MB-231. The NPs showed high *T*<sub>2</sub>-weighted MRI contrast in tumour bearing mouse with high targeting specificity and non-toxic.<sup>189</sup>

Iron oxide nanoparticles are not the only nanoparticles used for targeting CXCR4, organic nanoparticles were used by Liu and colleague to target this receptor. They prepared dual-functional NPs as targeting and therapeutic agents. The nanoparticles were functionalised with AMD3100 with encapsulation of siRNA against vascular endothelial growth factor (VEGF) into fibrotic liver. The constructed system showed blocking of CXCR4 and inhibition of VEGF expression.<sup>190</sup>

In addition, liposomes have been used for targeting CXCR4 receptor. Ierano and co-workers functionalised PEGylated liposomes with peptide R (Arg-Ala-[Cys-Arg-Phe-PheCys]) which is known as a CXCR4 antagonist. The formulated liposomes were loaded with anti-cancer drug doxorubicin. The in vitro studies showed DOX efficiently delivered to CXCR4 expressing cell lines.<sup>191</sup>

### **3.2.1 Multivalency and potential applications for nanoparticles**

Multivalency approaches have been explored, where the surface of nanoparticles is functionalised using multiple targeting vectors in close proximity to increase the strength and efficiency of the targeting interactions (i.e. for a single nanoparticle multiple interaction are possible either with a single or multiple cell surface receptors), see Figure 58.<sup>192</sup> If an individual ligand-receptor interaction is weak then multiple ligand-receptor interaction (multivalency) will increase overall affinity.

This process widely exists in nature and plays a crucial role in many biological process. For example, cell recognition and the adhesion of virus to cells. Nanoparticles have the capability to form multiple interactions with target cells which improves the adhesion strength by multivalency, this is an important aspect in the development of nanoparticle based bioimaging probes.

Functionalisation of the surface of nanoparticles with mono-macrocycles that have lower affinity than bis-macrocycles could still enable them to form high affinity constructs as the multivalent interactions will increase the overall affinity of the nanoparticle to the cell with a high density of CXCR4 chemokine receptors on the cell surface.

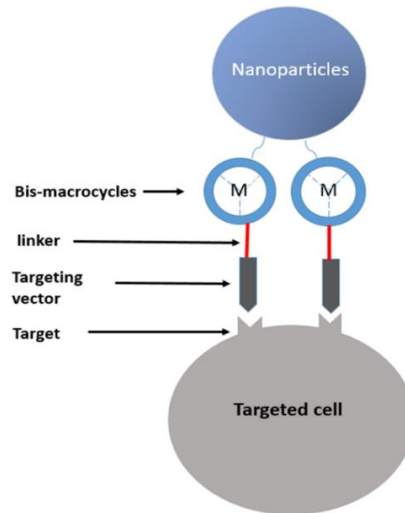


Figure 58: Schematic representation describes the multivalence approach.

Abstins *et al.* studied different factors determining multivalent nanoparticle-receptor interactions. The group investigated the effect of ligand density and PEG linker conjugated organic nanoparticles on the cellular uptake into U87 glioblastoma cell by flow cytometry. These cells known to overexpress the  $\alpha_v\beta_3$  receptor that can be targeted with cyclic RGD (*cRGD*). The results showed high binding efficiency toward the receptor that was attributed to the higher density of ligands on the nanoparticles surface, see Figure 59. Furthermore, it was found that the short length of PEG caused formation of clusters that increased the receptor binding. In general, these two factors can have a major influence on the multivalent nanoparticle-receptor interaction.<sup>193</sup>

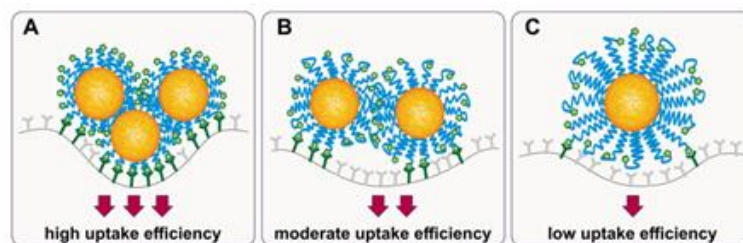


Figure 59: Schematic illustration of  $\alpha_v\beta_3$  receptor binding of A) NP-cRGD100-2k, B) NP-cRGD100-3.5k, C) NP-cRGD100-5k. Reproduced from Abstins *et al.*<sup>193</sup>

Dalal *et al.* showed that multivalency of nanoparticles controls the cellular mechanism including entry to or exit from the cells and subcellular targeting performance. The group functionalised QDs with a peptide characterised as “high and low multivalency” by the density of peptides on the NP surface. The results indicated that targeting efficiency prefers the low multivalency of NPs. However, they found that the reason for this was that the high multivalency NPs induce the exocytosis process despite increasing the cell uptake.<sup>194</sup>

In another study by the same group, QDs were functionalised with folate by varying the multivalency from 10-110 for targeting the folate receptor that is overexpressed in different cancer cells. The QDs were incubated in HeLa and KB cells to assess their uptake and localisation to receptor. The results showed that multivalency shifted the folate receptor mediated cellular internalisation mechanism.<sup>195</sup>

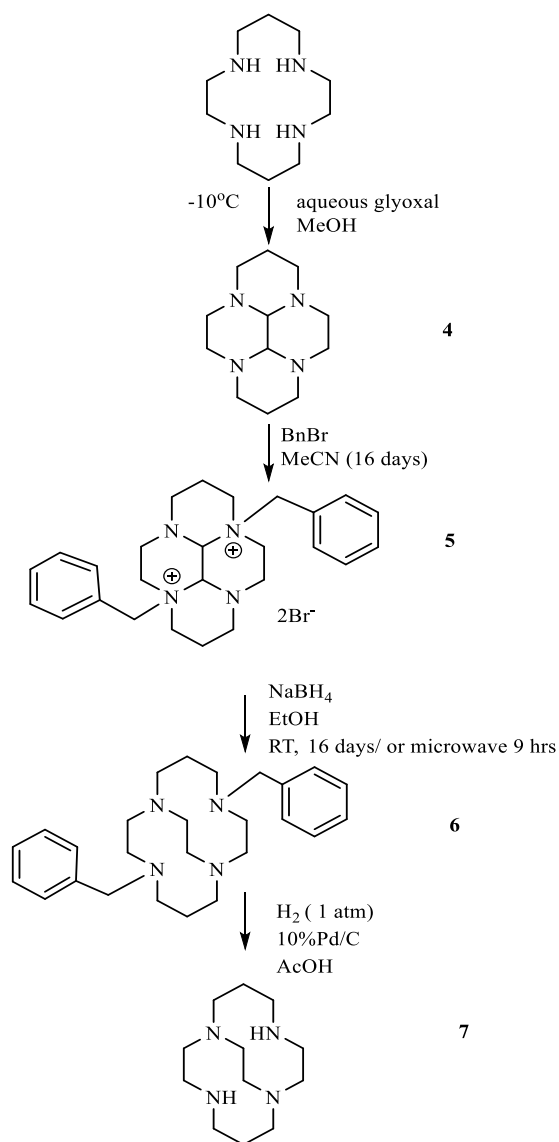
### 3.3 Design and functionalisation of CXCR4 targeted SPIONs

Cyclam derivatives, such as cross-bridged cyclam, provide an optimal metal ion geometry for protein binding by coordination bond formation (when copper(II), zinc(II) or nickel(II) are bound) with aspartate residues on the CXCR4 receptor.<sup>171, 172, 196, 197</sup> The aim of this work is to utilise the advantages of CB cyclam, combining multiple lower affinity mono-macrocyclic units on the surface of the nanoparticle to give a multivalency effect for targeting the CXCR4 receptor with high affinity NPs.

#### 3.3.1 Synthesis of CB cyclam (1, 4, 8, 11-tetraazabicyclo[6.6.2]-hexadecane)

In order to functionalise the surface of iron oxide nanoparticles with a CXCR4 antagonist, a series of reactions was carried out, following the literature procedures, to form CB cyclam, see Scheme 7.<sup>198, 199</sup> The ethylene bridge between non-adjacent nitrogen atoms gives the molecule a configurational restriction on complex formation with a transition metal ion with the generation of chiral nitrogen centres. The use of configurational restriction has been shown to increase the affinity for these molecules in binding to the CXCR4 receptors.

Following a literature protocol<sup>200</sup>, the synthesis of CB cyclam starts with the addition of glyoxal to cyclam, to form a bis-aminal bridged cyclam **4**, the reaction is carried out at low temperature (-10°C) to prevent the formation of oligomers.<sup>200</sup>



Scheme 7: Formation of CB cyclam from cyclam.

Alkyl halides can be reacted with the bridged cyclam to allow the formation of cross-bridge through a reduction step and, if benzyl groups are employed, they can later be removed to afford two secondary amines within the macrocycle.<sup>201</sup> This approach was developed by Weisman and co-workers to produce CB cyclam in good yields. There are two reasons for the use of benzyl groups for attachment to the bisaminal; (1) they are not affected by the reductive ring cleavage reaction, and (2) they are relatively easy to remove using hydrogenation in presence of a palladium catalyst. In the reaction carried out in this work, benzyl bromide was added to bridged cyclam which was dissolved in ethanol or methanol, this reaction needs 14-16 days to go to

completion and avoid the isolation of monoalkylated bridged cyclam, in this reaction compound **5** is formed.

Then, NaBH<sub>4</sub> is used to form the bis-benzylated cross-bridged cyclam **6**. This reaction also needs *ca.* 16 days at room temperature to give a high yield and avoid any formation of by-products. After the reduction step, the benzyl groups were removed by hydrogenation under an H<sub>2</sub> atmosphere in presence of 10% Pd/C catalyst to form the target cross-bridged cyclam **7**. In order to push the hydrogenation reaction to completion, high pressure and shaking for 24 hours in glacial acetic acid are required. The product was further purified by extraction into benzene or toluene according to a reported method.<sup>201</sup> All products were characterised by <sup>1</sup>H NMR and mass spectrometry, with all data in agreement with previously reported analysis from Wong and co-workers, see Figure 60.<sup>201</sup>

The configurational restriction of the cross-bridged cyclam forms a cavity that pre-organises the chelator to adopt a configuration which is suitable for many of the first row transition series metal ions.<sup>202</sup>

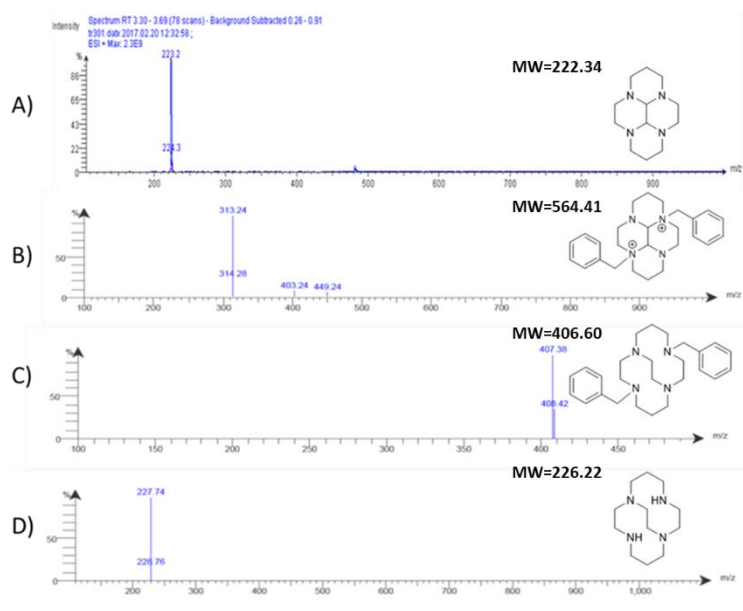


Figure 60: Electrospray mass spectra for synthesised macrocycles A) formation of bridged cyclam, B) formation of bis-benzy bridged cyclam, C) formation of bis-benzyl cross-bridged cyclam and D) formation of cross-bridged cyclam.

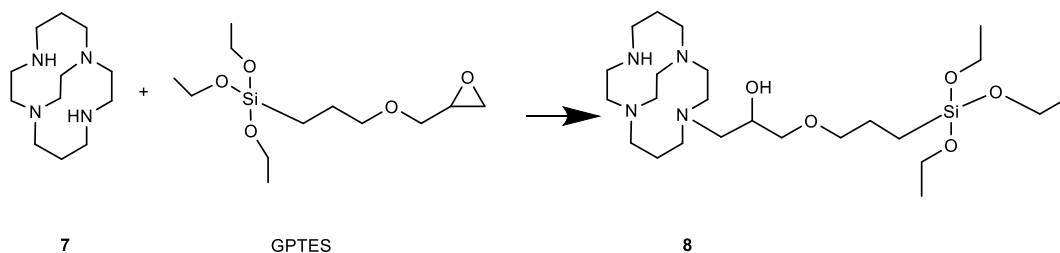
### 3.3.2 Attachment of a siloxane derivative the cross-bridged cyclam

SPIONS can be surface functionalised to attach targeting agents, drugs, metal complexes and biomolecules that will enhance their biodistribution or pharmacokinetic properties.<sup>123, 203</sup> Siloxane chemistry is a common method for coating and functionalising SPIONS. The formation of a silica shell on the surface of the iron oxide nanoparticles can be used to introduce functional groups for conjugation, as well as increasing the hydrophilicity to impart colloidal stability and avoid any aggregation to increases blood pool residence time.<sup>21, 123</sup>

Using appropriate alkoxysilane precursors can offer conjugation sites for drugs, targeting agents or imaging compounds.<sup>128, 204, 205</sup> Barreto and Spiccia *et al.* studied the use of siloxane chemistry to coat the surface of iron oxide NPs for <sup>64</sup>Cu radiolabelling in presence of different ring size macrocycles. The group used the siloxane derivative 3-glycidyloxypropyl)triethoxysilane (GPTES) to react with cyclam, cyclen and 1,4-bis(2-pyridylmethyl)-1,4,7-triazacyclononane (dmptacn) to coat the SPIONs and investigate the potential of these three macrocycles in <sup>64</sup>Cu complex formation and radiolabelling stability. The functionalised SPIONs have were labelled efficiently and the dmptacn complex showed stability in plasma.<sup>123</sup> The Archibald group have since used several methods for conjugation of GPTES to different macrocycles including heating of GPTES with CB and SB cyclam at reflux or by using microwave heating to form the CB cyclam derivative prior coating the surface of the SPIONs.<sup>21, 206</sup>

The CB cyclam **7** and GPTES were used in this work to modify the SPIONs to give a construct that can be radiolabeled with <sup>68</sup>Ga (chelator free) and also target the CXCR4 chemokine receptors on the surface of cancer cells. The microwave irradiation method was used to form siloxane cyclam compound similar to the method previously reported by our research group. CB cyclam was heated with GPTES in a 1:1 ratio in chloroform at 90°C for 30 minutes, this ratio allows formation of a single siloxane pendant arm attached to the macrocycle. The ring opening of epoxide offers

an efficient nucleophilic substitution at one of the secondary amines, see Scheme 8.<sup>21</sup>



Scheme 8: Macrocycle siloxane reaction to form siloxy-CB cyclam 8.

The siloxy-CB cyclam **8** was successfully synthesised and characterised by <sup>1</sup>H NMR spectroscopy and mass spectrometry. In Figure 61, the multiple signals in the <sup>1</sup>H NMR spectrum between 2.5-3.5 ppm are assigned to the protons (CH<sub>2</sub>) from the alkyl chain that links the cyclam to the siloxane group. The mass spectrum shows molecular ion peak at 506 confirming formation of the product.

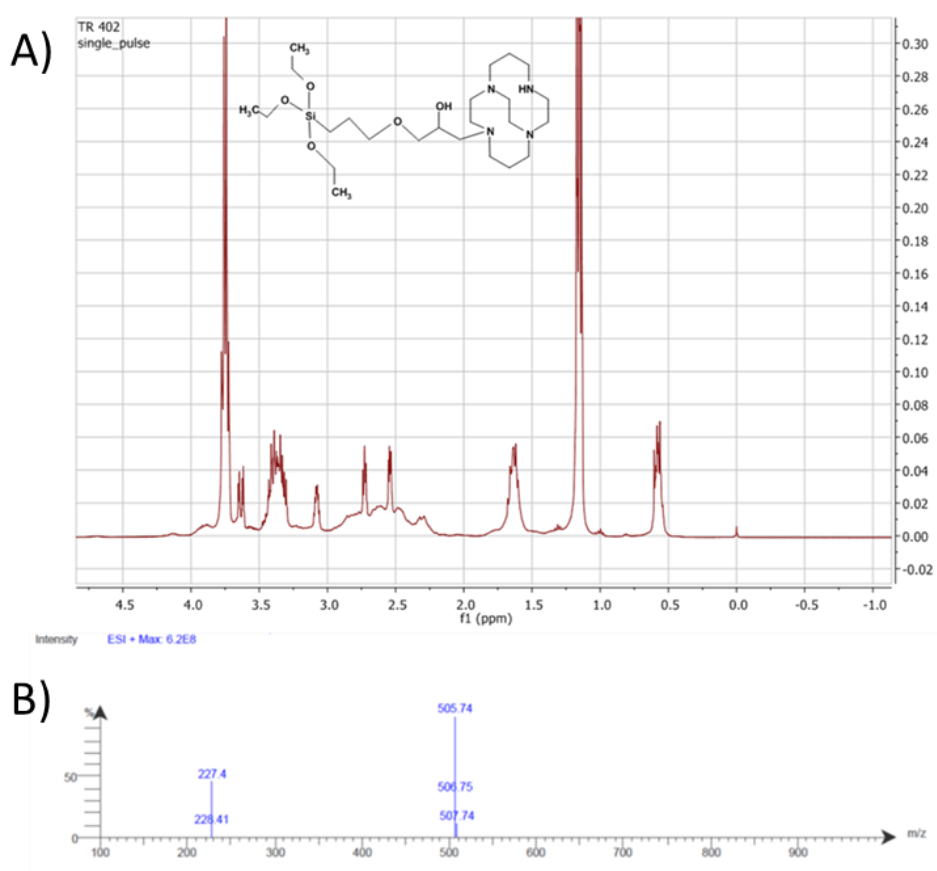
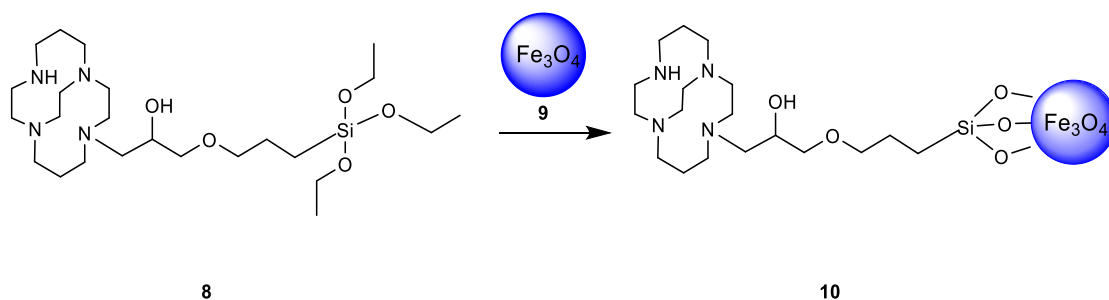


Figure 61: A) <sup>1</sup>H NMR and B) MS for Si-CB cyclam 8.

### 3.3.3 Functionalisation of SPIONs with Si-CB cyclam

Our group has successfully coated SPIONs (nanorods) previously using the siloxane macrocycle derivative via a range of different techniques. Siloxane derivatives can be attached to macrocycles with microwave heating or by refluxing macrocycles with siloxane in suitable solvent for days. In Neazar Baghdadi's PhD thesis, CB cyclam was functionalised with siloxane derivative by refluxing CB cyclam in a 1:1 molar ratio with GPTES in ethanol for 3 days.<sup>206</sup>

Surface modification of SPIONs with the siloxane derivative macrocycle was carried out using a similar protocol to the literature method used for other macrocycle derivatives with some modifications.<sup>123</sup> Briefly, uncoated SPIONs **9**, prepared by a modified co-precipitation method<sup>207</sup>, and siloxy-CB cyclam **8** were stirred in a basic 60% ethanol/water solution. The reaction proceeds in 48 hours at room temperature followed by separation steps using a strong rare earth magnet to remove any large particles followed by centrifugation with successive washings using a series of solvents, see Scheme 9.



*Scheme 9: Schematic representation the reaction of siloxy-CB cyclam with SPIONs.*

The resulting NPs were analysed by different techniques including PXRD, TEM, FTIR and elemental analysis. As previously discussed in chapter 2, see section 2.5.1, the diffraction peaks for the magnetite phase Fe<sub>3</sub>O<sub>4</sub> were observed in PXRD and indexed to the reflection planes of cubic inverse spinel, see Figure 62A. Analysis using TEM, images are shown in Figure 62B, indicated that the functionalised SPIONs were roughly spherically-shaped with uneven edges and an average diameter of 7.8 nm.

ICP-OES and elemental analysis were used to confirm the functionalisation of nanoparticles in the desired manner. The amount of carbon, nitrogen and silicon shows that the SPIONs-SiO<sub>2</sub>-CB cyclam had been isolated. The percentages of carbon, silicon and nitrogen present are 5.4%, 3.2% and 0.59% respectively.

Comparison can be made with the work of Barreto *et al.*<sup>123</sup> where they used a similar procedure to attach different tetraazamacrocyclic-siloxane derivatives to the surface of the SPIONs. In their study, the carbon percentage was in range of 4.4-5.5% which is similar to the result observed in this work. The size distribution of the functionalised SPIONs in suspension was measured by DLS and showed a mean hydrodynamic size of 121 nm.

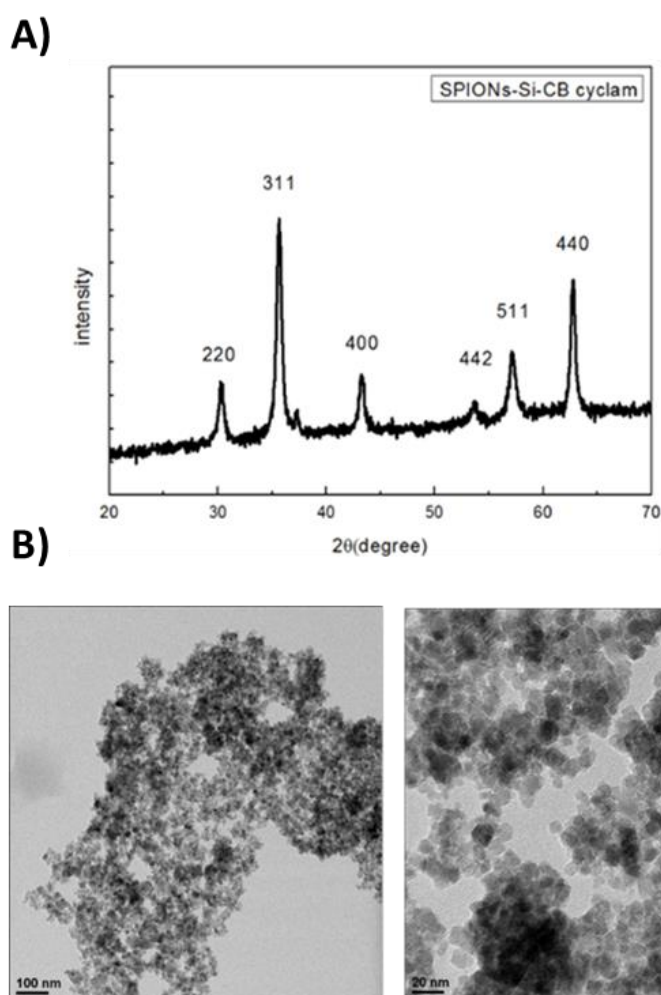


Figure 62: A) XRD pattern and B) TEM images for SPIONs-Si-CB cyclam **10**.

FT-IR spectroscopy has been used previously to validate the presence of different coatings on SPIONs core and is a useful technique for these constructs, see Figure 63. The expected peaks were observed, with Fe-O, and Si-O-Fe bands between 600 and 1000  $\text{cm}^{-1}$ . The OH stretch peak is at 3360  $\text{cm}^{-1}$  whereas the tetraazamacrocycle N-H stretch can be assigned at 3000  $\text{cm}^{-1}$  and the C-N stretch at 1337  $\text{cm}^{-1}$ .

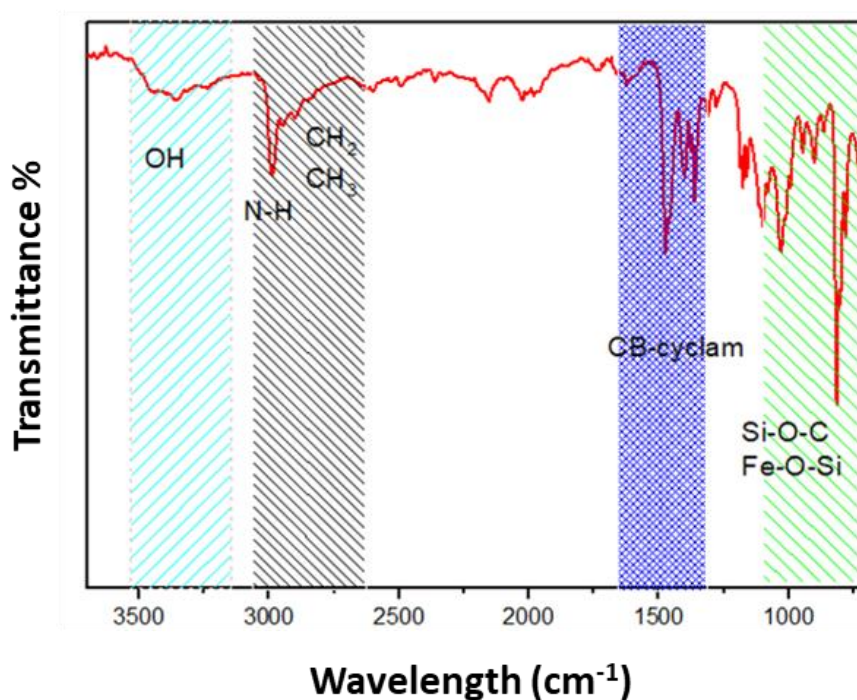
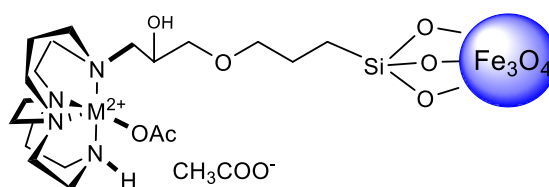


Figure 63: FT-IR spectrum of SPION-Si-CB cyclam 10.

### 3.3.4 Metal complex formation of SPION-SiO<sub>2</sub>-CB cyclam

Azamacrocycles, such as cyclam and cyclen, can offer a suitable cavity size and donor atoms to form complexes with metal ions, particularly the first row transition metals. Some azamacrocycles with metal ions present showed a higher affinity towards the CXCR4 chemokine receptor when compared to the free macrocycle, which is thought to be due to the formation of coordination bond between the metal centre and aspartate residues on the surface of the receptor.<sup>164</sup> This is particularly relevant for the cross-bridge cyclam compounds as the cross-bridge reduces the hydrogen bonding formation.

The functionalised SPIONs (SPION-SiO<sub>2</sub>-CB cyclam **10**) could be coordinated with different metal ions, copper(II), zinc(II) and nickel(II). The metal complex formation of these macrocycles is required in order to investigate the influence of metal centres on bind to the CXCR4 chemokine receptors. The coordination site on the metal will bind to aspartate and/or glutamate residues on the protein surface.<sup>165</sup> Following the method developed in the Archibald group for metal complexation of SPIONs, the first step is to suspend the conjugated SiO<sub>2</sub>-CB cyclam SPIONs in 60% ethanol/water solution for 15 minutes under nitrogen gas, then metal salt is then added and the reaction proceeds for 24 hours at room temperature, see Figure 64.



- 11** M= Cu<sup>2+</sup>  
**12** M= Zn<sup>2+</sup>  
**13** M= Ni<sup>2+</sup>

Figure 64: Metal complex formation of SPION-SiO<sub>2</sub>-CB cyclam with copper(II), zinc(II) and nickel(II).

The functionalised SPIONs after metal complex formation on the surface were characterised by several techniques. X-ray diffraction, see Figure 65 A, indicates the presence of magnetite phase with no changes after complex formation. These results are similar to the data mentioned previously, see section 2.5.1.

The TEM images shown in Figure 65 B, C and D indicate that the SPION size does not change significantly after metal complex formation and also the shape of particles was not affected by the modification step (the diameter remains at ca. 7.8-8.5 nm).

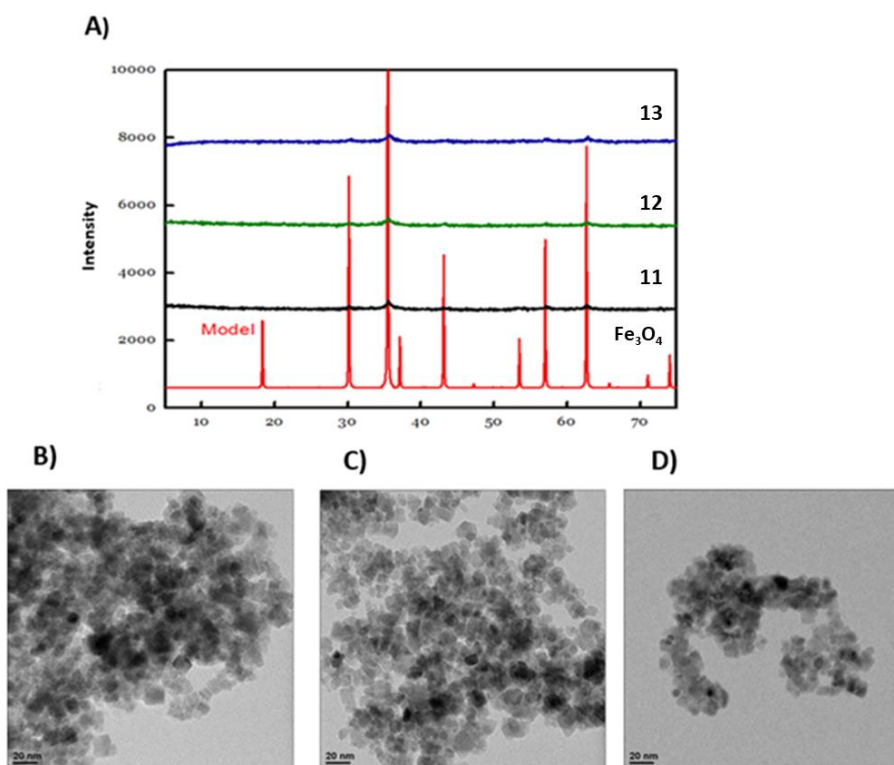


Figure 65: Analysis for three metal complexation SPIONs, A) PXRD for Fe<sub>3</sub>O<sub>4</sub> and complexes **11**, **12** and **13**. The TEM images for B) copper C) zinc and D) nickel complexed SPIONs.

DLS measurements were used to determine the mean hydrodynamic sizes of copper(II), zinc(II) and nickel(II) complex functionalised SPION and their core sizes are listed in Table 12. These results for **11** and **12** were similar to those observed by Barreto et al. in their related research. They functionalised the SPIONs with three different azamacrocycles and the hydrodynamic sizes for these SPIONs are 170, 180 and 160 nm respectively.<sup>123</sup>

Table 12: The DLS measurements and core sizes for **11**, **12** and **13**.

Sample	Z-average	PDI	Core size
<b>11</b>	159	0.14	8.2
<b>12</b>	158	0.14	8.0
<b>13</b>	165	0.20	7.7

To confirm the formation of desired functionalised SPIONs after metal complex formation, ICP and elemental analysis were used. The carbon percentage was in the range of 4.3 - 4.6%, the nitrogen percentage in the range 0.53-0.59% and for silicon the range was 3.3-6.8%. These results can be compared with the previous work by Burke *et al.*<sup>21</sup> on nanorods which used a similar methodology to synthesise siloxane-macrocycle derivatives conjugated with SPION as potential PET/MRI imaging agents. There are some similarities between the previous results and the results presented here, with 2.9-5.7% for carbon, 0.32-0.70% for nitrogen and 2.0-15% for silicon.

ICP-EOS can be used to determine the percentage of other transition metals present, after the metal complex formation reaction of functionalised SPIONs **10** (the percentage of copper, zinc and nickel were measured to give the following results: 2.7% for copper, 1.66% for zinc and 0.2% for nickel). The variability indicated that the nickel(II) complex had not formed efficiently and so the nickel(II) Nps were unlikely to show the same binding efficiency as the copper(II) and zinc(II) NPs.

### 3.4 Flow cytometry

The next step is to evaluate the binding efficiency of the metal complex SPIONs toward the CXCR4 receptor (that is overexpressed on many types of cancer cells). It is possible to use several techniques, for example, flow cytometry, ELISA and Western blotting. Flow cytometry is generally used to identify the cell surface properties and markers by counting individual cells properties and plotting the results in a histogram. The Archibald group has previously used different cancer cell line such as Jurkat and U87 successfully in binding assays to assess CXCR4 antagonist affinity by flow cytometry in an experiment that assesses binding competition with anti-CXCR4 monoclonal antibodies.

The Archibald group has previously synthesised CXCR4 antagonist, compound **13** and investigated the binding affinity toward the CXCR4 receptor as described in a PhD thesis of Neazar Baghdadi.<sup>206</sup> Flow cytometry was used to study the binding in a preliminary study of Ni-SPIONs-SiO<sub>2</sub>-CB cyclam binding CXCR4 receptors on Jurkat cancer cells. Further assessment of these NPs is required. The group found that there was a high affinity for the Ni-SPIONs-SiO<sub>2</sub>-CB cyclam sample to bind to the CXCR4 receptors on Jurkat cells, the calculation showed a binding efficiency of *ca.*100%. A similar study was carried out in this work for samples **10** and **11** in order to investigate their potential for CXCR4 targeted imaging *in vivo*.

The functionalised SPIONs before metal complex formation, compound **10**, and the copper(II) complex SPIONs **13** were evaluated for blocking of the anti-CXCR4 antibody in cancer cells. Transfected U87-CXCR4 cells for this assay, that have high receptor expression levels, and the *in vitro* cell binding assays were carried out by Dr Isaline Renard.

Binding affinity of the two SPIONs **10** and **13** was determined by flow cytometry through competition binding experiments with an anti-CXCR4 antibody, cells were exposed to two concentrations (10:90) and (50:50) dilution (SPIONs/Buffer). From Figure 66, it shows that there was no binding at either concentration between the non-complexed SPIONs-Si-CB cyclam (**10**) to the CXCR4 receptors as expected. However, no affinity for the receptor was observed for the low concentration

samples of the Cu-SPIONs-SiO<sub>2</sub>-CB cyclam (**11**), see Figure 66 right (orange line). Some shift was observed at the higher concentration (blue line) indicating that binding had occurred. This was an unexpected result, as high affinity was anticipated in line with other studies in the group. This issue requires further analysis and more experimental work to rationalise. It was observed that significant precipitation was occurring on mixing with the buffer required for the cell incubation. This buffer must be compatible with the growth media that is used to keep the cells alive and has a higher ionic strength than the buffers used in the preparation and labelling of the SPIONs. It is possible that the lower affinity may be linked to the higher diameter of the SPIONs (159 nm) compared to previous studies as larger particles may cause cell death. The most likely conclusion is that even larger particles are forming due to aggregation in the cell media and this step needs to be further optimised and the assays repeated.

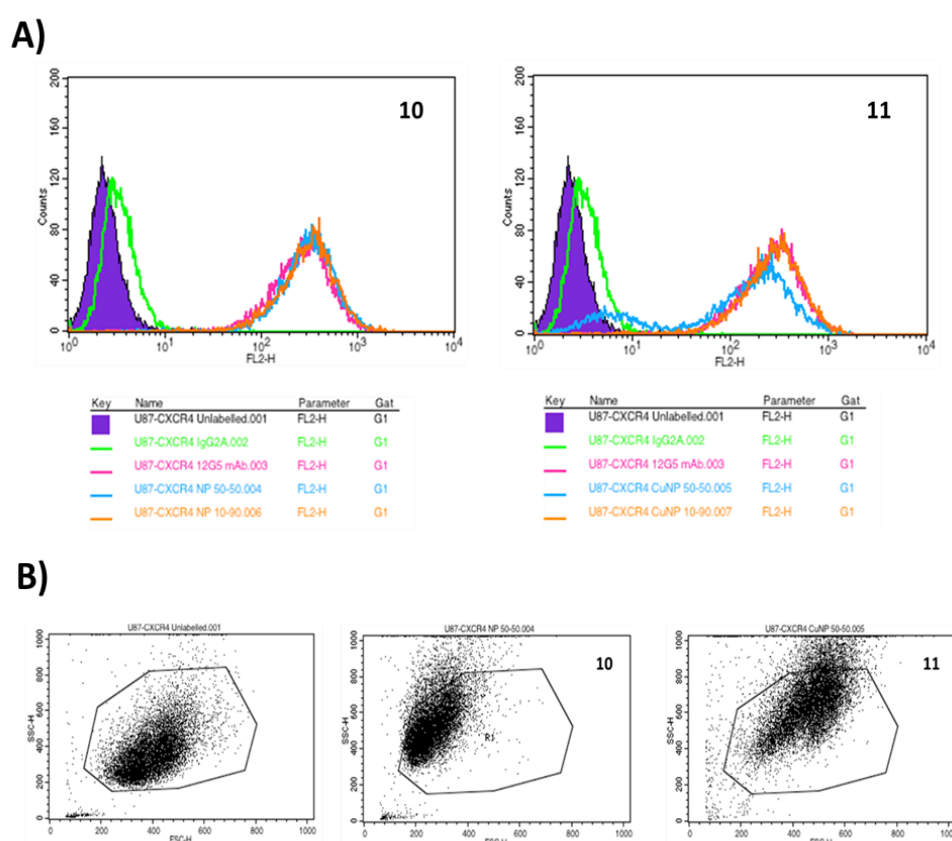


Figure 66: Flow cytometry A) histograms and B) dot plots for samples **10** and **11**.

### 3.5 Chelator-free $^{68}\text{Ga}$ radiolabelling of SPIONs-CXCR4 for PET imaging

The use of iron oxide nanoparticles in biomedical applications that combine PET imaging and cancer targeting is an emerging field. The aim of this part of the work is to determine whether the iron oxide nanoparticles, with a silica shell and functionalised with CXCR4 antagonist based on cross-bridged cyclam, can be efficiently radiolabelled using chelator-free methods. It should be noted that there may be CB cyclam chelators on the surface that are available, however, gallium(III) does not form complexes with CB cyclam under aqueous conditions and so labelling of the mesoporous silica surface is more likely. The radiolabelling and stability of SPIONs-SiO<sub>2</sub>-CB cyclam with gallium-68 was investigated in this work.

In a previous study by Archibald group, radiolabelling iron oxide nanorods with gallium-68, both chelator-free methods and chelator-based approaches were used. The rods were coated with siloxy polyethylene glycol (PEG) and/or a tetraazamacrocyclic chelator (DO3A). The results showed that in the presence of the silica coating, the macrocyclic chelator was not required for preparation of highly stable radiometal- nanorod constructs both *in vitro* and *in vivo*.<sup>19</sup>

In this work, the functionalised SPIONs with CXCR4 antagonist (SPIONs-SiO<sub>2</sub>-CXCR4) and the metal complex NPs (M-SPIONs-SiO<sub>2</sub>-CXCR4) were radiolabelled with gallium-68 under a range of conditions. After optimising the radiochemical yields, the functionalised nanoparticles were incubated in *apo*-transferrin to investigate the radiochemical stability of gallium-68 radiolabelling. Furthermore, the hydrodynamic size of functionalised SPIONs was measured before and after radiolabelling to determine if there was any variation/ particle aggregation.

#### 3.5.1 $^{68}\text{Ga}$ radiolabelling procedure for SPIONs-CXCR4 antagonist

The synthesised nanoparticles were tested under a range of conditions to radiolabel them with PET isotope gallium-68. The SPIONs-CXCR4 antagonist and metal complexes with copper(II), zinc(II) and nickel(II) were radiolabelled with gallium-68. To achieve this, initial optimisation was carried out on the copper-complex SPIONs-

SiO<sub>2</sub>-CXCR4 antagonist to determine radiolabelling yields at different reaction times and temperatures.

### **3.5.1.1 <sup>68</sup>Ga radiolabelling Cu-SPIONs-CXCR4 antagonist for 15 minutes at room temperature**

To optimise the radiochemical yield for the synthesised SPIONs-CXCR4 antagonist, the copper(II) complexed sample **11** was investigated first with gallium-68 at different temperatures following the standard procedure.<sup>19</sup> The first step after eluting gallium-68 as gallium chloride from <sup>68</sup>Ge/<sup>68</sup>Ga generator, was to dilute the eluted <sup>68</sup>GaCl<sub>3</sub> to 0.1 M before trapping on a solid phase extraction column. The radioisotope was eluted into a glass vial using acetone/0.1 M HCl solution, and then heated to 90°C under air flow to remove the solvent.

The gallium-68 was re-suspended in a solution containing the nanoparticles. 200 µl of a 1 mM (effective iron concentration) suspension of **11** in ammonium acetate pH 5 was used. The pH was selected to avoid the formation of unreactive/ insoluble gallium hydroxide species. The reaction was carried out at room temperature, 50°C or 90°C for 15 minutes. The radiolabelled SPIONs were centrifuged using spin filter (MWCO 100 kDa) at 12000 rpm for 10 minutes to remove any unreacted gallium-68, then 200 µl of ammonium acetate was added to the NPs that remain in the filter and re-centrifuge the solution at the same speed and time to wash the radiolabelled SPIONs from any free gallium-68. Finally, the two Eppendorf tubes contain the activated SPIONs and the wash were both measured using the dose calibrator to determine the radiochemical yield.

Figure 67 illustrates the radiolabelling procedure for SPIONs-CXCR4 antagonist starting from eluting gallium-68 from the generator followed by the reaction methods at different temperatures and time points, then measuring the final activity using the dose calibrator. The radiolabelling experiments were repeated in triplicate to assess reproducibility.

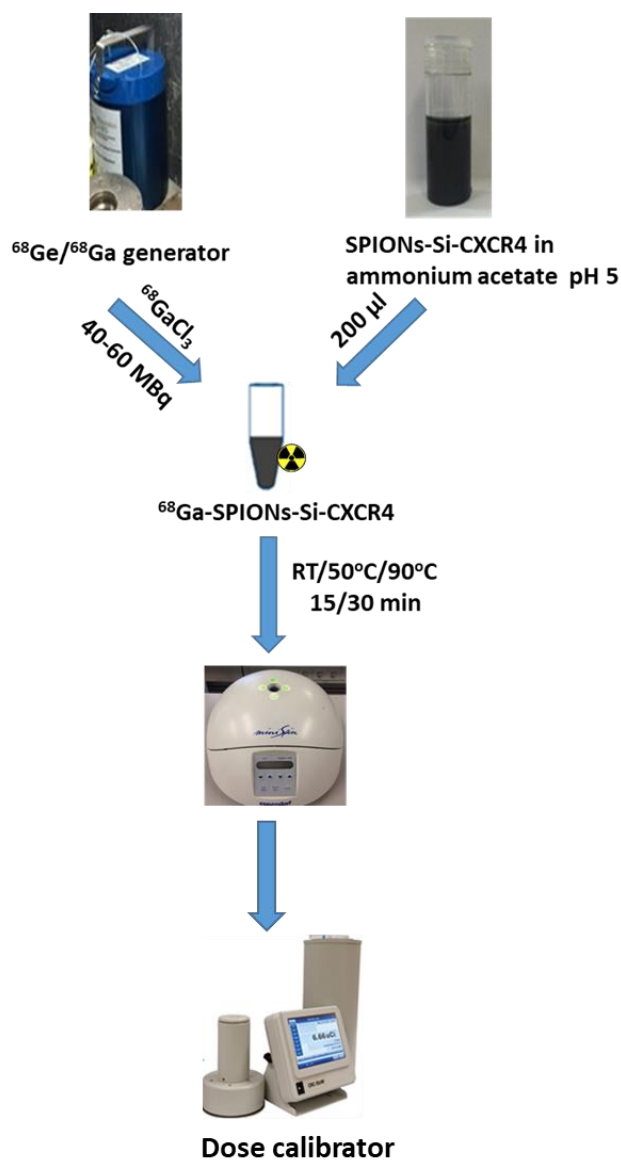


Figure 67: Schematic representation of  $^{68}\text{Ga}$  radiolabelling of SPIONs-Si-CXCR4 antagonist.

The radiochemical yields for radiolabelled Cu-SPIONs-Si-CXCR4 antagonist with gallium-68 was measured at room temperature, 50° and 90°C respectively after 15 minutes reaction, see Figure 68.

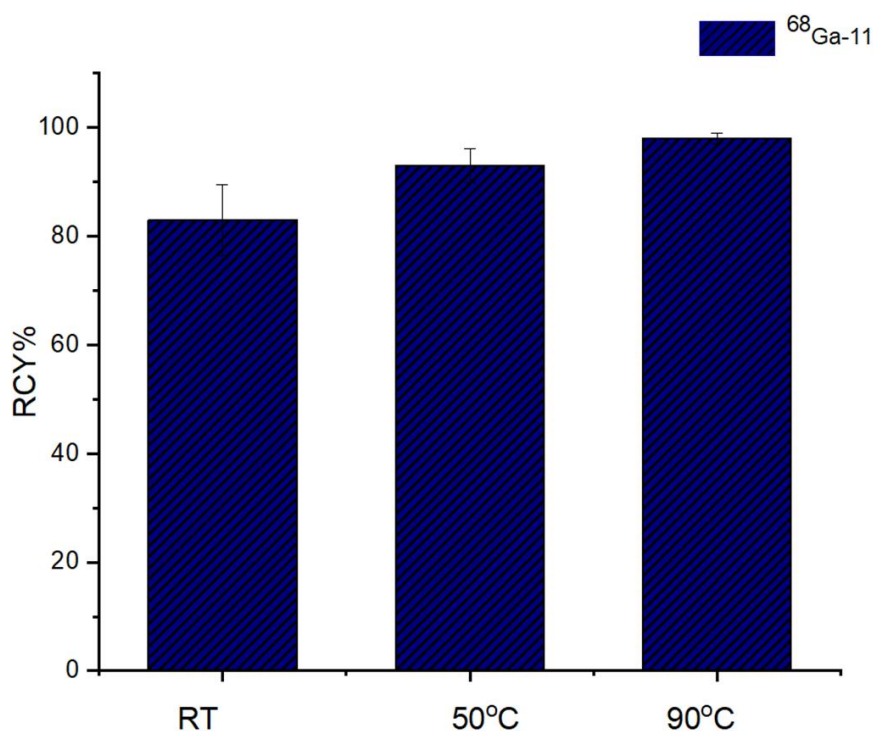


Figure 68:  $^{68}\text{Ga}$  radiolabelling of Cu-SPIONs-Si-CXCR4 in ammonium acetate buffer pH 5 at RT, 50 °C and 90 °C for 15 min (n=3).

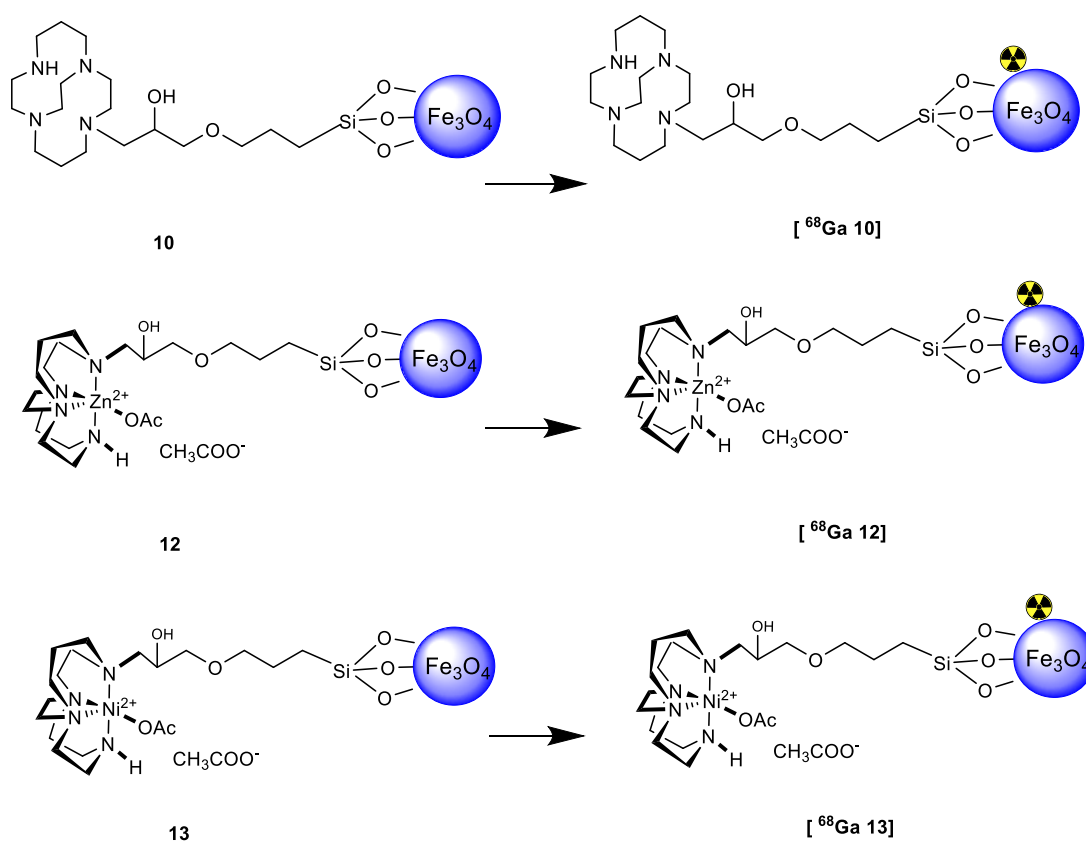
The chart illustrates the effect of temperature on radiochemical yield. It is clear that during the reaction time (15 minutes) there is a general trend towards increasing radiolabelling yield for these SPIONs with increasing temperature.

The reaction temperature to 50°C or 90°C causes a consistent increase in percentage incorporation of gallium-68, the Cu-SPIONs-Si-CXCR4 antagonist shows > 90% incorporation after 15 minutes at high temperature. The result is in agreement with the data observed by our group when iron oxide nanoparticles and nanorods were coated with siloxane and different types of macrocycles. Raising the temperature generally has a significant impact on radiolabelling yields.<sup>19, 21</sup>

A recent study by Hajiramezanali and co-workers, showed similar results. SPIONs were coated by chitosan and functionalised with DOTA as radioisotope chelator and bombesin as targeting moiety, the nanoparticles were radiolabelled with  $^{68}\text{Ga}$  (148 MBq) at 90°C for only 5 minutes. The radiolabelling yield for this construct were over 98%.<sup>208</sup>

### 3.5.1.2 $^{68}\text{Ga}$ radiolabelling of Zn(II), Ni(II) and metal-free SPIONs-CXCR4 antagonist at 50°C for 15 minutes

Applying the same method used for radiolabelling copper complexed SPIONs, other siloxane-macrocycles contain zinc(II) nickel(II) and the free metal SPION-SiO<sub>2</sub>-CXCR4 antagonist were reacted with gallium-68 at 50°C for 15 minutes, see Scheme 10.



Scheme 10: Formation of  $^{68}\text{Ga}$  complexation with SPIONs-Si-CXCR4 antagonist **10**, **12** and **13**.

Figure 69 shows the radiolabelling efficiency for the other nanoparticles with macrocycles; SPIONs-Si-CXCR4 **10**, Zn-SPIONs-Si-CXCR4 **12** and Ni-SPIONs-Si-CXCR4 **13** antagonist respectively.

As expected, forming the  $^{68}\text{Ga}$  complexes with nanoparticles at  $50^\circ\text{C}$  for 15 minutes gave similar results to those observed for the copper(II) complex sample, the three macrocycles derivatives [ $^{68}\text{Ga}$  **10**], [ $^{68}\text{Ga}$  **12**] and [ $^{68}\text{Ga}$  **13**] show a high radiolabelling yield  $> 94\%$  and all have a high reproducibility with low standard deviation (0.15-1).

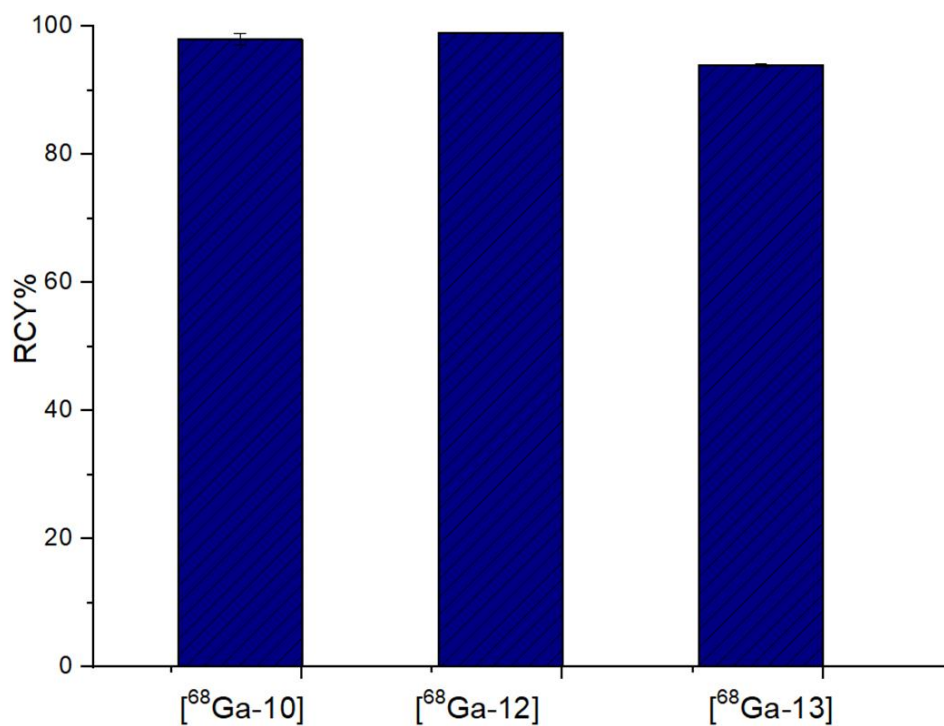


Figure 69:  $^{68}\text{Ga}$  radiolabelling of zinc(II), nickel(II) and free metal SPIONs-Si-CXCR4 antagonist in ammonium acetate pH 5 at  $50^\circ\text{C}$  for 15 min ( $n=3$ ).

### 3.5.2 Stability study of $^{68}\text{Ga}$ radiolabelling SPIONs-Si-CXCR4 antagonist

After conditions were optimised by which the four functionalised SPIONs with CXCR4 antagonists ( $^{68}\text{Ga}$  **10**],  $^{68}\text{Ga}$  **11**],  $^{68}\text{Ga}$  **12**] and  $^{68}\text{Ga}$  **13**]) could be successfully radiolabelled with RCY above 90%, competition experiments were required to determine the stability of attachment between the radioisotope and the nanoparticles.

The four constructs were first labelled with gallium-68 at 50°C and studied for stability under conditions as relevant to *in vivo* applications. Apo-transferrin was chosen for the stability tests due to its ability to complex efficiently with gallium(III) (which has a similar atomic radius to iron(III) therefore gallium(III) bioprocessing *in vivo* occurs through iron ion pathways).

The stability tests were carried out at physiological temperature (37°C) and the radioactivity were measured at 5, 15, 30 and 60 minutes by radio-TLC, see Figure 70.

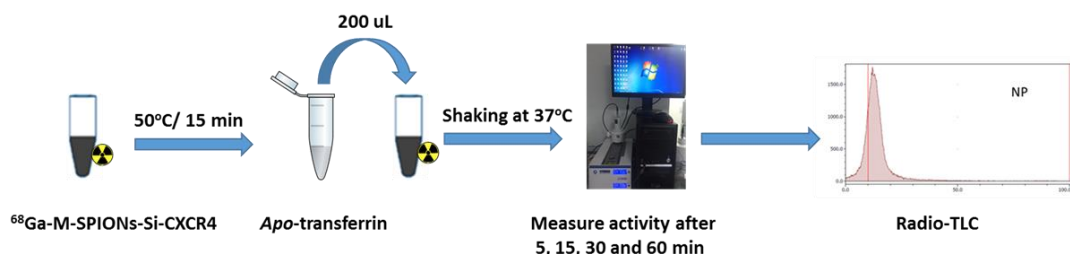


Figure 70: Schematic representation of the stability test for SPIONs-Si-CXCR4 antagonist with apo-transferrin.

The stability test in apo-transferrin is shown in Figure 71. It is clear that all constructs have a similar trend, all SPIONs show only a small percentage of radioactivity lost from the NP over the time investigated. After 30 minutes of incubation, the activity was still >90%, however, loss of >10% was observed after 60 minutes. These results are similar to those reported in the literature, the stability of iron oxide nanoparticles in physiological fluid after bounding to radioisotopes have been investigated in several studies.<sup>19, 208</sup>

Our group previously studied the gallium-68 radiolabelled silica-iron oxide nanorods coated with PEG and/or DO3A chelator. The constructs were incubated in serum and in apo-transferrin physiological temperature for 3 hours. In both proteins, >95% of gallium remained attached to SPIONs with no significant difference between the three SPIONs.<sup>19</sup>

In a study from Hajiramezanali, the conjugated SPIONs were incubated in serum for 180 minutes. The nanoparticles had 92% stability after 120 minutes which dropped to 86% at the end of the experiment.<sup>208</sup>

Setlter *et al.* have also studied the stability of SPIONs coated with aminosilane and with no other chelators present for multimodality imaging agents. The SPIONs were radiolabelled with gallium-68 successfully and incubated with chelating agent DTPA for 15 minutes at 40°C, the particles showed high stability in this competition test.<sup>205</sup>

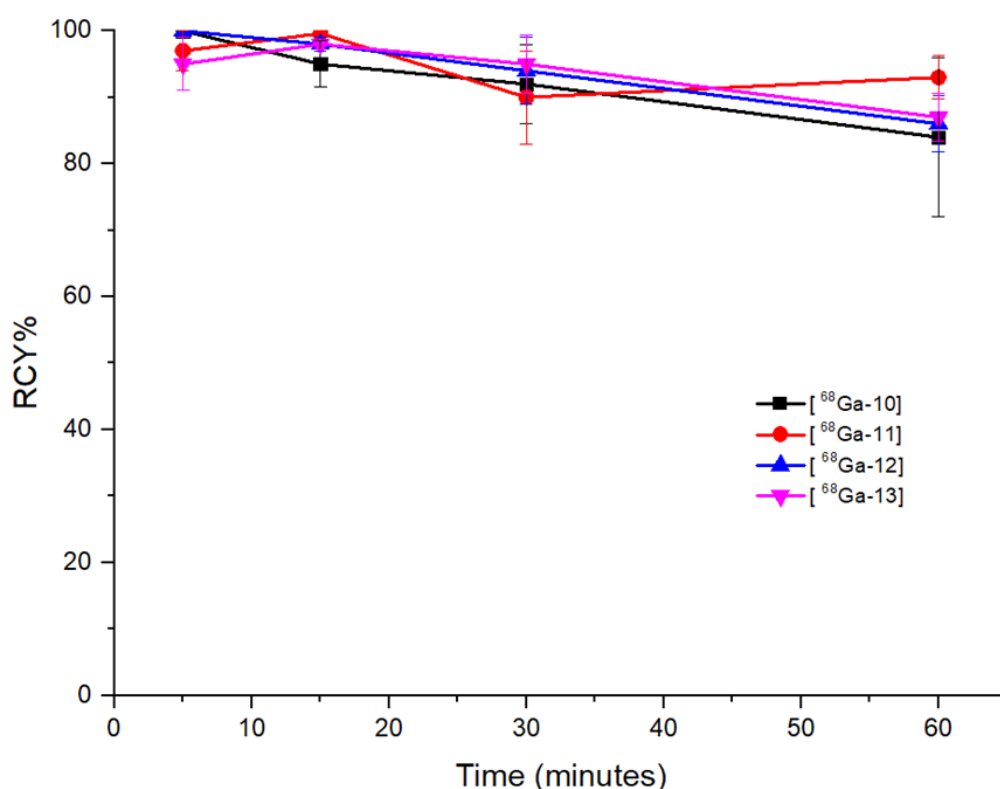


Figure 71: Stability test of <sup>68</sup>Ga-SPIONs-Si-CXCR4 antagonists **10**, **11**, **12** and **13** with apo-transferrin during 60 minutes (n=3).

### 3.5.3 Variation of hydrodynamic size

The size and size distribution are important properties for using nanoparticles in biomedical applications. As in section 2.6.3 studying the effect of radiolabelling reactions on the hydrodynamic size was important for the application. The hydrodynamic sizes for the four SPIONs constructs were measured prior and post radiolabelling with gallium-68, see Table 13.

It was observed that the size distributions for all SPIONs had increased. The copper(II) and the zinc(II) samples increased by around 12 nm, however, the nickel(II) and the free metal SPIONs have larger variation in size distribution of between 40-50 nm. The use of buffer and the reaction conditions could promote the aggregation of the SPIONs and this may require further investigation.

Table 13: The hydrodynamic sizes (diameter) for SPIONs-SiO<sub>2</sub>-CXCR4 before and after <sup>68</sup>Ga radiolabelling.

Before radiolabelling	Z-average	PDI	After radiolabelling	Z-average	PDI
<b>10</b>	121	0.20	<b><sup>68</sup>Ga-10</b>	163	0.4
<b>11</b>	159	0.14	<b><sup>68</sup>Ga-11</b>	171	0.35
<b>12</b>	158	0.14	<b><sup>68</sup>Ga-12</b>	170	0.32
<b>13</b>	165	0.20	<b><sup>68</sup>Ga-13</b>	220	0.4

### 3.6 Conclusion

Various approaches have been investigated for the development of gallium-68 labelled CXCR4 targeted SPIONs imaging agent. First, functionalised SPIONs coating with tetraazamacrocycle compound were synthesised by using GPTES as a linker, the presence of iron oxide core and the coating layer were confirmed by XRD, TEM and FTIR. Followed by metal complex formation of the CB cyclam on the surface of these nanoparticles with copper(II), nickel(II) and zinc(II). The average hydrodynamic sizes for these antagonist functionalised NPs were between 158-165 nm.

Four constructs **10**, **11**, **12** and **13** were successfully radiolabelled with gallium-68 and show excellent gallium-68 radiolabelling characteristics. The optimum reaction parameters were at 50°C for 15 minutes in ammonium acetate at pH 5. The functionalised SPIONs were then further tested to determine compatibility for *in vivo* use, in an *apo*-transferrin challenge stability test. The results showed a moderate loss of radioactivity was observed after 60 minutes, with *ca.* >85% remaining bound to the nanoparticles. The size and size distribution were analysed after <sup>68</sup>Ga radiolabelling, and there was a noticeable increase in size between 10-50 nm indicating minor aggregation of SPIONs after labelling.

Further work is needed on the *in vitro* validation of cell binding to CXCR4 expressing cells. SPIONs **11** appeared to show low affinity in the antibody competition assay by flow cytometry. However, further analysis indicated that precipitation was occurring in the high ionic strength buffer used in these experiments, and so experiments need to be repeated to accurately determine the affinity.

# Chapter 4

**$^{68}\text{Ga}$  radiolabelled nanocarriers  
(liposomes and micelles) for *in vivo*  
PET imaging**

## 4 Chapter four: $^{68}\text{Ga}$ radiolabelled nanocarriers (liposomes and polymeric micelles) for *in vivo* PET imaging

### 4.1 Aims

Different types of nanostructure carriers including liposomes and polymeric micelles (PM) have attracted attention due to their ability to function as imaging probes and, more importantly, as selective drug delivery vehicles to tumours or other tissues. These nanocarriers have unique characteristics, such as their morphology, narrow size distribution and surface properties that can favour their accumulation in the tumour cells.<sup>209</sup> Nanocarriers are used for theranostic techniques, i.e. for imaging and therapy at the same time to show delivery of a pharmaceutical to the desired location.<sup>210</sup>

The aim of this chapter is to evaluate the radiolabelling of liposomes and micelles with gallium-68, as a potential platform for using PET to track the nanocarriers *in vivo* with high sensitivity dynamic imaging.

Therefore, the two main objectives are:

- Characterisation of PEGylated liposomes and PM by dynamic light scattering (DLS) and transmission electron microscopy (TEM) to determine a suitable size distribution for a medical application.
- Radiolabelling optimisation of liposomes and PM with gallium-68, followed by *in vivo* studies used to assess the potential for using PET to track the nanocarriers *in vivo*, see Figure 72.

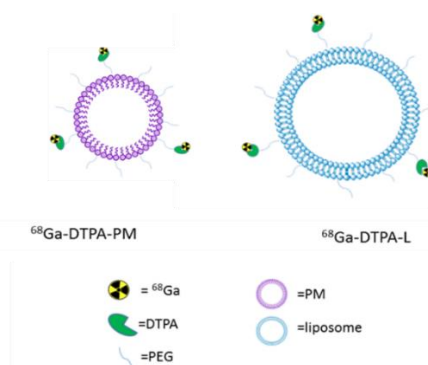


Figure 72: Schematic representation of radiolabelling liposomes and polymeric micelles with Ga-68.

## 4.2 Liposomes and polymeric micelles in medical applications

The development of imaging and therapeutic agents to improve drug delivery specifically and safely to a desired site of action is one of the most challenging tasks of pharmaceutical development. Among these systems, nanocarriers including nano-emulsions, lipids, polymeric micelles and liposomes have investigated. These nanoparticles offer additional advantages when compared with other colloidal drug carriers.<sup>61, 211</sup> For example, polymeric micelles (PM) and liposomes show a higher stability when in contact with biological fluids, and high drug-loading capacities which can increase the intracellular concentration of the drug. Moreover, the surface functionalisation of nanocarriers has improved drug delivery systems especially in cancer treatment by increasing the target tissue accumulation of nanocarriers while minimising systemic toxicity.<sup>97</sup>

The surface modification with polyethylene glycol (PEG) helps to increase the stability of nanocarriers in biological media by reducing the fusion rate and inhibiting protein adsorption. This enhances the *in vivo* circulation time required to reach the specific target, apart from clearance by the reticuloendothelial system (RES). Despite improving stability, the modified liposomes and polymeric micelles still suffer from selectivity for specific cell uptake and control of the timing and dosage of drug. To overcome these limitations, several engineering strategies have incorporated to improve their performance *in vivo*. One of these strategies is to functionalise the nanocarriers with peptides or proteins to bind to cell surface receptors. Chelating agent are also used to modify the surface of the nanocarriers to allow labelling for image based tracking, e.g. with  $Gd^{3+}$  (MRI) or,  $^{64}Cu$  or  $^{18}F$  (PET imaging).<sup>60, 97</sup> The integration of nanomedicine with imaging probes is a powerful technique for efficient development and clinical translation of nanocarrier drug delivery systems.

### 4.2.1 Liposomes

Over the past 30 years, liposomes have increased in importance as delivery systems for therapeutic agents (e.g. chemotherapeutics or immune-modulation agents), antigens and imaging agents. Liposomes are self-assembling vesicles with sizes

ranging from 20 nm to 10  $\mu$ m and exist as uni- or multilamellar vesicles. This construction gives liposomes some advantages, such as the potential for surface functionalisation to increase stability, encapsulation and release efficiency and delivery accuracy.<sup>98, 212</sup> Doxil<sup>®</sup> is considered the first successful nano-sized liposomal drug and it was introduced to the US market in 1995 for ovarian cancer treatment. Later, DaunoXome<sup>®</sup> was approved for HIV-associated Kaposi's sarcoma. Then further treatments were introduced for the management of various cancers. Caelys<sup>®</sup> and Myocet<sup>®</sup> are clinically approved therapeutic drugs used to treat ovarian and breast cancers.<sup>213</sup>

#### **4.2.2 Micelles**

Polymeric micelles are considered as a newer addition to the nanoparticles field as their applications were first reported in the late 80s by Kabanov *et al.* Micelles are self-assembled aggregates of amphiphilic molecules (unimers, a long polymer usually from 10-30 kDa).<sup>214</sup>

Polymeric micelles have small size less than 100 nm, this property can keep them away from the reticulo-endothelial system (RES) in liver, spleen and bone marrow after injection to the body and this will increase their blood circulation time.<sup>110, 215</sup>

The first micellar formulation was approved for use in South Korea in 2007, for breast and lung cancer treatment. The FDA has now approved polymeric micelles formed from a block copolymer mPEG-b-poly (D,L-lactic acid) with the anti-cancer drug paclitaxel encapsulated in the core of the micelles.<sup>216, 217</sup> Recently, several polymeric micelle products are currently being evaluated in clinical trials for cancer treatment. For example, NK911 is a drug delivery system contains of doxorubicin in a block copolymer of poly(ethylene glycol)-b-poly(a,b-aspartic acid) for targeting pancreatic and colorectal cancer.<sup>216</sup>

### 4.3 Radiolabelling of liposomes and polymeric micelles

The radiolabelling of nanocarriers is already used in preclinical studies to evaluate the performance of the NPs *in vivo*. Liposomes are readily labelled with number of SPECT and PET isotopes.  $^{99m}\text{Tc}$  is the most commonly used radionuclide followed by  $^{111}\text{In}$  and  $^{131}\text{I}$  for radiolabelling liposomes. More recently,  $^{18}\text{F}$ ,  $^{89}\text{Zr}$  and  $^{64}\text{Cu}$  have been increasingly used for PET imaging of these structures.

However, radiolabelling of polymeric micelles is not as widespread as labelling liposomes and most research utilises  $^{64}\text{Cu}$  for PET imaging or  $^{99m}\text{Tc}$  for SPECT imaging. Several techniques have been developed to incorporate radionuclides into nanocarriers for nuclear imaging. These methods can be classified into four categories; passive encapsulation, membrane labelling, surface chelation and remote loading. The last two methods are commonly used due to their high incorporation efficiency,<sup>218</sup> see Figure 73.

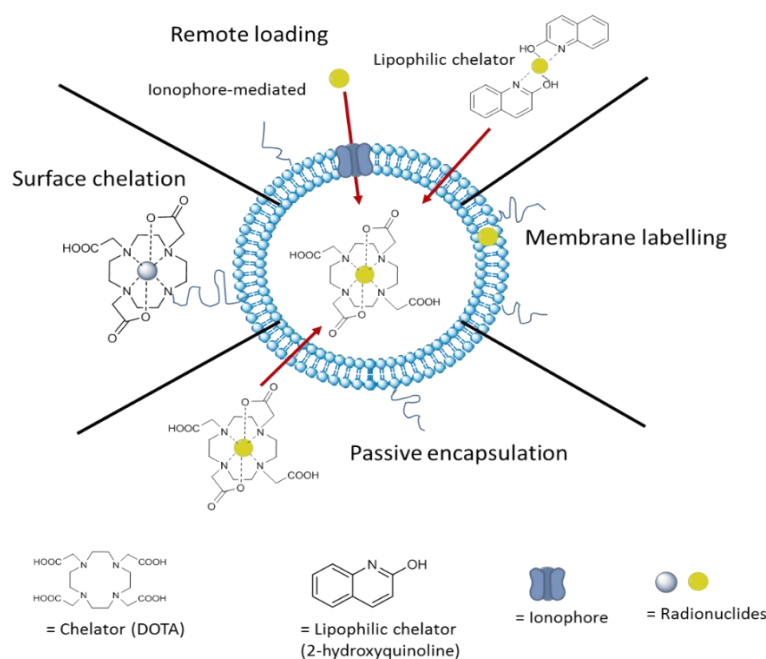


Figure 73: schematic diagram for radiolabelling methods of liposomes.<sup>219</sup>

In the past few years, there are several studies reporting radiolabelling of liposomes with SPECT or PET radionuclides. Ahkong *et al.* have radiolabelled liposomes with technetium-99m for SPECT imaging. The group used the surface chelation method for radiolabelling. They found that the addition of DTPA (diethylenediamine

pentaacetic acid) as chelator enhanced the stability of radiolabelled liposomes in physiological media.<sup>220</sup>

Copper-64 is a frequently used radioisotope for radiolabelling liposomes as PET imaging agent. Peterson *et al.* developed the surface chelation method for radiolabelling liposomes with <sup>64</sup>Cu under mild conditions at 20-50°C. The surface was functionalised with chelator DOTA (1, 4, 7, 10-Tetraazacyclododecane-1, 4, 7, 10-tetraacetic acid) to give high labelling efficiency of > 95%.<sup>221</sup>

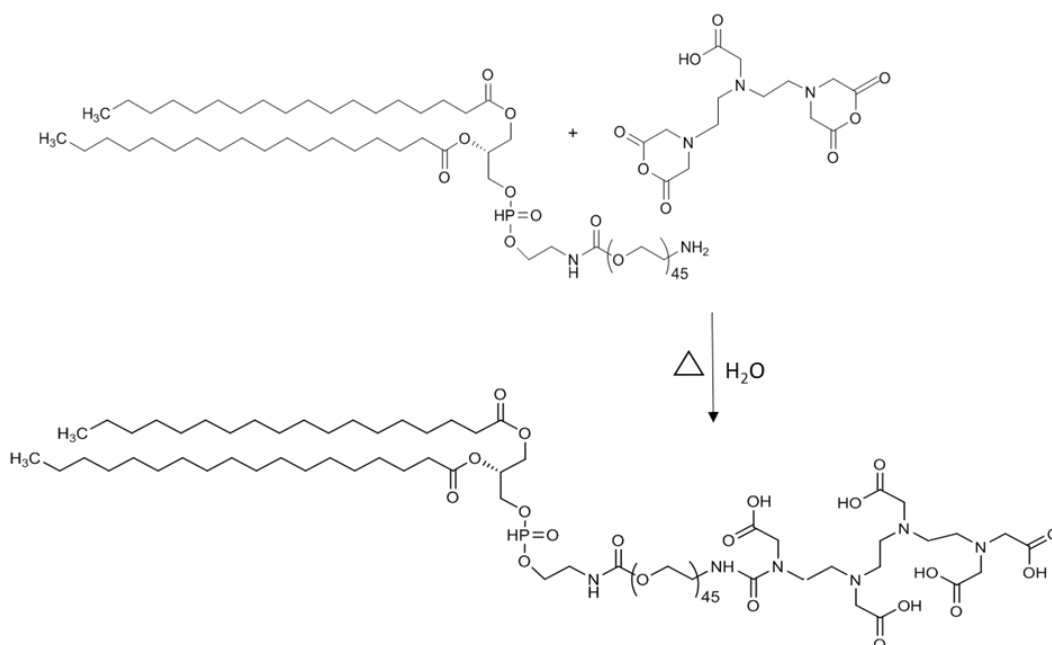
Continuing with surface chelation methods, Helbok *et al.* have made a comparison of the radiolabelling of DTPA-functionalised liposomes with different radiometals including <sup>111</sup>In and <sup>99m</sup>Tc for SPECT, <sup>68</sup>Ga for PET imaging and <sup>177</sup>Lu for therapeutic applications by varying amounts of DTPA, different compositions and size. All formulations have high labelling yields >90% with specific activities were highest for <sup>111</sup>In followed <sup>68</sup>Ga and <sup>177</sup>Lu, in case of <sup>99m</sup>Tc, high labelling yield and specific activity which were only achieved by using <sup>99m</sup>Tc-carbonyl.<sup>222</sup>

In the last decade, numbers of publications described the design, synthesis and characterisation of polymeric micelles for cancer-targeted PET imaging and drug delivery *in vivo* have increased.<sup>112</sup> Rossin *et al.* investigated polymeric micelles as PET imaging agent when radiolabelled with <sup>64</sup>Cu. The surface of micelles were functionalised with TETA (tetraazacyclotetradecane tetraacetic acid) as a BFC. These particles showed a high liver accumulation, they suggested it was due to the large number of negative charges on the chelator but it is also well known that the chelator TETA does not form stable *in vivo* with copper(II).<sup>223</sup>

Recently, Grotz *et al.* presented a study for Tuberculosis (TB) therapy using the oral anti-TB drug, Rifampicin (RIF). They synthesised inhalable RIF-loaded polymeric micelles and radiolabelled them with <sup>99m</sup>Tc. The direct injected intratracheally showing that the radiolabelled PMs were retained in the lungs over 24 hours in rats.<sup>224</sup>

Professor Andre' De Barros and his group have studied several functionalised liposomes and polymeric micelles as potential platforms for drug delivery, the biodistribution of these nanoparticles were evaluated using the SPECT isotope <sup>99m</sup>Tc.

Polymeric micelles have been prepared from 1,2-distearoyl-sn-glycero-3-phosphoethanolamine-N-[methoxy(polyethyleneglycol)-2000] (DSPE-PEG<sub>2000</sub>-DTPA) with a mean hydrodynamic size of  $9.6 \pm 0.6$  nm and zeta potential of  $-2.7 \pm 1.1$  mV, see Scheme 11.



Scheme 11: Representative scheme of the synthesis of DSPE-PEG<sub>2000</sub>-DTPA.<sup>209</sup>

The polymeric micelles were radiolabelled with technetium-99m in presence of SnCl<sub>2</sub> as reducing agent, and radiochemical purity higher than 90% was achieved. <sup>99m</sup>Tc-DTPA-PM showed high stability in saline media and plasma up to 8 hours. *In vivo* studies showed high uptake in liver, spleen, kidney and some accumulation in tumour site, see Figure 74.<sup>209</sup> These polymeric micelles were chosen for radiolabelling with gallium-68 in this chapter.

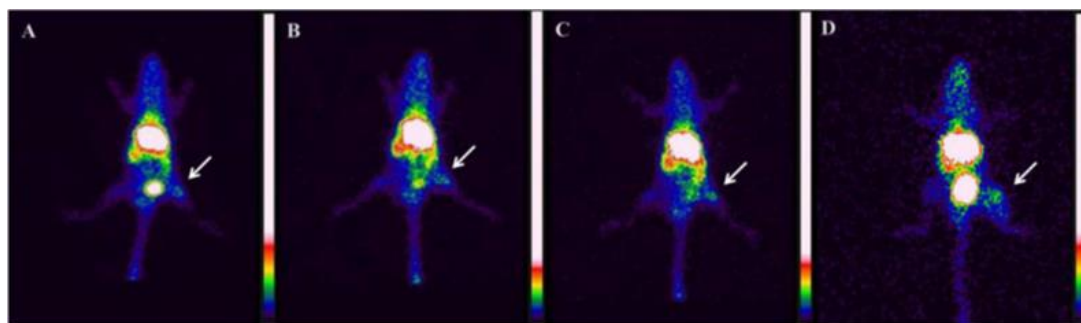


Figure 74: SPECT images for  $^{99m}\text{Tc}$ -DTPA-PM administration in tumour-bearing mice after 1 (A), 4 (B), 8 (C) and 24 hours (D), arrows indicate tumour site.

The Andre' De Barros and group first study was a comparison between liposomes and nanostructured lipid carriers (NLC) after both were loaded with doxorubicin (anti-cancer drug). The encapsulation of DOX into these structures did not change the mean diameters, which remained at 130 nm for liposomes and 93 nm for NLC. The zeta potential for liposomes was -2.03 mV attributed to the presence of DSPE-PEG<sub>2000</sub> which causes a high hydrodynamic resistance leading to a low electrophoretic mobility, while the zeta potential for NLC was -29.9 mV due to the presence of ionized oleic acid during preparation. The tumour-bearing mice were injected with the DOX-loaded nanocarriers as therapeutic agent, and after 14 days the  $^{99m}\text{Tc}$ -DOX was administered to the animals and SPECT images were acquired. The NLC-DOX showed more inhibition in tumour growth compared to Liposomes-DOX.<sup>61</sup>

Another category of liposomes, pH-sensitive liposomes, have been of interest in the last decade for their ability to control the drug release. The De Barros group prepared this type of liposome and tracked them *in vivo* with radiolabelling. The pH-sensitive liposomes (SpHL) encapsulated DOX and were radiolabelled with technetium-99m, a comparison between these structure and non-sensitive liposomes (nSpHL) in absence of CHEMS were carried out. The size distribution for both NPs was not affected by  $^{99m}\text{Tc}$  radiolabelling, and showed a high radiolabelling purity of >90%. Both formulations reached the tumour with high accumulation, however, there was a higher tumour uptake about 4-fold for the SpHL compared to nSpHL.<sup>211</sup> In another study by this group, pH-sensitive liposomes were encapsulated with the antitumor cisplatin (CDDP) and radiolabelled with technetium-99m. The *in vivo* studies showed

that the radiolabelled and functionalised liposomes were more effective in controlling tumour growth compared to the free-CDDP liposomes.<sup>60</sup>

None of the studies from the De Barros group used the higher sensitivity PET imaging that would also allow dynamic scanning to track the early biodistribution and accumulation with greater accuracy.

## 4.4 Radiolabelled liposomes **14** and micelles **15** for *in vivo* biodistribution studies

Nuclear imaging is an important tool for tracking the biodistribution and pharmacokinetics of nanocarriers.<sup>225</sup> The aim of this chapter is to evaluate the radiolabelled <sup>68</sup>Ga-liposomes and <sup>68</sup>Ga-polymeric micelles as potential platforms for drug delivery using PET imaging and to make a comparison with previous work that radiolabelled these types of nanocarriers with technetium-99m.<sup>61, 209</sup>

To achieve this goal, the functionalised liposomes and micelles with DSPE-PEG<sub>2000</sub>-DTPA that had been synthesised by Professor Andre' De Barros and his group at University Federal de Minas Gerais, Brazil, were characterised by DLS and subsequently radiolabelled with the PET isotope gallium-68 at the PET Research Centre at University of Hull.

### 4.4.1 Characterisation of liposomes and PM **14** and **15**

The nanoparticles were in a white powder form when received, and were suspended in saline 0.9% to form a colourless solution. The size distribution of liposomes **14** and polymeric micelles **15** were first measured in order to determine if there were any effects caused by storage of the nanoparticles. From Figure 75, it shows that the diameters for both samples according to DLS were close to the nanocarriers size distribution as synthesised, and mentioned in the literature.<sup>61, 209</sup> The dynamic light scattering shows that liposomes **14** and polymeric micelles **15** have a mono-modal distribution with average hydrodynamic diameter of 131 and 13 nm respectively. Compared to literature<sup>61, 209</sup> the liposomes have very similar size distribution; however, there was a small increase in case of polymeric micelles which was around 9.6 nm in the literature report.

The narrow sizes are an intrinsic feature of nanocarriers that should keep them in blood for a longer time and therefore avoid their rapid removal by the reticuloendothelial system.<sup>226</sup> The prepared liposomes and polymeric micelles with these hydrodynamic sizes remain under the suitable range size for *in vivo* applications.<sup>227, 228</sup>

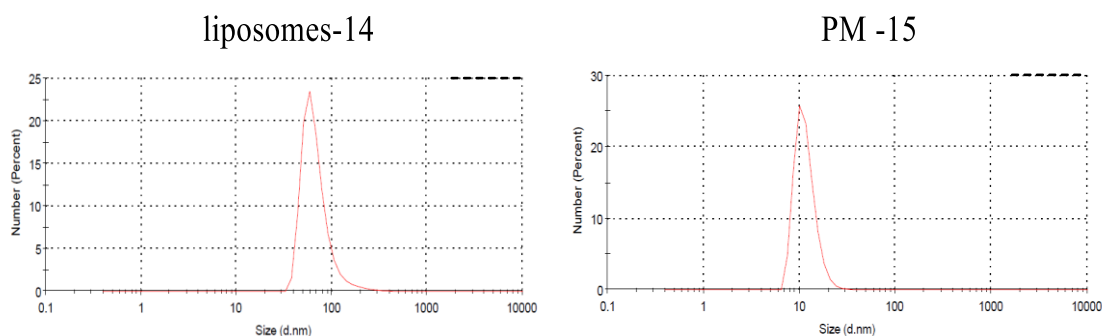


Figure 75: The hydrodynamic sizes for (A) DTPA-L **14** and (B) DTPA-PM **15**.

## 4.5 Radiochemistry reactions and radiolabelling stability studies for liposomes and polymeric micelles **14** and **15** with gallium-68

In this part of research work, the aim is to develop radiolabelling methods for liposomes and polymeric micelles with PET radionuclide gallium-68 and compare these results with known radiolabelling of the same particles with technetium-99m.<sup>61</sup>, 209

Therefore, the nanocarriers were labelled with gallium-68 and the radiochemistry studies included several experiments to optimise the radiochemical yield (RCY). Labelled particle stability analysis was also carried out in serum in order to mimic the labelled nanoparticle stability in physiological media to allow the work to proceed to an *in vivo* study.

### 4.5.1 <sup>68</sup>Ga radiolabelling procedure for liposomes and polymeric micelles **14** and **15**

The functionalised liposomes and polymeric micelles have already been radiolabelled with technetium-99m, with promising results for SPECT imaging. Gallium-68 was selected for study and radiolabelled liposomes and polymeric micelles due to favourable properties, as previously discussed, and the availability of gallium-68 generator in the preclinical PET Research Centre at the University of Hull. A disadvantage of gallium-68 is the relatively short half-life of 68 minutes, however,

the main aim of this work is to determine dynamic biodistribution on injection and so this will be sufficient. Future studies could be carried out with a longer-lived PET isotope (e.g. zirconium-89).

The radiolabelling procedure of liposomes and polymeric micelles were carried out under aqueous conditions. Gallium has oxidation state (III) at physiological pH and is generally eluted from  $^{68}\text{Ge}/^{68}\text{Ga}$  generator using 0.1 M hydrochloric acid. Most synthetic procedures are carried out in the presence of weak coordinating ligands such as acetate, citrate and oxalate at pH between 3-5. These conditions can prevent any production of insoluble  $\text{Ga}(\text{OH})_3$  and soluble  $\text{Ga}(\text{OH})_4^-$  which dramatically slows the kinetics of complex formation. Therefore, the presence of chelating ligands such as DOTA and DTPA (a bifunctional chelators) can be used to displace the weakly bound ligands to form a six coordinate complexes with an octahedral geometry. In this case, DTPA was used. These complexes are generally stable *in vivo* with additional reactive terminating group for bioconjugation.<sup>229, 230</sup>

In this work, the labelling procedure was carried out by suspending the liposomes **14** and polymeric micelles **15** in a solution of  $^{68}\text{GaCl}_3$  and experiments were carried out to determine the optimised radiolabelling conditions.

Initially, the preparation of the radionuclide was carried out by elution  $^{68}\text{GaCl}_3$  from  $^{68}\text{Ge}/^{68}\text{Ga}$  generator in 5 ml of 0.1 M HCl. The gallium solution was transferred to solution containing (acetone/0.1 M HCl) by cartridge, then dried at 90°C under airflow. The reactions for radiolabelling were carried out by incubation of the liposomes and micelles with  $^{68}\text{GaCl}_3$  for 15 min in different buffers and at different activities, see Figure 76.<sup>231, 232</sup>

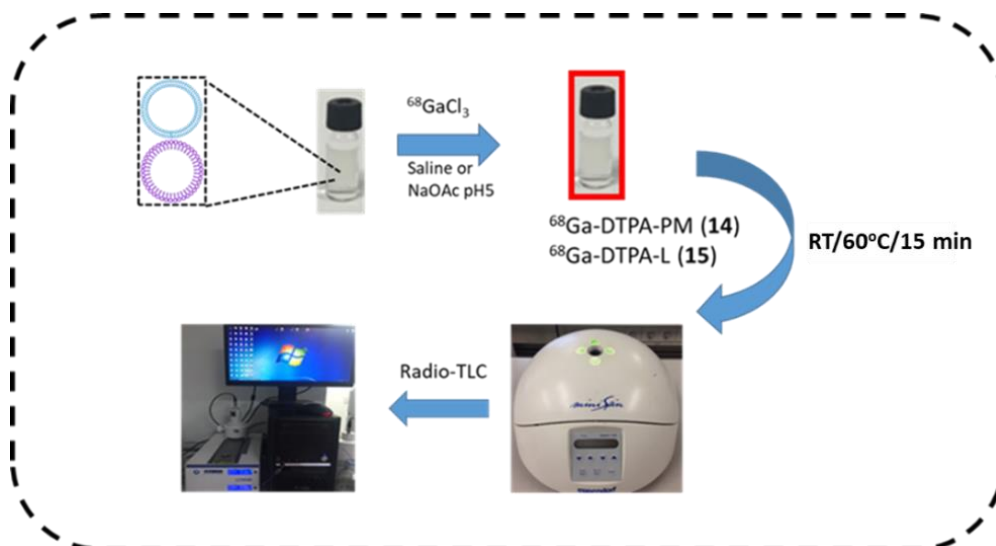


Figure 76: Schematic representation of the  $^{68}\text{Ga}$  radiolabelling procedure used for liposomes and micelles **14** and **15**.

#### 4.5.2 $^{68}\text{Ga}$ radiolabelling liposomes and polymeric micelles in saline

The first method used was the incubation of liposomes and polymeric micelles in saline. Although it is known that  $^{68}\text{GaCl}_3$  would give low radiolabelling efficiencies in saline, this step is needed to be able to make a comparison with the same nanocarriers that already radiolabelled with technetium-99m by the De Barros group (which gave a high radiolabelling yields over 90% in saline). The nanocarriers were incubated in saline at room temperature or at 60°C for 15 minutes.<sup>61, 209</sup>

##### 4.5.2.1 $^{68}\text{Ga}$ radiolabelling of liposomes and polymeric micelles **14** and **15** in saline at room temperature

The reaction was started by dissolving the liposomes **14** and polymeric micelles **15** in saline and added this solution to dry  $^{68}\text{GaCl}_3$  (50 MBq). The reaction was shaken for 15 minutes at room temperature. Radiochemical complex formation reactions were analysed by radio-TLC (thin layer chromatography), eluting with 0.1 M citric acid.

At room temperature, a small amount (<5%) of  $^{68}\text{Ga}$  is incorporated onto both nanoparticles after 15 minutes, as expected for the gallium-68 the process is inefficient in saline, see Figure 77.

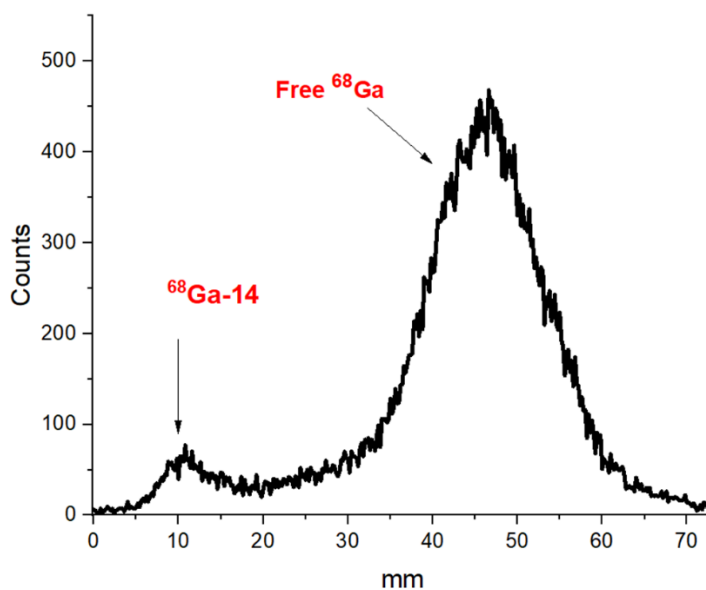


Figure 77: Radio-TLC scan for  $^{68}\text{Ga}$ -radiolabelled liposomes **14** in saline for 15 minutes at RT.

#### 4.5.2.2 $^{68}\text{Ga}$ radiolabelling liposomes and polymeric micelles **14** and **15** in saline at $60^\circ\text{C}$

To continue the investigation of radiolabelling **14** and **15** in saline, the temperature was increased to  $60^\circ\text{C}$ . Increasing the temperature between  $50$ - $90^\circ\text{C}$  should improve the radiochemical efficiency of the radiolabelling with gallium-68. Here, the dissolved nanocarriers in saline were incubated with dry  $^{68}\text{GaCl}_3$  (50 MBq) and the reaction was heated to at  $60^\circ\text{C}$  for 15 minutes. As before, the nanocarriers were then purified by centrifugation for 10 minutes with further elution with saline. The reaction mixture was measured by eluting the TLC in 0.1 M citric acid to detect any free gallium. The radio-TLC for both nanocarriers shown in Figure 78. It is clear that the higher temperature has enhanced the RCY for both types of radiolabelled nanoparticles. The radiolabelling yield for liposomes **14** was 45%, while the polymeric micelles **15** have a lower level of attachment with  $^{68}\text{Ga}$  around 30%. As mentioned before, these results in saline were as expected as it is not the optimal medium for the reaction.

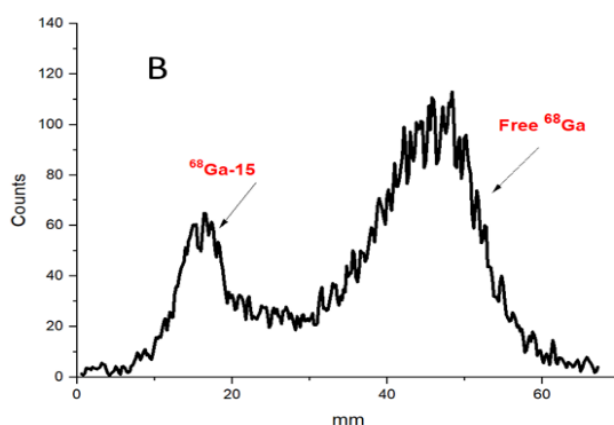
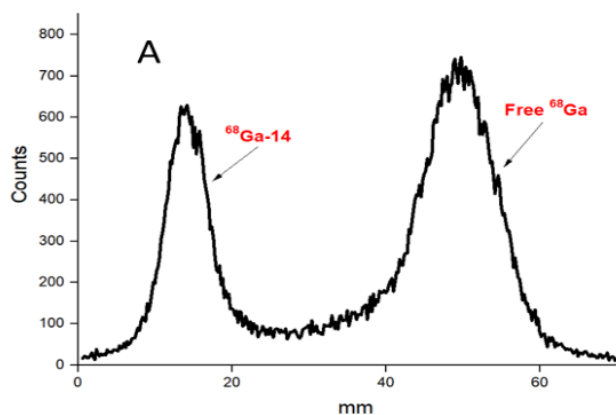


Figure 78: Radio-TLC in saline of the  $^{68}\text{Ga}$ -radiolabelled nanocarriers incubated for 15 minutes at 60°C for A) Liposome **14** and B) PM **15**.

#### 4.5.3 $^{68}\text{Ga}$ radiolabelling of liposomes **14** and polymeric micelles **15** in sodium acetate

To optimise the radiochemical reactions and increase  $^{68}\text{Ga}$  incorporation for the liposomes and polymeric micelles, the reactions were repeated in sodium acetate (NaOAc, 0.2 M, pH5) and incubation with dry  $^{68}\text{GaCl}_3$  (50 MBq) at room temperature or 60°C for 15 minutes.

The liposomes **14**, have a very low  $^{68}\text{Ga}$  incorporation at both temperatures, see Figure 79. The polymeric micelles **15**, seems to be more efficiently radiolabelled with  $^{68}\text{Ga}$  under these conditions. At room temperature, the radiochemical yield was 30%; however, increasing the reaction temperature increases the RCY to 50%.

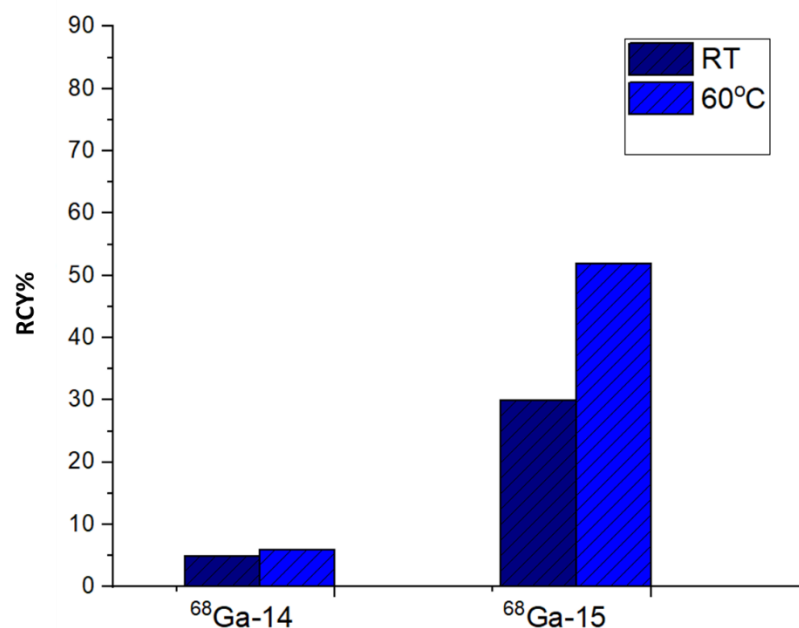


Figure 79: Radio-TLC of <sup>68</sup>Ga radiolabelled (50 MBq) **14** and **15** in sodium acetate buffer (pH 5) at RT and 60°C for 15 minutes.

#### 4.5.4 <sup>68</sup>Ga radiolabelling liposomes and polymeric micelles in sodium acetate at 250 MBq

The aims of improving the radiolabelling yields of liposomes and polymeric micelles with gallium-68 to over 90% were continued by changing the radiolabelling parameters. In the next set of experiments, the activity of dry <sup>68</sup>GaCl<sub>3</sub> was increased to 250 MBq instead of the 50 MBq used in previous methods.

By increasing the amount of radioactivity, the radiochemical efficiency was increased significantly for both liposomes **14** and polymeric micelles **15**, see Figure 80.

Using a higher amount of radioactivity in the presence of acetate buffer causes a consistent increase in percentage incorporation of <sup>68</sup>Ga, the radiochemical efficiencies were > 90% for both nanocarriers.

On comparison with the De Barros publications for radiolabelling the same liposomes and micelles with technetium-99m. These constructs had been successfully labelled with technetium-99m in a radiochemical yield of > 90%<sup>61, 209, 211</sup>, and the stability of these nanoparticles was then studied in human serum. As another comparison,

Helbok *at al.* radiolabelled liposomes with a range of different radiometals and all formulations showed high RCY. In case of  $^{68}\text{Ga}$ , the liposomes were incubated in sodium acetate buffer for 30 minutes at room temperature to give RCY of >95% that is comparable to the shorter reaction time used in this work (15 minutes).<sup>222</sup>

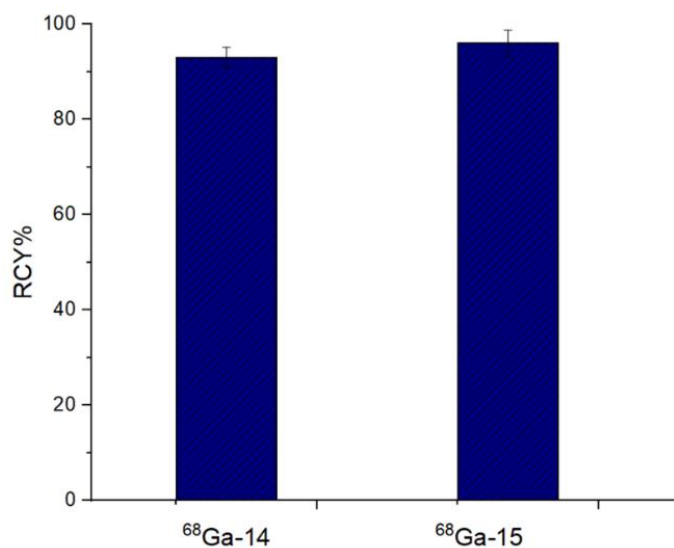


Figure 80: Radio-TLC of  $^{68}\text{Ga}$ -radiolabelled **14** and **15** with 250 MBq of activity in sodium acetate buffer, pH 5 at 60°C for 15 minutes (n=2).

#### 4.5.5 Radiolabelled stability test for liposomes 14 and polymeric micelles 15.

The stability test examines the strength of attachment between the nanocarriers and PET radioisotope  $^{68}\text{Ga}$ . The two nanocarriers radiolabelled with  $^{68}\text{Ga}$  at  $60^\circ\text{C}$  for 15 minutes were studied for stability under conditions relevant to *in vivo* applications.

The human blood contains different proteins, with many of these present in human serum including transferrin that has previously been used for stability studies. As mentioned in chapter 3, transferrin can bind with gallium(III) that has similar ionic radius for iron(III) as a result, the free gallium expected to be treated as iron and form a complex with *apo*-transferrin in blood plasma.<sup>233</sup> Serum was used in this case for consistency with the studies published by De Barros.

Human serum was used to investigate the release of gallium-68 from liposomes and micelles under physiological conditions. Following the same procedure for the stability test that was carried out in chapter 3, the solutions containing  $^{68}\text{Ga}$ -14 and  $^{68}\text{Ga}$ -15 (250  $\mu\text{l}$ ) in saline were incubated in human serum (100  $\mu\text{l}$ ) at  $37^\circ\text{C}$  for 1 hour with constant shaking. The samples were then analysed by radio-TLC at 5, 15, 30, 45 and 60 minutes.

In the serum stability test, both radiolabelled nanocarriers showed some slow transchelation during the incubation time. There was a little loss of activity during the time-period, and very clearly with polymeric micelles. In the case of the liposomes sample  $^{68}\text{Ga}$ -14, around 20% of free gallium-68 was observed for this sample after 60 minutes, for the polymeric micelles  $^{68}\text{Ga}$ -15 higher radiolabelling stability was observed, losing only 10% of the attached radioisotope, see Figure 81.

In the De Barros research for radiolabelling the same polymeric micelles with technetium-99m, the PM were incubated in saline for 24 hours and show a high stability. Furthermore, the particles exhibited a high stability in mouse plasma up to 8 hours, but a reduction of 20% was observed after 24 hours incubation.<sup>209</sup>

For the previously mentioned study by Grotz *et al.* for encapsulating liposomes with RIF and successful radiolabelling with technetium-99m, the stability in serum showed no release of  $^{99\text{m}}\text{Tc}$  occurs even after 24 hours incubation.<sup>224</sup> In the Helbok

study, the nanocarriers were stability tested against transchelation using DTPA, histidine and further stability in PBS (pH 7.4) and human serum for 24 hours at 37°C.  $^{111}\text{In}$ -NPs have stability of >80%, and  $^{99\text{m}}\text{Tc}$ -NPs have stability of >85% for. However, there was no data presented for gallium-68.<sup>222</sup>

Many researchers have discussed why PET imaging with radiolabelled liposomes and micelles has been studied less frequently in comparison to SPECT imaging. Torres de Rosales<sup>234</sup> and Van der Gees<sup>235</sup> in separate reviews explained that the half-life of PET isotopes could limit the duration of *in vivo* experiments with PET imaging. For example, liposomes were radiolabelled with  $^{18}\text{F}$  and  $^{68}\text{Ga}$  and showed stable radiolabel retention *in vivo* and accumulated in tumour lesions.<sup>222, 236</sup> However, the biological half-life for PEGylated liposomes can be between 24-48 hours, and these radionuclides have shorter half-lives with 110 and 68 minutes, and so the images at an earlier time point may not reflect the actual fate of these particles in the body. Therefore, nanocarriers could be radiolabelled with longer half-life PET radionuclides such as  $^{64}\text{Cu}$  and  $^{89}\text{Zr}$  with half-lives of 12.7 and 78.4 hours, respectively.

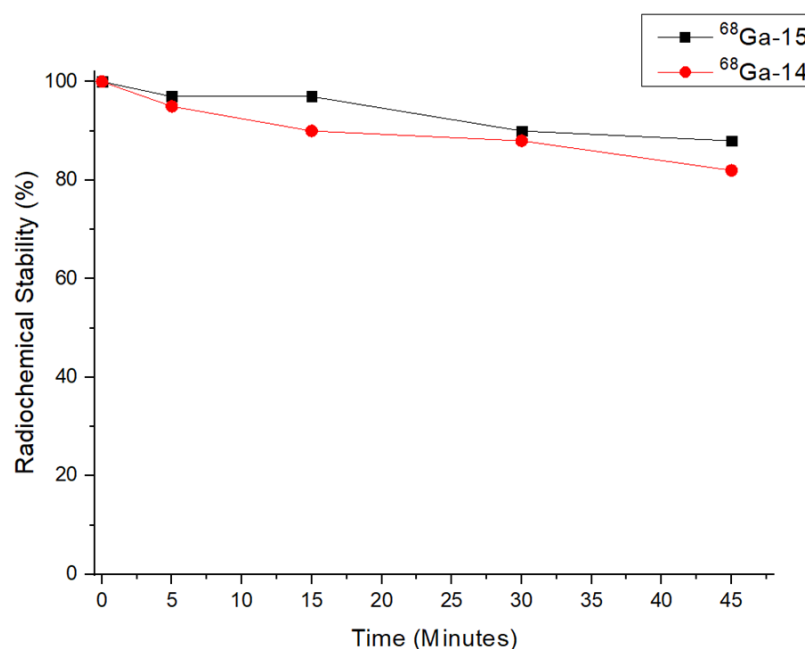


Figure 81: Plot of radio-TLC stability measurements for  $^{68}\text{Ga-14}$  and  $^{68}\text{Ga-15}$  incubated in serum after 5, 15, 30 and 45 minutes.

#### 4.5.6 Size distribution stability of $^{68}\text{Ga}$ -liposomes **14** and $^{68}\text{Ga}$ -polymeric micelles **15**.

The diameter for liposomes and micelles from the DLS measurements showed that these vesicles have a very narrow size distribution around 131 nm for liposomes **14** and 13 nm for polymeric micelles **15** which is agreement with the published work by De Barros that used the same nanocarriers and radiolabelled them with  $^{99\text{m}}\text{Tc}$ .<sup>61, 209</sup>

The DLS also can be used to determine the stability of nanoparticles after exposure to radiation and different reaction conditions. The hydrodynamic sizes of liposomes and micelles were measured after decay of gallium isotope. Figure 82, shows that the size distribution of liposomes **14** and polymeric micelles **15** was not greatly affected by radiation and labelling conditions. In the case of **15**, there was no effect on the average hydrodynamic size with the measured average was 14 nm compared to 13 nm before  $^{68}\text{Ga}$  radiation. However, the liposomes nanocarriers showed some size decrease from 131 nm to 113 nm after radiation, potentially due to effects on the PEG layer entanglement.

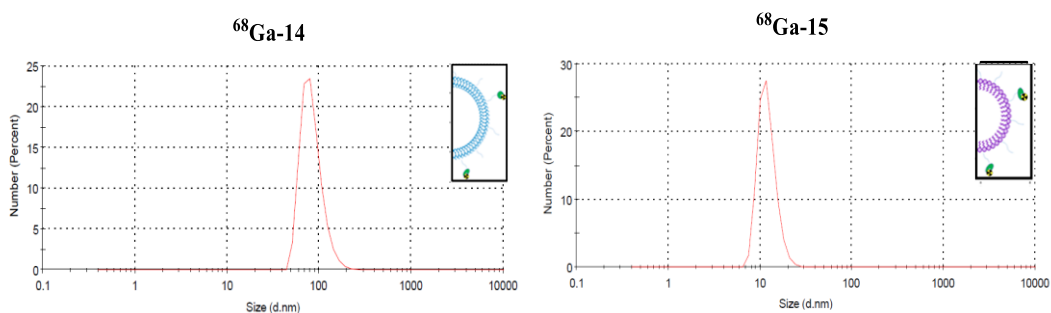


Figure 82: DLS analysis of the hydrodynamic sizes of  $^{68}\text{Ga}$ -radiolabelled **14** and **15**.

## 4.6 *In vivo* studies of $^{68}\text{Ga}$ radiolabelled liposomes and micelles

The development of nanocarriers for cancer therapy depends on their *in vivo* behaviour and this can be detected by non-invasive imaging techniques that allow for visualise, quantify and monitor their biodistribution over the time and can provide information regarding drug release. A number of imaging techniques are available to image nanocarriers *in vivo*, these techniques have different advantages and disadvantages for tracking these type of nanoparticles. Radiolabelling compounds with PET or SPECT radioisotopes can be used to non-invasively track nanoparticles. However, PET has higher sensitivity and spatial resolution when compared to SPECT and also allows effective dynamic imaging.<sup>234</sup>

De Barros and his group have radiolabelled liposomes and polymeric micelles with SPECT radioisotope technetium-99m and conducted *in vivo* SPECT imaging studies. In this work, similar batches of liposomes and polymeric micelles prepared by De Barros's group will be studied *in vivo* with PET isotope  $^{68}\text{Ga}$  to allow dynamic PET scanning and comparison with published results for  $^{99\text{m}}\text{Tc}$  radiolabelled nanocarriers.<sup>61, 209</sup> The results from radiolabelling liposomes and micelles and their stability under serum challenge were appropriate to continue to *in vivo* studies. Imaging biodistribution using dynamic scans provides information about the fate of nanoparticles when injected to the body

The radiolabelled liposomes and polymeric micelles with PET isotope gallium-68 were used for *in vivo* studies. Healthy female mice were anaesthetised and injected into the tail vein with  $^{68}\text{Ga}$ -14 and  $^{68}\text{Ga}$ -15 and the animals were imaged using a preclinical PET/CT scanner to track the nanocarriers biodistribution. All of the animal imaging experiments were carried out accordance to the United Kingdom guidance. PET imaging data were acquired on Sedecal Super Argus 2R PET scanner in two bed positions and CT scan was performed following each PET scan to show anatomical co-registration.

Radiolabelled liposomes  $^{68}\text{Ga}$ -**14** were injected to two animals (6.49 MBq, 13.8 g) and (6.62 MBq, 15.5 g) and dynamic PET scan were applied for 66 minutes, see Figure 83.

The dynamic PET/CT scan images showed a high liver and spleen uptake from the beginning of the scan and throughout the experiments as expected. These results might be due to the macrophages in reticuloendothelial system (RES), and means that the formulations have a short circulation time. Furthermore, no renal clearance via kidneys and bladder was observed due to the large size of liposomes with a diameter of 113 nm.

The biodistribution studies for DTPA-liposomes radiolabelled with gallium-68 in Helbok's work were carried out using PET/MRI scanner and showed similar results to the data in this research. The radiolabelled solution was injected intravenously into Lewis rat, and the activity was observed in liver, spleen also in heart and lungs.<sup>222</sup>

DSPE-PEGylated liposomes loaded with maghemite nanoparticles were used as PET/MRI imaging agents. Malinge *et al.* used these NPs and functionalised their surface with glucose targeting moiety and radiolabelled with  $^{68}\text{Ga}$ -NODAGA under several conditions. The RCY was 70% when temperature was raised to 80°C. The radiolabelled liposomes were injected through the retro-orbital sinus of U87MG tumour-bearing mice. PET images showed high liver uptake with accumulation at tumour sites.<sup>237</sup>

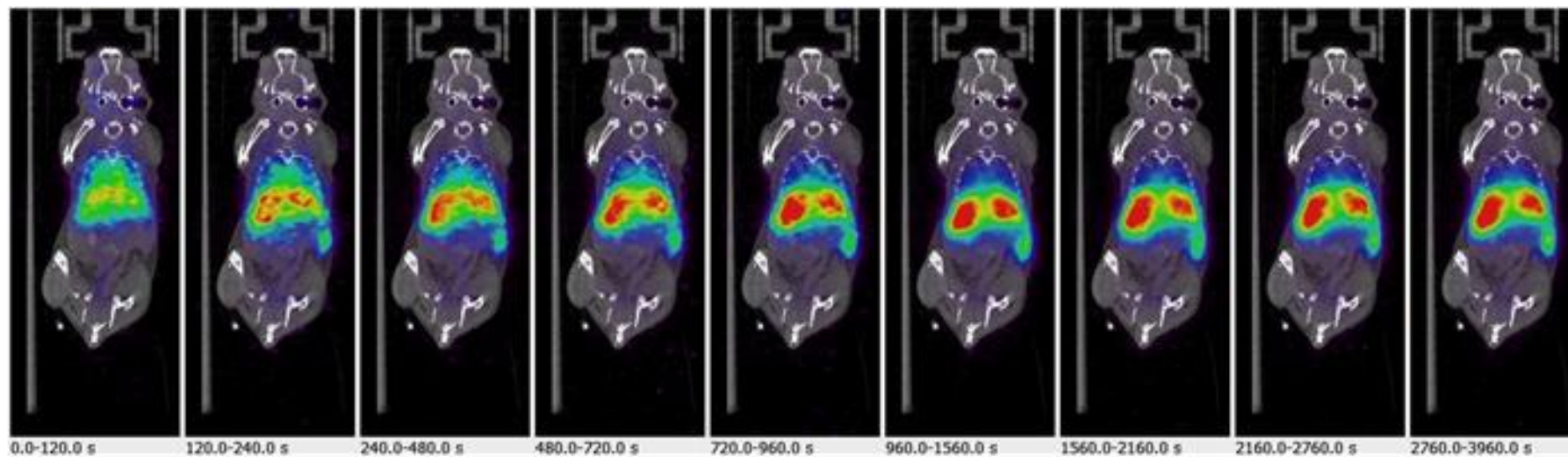


Figure 83: Dynamic PET/CT scan for gallium radiolabelling liposomes  $^{68}\text{Ga}$ -14 from 0 to 66 minutes.

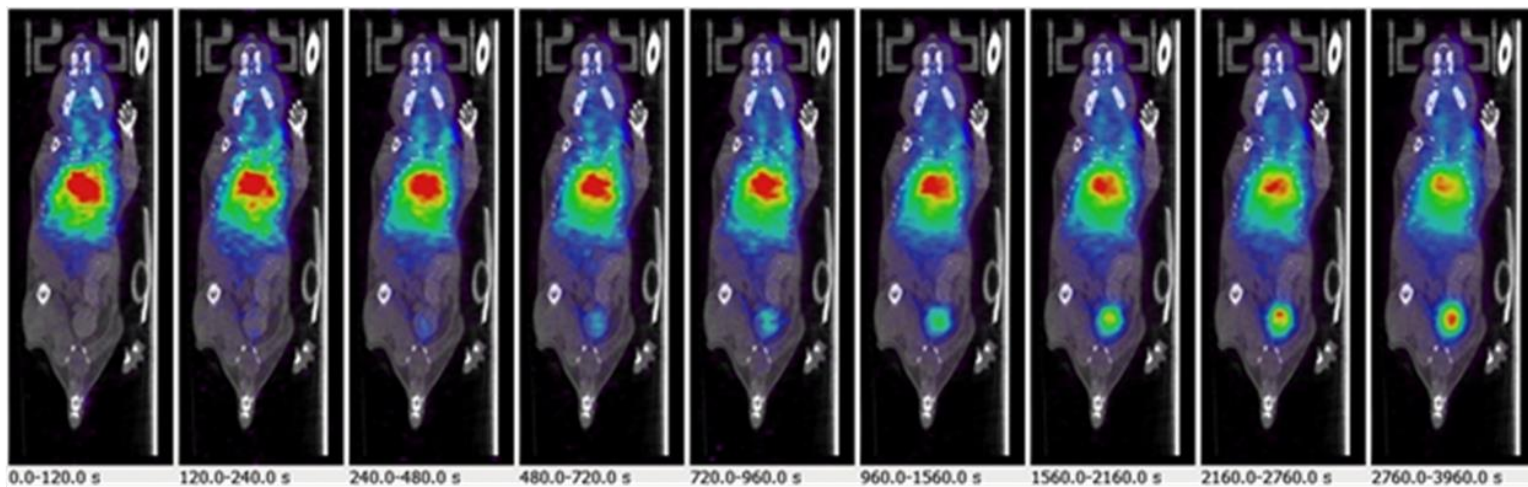
The radiolabelled polymeric micelles  $^{68}\text{Ga-15}$  were injected intravenously into healthy mice (9.79 MBq, 17.9 g) and (8.08 MBq, 17.9 g) and dynamic PET/CT scans were acquired for 66 minutes. Another time point was investigated using static PET/CT scan on animals with (6.18 MBq, 14.0 g) and (6.3 MBq, 15.5 g) to study the fate of  $^{68}\text{Ga}$ -radiolabelled polymeric micelles after 4 hours post injection. Figure 84A, presents the dynamic PET scans obtained for the tracer  $^{68}\text{Ga-15}$  after 66 minutes. The images show that between 0-66 minutes the tracer starts to accumulate in the lungs, trachea and probably in the heart and liver. Between 12-16 minutes the tracer starts to appear in bladder, and at the end of the scan the tracer remained in these places. The  $^{68}\text{Ga-15}$  showed lower uptake and retention in the liver than  $^{68}\text{Ga-14}$ .

On comparison with the De Barros work, similar polymeric micelles were radiolabelled with technetium-99m, and 3.7 MBq of  $^{99\text{m}}\text{Tc-DTPA-PM}$  were injected intravenously to healthy and tumour-bearing mice. The *in vivo* SPECT images were taken after 1, 4, 8 and 24 hours post-injection. The images showed a high uptake in liver, spleen and kidney with accumulation at the tumour site over time through tumour to muscle ratio measurements.<sup>209</sup>

After 4 hours post injection, the radiolabelled polymeric micelles do not appear to be intact, see Figure 84 B. The radioisotope seems to be distributed in the whole animal body which may indicate that gallium-68 has been detached from the functionalised nanoparticles and transchelation with animal serum occurred. This could indicate that the PM is no longer present and has been metabolised *in vivo*, however, this result is not consistent with the previous study and so it may be more likely that the gallium-68 has been released. Although, this is not consistent with the observed serum stability.

These results may indicate that these nanocarriers are more suitable for radiolabelling with SPECT radioisotopes or. Alternatively different chelators or the longer half-life PET isotopes may be a good choice for radiolabelling these types of nanoparticle.<sup>234, 235</sup> Further experiments are necessary to determine the identity of the gallium-68 species are for the radiolabelled PM. This could be carried out by dissection, extraction and analysis using radio-TLC and /or radio-HPLC to determine the identity of the gallium-68 species and whether it remains bound to the chelator.

A)



B)

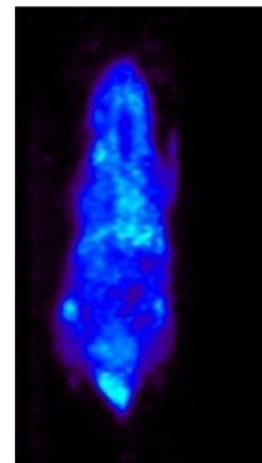


Figure 84: PET/CT scan for gallium radiolabelling polymeric micelles  $^{68}\text{Ga}$ -15 A) dynamic scan from 0 66 min, B) static scan after four hours (30 min acquisition).

## 4.7 Conclusions

This chapter describes the radiolabelled nanocarriers investigated to evaluate liposomes and micelles as a potential platform for drug delivery. Two types of nanocarriers that have been designed with PEG and DTPA chelators on the surface of nanoparticles were investigated, liposomes and polymeric micelles. The samples were characterised with DLS to ensure that they were suitable for *in vivo* studies.

This was followed up by  $^{68}\text{Ga}$  radiolabelling of functionalised liposomes and polymeric micelles. The radiochemical labelling conditions were optimised to increase the radiochemical efficiency. The radiolabelled nanocarriers showed efficient radiolabelling in presence of sodium acetate buffer (pH5) at 60°C for 15 minutes.

The radiolabelled nanocarriers were then taken for further investigation towards *in vivo* use, with serum stability testing. The  $^{68}\text{Ga}$ -**14** and  $^{68}\text{Ga}$ -**15** showed a loss of around 20% of their activity during 60 minutes. The size and size distribution were analysed after radiolabelling the nanocarriers with gallium-68 and found to still be within the preferred range for clinical application. There was no significant change in the hydrodynamic sizes for either sample.

The *in vivo* studies were carried out for both radiolabelled liposomes  $^{68}\text{Ga}$ -**14** and polymeric micelles  $^{68}\text{Ga}$ -**15** to track their biodistribution and fate in healthy animals. As expected, a high liver uptake was noted in  $^{68}\text{Ga}$ -**14** due to the macrophages in reticuloendothelial system the RES.  $^{68}\text{Ga}$ -**15** showed uptake in heart, lungs and some accumulation in the liver. There does appear to be an issue with stability for  $^{68}\text{Ga}$ -**15** and further investigation is required to determine whether the gallium-68 has detached from the chelator or the polymeric micelle is no longer intact.

# **Chapter 5**

## **Conclusion and future directions**

## 5 Chapter five: conclusion and future directions

### 5.1 Conclusion

This work highlights the development of radiolabeling methodologies for different nanoparticles with potential use as diagnostic agents or for *in vivo* tracking. There is an excellent synergy between the nanomaterials and nuclear imaging to form a powerful combination to generate multifunctional biomedical platforms that can impact imaging and therapy in the next generation of precision medicine tools.

Three types of biocompatible nanoparticles were explored in this work. Iron oxide nanoparticles, liposomes and polymeric micelles have been investigated and radiolabeled with different radioisotopes to potentially allow SPECT or PET imaging. The first material studied utilised magnetic nanoparticles iron oxide (SPIONs) as imaging and targeting agents. Chapters 2 and 3 focused on the advantages of these nanoparticles as dual modalities agents that could also be modified for potential targeting of the chemokine receptor CXCR4. Chapter 4 dealt with nanocarriers, liposomes and polymeric micelles, as potential theranostic agents.

The first aim of this work was the direct radiolabelling of chelator-free superparamagnetic iron oxide nanoparticles (SPIONs) with various coating materials that could potentially be used as SPECT/MRI imaging agents. Different synthetic procedures and coatings were explored. Firstly, the co-precipitation method was followed to synthesise the SPIONs core, with several parameters varied, including synthesis time, stirring rate and the addition time of the precipitant. As expected, all of these factors influenced the nanoparticle size. For example, a high stirring rate and slow addition of ammonia over one hour decreased the hydrodynamic size of the nanoparticles. A siloxane derivative was used for coating the core to produce a colloidal suspension with a diameter of *ca.* 100 nm. Following on from this, the polyol method was used for the synthesis and coating of the SPIONs with polyacrylic acid. The hydrodynamic size for these particles was 58 nm.

The purification method has major impact on the stability of the resulting iron oxide nanoparticles. Combining the magnetic separation and centrifugation with different

speeds increased the hydrophilicity of the resulting sample and hence the colloidal stability. The SPIONs were characterised with several analytical techniques including DLS, PXRD, FT-IR, ICP-EOS, TEM and C,H,N analysis. The relaxivity properties of the synthesised SPIONs were investigated. Both types of nanoparticles showed high transverse relaxation rates which indicates that the coating layers did not adversely affect the magnetic properties of the SPIONs core.

The second part of chapter 2 describes the development of novel methods for radiolabeling chelator-free SPIONs with the SPECT isotope technetium-99m.

In order to optimise the radiolabeling conditions, a series of reactions were carried out. Initially, the effect of the concentration of the SPIONs was studied. It showed high loading capacity at increasing concentrations of nanoparticles. Several reaction parameters, including temperature, type of buffer and pH, were investigated for technetium-99m radiolabelling of SPIONs and also how the coating can impact on the stability of the radiolabelled nanoparticles. Increasing the reaction temperature was shown to increase the radiolabelling yields in both the presence of saline and other buffers (PBS and sodium acetate). The pH also affected the radiolabelling yields; it was found that decreasing the pH of sodium acetate buffer increased the radiolabelling yield for both samples.

The  $^{99m}\text{Tc}$ -SPIONs showed high stability in a competition challenge, which indicates strong attachment between the SPIONs surface and technetium-99m. EDTA, variation of pH and different serum proteins were used for these experiments. The siloxane@SPIONs showed high stability against transferrin and bovine serum albumin over 48 hours, while the PAA@SPIONs release a high % of bound technetium-99m over a 24 hour period.

In chapter 3, the synthesis of CXCR4 antagonist conjugated SPIONs was carried out in an attempt to target the CXCR4 chemokine receptor that is overexpressed on the surface of various cancer cells. The CB cyclam tetraazamacrocycle was selected for SPIONs functionalisation. In order to form the targeting agent based on iron oxide nanoparticles, CB cyclam was attached to SPIONs using a siloxane derivative GPTES

as a linker to facilitate the attachment. This step forms a hydrophilic polymeric layer on the SPIONs surface to give colloidal stability nanoparticles.

The SPIONs functionalised with CB cyclam were characterised by various analytical techniques. The hydrodynamic size for this construct was 121 nm. Then metal complexes of the tetraazamacrocycles with copper(II), nickel(II) and zinc(II) were formed to further activate this component for CXCR4 binding. The average hydrodynamic sizes for these antagonist functionalised nanoparticles were between 158-165 nm. The aim of using a mono-macrocycle was to increase affinity of the nanoparticle construct using multivalency interactions.

The novelty of this part is the development of  $^{68}\text{Ga}$ -labelled SPIONs that are functionalised for CXCR4-targeting. The constructs were successfully radiolabelled with gallium-68 and show efficient  $^{68}\text{Ga}$  labelling characteristics. The optimum reaction parameters were at 50°C for 15 minutes in ammonium acetate at pH 5. The radiochemical stability of the  $^{68}\text{Ga}$ -labelled CXCR4-targeted SPIONs were tested against apo-transferrin, this showed that >85% of gallium remained bound to the nanoparticles surface after challenge. However, *in vitro* validation requires further investigation as there was an issue with nanoparticle precipitation in the cell growth media.

In chapter 4, the radiolabeling of a different class of nanoparticle was investigated, these are nanocarriers based on liposomes and polymeric micelles to allow evaluation of them as potential platforms for drug delivery. The nanocarriers were functionalized with PEG and DTPA as the radioisotope chelator. The samples were characterised with DLS and have average diameters of 131 nm for liposomes and 9.6 nm for polymeric micelles.

A series of radiochemical reactions were carried out to optimise the radiolabelling efficiencies. The first parameter investigated was the temperature, and the nanocarriers did not show any radiolabelling in saline at room temperature. However, after heating the reaction to 60°C, some enhancement of the radiolabelling was observed. Similar results were observed in ammonium acetate buffer at pH 5.

Several reactions were investigated to increase the radiolabelling yields. One change was to increase the amount of gallium-68 radioactivity (250 MBq). Under these conditions, complete radiolabelling of nanocarriers was achieved. The two types of nanocarrier were therefore taken on to further study to determine if the characteristics were appropriate for *in vivo* applications and to assess their stability under competition challenge. The  $^{68}\text{Ga}$ -DTPA and  $^{68}\text{Ga}$ -DTPA-PM showed a loss around 20% of their activity during 60 minutes incubation.

The radiolabelled constructs were investigated *in vivo* in wild type (non-tumour bearing) animals using dynamic scans which showed rapid location into organs indicating a short circulation time. The polymeric micelles showed a change in the biodistribution of the radiolabel after 4 hours and further investigation is required to determine if this is due to metabolism of the PM or release of the radioisotope from the intact PM.

## **5.1 Future directions**

Following on from the presented research, there is a scope for further developments of nanoparticles as nuclear imaging agents. Some of these future directions and the potential for further studies are summarised.

### **5.1.1 Radiolabeling of chelator-free SPIONs**

The synthesis of chelator-free SPIONs as a potential platform for SPECT/MRI dual-imaging agent in this work has been achieved. High radiochemical yields of incorporated technetium-99m to SPIONs with two different coatings were carried out. Siloxane coated SPIONs showed a high stability under challenge by proteins and it would be appropriate to continue to *in vivo* studies. However, some serum instability has been observed for the labelled SPIONs coated with polyacrylic acid. Further optimisation is required for these nanoparticles to enhance the stability in physiological environment by changing the radiolabeling conditions. When this is completed, an initial *in vivo* study would be carried out for each of the samples to determine biodistribution of the radiolabelled NPs.

The SPIONs could also be radiolabelled with other radionuclides including copper-64 (half-life of 12.7 hours) and yttrium-86 (half-life of 14.7 hours) for PET imaging, and with indium-111 (half-life of 2.8 days) as SPECT imaging agent. The SPIONs could potentially be used for radioisotope therapy after radiolabeling their surface with a beta-emitter such as yttrium-90 (half-life of 2.6 days) or lutetium-177 (half-life of 6.7 days).

The size and the shape of nanoparticles may have an impact for many applications. Several studies reported that the  $T_2$  relaxivity of magnetic nanoparticles can be increased by tuning the effective magnetic core radius through morphology control.<sup>238</sup> The Archibald group previously prepared iron oxide nanorods for dual modalities PET/MR imaging, the rods coated with siloxane derivative showed improvement in the  $T_2$  relaxivities and, as with this work, the chelator was not required to form a highly stable  $^{68}\text{Ga}$  radiolabelled nanorods.<sup>19</sup> Therefore, different shapes of iron oxide nanomaterials could influence the properties such as relaxivity and radiolabelling with radionuclides. Synthesis of nanomaterials with different morphology such as rods and octapod shapes could be used to develop new SPECT or PET/MR imaging agents with optimal properties.

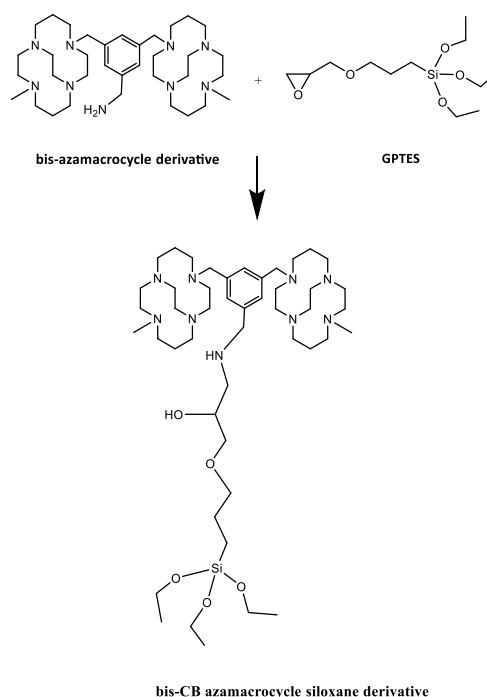
### **5.1.2 CXCR4-targeted SPIONs**

The functionalised iron oxide nanoparticles with CB cyclam and its metal complexes for targeting CXCR4 receptor were successfully radiolabeled with gallium-68. However, the colloidal stability for these constructs needs further optimization. This can be solved by reducing the size diameter for the nanoparticles by employing other synthetic procedure such as polyol or hydrothermal method that are known to form ultrasmall iron oxide nanoparticles.

The SPIONs coated with the macrocycle siloxane can be combined in a coating with a hydrophilic siloxane derivative such as PEG siloxane in order to increase their hydrophilicity. Different ratios of macrocycle to PEG could be examined to determine the optimised formulation for colloidal stability in order to form stable  $^{68}\text{Ga}$  complexes. Once the challenge of colloidal stability has been overcome and *in vitro* affinity has been assessed, then *in vivo* biodistribution can be carried out.

It would be interesting to examine the conjugation of iron oxide nanoparticles with bis-macrocycles that are also configurationally restricted with an ethylene bridged which forms either cross or side-bridged macrocycles. The Archibald group has previously reported a series of cross-bridged bis-tetraazamacrocycles metal complexes antagonists that bind with high affinity to CXCR4.<sup>196</sup>

These complexes showed higher affinity toward the receptors compared to mono-tetraazamacrocycles which can suffer from non-specific binding due to the single coordination bond interaction with the protein, although it was hoped that multivalent interactions would overcome this. Therefore, functionalising the surface of SPIONs with bis-macrocycles may be more effective for CXCR4 recognition. This could be achieved through functionalising the SPIONs surface with CB or SB bis-tetraazamacrocycles in presence of GPTES as a linker. The attachment of GPTES could be either to the primary amine in the macrocycle or through the xylyl group in the *meta* position. Furthermore, metal complex formation for these macrocycles with copper(II), zinc(II) and Ni(II) offers high affinity antagonists for the CXCR4 receptor as with the monomacrocyclic derivatives, see Scheme 12. The range of radioisotopes used in the radiolabeling of the mesoporous silica shell could then also be extended.



Scheme 12: Schematic representative showing the conjugation of CB bis-tetraazamacrocycle unit with GPTES in order to functionalise the SPIONs surface.

### 5.1.3 Radiolabeling of liposomes and polymeric micelles

The work presented in chapter 4 shows the potential application of nanocarriers including liposomes and polymeric micelles as nanotheranostic probes. The nanoparticles were radiolabelled with gallium-68 and the conditions were optimised. However, the *in vivo* biodistribution needs further modification. This could be achieved through different approaches. For example, macrocycles such as DOTA and NOTA derivatives can be attached to the liposomes or micelles to stabilize gallium-68 instead of the acyclic chelator DTPA, or an optimized acyclic chelator for gallium(III) such as a tris(hydroxypyridinone) chelator.

Longer half-life radionuclides such as copper-64, zirconium-89 or indium-111 could be used for radiolabeling these types of nanoparticles to determine the *in vivo* biodistribution over a longer time course. Once this has been successfully carried out, utilisation of nanocarriers and their efficient encapsulation to anti-cancer drug doxorubicin can be explored as drug delivery system using PET. SPIONs can also potentially be entrapped inside the cavity of the constructs for multimodality imaging.

# **Chapter 6**

## **Experimental**

## 6 Chapter six: Experimental

### 6.1 General methodologies

All reactions were performed at room temperature and under nitrogen atmosphere unless otherwise stated. Solvents were generally used as received, although in some reactions dried solvents were required. Acetonitrile (MeCN), methanol (MeOH) and ethanol (EtOH) were dried over 3 Å molecular sieves (dried at 200°C, 12 h) and degassed under an argon atmosphere.

Solvents were removed under reduced pressure by rotary evaporation on a Buchi RE 11 evaporator equipped with a diaphragm vacuum pump, if further drying was required before analysis, this was carried out by using a Schlenk line and oil vacuum pump.

Samples were filtered using syringe filters with a 33 mm diameter sterile syringe filter with a 0.22, 0.45 or 1 µm pore size hydrophilic cellulose membrane.

Samples that required spin filtration were filtered using Vivaspin 500 centrifugal concentration (MWCO 100 kDa).

Relaxivity measurements  $T_1/T_2$  were carried out using 1.4 T Oxford bench NMR machine, or using the 3 T clinical MR scanner (carried out by Dr Peter Gibbs and Dr Martin Pickles) at Hull Royal Infirmary Hospital.

Optical emission ICP was carried out by Dr Bob Knight and Michael Thompson. The elemental analysis (C, H and N) were carried out by Carol Kennedy and the TEM microscopy was carried out by Ann Lowry.

### 6.2 Materials

All chemicals and solvents used in this report were purchased from Sigma Aldrich, Alfa Aesar, Fisher Scientific Ltd, Acros, ABCR, TCI and VWR International and were either laboratory or analytical grade. Chemicals were used without further purification. Agarose (molecular biology grade) and x5 6x DNA loading dye were

provided by Fisher Scientific, the InstaBlue protein stain was purchased from Expedeon. The proteins used in this work (*apo*- transferrin and bovine serum albumin) were purchased from Sigma-Aldrich.

DTPA-PEGylated liposomes and polymeric micelles (1,2-distearoyl-Sn-glycero-3-phosphoethanolamine)-*N*-[methoxy (polyethylene glycol)-2000] were provided by Professor Andre' de Barros from Federal University of Minas Gerais, Brazil.

## **6.3 Instrumentation**

### **6.3.1 NMR spectroscopy**

<sup>1</sup>H NMR and <sup>13</sup>C NMR were recorded on a Jeol JNMLA400 spectrometer at 400 and 101 MHz, respectively. All NMR spectra were referenced to non-deuterated solvents or against an internal standard TMS signal. The chemical shifts ( $\delta$ ) were recorded in parts per million (ppm) and the splitting patterns are designated as s (singlet), d (doublet), t (triplet), q (quartet), quin (quintet), m (multiplet), dt (double triplet) and br (broad). The NMR spectra were processed using MestrReNova software (Mestrelab Research, version 6.0.2-2575).

### **6.3.2 MRI phantom images**

Magnetic resonance imaging was carried out using a clinical 3 T horizontal MR scanner (GE Signa™) at Hull Royal Infirmary Hospital.

### **6.3.3 Mass Spectrometry (MS)**

Low-resolution mass spectrometry data were recorded using a Varian 500 ion trap mass spectrometry system, a Finnegan MAT 900 XLT mass spectrometer or an Advion, Expression compact Mass Spectrometer. The samples were diluted with methanol before direct injection.

#### **6.3.4 CHN elemental analysis**

The elemental analysis to measure the carbon, hydrogen and nitrogen content was performed using an elemental analyser (CE Instruments 1108 CHN, UK). The sample results were measured as weight percentages.

#### **6.3.5 ICP-OES analysis**

ICP-OES analysis (Inductively Coupled Optical Emission Spectroscopy) was performed using a Perkin Elmer Optima 5300DV. The freeze dried powder samples were digested by nitric acid, other samples containing silica needed a mixture of hydrofluoric acid and nitric acid in 1:3 ratio.

#### **6.3.6 DLS and zeta potential**

Dynamic light scattering (DLS) was used to determine the size distribution and zeta potential with Zeta Nanosizer (Malvern instruments, ZEN3600, UK) at 25°C using 0.1 mM concentration of nanoparticles.

#### **6.3.7 TEM and EDX analysis**

For transmission electron microscopy (TEM) and energy dispersive x-ray (EDX), the diluted samples in ethanol were collected on carbon –coated copper grid and allowed to dry in air. The images were obtained using a Gatan US4000 digital camera (Gatan UK, Abingdon, Oxford) mounted onto a JEOL 2010 transmission electron microscope (Jeol UK) running at 200 kV.

#### **6.3.8 PXRD analysis**

Powder X-ray Diffraction (PXRD) patterns was collected using a Bruker D5000 diffractometer with Cu K $\alpha$  radiation.

#### **6.3.9 FT-IR spectroscopy**

FT-IR spectra were measured using a Fourier transform infra-red spectrometer, Perkin Elmer 20 (model Spectrum RXI).

### 6.3.10 UV-Vis spectroscopy

To determine iron concentrations in samples, the UV-Vis spectra were acquired using a Lambda Bio 10 UV/Vs spectrometer (Perkin Elmer, UK).

### 6.3.11 Hot cell (PET centre)

The radiochemical reactions were carried out in a lead shielded hot cell (Aquila, UK) equipped with a camera and Capintec CRC-55tPET dose calibrator (Capintec, New Jersey, USA), to measure the amount of radioactivity present in a given volume of radioactive materials.

### 6.3.12 Elution for $^{99}\text{Mo}/^{99\text{m}}\text{Tc}$ generator

The production of  $^{99\text{m}}\text{Tc}$  was carried out from an UltraTechnekow FM generator (Cyrium Medical Cat. No. DRN 4329), the generator contains the parent isotope molybdenum-99 that absorbed on a stationary phase of aluminium oxide column. A desired volume (3-5 ml) of  $^{99\text{m}}\text{TcO}_4^-$  from the generator was collected in sterile saline (0.9% w/v NaCl) to elute sodium pertechnetate. The elution procedure was performed in accordance with the University of Hull's standard operating procedure, "Elution of the  $^{99\text{m}}\text{Tc}$  generator and preparation of  $^{99\text{m}}\text{Tc(V)}$ ".

### 6.3.13 Preparation of $^{68}\text{Ga}$

$^{68}\text{Ga}$  was eluted as  $^{68}\text{GaCl}_3$  from 1100 MBq  $^{68}\text{Ge}/^{68}\text{Ga}$  generator (iThemba LABS, Somerset West, South Africa and distributed by IDB Holland, Baarle- Nassau, The Netherlands) by using HCl (0.6 N, 4 ml). The activity was transferred to hot cell and diluted with water to obtain HCl concentration of 0.1 N. the  $^{68}\text{Ga}$  solution was trapped on a solid phase extraction cartridge (Strata-X-C 33  $\mu\text{m}$ , Phenomenex, Cheshire, UK) followed by addition of a released solution contains of (acetone/water). The solvent was removed by heating to 90°C for few minutes. The elution procedure was performed in accordance with the University of Hull's standard operating procedure, SOP\_CHC\_007: "Elution of the iThemba  $^{68}\text{Ga}$  Generator".

### **6.3.14 Radio- TLC scanner**

Radiochemical reactions were monitored by thin layer chromatography, which were run on silica gel 60 F254 on aluminium sheets (Merck USA), and the samples were eluted with saline or sodium citrate, then read using the LabLogic Scan-Ram and Laura software (version 4.1.7.70). The procedure was performed in accordance with the University of Hull's standard operating procedure, SOP\_CHC\_004 "Use of High Performance Liquid Chromatography (HPLC) and Thin Layer Chromatography Systems".

### **6.3.15 Gamma counter**

The gel containing  $^{99m}\text{Tc}$ -SPIONs (60  $\mu\text{l}$ , 1.3 MBq of  $^{99m}\text{Tc}$  solution) that was incubated with proteins was sliced and put in tubes followed by measuring the activity by using a gamma counter, Automated Gamma Counter (Wizard 3 Wallac, UK)

### **6.3.16 PET/CT scanning**

The PET/CT imaging studies were carried out by Dr Chris Cawthorne, and the data processing were carried out by Dr Isaline Renard with contribution from Dr James Thompson.

All animal procedures were approved by the University of Hull Animal Welfare Ethical Review Body and carried out in accordance with the United Kingdom's Guidance on the Operation of Animals (Scientific Procedures) Act 1986 and the UKCCCR Guidelines 2010 (Home Office Project License number 60/4549 held by Dr. Cawthorne).

PET imaging data were acquired on a Sedecal SuperArgus 2R PET scanner. Mice were induced with 5% and maintained under with 3% isoflurane (oxygen at 1 L/min). Whole body PET data acquisition (2 bed positions, 66 minutes dynamic scan) was synchronised with radiotracer i.v. injection (6-10 MBq, 200  $\mu\text{L}$ ); temperature and respiration were monitored throughout the scan. A CT scan (40 kV, 140  $\mu\text{A}$ , 360 projections, 8 shots) was acquired following each PET scan to show anatomical co-registration.

PET data were reconstructed using 3D Ordered Subset Expectation Maximisation (3D-OSEM) algorithm with 16 subsets and 2 iterations and corrections for random, scatter and attenuation. Images were normalised using the injected dose and animal weight to give Standardised Uptake Values (SUV). Data was analysed using AMIDE software.

## 6.4 Synthesis of coated SPIONs

### 6.4.1 Synthesis of “bare” iron oxide (magnetite nanoparticles) 1

Synthesis of bare iron oxide nanoparticles was carried out following literature method with some minor changes.<sup>85</sup>



1

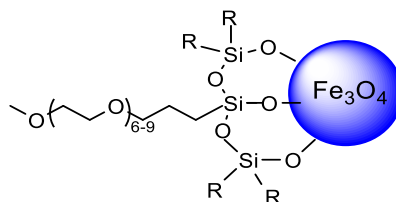
#### Method 1 (preferred method) with narrowest hydrodynamic size

In a three neck flask,  $\text{FeCl}_3$  (0.16 g, 1 mmol) and  $\text{FeCl}_2 \cdot 4\text{H}_2\text{O}$  (0.10 g, 0.5 mmol) were dissolved in 10 ml distilled water and kept under nitrogen gas for 15 minutes, heated to  $80^\circ\text{C}$  with high rate of stirring (450 rpm), aqueous ammonia solution (1.24 ml, 28%) was injected dropwise to the reaction vessel during 10 minutes, and the black precipitate immediately formed. The reaction was carried out for 60 minutes, and then the particles were magnetically decanted and washed three times with 20 ml distilled water. Diluted hydrochloric acid (0.1 M) was added to stabilise the particles for 15 minutes, the particles were washed again with distilled water and magnetically decanted and, finally, the particles were dried by freeze-dried.

Hydrodynamic size	Fe%
190 nm	71

## 6.4.2 Synthesis of siloxane coated SPIONs 2

Synthesis of siloxane derivative coated- iron oxide nanoparticles was carried out following literature method with some changes in purification steps.<sup>123</sup>



**2**

### Method 1 (preferred)

0.10 g (0.42 mmol) of bare iron oxide nanoparticles (SPIONs) synthesised from **6.4.1**, were suspended in 60% ethanol (35 ml), and sonicated for 10 minutes. The vessel was kept under nitrogen, and ammonium hydroxide (6.7 ml, 28%) was injected dropwise into the reaction mixture and stirred for 30 min. 0.035 mmol of siloxane derivative [2-methoxy (polyethyleneoxy)propyltrimethoxysilane] (Mw=1185) was dissolved in ethanol (3.6 ml) and added slowly to the reaction vessel. The mixture was stirred for 48 h at room temperature. The product was subjected to an external magnet for 15 min to remove any large particles, and then the supernatant was centrifuged at 13000 rpm for 45 minutes, after the supernatant was removed, 20 ml of ethanol was added to the precipitate and centrifuged for 20 minutes. The particles were washed with distilled water (20 ml) and centrifuged for another 20 minutes at the same speed. Finally, 5 ml of distilled water was added to the nanoparticles and centrifuged at 5000 rpm for 5 minutes.

Hydrodynamic size	Zeta potential	Elemental analysis %				
		C	H	N	Fe	Si
73 nm	-10.98 mV	5.63	0.70	0.00	55.25	1.20

FT-IR:  $\text{OH}$  hydrated ( $3310\text{ cm}^{-1}$ , strong),  $\text{CH}_2$  stretching ( $2890\text{ cm}^{-1}$ , weak),  $\text{Si-O-Fe}$  ( $800$  and  $630\text{ cm}^{-1}$ , weak) and  $\text{Fe-O}$  stretching ( $587\text{ cm}^{-1}$ , strong).

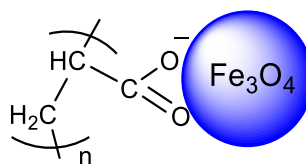
## Method 2

0.10 g (0.42 mmol) of SPIONs was suspended in 60% ethanol (35 ml), and sonicated for 10 minutes. The vessel was kept under nitrogen and ammonium hydroxide (6.7 ml, 28%) was injected dropwise to the reaction mixture and stirred for 30 minutes. The siloxane derivative [2-methoxy, (polyethyleneoxy), propyltrimethoxy silane] (0.035 mmol) was dissolved in ethanol (3.6 ml) and added to the reaction over 10 minutes, under stirring for 48 h at room temperature. The precipitate was attracted to magnet and the clear aqueous supernatant was decanted. The washing and decanting process was repeated with 60% ethanol (2x 100 ml), methanol (2x 100 ml) and diethyl ether (100 ml).

DLS measurement= 157 nm.

### 6.4.3 Synthesis of PAA coated SPIONs 3

The procedure for synthesis polyacrylic acid coated iron oxide nanoparticles was carried out according to He *et al.*<sup>140</sup>



**3**

Data analysis:

Hydrodynamic size	Zeta potential	Elemental analysis %			
		C	H	N	Fe
58 nm	-24 mV	34.57	6.66	0.00	12.00

FT-IR: Carboxylic OH ( $3315\text{ cm}^{-1}$ , broad),  $\text{CH}_2$  stretching ( $2934$  and  $2875\text{ cm}^{-1}$ , weak), carboxylate group (asymmetric  $1575$  and symmetric  $1409\text{ cm}^{-1}$ , strong), CO ( $1126\text{ cm}^{-1}$ , weak).

Relaxivity studies:

SPIONs concentrations (mM)	$T_1$		$T_2$	
	2	3	2	3
<b>1</b>	<b>3.624</b>	<b>4.659</b>	<b>25.184</b>	<b>45.243</b>
<b>0.5</b>	<b>1.817</b>	<b>3.455</b>	<b>10.845</b>	<b>23.345</b>
<b>0.25</b>	<b>1.943</b>	<b>2.458</b>	<b>6.442</b>	<b>15.554</b>
<b>0.125</b>	<b>1.409</b>	<b>1.964</b>	<b>3.729</b>	<b>7.983</b>

## 6.5 $^{99m}\text{Tc}$ radiolabelled SPIONs

### 6.5.1 Reducing $^{99m}\text{Tc(VII)}$ to $^{99m}\text{Tc(V)}$

Technetium-99m was produced from an UltraTechnekow FM generator (Curium Medical Cat. No. DRN 4329).  $^{99m}\text{Tc}$  was eluted with sterile saline to form sodium pertechnetate [ $^{99m}\text{Tc}$ ]NaTcO<sub>4</sub>. To reduce the  $^{99m}\text{Tc(VII)}$  to  $^{99m}\text{Tc(V)}$ , stannous chloride approach was used.<sup>120</sup> In a typical reaction, 100  $\mu\text{l}$  of  $^{99m}\text{Tc(VII)}$  was added to 200  $\mu\text{l}$  of SnCl<sub>2</sub> and the mixture shaken for 5 minutes. The reduction process was monitored by radio-TLC by spotting 3  $\mu\text{l}$  of reaction mixture onto silica TLC plate, eluted with saline solution. The reduced technetium-99m(V) remained at the base line, while  $^{99m}\text{Tc(VII)}$  migrated with solvent front.

### 6.5.2 <sup>99m</sup>Tc(VII) radiolabelled SPIONs

In separate HPLC vials, 100 µl of synthesised SPIONs from **6.4.2** siloxane coated SPIONs **2** and **6.4.3** PAA coated SPIONs **3** (1.5 mg of NPs/ 1 ml saline 0.9% ) were added to <sup>99m</sup>Tc(VII) solution (15 µl, 1.2 MBq), the mixtures were incubation under vigorous shaking for 30 minutes at RT. The radiolabelled SPIONs were isolated by spin filter MWCO 100 KDa and centrifuged for 10 minutes, then washed twice with saline. The radiolabelling efficiency was determined by dose calibrator after measuring the activity for both the spin filter that contains the radiolabelled nanoparticles and its washings.

SPIONs	RCY% Trial 1	RCY% Trial 2
<b>2</b>	<b>37</b>	<b>24</b>
<b>3</b>	<b>30</b>	<b>26</b>

### 6.5.3 <sup>99m</sup>Tc(I) radiolabelled of SPIONs 2 and 3

The procedure for reduction <sup>99m</sup>Tc(VII) to <sup>99m</sup>Tc(I) was carried out according to the literature.<sup>239</sup> In separate HPLC vials, 100 µl of SPIONs in saline 0.9% (siloxane@SPIONs and PAA@SPIONs) were added to reduced <sup>99m</sup>Tc(I) solution (20 µl, 6 MBq), the mixtures were incubated with shaking for 30 minutes at RT. The radiolabelled SPIONs were isolated by spin filter MWCO 100 KDa and centrifuged for 10 minutes, washed twice with saline. The radiolabelling yield was measured by dose calibrator.

SPIONs	RCY%
2	22
3	8.0

#### 6.5.4 <sup>99m</sup>Tc radiolabelling SPIONs 2 and 3 at different concentrations

<sup>99m</sup>Tc(V) solution (25 µl, 1.2-2.8 MBq) was added to 100 µl of SPIONs at different concentrations (0.5, 1 and 1.5 mg NPs/ml of saline 0.9%) the solutions were incubated under constant shaking for 30 minutes at RT to give the labelled product. The reaction mixtures were purified by centrifugation and wash with saline solution, and the samples were then analysed using the dose calibrator.

For 2

Concentration of siloxane @ SPIONs (2)	RCY%	RCY%
0.5 mg/ml	84	80
1 mg/ml	90	91
1.5 mg/ml	92	93

For 3

Concentration of PAA@SPIONs (3)	RCY%	RCY%
0.5 mg/ml	62	66
1 mg/ml	73	63
1.5 mg/ml	81	89

### 6.5.5 <sup>99m</sup>Tc radiolabelling of SPIONs 2 and 3 in different buffers

SPIONs were dissolved in PBS and NaOAc (1 mg of NPs/1 ml of buffer), pH 7. 100 µl of SPIONs solutions were added to <sup>99m</sup>Tc(V) solution (20 µl, 1.88 MBq) and the reaction was mixed at RT using a vortex stirrer for 30 minutes. The reaction mixtures were purified by centrifugation and washing with buffer solution. The samples were analysed using the dose calibrator.

SPIONs	In PBS		In NaOAc	
	RCY%	RCY%	RCY%	RCY%
<b>2</b>	<b>72</b>	<b>69</b>	<b>54</b>	<b>63</b>
<b>3</b>	<b>61</b>	<b>72</b>	<b>47</b>	<b>52</b>

### 6.5.6 <sup>99m</sup>Tc radiolabelling of SPIONs 2 and 3 in NaOAc at different pH

SPIONs were dissolved in NaOAc (1 mg of NPs/1 ml of buffer) at pH 4, 5 and 7. 100 µl of SPIONs solutions were added to <sup>99m</sup>Tc(V) solution (25 µl, 2-3.4 MBq) and the reaction was mixed at RT using vortex stirrer for 30 minutes. The reaction mixtures were purified by centrifugation and washed with buffer solution. The samples were analysed using the dose calibrator.

SPIONs	pH 4		pH 5		pH 7	
	RCY% Trial 1	RCY% Trial 2	RCY% Trial 1	RCY% Trial 2	RCY% Trial 1	RCY% Trial 2
<b>2</b>	<b>75</b>	<b>80</b>	<b>71</b>	<b>77</b>	<b>54</b>	<b>64</b>
<b>3</b>	<b>70</b>	<b>65</b>	<b>52</b>	<b>60</b>	<b>47</b>	<b>51</b>

### 6.5.7 <sup>99m</sup>Tc radiolabelling of SPIONs 2 and 3 in NaOAc at different pH

SPIONs were dissolved in NaOAc (1 mg of NPs/1 ml of buffer) at pH 4, 5 and 7. 100 µl of SPIONs solutions were added to <sup>99m</sup>Tc(V) solution (25 µl, 2-3.4 MBq) and the reaction was mixed at RT using vortex stirrer for 30 minutes. The reaction mixtures were purified by centrifugation and washed with buffer solution. The samples were analysed using the dose calibrator.

SPIONs	pH 4		pH 5		pH 7	
	RCY% Trial 1	RCY% Trial 2	RCY% Trial 1	RCY% Trial 2	RCY% Trial 1	RCY% Trial 2
<b>2</b>	<b>75</b>	<b>80</b>	<b>71</b>	<b>77</b>	<b>54</b>	<b>64</b>
<b>3</b>	<b>70</b>	<b>65</b>	<b>52</b>	<b>60</b>	<b>47</b>	<b>51</b>

### 6.5.8 <sup>99m</sup>Tc radiolabelling of SPIONs 2 and 3 in saline at 37°C

100 µl of SPIONs (1 mg of NPs/ 1 ml of saline 0.9%), was added to <sup>99m</sup>Tc(V) solution (25 µl, 0.8-1.4 MBq) and the reaction was mixed and heated to 37°C with continuous shaking for 30 minutes. The reaction mixtures were purified by centrifugation and washed with saline solution. The samples were analysed using the dose calibrator.

SPIONs	At 37°	
	RCY% Trial 1	RCY% Trial 2
<b>2</b>	<b>92</b>	<b>96</b>
<b>3</b>	<b>94</b>	<b>90</b>

### 6.5.9 <sup>99m</sup>Tc radiolabelling of SPIONs 2 and 3 in saline at 90°C

100 µl of SPIONs (1 mg of NPs/ 1 ml of saline), was added to <sup>99m</sup>Tc(V) solution (25 µl, 1.6 MBq) and the reaction was mixed and heated to 90°C with continuous shaking for 30 minutes. The reaction mixtures were purified by centrifugation and washed with saline solution. The samples were analysed using the dose calibrator.

SPIONs	At 90°	
	RCY% Trial 1	RCY% Trial 2
2	98	94
3	96	94

### 6.5.10 <sup>99m</sup>Tc radiolabelling of SPIONs 2 and 3 in NaOAc and PBS at 37°C

SPIONs were dissolved in NaOAc, pH 4 and PBs, pH 7 (1 mg of NPs/1 ml of buffer). 100 µl of SPIONs solutions were added to <sup>99m</sup>Tc(V) solution (25 µl, 2-3.4 MBq). The solutions were mixed and heated to 37°C with continuous shaking for 30 minutes. The reaction mixtures were purified by centrifugation and washed with saline solution. The samples were analysed using the dose calibrator.

SPIONs	In NaOAc		In PBS	
	RCY% Trial 1	RCY% Trial 2	RCY% Trial 1	RCY% Trial 2
2	96	94	92	95
3	93	90	60	71

### 6.5.11 <sup>99m</sup>Tc radiolabelling of SPIONs 2 and 3 in NaOAc and PBS at 90°C

SPIONs were dissolved in NaOAc, pH 4 and PBs, pH 7 (1 mg of NPs/1 ml of buffer). 100 µl of SPIONs solutions were added to <sup>99m</sup>Tc(V) solution (25 µl, 1-3 MBq). The solutions were mixed and heated to 90°C with continuous shaking for 30 minutes. The reaction mixtures were purified by centrifugation and washed with saline solution. The samples were analysed using the dose calibrator.

SPIONs	In NaOAc		In PBS	
	RCY% Trial 1	RCY% Trial 2	RCY% Trial 1	RCY% Trial 2
2	96	96	92	96
3	98	93	81	85

### 6.5.12 Stability of <sup>99m</sup>Tc radiolabelling of SPIONs 2 and 3 in EDTA

100 µl of SPIONs (1 mg of NPs/ 1 ml of sodium acetate, pH 4), was added to <sup>99m</sup>Tc(V) solution (25µl, 1.4 MBq) and the reaction was mixed and heated to 90°C with continuous shaking for 30 minutes. After cooling, 100 µl of 0.1 M of EDTA solution was added to the radiolabelled suspensions and shaking carried out for 30 or 60 minutes at RT. The mixtures were analysed by dose calibrator to determine the percentage of EDTA/<sup>99m</sup>Tc and <sup>99m</sup>Tc-SPIONs.

SPIONs	30 min		60 min	
	RCY% Trial 1	RCY% Trial 2	RCY% Trial 1	RCY% Trial 2
2	97	97	94	96
3	93	91	86	91

### 6.5.13 Stability of <sup>99m</sup>Tc radiolabelling of SPIONs 2 and 3 over a range of pH values

100 µl of SPIONs (1 mg of NPs/ 1 ml of sodium acetate, pH 4), was added to <sup>99m</sup>Tc(V) solution (25 µl, 0.4 MBq) and the reaction was mixed and heated to 90°C with continuous shaking for 30 minutes. After cooling, 50 µl of NaOAc solutions at pH 3, 5 and 11 were added to the radiolabelled suspensions and shaking carried out for 30 minutes at RT, the mixtures were analysed by dose calibrator.

SPIONS	pH 3	pH 5	pH 11
	RCY%	RCY%	RCY%
2	76	80	78
3	85	88	84

#### **6.5.14 Stability of <sup>99m</sup>Tc radiolabelling SPIONs at different proteins**

100 µl of SPIONs in saline, was added to (60 µl, 1.3 MBq of <sup>99m</sup>Tc (V)) solution and the reaction was mixed and heated to 90°C with continuous shaking for 30 minutes. After cooling, 50 µl of proteins (0.4 g of transferrin/ml saline) and 50% of bovine serum albumin and 90 µl of saline were added to the radiolabelled samples with gentle shaking for 2, 24 and 48 hours.

#### **The stability of SPIONs in proteins was investigated by gel electrophoresis.**

Gel preparation: 0.6 g of agarose were dissolved in 50 ml of TBE (tris borate-EDTA buffer) and heated in the microwave. After cooling, the agarose was placed in the gel electrophoresis kit and holes were created using the comb to form the wells. When the gel had completely dried, 17 µl of the <sup>99m</sup>Tc-SPIONs solutions were placed in small tubes that contain 3 µl of DNA loaded dye and the 20 µl products were injected in the wells. The gel was covered with extra TBE solution and the machine was operated at 60 volts for 90 minutes.

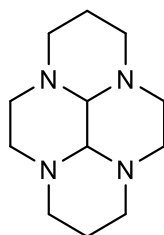
After 90 minutes, the gel was placed in horizontal shaker and covered with InstaBlue stain for 20 minutes, later the gel was sliced and measured by gamma counter.

## 6.6 Synthesis of CXCR4 antagonist-conjugated SPIONs

### 6.6.1 Synthesis of cis-3a, 5a, 8a, 10a-tetraazaperhydropyrene

#### (Bridged cyclam) 4<sup>200</sup>

The synthetic procedure of bridged cyclam was carried out following the method reported by Le Baccon *et al.*



4

<sup>1</sup>H NMR (CDCl<sub>3</sub>): δ 3.53 (t, 2H, *J*= 10.0 Hz, CH<sub>2</sub>-N), 3.08 (s, 2H, N-CH-N), 3.00-2.90 (m, 6H, CH<sub>2</sub>-N), 2.73 (d, 2H, *J*= 11.0 Hz, CH<sub>2</sub>-N), 2.30 (d, 2H, *J*= 11.0 Hz, CH<sub>2</sub>-N), 2.28-2.16 (m, 4H, CH<sub>2</sub>-N and CH<sub>2</sub>-β-N), 2.11-2.07 (m, 2H, CH<sub>2</sub>-N), 1.20 (dp, 2H, *J*= 13.0, 2.5 Hz, CH<sub>2</sub>-β-N).

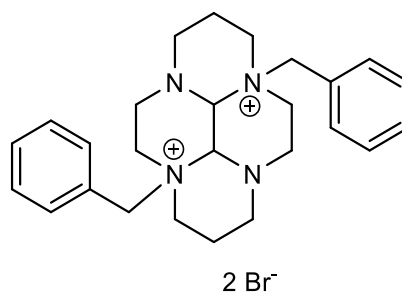
<sup>13</sup>C NMR (CDCl<sub>3</sub>): δ 20.6 (N-β-CH<sub>2</sub>), 45.7 (N-α-CH<sub>2</sub>), 53.5 (N-α-CH<sub>2</sub>), 55.3 (N-α-CH<sub>2</sub>), 56.1 (CH).

ES-MS (*m/z*): [M+H]<sup>+</sup> = 223

Elemental analysis %		
	Analysis % Expected	Results % Found
C	64.83	64.57
H	9.97	10.20
N	25.2	24.65

## 6.6.2 Synthesis of 3a, 8a-dibenzyl-decahydro-3a, 5a, 8a, 10a-tetraazapyrenium dibromide <sup>5</sup><sup>201</sup>

The synthesis procedure of bis-benzylated bridged cyclam bromide macrocycle was carried out following the Wong method.



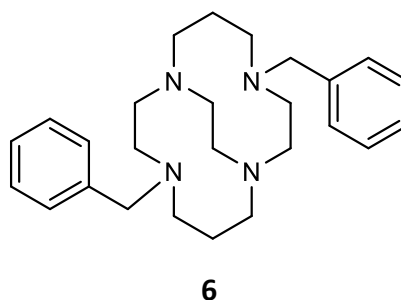
**5**

<sup>1</sup>H NMR (D<sub>2</sub>O) =  $\delta$  7.62 (10H, m), 5.24 and 4.72 (4H, AB,  $J$ = 13.0 Hz), 5.05 (2H, s), 4.38 (2H, td,  $J$ = 13.0, 4.0 Hz), 3.70 (2H, td,  $J$ = 13.0, 3.0 Hz), 3.57-3.37 (6H, m), 3.22-3.18 (4H, dm,  $J$ = 13.0 Hz), 2.78 (2H, td,  $J$ = 12.0, 3.0 Hz), 2.29-2.19 (2H, m), 1.89-1.85 (2H, dm,  $J$ = 15.0 Hz).

ES-MS ( $m/z$ ): [M-benzyl +H<sup>+</sup>] = 313, [M-H]<sup>+</sup> = 403, [M+HCOO]<sup>+</sup> = 449.

### 6.6.3 Synthesis of 4,11-dibenzyl-1,4,8,11-tetraazabicyclo [6.6.2] hexadecane **6**<sup>201</sup>

The synthesis procedure of bis-benzylated cross-bridged cyclam macrocycle was carried out following the Wong method.

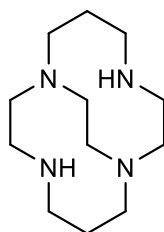


<sup>1</sup>H NMR (CDCl<sub>3</sub>): δ 7.37–7.20 (m, 10H, H(Ar)), 3.95 (ddd, 2H, *J* = 12.5, 11.0, 4.0 Hz, CH<sub>2</sub>-N), 3.78 and 3.18 (AB, 4H, *J* = 13.5 Hz, CH<sub>2</sub>-Ar), 3.22–3.19 (m, 2H, CH<sub>2</sub>-N), 2.85 (ddd, 2H, *J* = 12.5, 11.0, 4.0 Hz, CH<sub>2</sub>-N), 2.48–2.30 (m, 12H, CH<sub>2</sub>-N), 1.62–1.52 (m, 2H, CH<sub>2</sub>-β-N), 1.43–1.33 (m, 2H, CH<sub>2</sub>-β-N).

ES-MS (*m/z*): [M+H]<sup>+</sup> = 407, [M-benzyl+H]<sup>+</sup> = 317.

#### 6.6.4 Synthesis of 1,4,8,11-tetraazabicyclo[6.6.2]hexadecane (Cross-bridged cyclam) **7**

The synthesis procedure of cross-bridged cyclam macrocycle was carried out following the Wong method.<sup>201</sup>



**7**

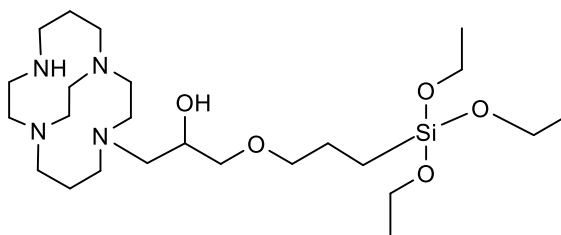
<sup>1</sup>H NMR (C<sub>6</sub>D<sub>6</sub>): δ 1.16 (dtt, 2H, CH<sub>2</sub>-β-N), 1.53 (m, 2H, CH<sub>2</sub>-β-N), 2.07-2.26 (m, 6H, CH<sub>2</sub>-N), 2.31 (m, 2H), 2.42-2.64 (m, 6H, CH<sub>2</sub>-N), 2.74-2.86 (m, 4H, CH<sub>2</sub>-N), 3.21 (ddd, 2H, *J* = 10Hz, CH<sub>2</sub>-N), 3.59 (s, 2H, NH).

ES-MS (m/z): [M+H]<sup>+</sup> = 227.

Elemental analysis %		
	Analysis % Expected	Results % Found
<b>C</b>	63.67	63.33
<b>H</b>	11.58	11.70
<b>N</b>	24.75	23.78

### 6.6.5 Synthesis of siloxane derivative ligand on cross-bridged cyclam (Si-CB cyclam) 8

The synthetic procedure for attachment of the siloxane derivative to the macrocycle was carried out following the method communicated by Burke.<sup>21</sup>



8

A solution of cross-bridged cyclam (0.20 g, 0.88 mmol) in chloroform (16 ml) was placed in a microwave tube. In separate vessel, (0.24 g, 0.88 mmol) of GPTES was dissolved in chloroform (16 ml) and added in dropwise manner to the macrocyclic solution. The mixture was heated in microwave at 90°C for 30 minutes. The solvent was removed to form a dark yellow oil (0.4 g, 89%).

<sup>1</sup>H NMR (CDCl<sub>3</sub>): δ 1.30 (m), 1.705 (m), 2.08 (td), 2.20-2.30 (m), 2.35-2.8 (m), 2.98-3.02 (m), 3.22-3.32 (m), 3.65(s).

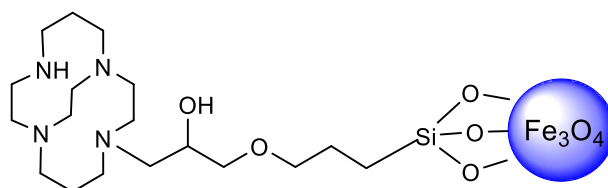
ES-MS (m/z): [M+H<sup>+</sup>] = 506 and [M-GPTES]<sup>+</sup> = 227.

### 6.6.6 Synthesis of SPIONs core compound 9

The synthesis procedure of iron oxide nanoparticles core was carried out following a literature report.<sup>207</sup>

### 6.6.7 Functionalisation of SPIONs with Si-CB cyclam (SPIONs-Si-CB cyclam)

The synthesis procedure for attachment of the SPIONs with the siloxane macrocycle was carried out following Barreto's method with some modifications.<sup>123</sup>



10

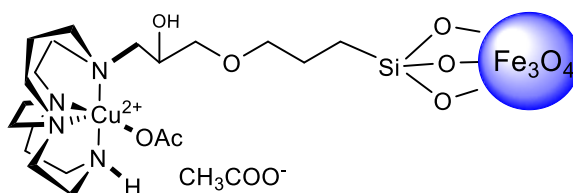
0.3 g (1.29 mmol) of freshly prepared SPIONs was washed with ethanol twice, and re-suspended in 25 ml of 60% ethanol and sonicated for 15 minutes. The black suspension was fixed under nitrogen, and 2.5 ml of 28% ammonia was added under continuous stirring for 15 minutes. To this mixture, 0.8 mmol of siloxane modified CB cyclam (Si-CB cyclam) was dissolved in 3 ml of ethanol and added to SPIONs dropwise. The mixture was stirred for 48 hours at RT. The product was separated first by a rare earth metal magnet to get rid of any large particles, and the black supernatant was centrifuged at 12,000 rpm for 20 minutes, then washed successively with ethanol (20 ml x 2) and with deionised water (20 x 2) and centrifuged at the same speed and time on each occasion. Finally, 12 ml of water was added and centrifuged at 3000 rpm for only 5 minutes, a dark stable suspension was formed.

FT-IR: OH ( $3360\text{ cm}^{-1}$ , strong), N-H ( $2720\text{ cm}^{-1}$ , weak), C-N ( $1337\text{ cm}^{-1}$ , weak) Si-O-Fe ( $780\text{ cm}^{-1}$ , strong).

Hydrodynamic size	Elemental analysis %							
	C	H	N	Fe	Si	Cu	Zn	Ni
121 nm	5.44	0.99	0.59	47.4	3.26	0.00	0.00	0.00

### 6.6.8 Metal complexation of SPIONs-Si-CB cyclam 11

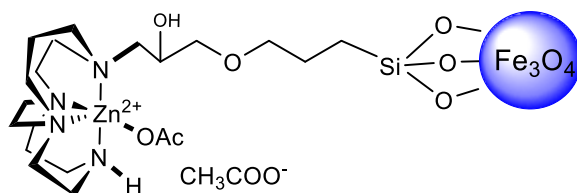
Copper acetate attached SPIONs-Si-CB cyclam (Cu-SPIONs-Si-CB cyclam)



2 ml (30 mg of SPIONs) suspension was added to 30 ml of ethanol 60% and sonicated for 30 minutes with no sign of any nanoparticle precipitation. The mixture was kept under nitrogen and 10 mg of copper acetate was dissolved in 10 ml of ethanol and added to SPIONs suspension dropwise over 5 minutes with stirring for 24 hours at RT. The product was separated first by a rare earth metal magnet to get rid of any large particles, and the black supernatant was centrifuged at 12,000 rpm for 20 minutes, then washed successively with ethanol (20 ml x 2) and with deionised water (20 x 2) and centrifuged at the same speed and for the same time. Finally, 12 ml of water was added and centrifuged at 3000 rpm for 5 minutes, a dark stable suspension was formed.

Hydrodynamic size	Elemental analysis %							
	C	H	N	Fe	Si	Cu	Zn	Ni
159 nm	4.46	0.94	0.56	53.98	3.29	2.70	0.00	0.00

### 6.6.9 Zinc acetate attached SPIONs-Si-CB cyclam (Zn-SPIONs-Si-CB cyclam) 12

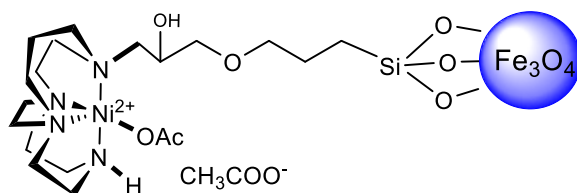


**12**

2 ml (30 mg of SPIONs) suspension was added to 30 ml of ethanol 60% and sonicated for 30 minutes with no sign of any nanoparticle precipitation. The mixture was kept under nitrogen and 10 mg of zinc acetate was dissolved in 10 ml of ethanol and added to the SPIONs suspension dropwise for 5 minutes followed by stirring for 24 hours at RT. The product was separated first by a rare earth metal magnet to get rid of any large particles, and the black supernatant was centrifuged at 12,000 rpm for 20 minutes, then washed successively with ethanol (20 ml x 2) and with deionised water (20 x 2), all centrifuged at the same speed and time. Finally, 12 ml of water was added and centrifuged at 3000 rpm for 5 minutes, a dark stable suspension was formed.

Hydrodynamic size	Elemental analysis %							
	C	H	N	Fe	Si	Cu	Zn	Ni
158 nm	4.33	1.06	0.53	49.21	5.62	0.00	1.66	0.00

### 6.6.10 Nickel acetate attached SPIONs-Si-CB cyclam (Ni-SPIONs-Si-CB cyclam) 13



**13**

2 ml (30 mg of SPIONs) suspension was added to 30 ml of ethanol 60% and sonicated for 30 minutes with no sign of any nanoparticle precipitation. The mixture was kept under nitrogen and 10 mg of nickel acetate was dissolved in 10 ml of ethanol and added to SPIONs suspension dropwise for 5 minutes followed by stirring for 24 hours at RT. The product was separated first by a rare earth metal magnet to get rid of any large particles, and the black supernatant was centrifuged at 12,000 rpm for 20 minutes, then washed successively with ethanol (20 ml x 2) and with deionised water (20 x 2), all centrifuged at the same speed and time. Finally, 12 ml of water was added and centrifuged at 3000 rpm for 5 minutes, a dark stable suspension was formed.

Hydrodynamic size	Elemental analysis %							
	C	H	N	Fe	Si	Cu	Zn	Ni
165 nm	4.30	1.02	0.50	44.77	6.81	0.00	0.00	0.20

## 6.7 <sup>68</sup>Ga radiolabelling SPIONs-Si-CB cyclam

Four functionalised SPIONs with CB cyclam macrocycles on the surface were radiolabelled with the <sup>68</sup>Ga radioisotope after elution from the generator.

### 6.7.1 <sup>68</sup>Ga radiolabelled Cu-SPIONs-Si-CB cyclam at RT, 50°C and 90°C

A suspension of Cu-SPIONs-Si-CB cyclam (**11**) (200 µl, 1mM Fe) in ammonium acetate buffer (0.4 M, pH 5) was added to formulated <sup>68</sup>GaCl<sub>3</sub> (40-60 MBq) and the reaction was mixed at room temperature, 50°C or 90°C for 15 minutes. Then centrifugation was carried out at 10000 rpm for 10 minutes, the samples were filtered by spin filter (100 K) and washed with 200 µl ammonium acetate.

SPIONs	RCY%								
	RT			50°C			90°C		
	1	2	3	1	2	3	1	2	3
11	89	84	76	95	96	90	98	99	97

### 6.7.2 <sup>68</sup>Ga radiolabelled different SPIONs-Si-CB cyclam at 50°C

Suspensions of SPIONs-Si-CB cyclam (**10**), (**12**) and (**13**) (200 µl, 1mM Fe) in ammonium acetate buffer (0.4 M, pH 5) were added to formulated <sup>68</sup>GaCl<sub>3</sub> (40-60 MBq) and the reactions were mixed at 50°C using vortex stirrer for 15 minutes. Then centrifugation was carried out at 10000 rpm for 10 minutes, the samples were filtered by spin filter (100 K) and washed with 200 µl ammonium acetate.

SPIONs	RCY%		
	1	2	3
<b>10</b>	<b>99</b>	<b>99</b>	<b>98</b>
<b>12</b>	<b>99</b>	<b>100</b>	<b>99</b>
<b>13</b>	<b>100</b>	<b>99</b>	<b>99</b>

### 6.7.3 Stability of <sup>68</sup>Ga radiolabelled SPIONs-Si-CB cyclam 10 in Apo-transferrin

Apo-transferrin (200 µl) was added to the <sup>68</sup>Ga complex of SPIONs-Si-CB cyclam (**10**) (200 µl, 1 mM of Fe, 40 MBq). The reaction was incubated at 37°C for 1 hour, and radio-TLC was measured after 5, 15, 30 and 60 minutes.

Time (min)	RCY% Trial 1	RCY% Trial 2	RCY% Trial 3
<b>5</b>	<b>100</b>	<b>100</b>	<b>100</b>
<b>15</b>	<b>95</b>	<b>91</b>	<b>98</b>
<b>30</b>	<b>94</b>	<b>96</b>	<b>85</b>
<b>60</b>	<b>86</b>	<b>71</b>	<b>95</b>

#### 6.7.4 Stability of <sup>68</sup>Ga radiolabelled Cu-SPIONs-Si-CB cyclam **11** in *Apo-transferrin*

Apo-transferrin (200 µl) was added to the <sup>68</sup>Ga complex of Cu-SPIONs-Si-CB cyclam (**11**) (200 µl, 1 mM of Fe, 40 MBq). The reaction was incubated at 37°C for 1 hour, and radio-TLC was measured after 5, 15, 30 and 60 minutes.

Time (min)	RCY% Trial 1	RCY% Trial 2	RCY% Trial 3
5	98	94	100
15	99	100	96
30	82	95	93
60	90	96	95

#### 6.7.5 Stability of <sup>68</sup>Ga radiolabelled Zn-SPIONs-Si-CB cyclam **12** in *Apo-transferrin*

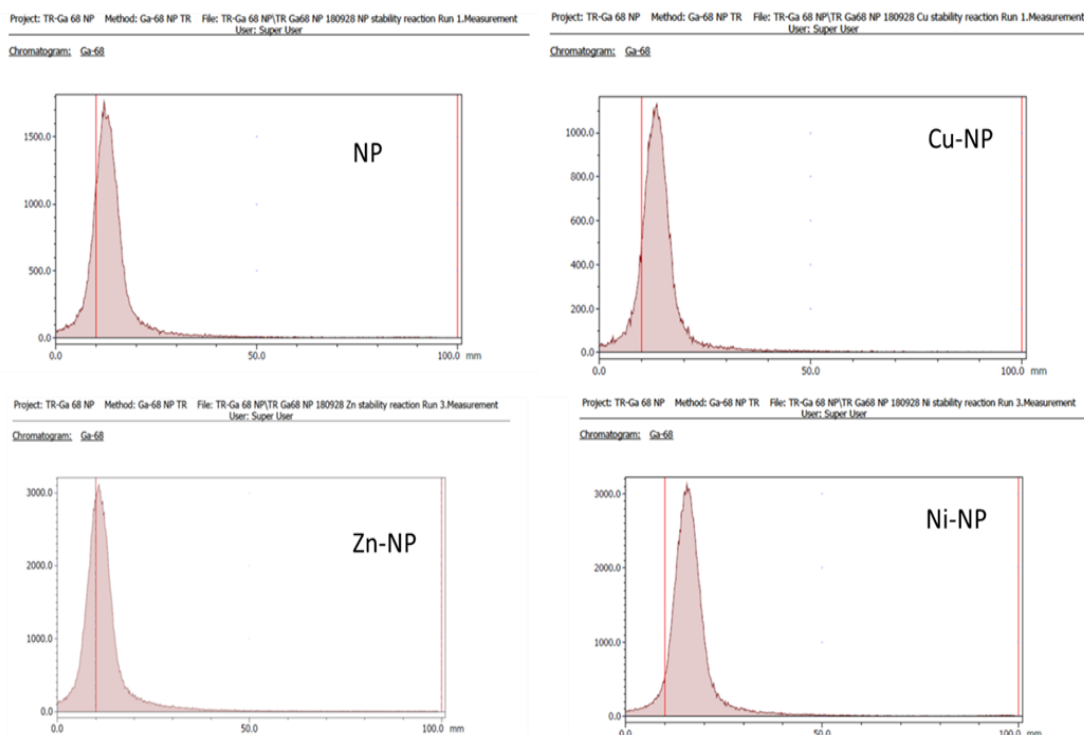
Apo-transferrin (200 µl) was added to the <sup>68</sup>Ga complex of Zn-SPIONs-Si-CB cyclam (**12**) (200 µl, 1 mM of Fe, 40 MBq). The reaction was incubated at 37°C for 1 hour, and radio-TLC was measured after 5, 15, 30 and 60 minutes.

Time (min)	RCY% Trial 1	RCY% Trial 2	RCY% Trial 3
5	100	100	100
15	99	98	99
30	90	93	100
60	90	82	88

## 6.7.6 Stability of $^{68}\text{Ga}$ radiolabelled Ni-SPIONs-Si-CB cyclam **13** in Apo-transferrin

Apo-transferrin (200  $\mu\text{l}$ ) was added to the  $^{68}\text{Ga}$  complex of Ni-SPIONs-Si-CB cyclam (**13**) (200  $\mu\text{l}$ , 1 mM of Fe, 40 MBq). The reaction was incubated at 37°C for 1 hour, and the radiolabelling yield was measured by radio-TLC after 5, 15, 30 and 60 minutes (radio-TLC traces shown below).

Time (min)	RCY% Trial 1	RCY% Trial 2	RCY% Trial 3
5	100	93	93
15	100	99	97
30	100	92	93
60	90	83	88



## 6.8 Radiolabelling liposomes 14 and micelles 15 with $^{68}\text{Ga}$

Liposomes **14** and polymeric micelles **15** were synthesised by Professor Andre' de Barros from Federal University of Minas Gerais, Brazil. The hydrodynamic size for these nanocarriers were determined to be:

Compound	Z-average (nm)
<b>14</b>	<b>131</b>
<b>15</b>	<b>13</b>

### 6.8.1 Radiolabelling method for liposomes 14 and micelles 15 with $^{68}\text{Ga}$

The nanoparticles were radiolabelled with gallium-68 after elution of the gallium-68 from the  $^{68}\text{Ge}/^{68}\text{Ga}$  generator as already described.

### 6.8.2 $^{68}\text{Ga}$ radiolabelling liposomes 14 and polymeric micelles 15 in saline at room temperature

Liposomes **14** and polymeric micelles **15** were dissolved in saline (100  $\mu\text{l}$ , 0.9%) and filtered with polycarbonate syringe filter (0.2  $\mu\text{m}$ ), then added to dry  $^{68}\text{GaCl}_3$  (50 MBq). The reaction was shaken for 15 minutes at room temperature. Radiochemical complex formation reactions were analysed by radio-TLC, eluting with 0.1 M citric acid.

Compound	RCY%
<b>14</b>	<5
<b>15</b>	<5

### 6.8.3 <sup>68</sup>Ga radiolabelling liposomes **14** and polymeric micelles **15** in saline at 60°C

Liposomes **14** and polymeric micelles **15** were dissolved in saline (100 µl, 0.9%) and filtered with a polycarbonate syringe filter (0.2 µm), then added to dry <sup>68</sup>GaCl<sub>3</sub> (50 MBq). The reaction was heated at 60°C for 15 minutes. The nanocarriers were purified by centrifugation by using spin filter (MWCO 100 kDa) and washed with saline. Radiochemical complex formation reactions were analysed by radio-TLC, eluting with 0.1 M citric acid.

Compound	RCY%
<b>14</b>	<b>45</b>
<b>15</b>	<b>30</b>

#### 6.8.4 <sup>68</sup>Ga radiolabelling liposomes **14** and polymeric micelles **15** in sodium acetate

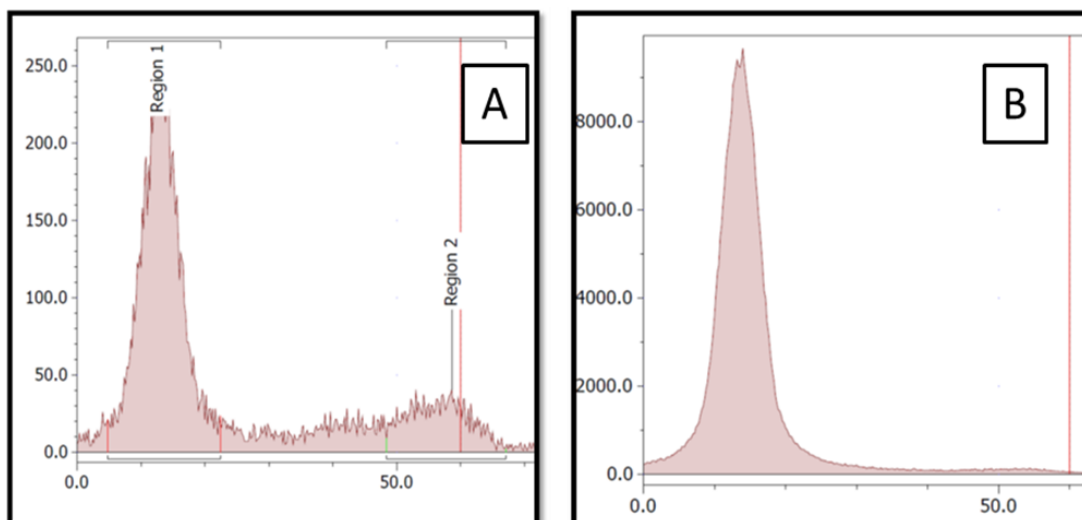
Liposomes **14** and polymeric micelles **15** were dissolved in sodium acetate (200 µl, pH 5) and filtered with a polycarbonate syringe filter (0.2 µm), then added to dry <sup>68</sup>GaCl<sub>3</sub> (50 MBq). The reaction was carried out at either room temperature or 60°C for 15 minutes. The nanocarriers were purified by centrifugation by using spin filtration (MWCO 100 kDa) and washed with sodium acetate. Radiochemical complex formation reactions were analysed by radio-TLC, eluting with 0.1 M citric acid.

Compound	RT	60°C
	RCY%	RCY%
<b>14</b>	<5	<5
<b>15</b>	<b>30</b>	<b>45</b>

### 6.8.5 $^{68}\text{Ga}$ radiolabelling liposomes **14** and polymeric micelles **15** in sodium acetate at 250 MBq

Liposomes **14** and polymeric micelles **15** were dissolved in sodium acetate (200  $\mu\text{l}$ , pH 5) and filtered with a polycarbonate syringe filter (0.2  $\mu\text{m}$ ), then added to dry  $^{68}\text{GaCl}_3$  (250 MBq). The reaction was heated at 60°C for 15 minutes. The nanocarriers were purified by centrifugation by using spin filter (MWCO 100 kDa) and washed three times with sodium acetate. Radiochemical complex formation reactions were analysed by radio-TLC, eluting with 0.1 M citric acid (radio-TLC traces shown below).

Compound	Average RCY%
<b>14</b>	<b>&gt;90</b>
<b>15</b>	<b>&gt;90</b>

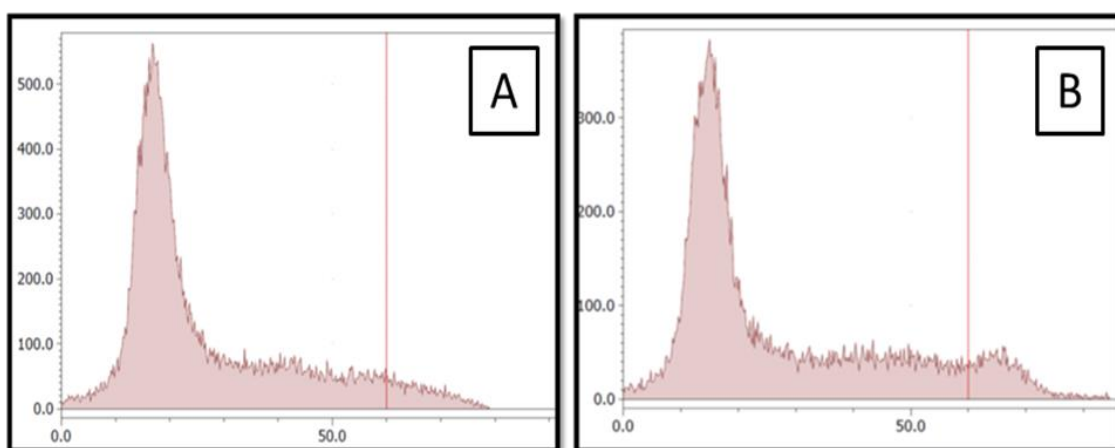


### 6.8.6 Radiolabelling stability of liposomes **14** and polymeric micelles

#### **15**

250 µl of liposomes **14** and polymeric micelles **15** in sodium acetate were radiolabelled with  $^{68}\text{GaCl}_3$  (250 MBq) at 60°C for 15 minutes. The nanocarriers were then incubated with *Apo*-transferrin (100 µl, 1%) at 37°C for 60 minutes. Radiochemical stability was analysed by radio-TLC at 5, 15, 30, 45 and 60 minutes (radio-TLC traces shown below).

Time (min)	RCY%	
	14	15
5	94	97
15	92	97
30	90	92
45	85	90
60	75	88



## References

1. A. Louie, *Chem. Rev.*, 2010, **110**, 3146-3195.
2. T. Skotland, T.-G. Iversen and K. Sandvig, *Nanomed. Nanotechnol. Biol. Med.*, 2010, **6**, 730-737.
3. A. A. Appel, M. A. Anastasio, J. C. Larson and E. M. Brey, *Biomaterials*, 2013, **34**, 6615-6630.
4. D.-E. Lee, H. Koo, I.-C. Sun, J. H. Ryu, K. Kim and I. C. Kwon, *Chem. Soc. Rev.*, 2012, **41**, 2656-2672.
5. S. Achilefu, *Chem. Rev.*, 2010, **110**, 2575-2578.
6. M. N. Wernick and J. N. Aarsvold, *Emission tomography: the Fundamentals of PET and SPECT*, Academic Press, 2004.
7. A. Van Der Veldt, E. Smit and A. A. Lammertsma, *Front. Oncol.*, 2013, **3**.
8. P. J. Blower, *Dalton Trans.*, 2015, **44**, 4819-4844.
9. I. Tworowska, D. Ranganathan, S. Thamake, E. Delpassand, A. Mojtahedi, M. K. Schultz, K. Zhernosekov and S. Marx, *Nucl. Med. Biol.*, 2016, **43**, 19-26.
10. G. B. Saha and G. B. Saha, *Fundamentals of Nuclear Pharmacy*, Springer, 2004.
11. N. J. Long and W.-T. Wong, *The Chemistry of Molecular Imaging*, John Wiley & Sons, 2014.
12. Z. Li and P. S. Conti, *Adv. Drug Del. Rev.*, 2010, **62**, 1031-1051.
13. K. Serdons, A. Verbruggen and G. M. Bormans, *Methods*, 2009, **48**, 104-111.
14. P. W. Miller, N. J. Long, R. Vilar and A. D. Gee, *Angew. Chem. Int. Ed.*, 2008, **47**, 8998-9033.
15. L. R. Bernstein, *Pharmacol. Rev.*, 1998, **50**, 665-682.
16. S. R. Banerjee and M. G. Pomper, *Appl. Rad. Isotop.*, 2013, **76**, 2-13.
17. P. Atkins and T. Overton, *Shriver and Atkins' Inorganic Chemistry*, Oxford University Press, USA, 2010.
18. S. Abada, A. Lecointre, I. Déchamps-Olivier, C. Platas-Iglesias, C. Christine, M. Elhabiri and L. Charbonnière, *Radiochemica Acta*, 2011, **99**, 663-678.
19. B. P. Burke, N. Baghdadi, A. E. Kownacka, S. Nigam, G. S. Clemente, M. M. Al-Yassiry, J. Domarkas, M. Lorch, M. Pickles, P. Gibbs and S. Archibald, *Nanoscale*, 2015, **7**, 14889-14896.
20. S. Liu and D. S. Edwards, *Bioconjug. Chem.*, 2001, **12**, 7-34.
21. B. P. Burke, PhD Thesis, University of Hull, 2013.
22. G. T. Gullberg, B. W. Reutter, A. Sitek, J. S. Maltz and T. F. Budinger, *Phys. Med. Biol.*, 2010, **55**, R111.
23. M. M. Khalil, J. L. Tremoleda, T. B. Bayomy and W. Gsell, *Int. J. Mol. Imaging*, 2011, **2011**.
24. M. D. Bartholoma, A. S. Louie, J. F. Valliant and J. Zubieta, *Chem. Rev.*, 2010, **110**, 2903-2920.
25. I. Zolle, *Technetium-99m pharmaceuticals*, Springer, 2007.
26. M. J. Welch, *Handbook of Radiopharmaceuticals: Radiochemistry and Applications*, John Wiley & Sons, 2003.
27. S. Liu, *Chem. Soc. Rev.*, 2004, **33**, 445-461.
28. T. Storr, Y. Sugai, C. A. Barta, Y. Mikata, M. J. Adam, S. Yano and C. Orvig, *Inorg. Chem.*, 2005, **44**, 2698-2705.
29. P. Caravan, *Chem. Soc. Rev.*, 2006, **35**, 512-523.
30. M. Bottrill, L. Kwok and N. J. Long, *Chem. Soc. Rev.*, 2006, **35**, 557-571.
31. L. Faucher, Y. Gossuin, A. Hocq and M.-A. Fortin, *Nanotechnology*, 2011, **22**, 295103.

32. M. A. Brown and R. C. Semelka, *MRI: basic principles and applications*, John Wiley & Sons, 2011.
33. A. E. Merbach and É. Tóth, *The Chemistry of Contrast Agents in Medical Magnetic Resonance Imaging*, Wiley Online Library, 2001.
34. C. S. Kumar, *Magnetic nanomaterials*, John Wiley & Sons, 2009.
35. R. A. De Graaf, *In vivo NMR spectroscopy: principles and techniques*, John Wiley & Sons, 2013.
36. M. Colombo, S. Carregal-Romero, M. F. Casula, L. Gutierrez, M. P. Morales, I. B. Bohm, J. T. Heverhagen, D. Prospero and W. J. Parak, *Chem. Soc. Rev.*, 2012, **41**, 4306-4334.
37. Website: <http://www.radiologyassistant.nl> Accessed on 10<sup>th</sup> July 2020
38. K. Niemirowicz, K. Markiewicz, A. Wilczewska and H. Car, *Adv. Med. Sci.*, 2012, **57**, 196-207.
39. L. N. Goswami, L. Ma, S. Chakravarty, Q. Cai, S. S. Jalisatgi and M. F. Hawthorne, *Inorg. Chem.*, 2012, **52**, 1694-1700.
40. P. Hermann, J. Kotek, V. Kubíček and I. Lukeš, *Dalton Trans.*, 2008, 3027-3047.
41. J. Perez-Rodriguez, S. Lai, B. D. Ehst, D. M. Fine and D. A. Bluemke, *Radiology*, 2009, **250**, 371-377.
42. R. E. Mewis and S. J. Archibald, *Coord. Chem. Rev.*, 2010, **254**, 1686-1712.
43. M.-A. Fortin, R. M. Petoral Jr, F. Söderlind, A. Klasson, M. Engström, T. Veres, P.-O. Käll and K. Uvdal, *Nanotechnology*, 2007, **18**, 395501.
44. E. Amstad, M. Textor and E. Reimhult, *Nanoscale*, 2011, **3**, 2819-2843.
45. Y. Shi, M. Lin, X. Jiang and S. Liang, *Biomedicine*, 2015, **21**, 22.
46. L. E. Jennings and N. J. Long, *Chem. Commun.*, 2009, 3511-3524.
47. F. Gerstl, C. Windischberger, M. Mitterhauser, W. Wadsak, A. Holik, K. Kletter, E. Moser, S. Kasper and R. Lanzemberger, *Neuroimage*, 2008, **41**, 204-211.
48. M. J. Garcia, *Non-invasive cardiovascular imaging: a multimodality approach*, Lippincott Williams & Wilkins, 2012.
49. Z. R. Stephen, F. M. Kievit and M. Zhang, *Mater. Today*, 2011, **14**, 330-338.
50. R. Torres Martin de Rosales, R. Tavaré, R. L. Paul, M. Jauregui - Osoro, A. Protti, A. Glaria, G. Varma, I. Szanda and P. J. Blower, *Angew. Chem. Int. Ed.*, 2011, **50**, 5509-5513.
51. Website: <http://www.imagingcdt.com> Accessed on 10<sup>th</sup> July 2020
52. C. Glaus, R. Rossin, M. J. Welch and G. Bao, *Bioconjug. Chem.*, 2010, **21**, 715-722.
53. A. K. D. Patel, B. Simard and B. Xing, *Biomaterials*, 2010, **31**, 2866.
54. R. Misri, D. Meier, A. C. Yung, P. Kozlowski and U. O. Häfeli, *Nanomed. Nanotechnol. Biol. Med.*, 2012, **8**, 1007-1016.
55. R. Madru, P. Kjellman, F. Olsson, K. Wingårdh, C. Ingvar, F. Ståhlberg, J. Olsrud, J. Lätt, S. Fredriksson and L. Knutsson, *J. Nucl. Med.*, 2012, **53**, 459-463.
56. Y. Wang and G. Cao, *Chem. Mater.*, 2006, **18**, 2787-2804.
57. A. K. Gupta and M. Gupta, *Biomaterials*, 2005, **26**, 3995-4021.
58. M. Ferrari, *Nat. Rev. Cancer*, 2005, **5**, 161.
59. Z. Liu, F. Kiessling and J. Gärtjens, *J. Nanomater.*, 2010, **2010**, 51.
60. F. N. Carlesso, R. S. Araújo, L. L. Fuscaldi, S. E. M. Miranda, D. Rubello, C. S. Teixeira, D. C. Dos Reis, E. A. Leite, J. N. Silveira and S. O. Fernandes, *Nucl. Med. Commun.*, 2016, **37**, 727-734.
61. R. S. Fernandes, J. O. Silva, L. O. Monteiro, E. A. Leite, G. D. Cassali, D. Rubello, V. N. Cardoso, L. A. Ferreira, M. C. Oliveira and A. L. de Barros, *Biomed. Pharmacother.*, 2016, **84**, 252-257.
62. B. P. Burke, C. Cawthorne and S. J. Archibald, *Phil. Tans. R. Soc.*, 2017, **375**, 20170261.

63. B. P. Burke, C. Cawthorne and S. J. Archibald, in *Radionuclide Labeling and Imaging of Magnetic Nanoparticles*, Taylor and Francis 2018.
64. E. W. Price and C. Orvig, *Chem. Soc. Rev.*, 2014, **43**, 260-290.
65. N. Lewinski, V. Colvin and R. Drezek, *Small*, 2008, **4**, 26-49.
66. M. Bennet, L. Bertinetti, R. K. Neely, A. Schertel, A. Körnig, C. Flors, F. D. Müller, D. Schüler, S. Klumpp and D. Faivre, *Faraday Discuss.*, 2015, **181**, 71-83.
67. Q. Pankhurst, N. Thanh, S. Jones and J. Dobson, *J. Phys. D: Appl. Phys.*, 2009, **42**, 224001.
68. R. Qiao, C. Yang and M. Gao, *J. Mater. Chem.*, 2009, **19**, 6274-6293.
69. D. Ramimoghadam, S. Bagheri and S. B. A. Hamid, *J. Magn. Magn. Mater.*, 2014, **368**, 207-229.
70. J. Huang, X. Zhong, L. Wang, L. Yang and H. Mao, *Theranostics*, 2012, **2**, 86-102.
71. K. Hola, Z. Markova, G. Zoppellaro, J. Tucek and R. Zboril, *Biotechnol. Adv.*, 2015, **33**, 1162-1176.
72. O. ur Rahman, S. C. Mohapatra and S. Ahmad, *Mat. Chem. Phys.*, 2012, **132**, 196-202.
73. A. H. Lu, E. e. L. Salabas and F. Schüth, *Angew. Chem. Int. Ed.*, 2007, **46**, 1222-1244.
74. I. Nedkov, T. Merodiiska, L. Slavov, R. Vandenberghe, Y. Kusano and J. Takada, *J. Magn. Magn. Mater.*, 2006, **300**, 358-367.
75. Y. Wei, B. Han, X. Hu, Y. Lin, X. Wang and X. Deng, *Procedia Engineering*, 2012, **27**, 632-637.
76. A. K. Hauser, R. Mathias, K. W. Anderson and J. Z. Hilt, *Mat. Chem. Phys.*, 2015, **160**, 177-186.
77. P. S. Mueller, C. P. Parker and S. C. Larsen, *Microporous Mesoporous Mater.*, 2015, **204**, 173-179.
78. M. Kim, Y. Chen, Y. Liu and X. Peng, *Adv. Mater.*, 2005, **17**, 1429-1432.
79. C. J. Meledandri, T. Ninjbadgar and D. F. Brougham, *J. Mater. Chem.*, 2011, **21**, 214-222.
80. R. Hufschmid, H. Arami, R. M. Ferguson, M. Gonzales, E. Teeman, L. N. Brush, N. D. Browning and K. M. Krishnan, *Nanoscale*, 2015, **7**, 11142-11154.
81. A. S. Teja and P.-Y. Koh, *Prog. Cryst. Growth Charact. Mater.*, 2009, **55**, 22-45.
82. C. Solans, P. Izquierdo, J. Nolla, N. Azemar and M. Garcia-Celma, *Curr. Opin. Colloid Interface Sci.*, 2005, **10**, 102-110.
83. J. C. Bear, B. Yu, C. Blanco-Andujar, P. D. McNaughten, P. Southern, M.-K. Mafina, Q. A. Pankhurst and I. P. Parkin, *Faraday Discuss.*, 2014, **175**, 83-95.
84. D. Ling and T. Hyeon, *Small*, 2013, **9**, 1450-1466.
85. R. Massart, *IEEE Trans*, 1981, **17**, 1247.
86. J.-P. Jolivet, É. Tronc and C. Chanéac, *Comptes Rendus Chimie*, 2002, **5**, 659-664.
87. N. Fauconnier, A. Bee, J. Roger and J. Pons, in *Trends in Colloid and Interface Science X*, Springer, 1996, pp. 212-216.
88. R. M. Fratila, S. Rivera-Fernández and M. Jesús, *Nanoscale*, 2015, **7**, 8233-8260.
89. K. Turcheniuk, A. V. Tarasevych, V. P. Kukhar, R. Boukherroub and S. Szunerits, *Nanoscale*, 2013, **5**, 10729-10752.
90. B. I. Kharisov, H. R. Dias, O. V. Kharissova, A. Vázquez, Y. Peña and I. Gómez, *RSC Advances*, 2014, **4**, 45354-45381.
91. Y. Zhang, C. Sun, N. Kohler and M. Zhang, *Biomed. Microdevices*, 2004, **6**, 33-40.
92. M. Kuhara, H. Takeyama, T. Tanaka and T. Matsunaga, *Anal. Chem.*, 2004, **76**, 6207-6213.
93. A. Ito, Y. Takizawa, H. Honda, K.-i. Hata, H. Kagami, M. Ueda and T. Kobayashi, *Tissue Eng.*, 2004, **10**, 833-840.
94. L.-S. Wang, M.-C. Chuang and J.-a. A. Ho, *Int. J. Nanomedicine*, 2012, **7**, 4679-4695.

95. M. S. Muthu, D. T. Leong, L. Mei and S.-S. Feng, *Theranostics*, 2014, **4**, 660-677.
96. N. Schleich, F. Danhier and V. Préat, *J. Control. Release*, 2015, **198**, 35-54.
97. H. Xing, K. Hwang and Y. Lu, *Theranostics*, 2016, **6**, 1336.
98. J. Y. Hwang, Z. Li and X. J. Loh, *RSC Advances*, 2016, **6**, 70592-70615.
99. J. Wang, W. Li and J. Zhu, *Polymer*, 2014, **55**, 1079-1096.
100. W. T. Al-Jamal and K. Kostarelos, *Acc. Chem. Res.*, 2011, **44**, 1094-1104.
101. V. P. Torchilin, *Nat. Rev. Drug Discov.*, 2005, **4**, 145-160.
102. A. D. Bangham and R. Horne, *J. Mol. Biol.*, 1964, **8**, 660-668.
103. M. L. Immordino, F. Dosio and L. Cattel, *Int. J. Nanomedicine*, 2006, **1**, 297.
104. Y. C. Barenholz, *J. Control. Release*, 2012, **160**, 117-134.
105. Y. Malam, M. Loizidou and A. M. Seifalian, *Trends Pharmacol. Sci.*, 2009, **30**, 592-599.
106. N. Bertrand, J. Wu, X. Xu, N. Kamaly and O. C. Farokhzad, *Adv. Drug Del. Rev.*, 2014, **66**, 2-25.
107. G. Strijkers, W. Mulder, R. Van Heeswijk, P. Frederik, P. Bomans, P. Magusin and K. Nicolay, *Magn. Reson. Mater. Phys., Biol. Med.*, 2005, **18**, 186-192.
108. W. T. Phillips, B. A. Goins and A. Bao, *WIREs. Nanomed. Nanobi.*, 2009, **1**, 69-83.
109. N. Wiradharma, Y. Zhang, S. Venkataraman, J. L. Hedrick and Y. Y. Yang, *Nano Today*, 2009, **4**, 302-317.
110. M. Elsabahy, M.-È. Perron, N. Bertrand, G.-e. Yu and J.-C. Leroux, *Biomacromolecules*, 2007, **8**, 2250-2257.
111. A. R. Bilia, M. C. Bergonzi, C. Guccione, M. Manconi, A. M. Fadda and C. Sinico, *J. Drug Deliv. Sci. Technol.*, 2016, **32**, 241-255.
112. Y. Xiao, H. Hong, A. Javadi, J. W. Engle, W. Xu, Y. Yang, Y. Zhang, T. E. Barnhart, W. Cai and S. Gong, *Biomaterials*, 2012, **33**, 3071-3082.
113. S.-C. Chen, M.-H. Yang, T.-W. Chung, T.-S. Jhuang, J.-D. Yang, K.-C. Chen, W.-J. Chen, Y.-F. Huang, S.-B. Jong and W.-C. Tsai, *BioMed Res. Int.*, 2017, **2017**.
114. R. Kumar, A. Kulkarni, D. K. Nagesha and S. Sridhar, *Theranostics*, 2012, **2**, 714-722.
115. Y. Pathak and D. Thassu, *Drug delivery nanoparticles formulation and characterization*, CRC Press, 2016.
116. R. Hao, R. Xing, Z. Xu, Y. Hou, S. Gao and S. Sun, *Adv. Mater.*, 2010, **22**, 2729-2742.
117. A. C. Anselmo and S. Mitragotri, *The AAPS journal*, 2015, **17**, 1041-1054.
118. N. Kohler, C. Sun, A. Fichtenholtz, J. Gunn, C. Fang and M. Zhang, *Small*, 2006, **2**, 785-792.
119. M. Pillai, *Technetium-99m radiopharmaceuticals: status and trends*, International Atomic Energy Agency, 2009.
120. R. J. Kowalsky, *Technetium Radiopharmaceutical Chemistry CPD*, The University of New Mexico Health Sciences Center College of Pharmacy, Albuquerque, New Mexico, 2006.
121. P. Bouziotis, D. Psimadas, T. Tsoதாகos, D. Stamopoulos and C. Tsoukalas, *Curr. Top. Med. Chem.*, 2012, **12**, 2694-2702.
122. L. Sandiford, A. Phinikaridou, A. Protti, L. K. Meszaros, X. Cui, Y. Yan, G. Frodsham, P. A. Williamson, N. Gaddum and R. M. Botnar, *ACS Nano*, 2012, **7**, 500-512.
123. J. A. Barreto, M. Matterna, B. Graham, H. Stephan and L. Spiccia, *New J. Chem.*, 2011, **35**, 2705-2712.
124. C. Fu and N. M. Ravindra, *Bioinspir. Biomim Nanobiomater*, 2012, **1**, 229.
125. S. Laurent, D. Forge, M. Port, A. Roch, C. Robic, L. Vander Elst and R. N. Muller, *Chem. Rev.*, 2008, **108**, 2064-2110.
126. O. Bomat-Miguel, P. Tartaj, M. P. Morales, P. Bonville, U. Golla - Schindler, X. Q. Zhao and S. Veintemillas-Verdaguer, *Small*, 2006, **2**, 1476-1483.

127. L. Babes, B. T. Denizot, G. Tanguy, J. J. Le Jeune and P. Jallet, *J. Colloid Interface Sci.*, 1999, **212**, 474-482.
128. W. Wu, Q. He and C. Jiang, *Nanoscale Res. Lett.*, 2008, **3**, 397.
129. R. Hachani, M. Lowdell, M. Birchall, A. Hervault, D. Mertz, S. Begin-Colin and N. T. K. Thanh, *Nanoscale*, 2016, **8**, 3278-3287.
130. A. Gharib, Z. Faezizadeh, S. A. R. Mesbah-Namin and R. Saravani, *DARU J. Pharmac.Sci.*, 2014, **22**, 44.
131. I. Hamley, *Angew. Chem. Int. Ed.*, 2003, **42**, 1692-1712.
132. H. Dong, Y.-C. Chen and C. Feldmann, *Green Chem.*, 2015, **17**, 4107-4132.
133. F. Fievet, J. Lagier and M. Figlarz, *MRS Bull.*, 1989, **14**, 29-34.
134. N. Lee and T. Hyeon, *Chem. Soc. Rev.*, 2012, **41**, 2575-2589.
135. W. Cai and J. Wan, *Journal of colloid and interface science*, 2007, **305**, 366-370.
136. F. Fiévet, S. Ammar-Merah, R. Brayner, F. Chau, M. Giraud, F. Mammeri, J. Peron, J.-Y. Piquemal, L. Sicard and G. Viau, *Chem. Soc. Rev.*, 2018.
137. A. Testino, F. Pilger, M. A. Lucchini, J. E. Q. Quinsaat, C. Stähli and P. Bowen, *Molecules*, 2015, **20**, 10566-10581.
138. J. Fresnais, M. Yan, J. Courtois, T. Bostelmann, A. Bée and J.-F. Berret, *J. Colloid Interface Sci.*, 2013, **395**, 24-30.
139. P. Padwal, R. Bandyopadhyaya and S. Mehra, *Langmuir*, 2014, **30**, 15266-15276.
140. H. He, Y. Zhang, C. Gao and J. Wu, *Chem. Commun.*, 2009, 1655-1657.
141. H. Savaloni and M. Gholipour-Shahraki, 2007.
142. A. Bushroa, R. Rahbari, H. Masjuki and M. Muhamad, *Vacuum*, 2012, **86**, 1107-1112.
143. Y. Kuwahara, T. Miyazaki, Y. Shirosaki and M. Kawashita, *RSC Adv.*, 2014, **4**, 23359-23363.
144. M. C. Mascolo, Y. Pei and T. A. Ring, *Materials*, 2013, **6**, 5549-5567.
145. J. Kumirska, M. Czerwicka, Z. Kaczyński, A. Bychowska, K. Brzozowski, J. Thöming and P. Stepnowski, *Mar. Drugs*, 2010, **8**, 1567-1636.
146. M. Mahmoudi, A. Simchi, M. Imani, A. S. Milani and P. Stroeve, *J. Phys. Chem. B*, 2008, **112**, 14470-14481.
147. H. Zhang, R. Wang, G. Zhang and B. Yang, *Thin Solid Films*, 2003, **429**, 167-173.
148. T. Ahmad, H. Bae, I. Rhee, Y. Chang, J. Lee and S. Hong, *Current Applied Physics*, 2012, **12**, 969-974.
149. C. Zhang, H. Liu, Y. Cui, X. Li, Z. Zhang, Y. Zhang and D. Wang, *Int. J. Nanomedicine*, 2016, **11**, 1097.
150. L. E. LaConte, N. Nitin, O. Zurkiya, D. Caruntu, C. J. O'connor, X. Hu and G. Bao, *JMRI*, 2007, **26**, 1634-1641.
151. Q. L. Vuong, J. F. Berret, J. Fresnais, Y. Gossuin and O. Sandre, *Adv. Healthc. Mater.*, 2012, **1**, 502-512.
152. C. L. Rulfs, R. A. Pacer and R. Hirsch, *J. Inorg. Nucl. Chem.*, 1967, **29**, 681-691.
153. H. Palmedo, C. Marx, A. Ebert, B. Kreft, Y. Ko, A. Türler, R. Vorreuther, U. Göhring, H. Schild and T. Gerhardt, *Eur. J. Nucl. Med. Mol. Imaging*, 2014, **41**, 59-67.
154. U. Abram and R. Alberto, *J. Braz. Chem. Soc.*, 2006, **17**, 1486-1500.
155. R. Torres Martin de Rosales, R. Tavaré, A. Glaria, G. Varma, A. Protti and P. J. Blower, *Bioconjug. Chem.*, 2011, **22**, 455-465.
156. I. Tsiapa, E. K. Efthimiadou, E. Fragogeorgi, G. Loudos, A. D. Varvarigou, P. Bouziotis, G. C. Kordas, D. Mihailidis, G. C. Nikiforidis and S. Xanthopoulos, *J. Colloid Interface Sci.*, 2014, **433**, 163-175.
157. M. Motiei, T. Dreifuss, T. Sadan, N. Omer, T. Blumenfeld-Katzir, E. Fragogeorgi, G. Loudos, R. Popovtzer and N. Ben-Eliezer, *Chem. Lett.*, 2019, **48**, 291-294.

158. F. L. Portilho, E. Helal-Neto, S. S. Cabezas, S. R. Pinto, S. N. dos Santos, L. Pozzo, F. Sancenón, R. Martínez-Máñez and R. Santos-Oliveira, *Artif. Cell Nanomed B.*, 2018, **46**, 1080-1087.
159. B. A. Teicher and S. P. Fricker, *Clin. Cancer Res.*, 2010, **16**, 2927-2931.
160. A. Zlotnik and O. Yoshie, *Immunity*, 2012, **36**, 705-716.
161. F. Balkwill, *Nat. Rev. Cancer*, 2004, **4**, 540.
162. M. Hachet-Haas, K. Balabanian, F. Rohmer, F. Pons, C. Franchet, S. Lecat, K. Y. Chow, R. Dagher, P. Gizzi and B. Didier, *J. Biol. Chem.*, 2008, **283**, 23189-23199.
163. E. A. Berger, P. M. Murphy and J. M. Farber, *Annu. Rev. Immunol.*, 1999, **17**, 657-700.
164. J. A. Esté, C. Cabrera, E. De Clercq, S. Struyf, J. Van Damme, G. Bridger, R. T. Skerlj, M. J. Abrams, G. Henson and A. Gutierrez, *Mol. Pharmacol.*, 1999, **55**, 67-73.
165. A. Y. Odendaal, A. L. Fiamengo, R. Ferdani, T. J. Wadas, D. C. Hill, Y. Peng, K. J. Heroux, J. A. Golen, A. L. Rheingold and C. J. Anderson, *Inorg. Chem.*, 2011, **50**, 3078-3086.
166. L. O. Gerlach, R. T. Skerlj, G. J. Bridger and T. W. Schwartz, *J. Biol. Chem.*, 2001, **276**, 14153-14160.
167. R. T. Skerlj, G. J. Bridger, A. Kaller, E. J. McEachern, J. B. Crawford, Y. Zhou, B. Atsma, J. Langille, S. Nan and D. Veale, *J. Med. Chem.*, 2010, **53**, 3376-3388.
168. S. Hatse, K. Princen, E. De Clercq, M. M. Rosenkilde, T. W. Schwartz, P. E. Hernandez-Abad, R. T. Skerlj, G. J. Bridger and D. Schols, *Biochem. Pharmacol.*, 2005, **70**, 752-761.
169. V. Vinader, D. S. Ahmet, M. S. Ahmed, L. H. Patterson and K. Afarinkia, *PLoS One*, 2013, **8**, e78744.
170. L. O. Gerlach, J. S. Jakobsen, K. P. Jensen, M. R. Rosenkilde, R. T. Skerlj, U. Ryde, G. J. Bridger and T. W. Schwartz, *Biochemistry*, 2003, **42**, 710-717.
171. R. Smith, D. Huskens, D. Daelemans, R. E. Mewis, C. D. Garcia, A. N. Cain, T. N. C. Freeman, C. Pannecouque, E. De Clercq and D. Schols, *Dalton Trans.*, 2012, **41**, 11369-11377.
172. G. C. Valks, G. McRobbie, E. A. Lewis, T. J. Hubin, T. M. Hunter, P. J. Sadler, C. Pannecouque, E. De Clercq and S. J. Archibald, *J. Med. Chem.*, 2006, **49**, 6162-6165.
173. S. M. Dadfar, K. Roemhild, N. I. Drude, S. von Stillfried, R. Knüchel, F. Kiessling and T. Lammers, *Adv. Drug Del. Rev.*, 2019, **138**, 302-325.
174. L. L. Israel, A. Galstyan, E. Holler and J. Y. Ljubimova, *J. Control. Release*, 2020.
175. X. Wang, Y. Wang, Z. G. Chen and D. M. Shin, *Cancer Res. Treat.*, 2009, **41**, 1.
176. J. D. Byrne, T. Betancourt and L. Brannon-Peppas, *Adv. Drug Del. Rev.*, 2008, **60**, 1615-1626.
177. H. Maeda, Y. Matsumura, T. Oda and K. Sasamoto, 1986.
178. J. Kemsheadl and J. Ugelstad, *Molecular and cellular Biochemistry*, 1985, **67**, 11-18.
179. T. Islam and L. Josephson, *Cancer Biomark.*, 2009, **5**, 99-107.
180. F. Kiessling, M. Heilmann, S. Vosseler, M. Lichy, M. Krix, C. Fink, I. Kiessling, H. Steinbauer, L. Schad and N. E. Fusenig, *Int. J. Cancer*, 2003, **104**, 113-120.
181. S. D. Konda, M. Aref, S. Wang, M. Brechbiel and E. C. Wiener, *Magn. Reson. Mater. Phys., Biol. Med.*, 2001, **12**, 104-113.
182. F. Kiessling, J. Huppert, C. Zhang, J. Jayapaul, S. Zwick, E. C. Woenne, M. M. Mueller, H. Zentgraf, M. Eisenhut and Y. Addadi, *Radiology*, 2009, **253**, 462-469.
183. H.-Y. Lee, Z. Li, K. Chen, A. R. Hsu, C. Xu, J. Xie, S. Sun and X. Chen, *J. Nucl. Med.*, 2008, **49**, 1371-1379.
184. X. Shi, S. H. Wang, S. D. Swanson, S. Ge, Z. Cao, M. E. Van Antwerp, K. J. Landmark and J. R. Baker Jr, *Adv. Mater.*, 2008, **20**, 1671-1678.

185. Y. He, W. Song, J. Lei, Z. Li, J. Cao, S. Huang, J. Meng, H. Xu, Z. Jin and H. Xue, *Acta Radiol.*, 2012, **53**, 1049-1058.
186. J. Gallo, N. Kamaly, I. Lavdas, E. Stevens, Q. D. Nguyen, M. Wylezinska-Arridge, E. O. Aboagye and N. J. Long, *Angew. Chem. Int. Ed.*, 2014, **53**, 9550-9554.
187. S. Khan, S. Setua, S. Kumari, N. Dan, A. Massey, B. B. Hafeez, M. M. Yallapu, Z. E. Stiles, A. Alabkaa and J. Yue, *Biomaterials*, 2019, **208**, 83-97.
188. V. Vilas-Boas, B. Espina, Y. V. Kolen'ko, M. Banobre-Lopez, M. Brito, V. Martins, J. A. Duarte, D. Y. Petrovykh, P. Freitas and F. Carvalho, *ACS Omega*, 2019, **4**, 1931-1940.
189. G. F. Liu, H. D. Chen, S. N. Yu, X. D. Li and Z. X. Wang, *Chem. Res. Chin. Univ.*, 2018, **34**, 584-589.
190. C.-H. Liu, K.-M. Chan, T. Chiang, J.-Y. Liu, G.-G. Chern, F.-F. Hsu, Y.-H. Wu, Y.-C. Liu and Y. Chen, *Mol. Pharm.*, 2016, **13**, 2253-2262.
191. C. Ieranò, L. Portella, S. Lusa, G. Salzano, C. D'Alterio, M. Napolitano, M. Buoncervello, D. Macchia, M. Spada and A. Barbieri, *Nanoscale*, 2016, **8**, 7562-7571.
192. N. C. Okoye, J. E. Baumeister, F. N. Khosroshahi, H. M. Hennkens and S. S. Jurisson, *Radiochimica Acta*, 2019, **107**, 1087-1120.
193. K. Abstiens, M. Gregoritzka and A. M. Goepferich, *ACS Appl. Mater. Interfaces*, 2019, **11**, 1311-1320.
194. C. Dalal and N. R. Jana, *J. Phys. Chem. B*, 2017, **121**, 2942-2951.
195. C. Dalal, A. Saha and N. R. Jana, *J. Phys. Chem. C*, 2016, **120**, 6778-6786.
196. A. Khan, G. Nicholson, J. Greenman, L. Madden, G. McRobbie, C. Pannecouque, E. De Clercq, R. Ullom, D. L. Maples and R. D. Maples, *J. Am. Chem. Soc.*, 2009, **131**, 3416-3417.
197. T. J. Hubin, N. W. Alcock and D. H. Busch, *Acta Crystallogr. Sect. C: Cryst. Struct. Commun.*, 2000, **56**, 37-39.
198. G. R. Weisman, M. E. Rogers, E. H. Wong, J. P. Jasinski and E. S. Paight, *Journal of the American Chemical Society*, 1990, **112**, 8604-8605.
199. M. Boiocchi, M. Bonizzoni, L. Fabbrizzi, F. Foti, M. Licchelli, A. Poggi, A. Taglietti and M. Zema, *Chem. Eur. J.*, 2004, **10**, 3209-3216.
200. M. Le Baccon, F. Chuburu, L. Toupet, H. Handel, M. Soibinet, I. Déchamps-Olivier, J.-P. Barbier and M. Aplincourt, *New J. Chem.*, 2001, **25**, 1168-1174.
201. E. H. Wong, G. R. Weisman, D. C. Hill, D. P. Reed, M. E. Rogers, J. S. Condon, M. A. Fagan, J. C. Calabrese, K.-C. Lam and I. A. Guzei, *J. Am. Chem. Soc.* 2000, **122**, 10561-10572.
202. J. Springborg, C. Olsen and I. Sotofte, *Acta Chem. Scand.*, 1995, **49**, 555-563.
203. O. Veiseh, F. M. Kievit, C. Fang, N. Mu, S. Jana, M. C. Leung, H. Mok, R. G. Ellenbogen, J. O. Park and M. Zhang, *Biomaterials*, 2010, **31**, 8032-8042.
204. A. del Campo, T. Sen, J.-P. Lellouche and I. J. Bruce, *J. Magn. Magn. Mater.*, 2005, **293**, 33-40.
205. L. Stelter, J. G. Pinkernelle, R. Michel, R. Schwartländer, N. Raschzok, M. H. Morgul, M. Koch, T. Denecke, J. Ruf and H. Bäumlner, *Molecular Imaging and Biology*, 2010, **12**, 25-34.
206. N. E. Baghdadi, Ph.D Thesis, University of Hull, 2016.
207. C. Zhang, B. Wängler, B. Morgenstern, H. Zentgraf, M. Eisenhut, H. Untenecker, R. Krüger, R. Huss, C. Seliger and W. Semmler, *Langmuir*, 2007, **23**, 1427-1434.
208. M. Hajiramezanali, F. Atyabi, M. Mosayebnia, M. Akhlaghi, P. Geramifar, A. R. Jalilian, S. M. Mazidi, H. Yousefnia, S. Shahhosseini and D. Beiki, *Int. J. Nanomedicine*, 2019, **14**, 2591.

209. C. M. R. Oda, R. S. Fernandes, S. C. de Araújo Lopes, M. C. de Oliveira, V. N. Cardoso, D. M. Santos, A. M. de Castro Pimenta, A. Malachias, R. Paniago and D. M. Townsend, *Biomed. Pharmacother.*, 2017, **89**, 268-275.
210. T. S. Levchenko, W. C. Hartner and V. P. Torchilin, *Methodist Debakey Cardiovasc. J.*, 2012, **8**, 36.
211. J. O. Silva, R. S. Fernandes, S. C. Lopes, V. N. Cardoso, E. A. Leite, G. D. Cassali, M. C. Marzola, D. Rubello, M. C. Oliveira and A. L. B. de Barros, *Mol. Imaging Biol.*, 2016, **18**, 898-904.
212. P. Parhi, C. Mohanty and S. K. Sahoo, *Drug discovery today*, 2012, **17**, 1044-1052.
213. U. Bulbake, S. Doppalapudi, N. Kommineni and W. Khan, *Pharmaceutics*, 2017, **9**, 12.
214. A. V. Kabanov, V. Chekhonin, V. Y. Alakhov, E. Batrakova, A. Lebedev, N. Melik-Nubarov, S. Arzhakov, A. Levashov, G. Morozov and E. Severin, *FEBS Lett.*, 1989, **258**, 343-345.
215. V. P. Torchilin, *Pharm. Res.*, 2007, **24**, 1.
216. A. Varela-Moreira, Y. Shi, M. H. Fens, T. Lammers, W. E. Hennink and R. M. Schiffelers, *Mater. Chem. Front.*, 2017, **1**, 1485-1501.
217. H. Cabral and K. Kataoka, *J. Control. Release*, 2014, **190**, 465-476.
218. A. L. Petersen, A. E. Hansen, A. Gabizon and T. L. Andresen, *Adv. Drug Del. Rev.*, 2012, **64**, 1417-1435.
219. V. Richardson, B. Ryman, R. Jewkes, K. Jeyasingh, M. Tattersall, E. Newlands and S. Kaye, *Br. J. Cancer*, 1979, **40**, 35.
220. Q. F. Ahkong and C. Tilcock, *Int. J. Rad. Appl. Instrum. B*, 1992, **19**, 831839-837840.
221. A. L. Petersen, T. Binderup, P. Rasmussen, J. R. Henriksen, D. R. Elema, A. Kjær and T. L. Andresen, *Biomaterials*, 2011, **32**, 2334-2341.
222. A. Helbok, C. Decristoforo, G. Dobrozemsky, C. Rangger, E. Diederer, B. Stark, R. Prassl and E. von Guggenberg, *J. Liposome Res.*, 2010, **20**, 219-227.
223. D. P. R. Rossin, K. Wooley and M. Welsh, *J. Nucl. Med.*, 2005, 1210-1218.
224. E. Grotz, N. L. Tateosian, J. Salgueiro, E. Bernabeu, L. Gonzalez, M. L. Manca, N. Amiano, D. Valenti, M. Manconi and V. García, *J. Drug Deliv. Sci. Technol.*, 2019, **53**, 101170.
225. S.-H. Cheng, D. Yu, H.-M. Tsai, R. A. Morshed, D. Kanojia, L.-W. Lo, L. Leoni, Y. Govind, L. Zhang and K. S. Aboody, *J. Nucl. Med.*, 2016, **57**, 279-284.
226. A. A. Gabizon, *Clin. Cancer Res.*, 2001, **7**, 223-225.
227. Y. Li, J. Wang, M. G. Wientjes and J. L.-S. Au, *Adv. Drug Del. Rev.*, 2012, **64**, 29-39.
228. H. Maeda, J. Wu, T. Sawa, Y. Matsumura and K. Hori, *J. Control. Release*, 2000, **65**, 271-284.
229. M. D. Bartholomä, A. S. Louie, J. F. Valliant and J. Zubieta, *Chem. Rev.*, 2010, **110**, 2903-2920.
230. D. Shetty, Y.-S. Lee and J. M. Jeong, *Nucl. Med. Mol. Imaging (2010)*, 2010, **44**, 233-240.
231. M. A. Green and M. J. Welch, *Int. J. Rad. Appl. Instrum. B*, 1989, **16**, 435-448.
232. T. J. Wadas, E. H. Wong, G. R. Weisman and C. J. Anderson, *Chem. Rev.*, 2010, **110**, 2858-2902.
233. W. R. Harris and V. L. Pecoraro, *Biochemistry*, 1983, **22**, 292-299.
234. F. Man, P. J. Gawne and R. T. de Rosales, *Adv. Drug Del. Rev.*, 2019.
235. T. van der Geest, P. Laverman, J. M. Metselaar, G. Storm and O. C. Boerman, *Expert Opin. Drug Del.*, 2016, **13**, 1231-1242.
236. F. Emmetiere, C. Irwin, N. T. Viola-Villegas, V. Longo, S. M. Cheal, P. Zanzonico, N. Pillarsetty, W. A. Weber, J. S. Lewis and T. Reiner, *Bioconjug. Chem.*, 2013, **24**, 1784-1789.

237. J. Malinge, B. Géraudie, P. Savel, V. Nataf, A. Prignon, C. Provost, Y. Zhang, P. Ou, K. Kerrou and J.-N. Talbot, *Mol. Pharm.*, 2017, **14**, 406-414.
238. Z. Zhao, Z. Zhou, J. Bao, Z. Wang, J. Hu, X. Chi, K. Ni, R. Wang, X. Chen and Z. Chen, *Nat. Commun.*, 2013, **4**, 2266.
239. R. Alberto, K. Ortner, N. Wheatley, R. Schibli and A. P. Schubiger, *J. Am. Chem. Soc.*, 2001, **123**, 3135-3136.